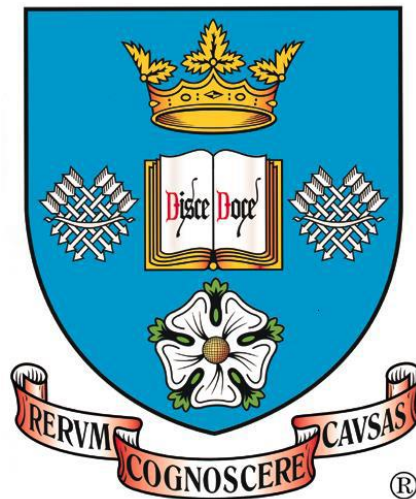# On the mechanism of tool crater wear in titanium alloy machining

Oliver J. Hatt

Department of Materials Science and Engineering

The University of Sheffield

Thesis submitted for the degree of Doctor of Engineering

December 2016

"I like new ideas and old wines. New software and old books. Water fountains and fountain pens. New discoveries and old friends."

<div align="right">Neil deGrasse Tyson</div>

Summary

Today the aerospace industry spends hundreds of millions of dollars on the machining of titanium alloy components. And with increasing aircraft orders, there is pressure to machine at higher production rates and develop more machinable alloys (e.g. TIMETAL® 54M, TMETAL® 407) without compromising titanium's excellent mechanical properties. Increasing the tool life by a factor of minutes can have a dramatic effect on machining cost. Unlike steels, the same tool grade is used for all titanium alloy types from alpha to beta rich, with the latter being more difficult to machine. Diffusion dominated crater wear is the primary tool wear phenomena which has yet to be fully understood. This thesis demonstrates the application of a low cost diffusion couple technique which gives a strong indication of the complex reaction mechanisms occurring at the tool-chip interface during the machining of titanium alloys. These small scale tests have been validated with large scale dynamic machining trials and strong agreement has been observed. The results have allowed for hypotheses to be made over the reaction mechanisms behind tool crater wear underpinned by key observations in the literature. Such a testing regime can be incorporated into alloy design approaches to inform the industry e.g. TIMET and Rolls-Royce about the 'machinability' qualities at a much earlier stage before costly machining trials. Such a method will also aid tool manufacturers to tailor tool carbide grades as well as new coatings to specific alloy chemistries.

This is the first time that small scale testing such as this has shown why different alloy chemistries exhibit different tool wear characteristics. The technique is now being developed further by the aerospace manufacturing supply chain including tool manufacturers and titanium alloy producers. It will be used to; (a) develop more machinable alloys at an earlier stage in the alloy design development and (b) match different titanium alloys to more appropriate tool materials and new coatings. As such this thesis should be of interest to a broad readership including mechanical engineers and materials scientists as well as the machining and manufacturing community.

Contents

Preface

This thesis is submitted for the degree of Doctor of Engineering at the University of Sheffield. It describes research carried out at the Department of Materials Science and Engineering under the supervision of Dr Martin Jackson.

Parts of this thesis have been published and are listed below:

O. Hatt, H. Larsson, F. Giuliani, P. Crawforth, B. P. Wynne and M. Jackson, "Predicting chemical wear in machining titanium alloys via a novel low cost diffusion couple method", Procedia CIRP, 45 (2016) 219-222. (Chapters 4 and 6).

O. Hatt, P. Crawforth and M. Jackson, "On the mechanism of tool crater wear in titanium alloy machining", Wear, 374 (2017) 15. (Chapters 4 and 5).

Acknowledgements

I would first like to thank Dr Martin Jackson for his tremendous support, guidance and enthusiasm for the project. I would also like to thank Prof Brad Wynne for keeping me on my toes academically and regularly taking the mick out of me personally. I also thank Dr Pete Crawforth for useful discussions on the work and for helping guide the project at the early stages.

I am particularly grateful to Dr Henrik Larsson at KTH Royal Institute of Technology, Stockholm for helping develop the DICTRA model for this work. I would also like to give special thanks to Dr Xiangguang Liu for his help and expertise with the FIB instrument. I also thank Dr Peng Zeng for (begrudgingly!) helping me with the TEM. I further extend thanks to the capital where Dr Finn Giuliani and Dr Yatish Patel were gracious enough to let me use the thermomechanical compression rig at Imperial College London.

I was also fortunate to have some great project students over the years, and so I thank Sean Roche, Tom Millington and Zak Lomas for their enthusiasm and contribution to the work in this thesis. I also want to thank all the technical staff who have helped me carry out my experimental work, especially Mike Bell, Paul Hawksworth, Paul Rigden and Kyle Arnold.

I thank all my friends and colleagues, past and present in D1 and the IDC. Whether discussing work at the University or football in the Red Deer, it was always helpful. Cheers for the Tuesday evening trips to Bramall Lane (and more importantly Spoonies) to Coxy, Kyle, Jamie and Jules.

I would like to give personal thanks to my parents and brother who have fully supported me throughout this programme and encouraged me to reach the finish line.

Finally, I reserve heartfelt thanks for my partner Lorena who has sacrificed so much for us both and who has made this work possible. For that, I dedicate this thesis to her.

List of figures

x

List of tables

Nomenclature

BCC	Body centred cubic
BEPM	Blended elemental powder metallurgy
BF	Bright field
BUE	Built up edge
CBN	Cubic boron nitride
CFRP	Carbon fibre reinforced polymer
CP	Commercially pure
EDM	Electric discharge machining
EPMA	Electron probe microanalysis
FCC	Face centred cubic
FIB	Focussed ion beam
HCP	Hexagonal close packed
OCP	Open circuit potential
OD	Outer diameter
PCD	Polycrystalline diamond
PDZ	Primary deformation zone
RT	Room temperature
R_t	Corrosion reaction resistance
SDZ	Secondary deformation zone
SEM	Scanning electron microscope
STA	Solution heat treated and aged
TDZ	Tertiary deformation zone
TEM	Transmission electron microscopy
T_β	Beta transus temperature
VCR	Vacuum compression rig
VW	Vacuum weight
X-EDS	X-ray energy dispersive spectroscopy
XRD	X-ray diffraction
α	Hexagonal close packed alpha phase
α_p	Equiaxed primary alpha
β	Body centred cubic beta phase
χ	Mole fraction

Chapter 1 - Introduction

1.1 Background

With a shift in the aerospace industry towards the production of carbon fibre composite wing, empennage and fuselage aircraft structures, there has been a corresponding increase in the volume of titanium required for high strength forgings and fasteners. This is due to titanium's galvanic corrosion compatibility with carbon, compared to steel or aluminium. In the aero-engine compressor and fan sections there is an increasing move to design titanium alloys with lower densities, enhanced fatigue and ductilities for parts in the next generation of greener, more efficient engines. The aerospace sector continues to be the principle market for titanium which saw a buy-in weight of nearly 60 kt of material in 2012 [1]. Global market forecasts for 2016-2035 anticipate a 4.5% annual growth in air traffic which will require approximately 33,000 new passenger and freighter aircraft to be constructed at a value of US $5.2 trillion [2]. As aircraft companies continue to strive for improvements in fuel efficiency and noise reduction, modern aircraft such as the Airbus A350 XWB and the Boeing 787 Dreamliner are using more carbon fibre reinforced polymers (CFRPs) than ever before. Titanium has a renowned compatibility with CFRPs which will result in titanium remaining an important material in aircraft manufacture for the foreseeable future. In acknowledgement of the increased demand for titanium alloys there is ever increasing pressure for novel high speed machining procedures which is crucial for the UK to remain competitive in the high value manufacturing sector. A recent report from Innovate UK states that "high value manufacturing accounted for 35% of all UK exports in 2010, contributing £151bn to the UK economy" [3].

The growth in titanium use for Boeing and Airbus aircraft has been steadily rising through the years. Figure 1.1 shows how modern aircraft use up to 15% of the total gross empty weight as titanium.
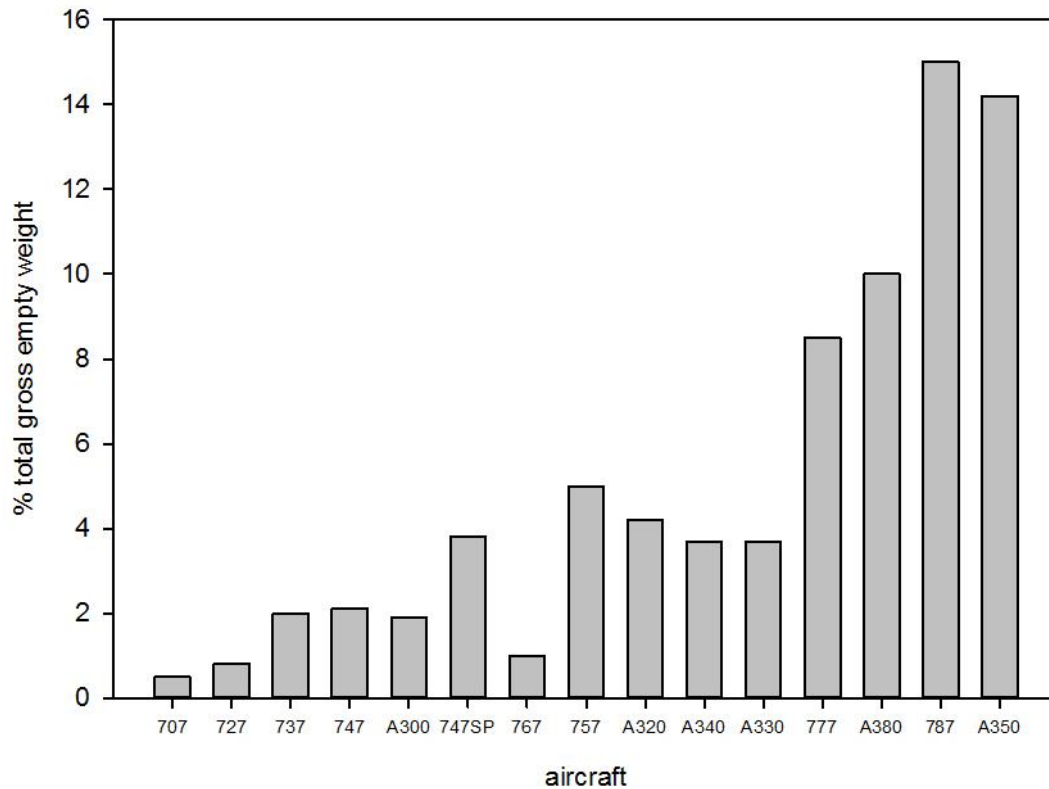
Figure 1.1. Growth in titanium use as % of total gross empty weight in Boeing and Airbus aircraft [4].

There is of course a trade-off, as it is widely known that titanium comes at a high cost and is significantly more expensive than aluminium and steel. Despite the abundancy of titanium in the earth's crust, it is often found in low concentrations and is expensive to extract from the ore due to a high enthalpy of TiO_2 formation. Other aspects of the high cost include ingot melting and machining. Almost all titanium components are intensively machined and this is one of the costliest stages of the multi-stage manufacturing route. Therefore, titanium producers are striving to incorporate good machinability and manufacturability properties as part of their alloy design and product competitiveness.

For the current titanium alloy component machining, tool manufacturers do not offer different tooling solutions to customers based on the alloy chemistry or phase morphology of the billet material. However, it is common knowledge in the machining community that metastable β alloys are more challenging to machine than near α alloys with respect to both tool wear and workpiece surface integrity [5]. Machinists tend to adjust machining speeds depending on the titanium alloy chemistry. An alloy which is more difficult to machine is cut at a lower speed to avoid premature tool failure. Aside from optimising machining parameters, current modern machining practice has seen research mainly focus on cutting

2

tool geometry and tooling systems including high pressure jet-assisted machining [6], compressed air [7], laser-assisted machining [8] and cryogenic cooling [9, 10]. Further advances in improving titanium alloy machining efficiency include the use of modern tool materials such as polycrystalline diamond (PCD) and cubic boron nitride (CBN). Due to the higher thermal conductivity of PCD (250-560 W/mK) compared tungsten carbide (80 W/mK), the material could potentially offer benefits in finish machining operations [7]. CBN tools have also shown promise in terms of tool wear rate in titanium alloy machining for moderate cutting speeds [11]. However, the high cost of PCD and CBN tool materials does limit their application. The poor machinability of titanium alloys requires the use of innovative tool and coating materials as well as intelligent machining conditions if satisfactory tool life is to be achieved [12]. With the exception of broaching, straight grade, uncoated tungsten carbide tooling is generally used for titanium alloy machining. There is no observed increase in tool life when turning titanium alloys with hardmetal and ceramic based coated tools due to the high chemical reactivity of the workpiece material [13]. However, when operating at higher cutting speeds and elevated temperatures, tool manufacturers do recommend TiAlN coated carbide grades deposited via physical vapour deposition (PVD) [14]. With regard to milling operations though, comparative studies in the literature mostly show that uncoated tools outperform coated tools [15-17]. Recent advances in machine tool platforms have also aided titanium alloy machining. Modern 5-axis mill/turn machines allow for the support and monitoring of process kinematics and dynamics as well as the thermal control of cutting processes. Modern machining centres allow for a marked increase in productivity as there are much fewer process steps involved [13]. Furthermore, these machining platforms can also now incorporate ultrasonic assisted machining and laser processing in tandem with high speed machining [18].

Despite the recent progress in cutting tool development and high performance cutting technologies there is still a reliance on uncoated WC-6%Co tool materials for titanium alloy machining (Table 1.1).

TABLE 1.1. A SELECTION OF TITANIUM ALLOYS, THEIR APPLICATIONS, TYPICAL MACHINING SPEED, AND CORRESPONDING TOOL USED. THE MAXIMUM MACHINING SPEEDS QUOTED ARE FOR A TYPICAL FINISHING OPERATION WITH A FEED RATE OF 0.1 MM.REV^{-1} AND A DEPTH OF CUT OF 2 MM.

Titanium alloy	Application	Max. machining speed (m.min^{-1})	Recommended tool
CP-Ti	Heat exchangers	195 [19]	Uncoated WC-6%Co
Ti-834	Compressor discs	70 [20]	Uncoated WC-6%Co
Ti-64	Fan blades	80 [21]	Uncoated WC-6%Co
Ti-6246	Turbine blades	60 [21]	Uncoated WC-6%Co
Ti-5553	Landing gear	30-50 [22]	Uncoated WC-6%Co

Tool wear can be summarised as a combined effect of abrasion, plastic deformation, adhesion and chemical reaction between the workpiece and cutting tool [23]. The latter resulting in diffusion bonding between the tool and workpiece. This leads to crater wear which severely limits tool life and the economics of machining [24]. It was Kramer and Suh [25] who first proposed a quantitative understanding of tool wear by "solution" – a diffusion mechanism; where solution of tool material in the workpiece is primarily responsible for the wear of tool material. Hartung and Kramer [26] found that when machining titanium alloys at cutting speeds of 61-122 m.min^{-1} the main limiting factor for tool life is crater wear. Flank wear does not contribute to the detriment of tool life until crater wear causes edge damage. Past this point, accelerated wear at the flank face of the tool is caused by plastic deformation. Since then, there have been numerous investigations into understanding diffusion wear mechanisms for titanium alloy machining. In most cases this involves complex, costly and time-consuming machining trials [27-31]. More recently though, work has been carried out using static diffusion couple tests in order to study the chemical interdiffusivity between carbide cutting tools and titanium alloys [32-34]. These diffusion couple techniques aim to replicate the intimate contact between the tool and workpiece observed in machining trials. However, despite some success in identifying elemental diffusion and formation of interfacial reaction species, such work has yet to give these preliminary results any real application by way of directly relating them to tool wear or machining performance.

In this work we use a vacuum diffusion couple technique in tandem with outer diameter (OD) turning trials to determine the key mechanism for tool crater wear during the machining of titanium alloys. Thermodynamic modelling of elemental diffusion during the machining process is also employed as a further embellishment to this investigation.

4

1.2 Thesis outline

Chapter 2 is a literature review that includes a general overview of titanium metallurgy including applications, alloy classification, diffusion, corrosion and oxidation. The mechanics of machining are then discussed incorporating orthogonal cutting and the principles of tool wear. A discussion of modern tool materials used for machining processes is then presented alongside the role of titanium alloy chemistry. The chapter concludes by investigating the current literature on diffusion in titanium alloy machining.

Chapter 3 outlines the experimental techniques which were employed during the investigation. These include metallographic sample preparation techniques, optical microscopy, scanning electron microscopy, transmission electron microscopy, focused ion beam milling and X-ray energy dispersive spectroscopy. Further bespoke experimental methodologies are discussed in the relevant experimental chapters which are specific to those investigations.

Chapter 4 uses two novel diffusion couple techniques which replicate diffusion tool wear mechanisms observed in titanium alloy machining. The diffusion couple tests are modelled on the sticking or seizure region at the tool-chip interface. Six different titanium alloys formed a diffusion bond with the tool with the exception of Ti-6Al-2Sn-4Zr-6Mo which did not form a diffusion bond with the tool. This is hypothesised to be due to the high molybdenum content of Ti-6Al-2Sn-4Zr-6Mo which helps the alloy to preserve a protective oxide layer preventing the formation of a diffusion bond with the tool.

Chapter 5 verifies the diffusion couple results obtained from the previous chapter by reporting on outer diameter turning trials using TIMETAL® 54M and Ti-6Al-2Sn-4Zr-6Mo. These alloys are used in the machining trials as they represent the two different behaviours observed in the diffusion couple tests, bonding and non-bonding. High resolution techniques including transmission electron microscopy show how Ti-6Al-2Sn-4Zr-6Mo is more prone to tool crater wear than TIMETAL® 54M despite a greater maximum damage depth being observed in the latter alloy. Strong agreement is observed between the dynamic machining trials and static diffusion couple tests whereby the formation of TiC is found to play a key role in the prevention of tool crater wear.

Chapter 6 investigates the thermodynamic modelling software package, Thermo-Calc and its kinetic module DICTRA in developing a reliable model for the simulation of elemental diffusion between the tool and workpiece during titanium alloy machining. Furthermore, it explores whether such a model can accurately predict the formation of reaction species and phase changes at the tool-workpiece interface. The results of the model are compared with the experimental findings from both the diffusion couple experiments in Chapter 4 and the outer diameter turning trials in Chapter 5.

Chapter 7 concludes this investigation with an impact case study which first sees further diffusion couple tests conducted using titanium-aluminium binary alloys. These tests, coupled with the key findings made throughout this investigation allows for the prediction of the machinability, in terms of tool wear, of two new aerospace development alloys: TIMETAL® 407 and TIMETAL® 575. The potential industrial impact of the work is then discussed before the principal observations made throughout the study are drawn as conclusions. Finally, a further work subsection is detailed which highlights the author's suggested areas of further research.

Chapter 2 - Literature review

2.1 Applications of titanium alloys

The aerospace sector is one the largest users of titanium alloys primarily due to its excellent strength to weight ratio and elevated temperature properties. The high strength, coupled with low density (60% of that of steel [35]) offer attractive weight savings. For example, the landing gear of the Boeing 777 and the Airbus A380 achieved weight savings of over 580 kg [36] by substituting certain struts, rods and beams of steel (4340M) for the titanium alloy Ti-10V-2Fe-3Al. It is also interesting to note that using titanium in landing gear can also significantly reduce maintenance costs due to its corrosion resistance [37]. Titanium alloys are also used in airframes, aero engines and casings. In the intermediate and high pressure compressor stages of gas turbines, titanium alloys have been designed to operate at over 600°C. Other advantages of titanium alloys for aerospace applications include their compatibility with CFRPs; low modulus of elasticity and high ballistic resistance. Figure 2.1 shows the typical titanium alloy usage in the GE-90 aero-engine.
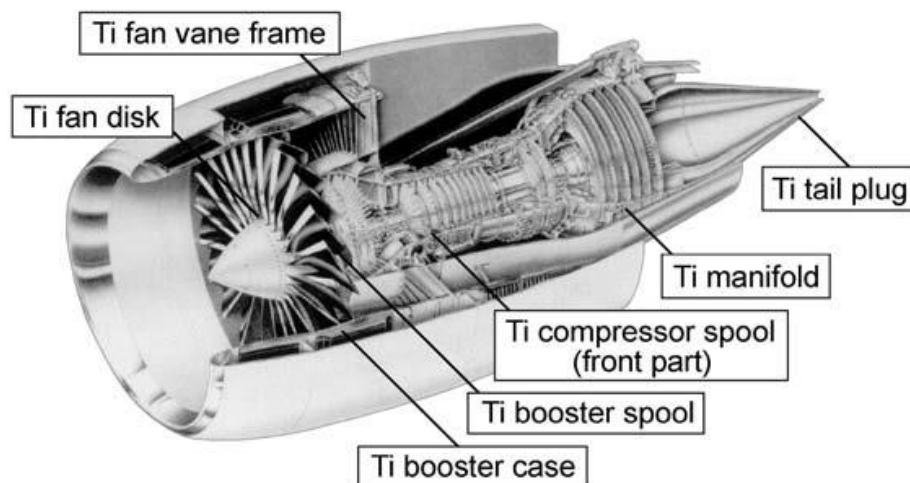
Figure 2.1. Titanium usage in the GE-90 aero-engine [38].

The chemical industry also finds great use in titanium alloys. They are used extensively in reaction vessels due to their corrosion resistance and also in heat exchangers. Aside from chemical and aerospace applications, titanium alloys find their use in many other sectors. Marine and offshore applications utilise the corrosion resistance of titanium alloys due to the destructive nature of seawater. For example, drilling platforms for gas and oil platforms are manufactured from titanium alloys on a huge scale. The sports car industry utilises titanium alloys for coil springs and engine valves because of its high strength to weight ratio. Furthermore, titanium alloys are also employed in the sports and leisure industry for golf

clubs, bicycles and scuba diving equipment for example. Titanium alloys also find their use in medical applications such as hip and dental implants due to its biocompatibility.

2.2 Classification of titanium alloys

Titanium exists as two elemental crystal structures, hexagonal close packed (hcp) at room temperature and body centred cubic (bcc) at higher temperatures. Titanium's two crystal structures (Figure 2.2) are known as α (hcp) and β (bcc). These two systems are the basis for the five classes of titanium alloys: α, near-α, α+β, near-β and β. The temperature at which the material transforms to 100% β is known as the β transus temperature ($T_β$).
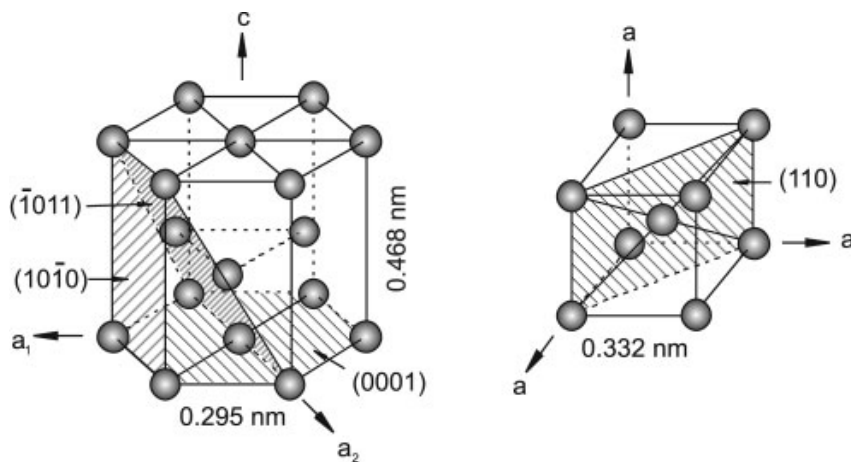
Figure 2.2. Crystal structure of hcp α and bcc β phase [39].

Properties such as plastic deformation and diffusion rate are closely connected with the respective crystal structure.

Alloying elements are classified as neutral, α-stabilisers or β-stabilisers depending on their influence on $T_β$ (Figure 2.3).
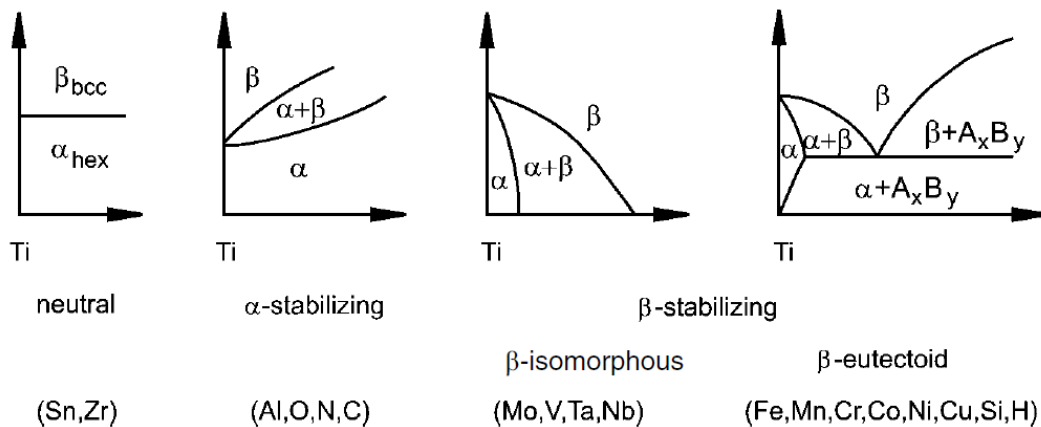
Figure 2.3. Influence of alloying elements on phase diagrams of titanium alloys [39].

The α phase field is extended to higher temperatures by α-stabilising elements, while the β phase field is shifted to lower temperatures by β-stabilising elements. Neutral elements have a negligible effect on T_β. Examples of α stabilisers include Al, O and N, and β stabilisers include Mo, Cr, Mn, V and Fe. Figure 2.4 shows a schematic quasi-vertical section of a ternary titanium system containing both α and β stabilising solute species [40].
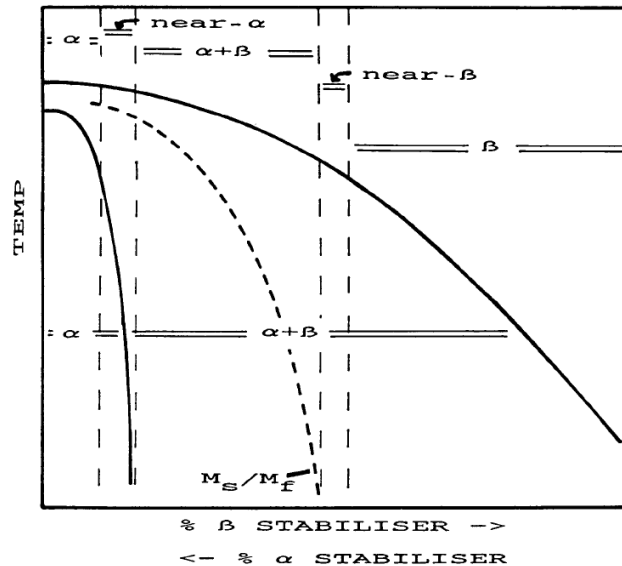
Figure 2.4. Schematic quasi-vertical section for ternary titanium alloys containing both α and β stabilising solute elements [40].

The schematic shows the martensitic start and finish lines denoted as M_s/M_f which are naturally close together. The classes of titanium alloy are marked at the top of the diagram.

2.2.1 α alloys

Examples of α alloys include commercially pure titanium (CP-Ti), Ti-5Al-2.5Sn and Ti-0.3Mo-0.9Ni. This class of alloys is predominantly α phase with a very small volume fraction (several per cent maximum) of β. Compared with the other classes of titanium alloys; the microstructure is relatively simple to comprehend. α alloys have sufficiently small total alloying additions that they essentially do not respond to heat treatment, but which gives them excellent weldability. Furthermore, contrary to α+β and β alloys, thermomechanical processing is used to control texture and grain size rather than manipulate the microstructure. As there is always a small amount of Fe present in all grades of CP titanium there is a small amount of residual β phase. This is because of the low solubility of Fe in the α phase so it is rejected into the β phase during solidification or subsequent cooling. The Fe pins the α grain boundaries and helps control the grain size during recrystallisation, thus the Fe is deliberately alloyed. Further to their high weldability, α alloys exhibit excellent corrosion resistance. For

this reason, CP-Ti is the material of choice for manufacture of chemical and petrochemical processing equipment [41]. The weldability also gives its purpose to use in heat exchangers and other piping applications [42].

2.2.2 Near α alloys

Due to the combination of the excellent creep behaviour of α alloys combined with the high strength of α+β alloys, near α alloys are optimal for high temperature applications. At equilibrium, near α alloys have a small quantity of retained β within their microstructure at room temperature. This gives way for improved workability during forging as this small volume of β phase further increases and stabilises the α+β phase field [43]. The current leading near α alloy is TIMETAL®834 (Ti-834) which has the composition Ti-5Al-4Sn-3.5Zr-0.7Nb-0.5Mo-0.35Si-0.06C. Careful prior processing ensures its exceptional high temperature fatigue and creep performance. This stems from the final microstructure containing 18% residual primary α ($α_p$) with 88% coming from the transformed β. Figure 2.5 shows how Ti-834 is engineered to achieve an ideal ratio of both α and β phases which gives way to a bi-modal structure. This gives the alloy exceptional properties including resistance to creep and crack propagation, high fatigue and fracture toughness, and stability at high temperatures [43]. Ti-834 is primarily used in aero engines for rings, blades and compressor discs.
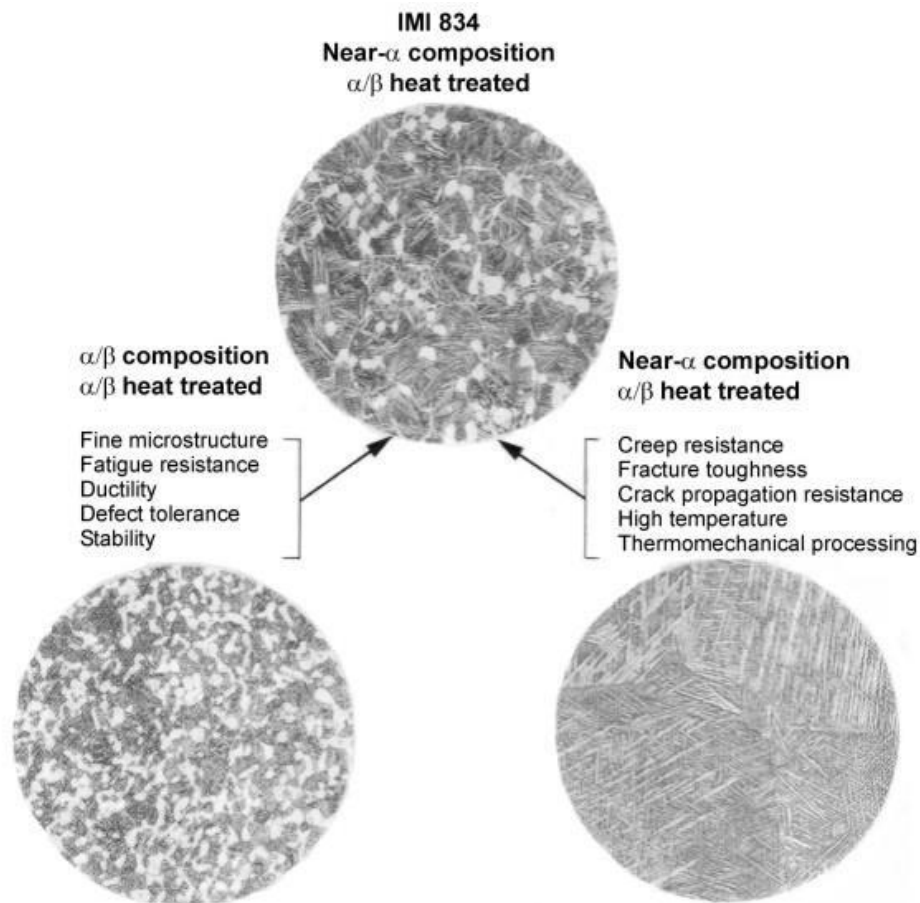
Figure 2.5. Composite light micrographs showing the design of Ti-834 where the resulting bi-modal microstructure can be achieved [44].

2.2.3 α+β alloys

Ti-6Al-4V (Ti-64) is above and beyond the most popular titanium alloy in the aerospace industry. This α+β alloy accounts for more than 50% of all alloys in use today and accounts for near 90% of the titanium used in the aerospace market. Ti-64 is moderately heat treatable and can be heat treated up to tensile strengths of 1100 MPa via a solution treatment and aging (STA) process. These alloys have the best combination of producibility, strength, ductility, durability, and damage tolerance properties. They are reasonably formable and can be superplastically formed. Exploitation of such properties are exhibited by Rolls-Royce who superplastically form Ti-64 in production of their hollow wide chord fan blades. Ti-64 is weldable by almost all welding methods too. These α+β-alloys, particularly Ti-64, are utilised in almost every section of the aircraft including the fuselage, wing, empennage, nacelle and landing gear, usually in the annealed condition [45]. Figure 2.6 shows an example of one of the world's largest titanium forgings fabricated from Ti-64.

Figure 2.6. F-22 bulkhead forging. Approx. 3000 kg, 1.7 m high by 4 m wide [45].

Thermomechanical processing of α+β alloys can produce three distinctly different types of microstructures: fully lamellar structures, fully equiaxed structures, and bimodal (duplex) microstructures containing equiaxed primary α in a lamellar α+β matrix.

2.2.4 Near β alloys

To the right of M_s/M_f in Figure 2.4 lies the compositions of the near or metastable β alloys. Although they only represent a small fraction of overall titanium alloy production, they offer a wealth of properties currently finding applications in structurally critical components. Near β alloys exhibit high specific strength, good formability and reasonable corrosion resistance. Large landing gear truck beam forgings in the aerospace sector are manufactured from near β alloys due to their resistance to fatigue crack propagation, favourable fracture toughness and strength [43]. Today, near β titanium alloys in steady production include Ti-10V-2Fe-3Al (Ti-10-2-3) and Ti-5V-5Mo-5Al-3Cr (Ti-5553). To develop their desirable properties, these alloys undergo a solution treat and age heat-treatment where the α precipitates as the hardening phase in the β matrix. The structure of near β alloys can become fully β if processed above $T_β$ (> 800°C) as this results in α dissolution and gives rise to enhanced β grain growth. Processing at temperatures below $T_β$ allows for a low quantity of $α_p$ which inhibits the excessive β grain growth. Near β alloys have excellent properties which prevent crack initiation and propagation due to their high strength and fracture toughness. Upon formation, the retained β is metastable where a fine α scale can be precipitated via subsequent aging resulting in heightened strength properties. This class of titanium alloys are generally considered to be the highest strength of all with yield stresses in excess of 1200 MPa [40, 43].

2.2.5 β alloys

β alloys contain an extremely high concentration of β stabilising elements which results in the β phase being thermodynamically stable at room temperature. So stable in fact, that even industrial thermodynamic treatment does not result in the alloy decomposing into α and β equilibrium. An example of a β alloy is Ti-13V-11Cr-3Mo which found its application on the SR-71 Blackbird (1964-1998) where 93% of the aircraft was manufactured from titanium

alloys, the majority being β alloys. However, use of such alloys has been limited since [46]. The primary advantages of β alloys include high tensile and fatigue strengths along with easy fabrication into sheet-type products. On the other hand, the disadvantages are numerous including low resistance to crack propagation; poor weldability; and that this class of titanium alloys exhibit virtually no work hardening resulting in difficulty to form into complex shapes [46].

2.3 Diffusion

Diffusion rates are considerably higher in bcc β titanium than the densely packed hcp α titanium. Table 2.1 shows how the diffusion coefficient for α titanium is orders of magnitude smaller than for β titanium. The following coefficients are given for self-diffusion of titanium at 500°C and 1000°C. The resulting diffusion paths, d, support these differences [39].

TABLE 2.1. DIFFUSION COEFFICIENTS AND DIFFUSION PATHS FOR α AND β TITANIUM [39].

Temperature (°C)	Diffusion coefficient (m^2s^{-1})	Time (h)	Diffusion path d (μm)
500	$D_{\alpha\text{-Ti}} \approx 10^{-19}$	50	0.8
	$D_{\beta\text{-Ti}} \approx 10^{-18}$		0.9
1000	$D_{\alpha\text{-Ti}} \approx 10^{-15}$	1	4
	$D_{\beta\text{-Ti}} \approx 10^{-13}$		40

The limited diffusion in α titanium also results in superior mechanical performance compared to β titanium. This is due to the diffusion coefficients being influenced by the microstructure. As the diffusion coefficient of α is more than two orders of magnitude lower than that of β, resistance to creep and oxidation increases with increasing aluminium content. Conversely, the ductility and deformation capability deteriorate [39].

For titanium alloys, many production and processing routes such as annealing and solution treatment ageing are dependent on diffusion properties. Therefore, it is important to understand the diffusion rates of interstitial and substitutional alloying elements in the α and β phases of titanium as well as self-diffusion rates. Furthermore, many application aspects such as creep and oxidation behaviour are diffusion dependent.

Figure 2.7 shows some diffusivity data in the form of Arrhenius plots.
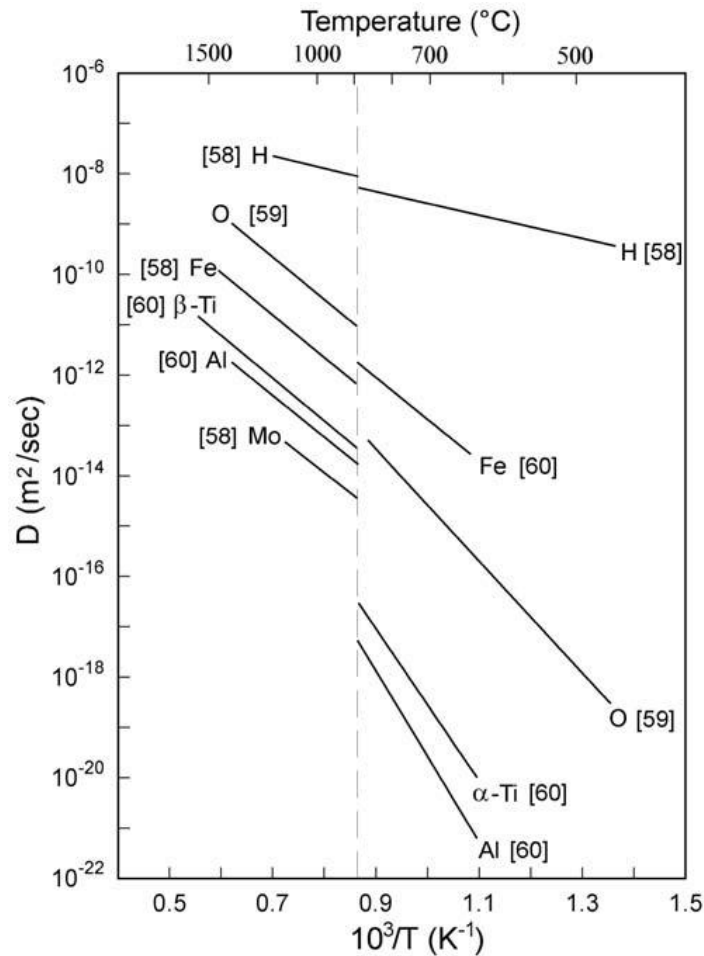
Figure 2.7. Arrhenius diagram of titanium self-diffusion and various alloying elements in the β and α phases of titanium. The delineated line represents the β to α transformation temperature [38].

The figure shows that the self-diffusion rate of β phase titanium is approximately three orders of magnitude faster than that of the α phase. Al and Mo are slow diffusing elements, close to V and Sn, and Nb lies between Al and Mo. Fe and Ni are faster diffusing elements whereas Cr and Mn fall in between Fe and the β-Ti self-diffusion line.

Fe, Ni and Co exhibit a high diffusivity in α-Ti and the diffusivity data of substitutional elements in α titanium depend strongly on the Fe impurity level of the material. This effect is particularly important for the diffusion of aluminium in the α phase for commercial titanium alloys. The interstitial element hydrogen shows very high diffusion rates in both the α and β phase which has serious consequences for applications of titanium alloys under high static loads or fatigue loading because of hydrogen embrittlement [38].

Carman *et al.* [47] have studied the diffusivity and solubility of alloying elements in titanium in regards to sintering of a near β titanium alloy. They used blended elemental powder

metallurgy (BEPM) to achieve near net shape titanium alloy components and found different rates of diffusivity into the titanium matrix for different alloying elements. Tables 2.2 and 2.3 summarise the diffusivities and solubilities of alloying elements at two different temperatures.

TABLE 2.2. SOLUBILITY OF ALLOYING ELEMENTS IN TITANIUM AT THE TEMPERATURES OF PROCESSING [48].

Temp.	Al (wt.%)	V (wt.%)	Mo (wt.%)	Cr (wt.%)	Fe (wt.%)
1250 °C	< 27	Not limited	Not limited	< 44	< 24.7
1020 °C	12	Not limited	Not limited	< 27	< 24
α-Ti	6-10	< 3	<1	< 1	< 0.047

TABLE 2.3. AVERAGE DIFFUSIVITY OF ALLOYING ELEMENTS IN β-TITANIUM AT SINTERING TEMPERATURES [38, 49-59].

Temp.	Al $(\times 10^{-13} \text{m}^2\text{s}^{-1})$	V $(\times 10^{-13} \text{m}^2\text{s}^{-1})$	Mo $(\times 10^{-13} \text{m}^2\text{s}^{-1})$	Cr $(\times 10^{-13} \text{m}^2\text{s}^{-1})$	Fe $(\times 10^{-13} \text{m}^2\text{s}^{-1})$
1250 °C	≈ 12.5 ± 7.5	14 ± 0.1	3.25 ± 1.25	≈ 40	≈ 300
1020 °C	1 ± 0.2	1.25 ± 0.25	0.33 ± 0.15	≈ 4	≈ 30

Figures 2.8a and b illustrate the temperature dependence of the diffusion coefficients.
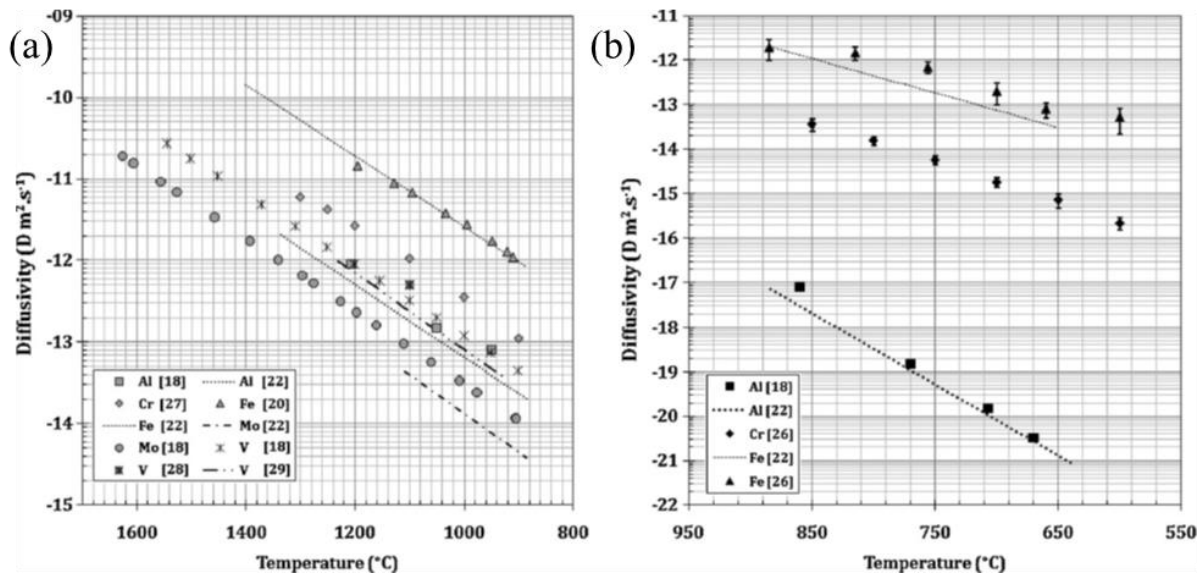
Figure 2.8. Temperature dependence of diffusion coefficients for solute diffusion in pure titanium: (a) β-titanium; (b) α-titanium [47].

For both α and β titanium, Fe and Cr are the fastest diffusers followed by Al in β titanium. Tables 2.2 and 2.3 show that the faster the diffusion of the alloying element, the lower its

solubility in titanium [48-50]. It is known that, due to stabilisation of corresponding phase barriers, α and β stabilisers can hinder redistribution of each other [60, 61].

The knowledge of diffusion characteristics and the understanding of diffusion mechanisms in different phases of the Ti-Al system are of great importance. This is because most commercial titanium alloys are alloyed with aluminium to strengthen the α phase and give resistance to creep and oxidation [39]. In a review by Mishin and Herzig [52] they stress that the understanding of diffusion processes in the Ti-Al system is "very incomplete". The go on to argue that knowledge of the respective atomic mechanisms of diffusion is "poor". Part of their experimental work looked at impurity diffusion in the Ti-Al system. They classified impurities as either normal or fast diffusers. The fast impurity effect observed for some transition elements (e.g. Fe, Co, Ni) was strongest in α-Ti, weaker in β-Ti and Ti_3Al, and smallest in TiAl. This effect was explained by an interstitial-related mechanism. The trend to interstitial solubility sensitivity depends on the availability of Ti atoms in the local environment of an interstitial atom.

2.4 Corrosion and oxidation

Titanium has a standard potential of -1.63 V [38] and demonstrates excellent corrosion resistance. This is due to its ability to form a stable oxide layer of TiO_2 which acts as a protective surface film. This protective layer can passivate titanium for as long as the integrity of the layer is maintained. However, titanium only exhibits this strong corrosion resistance in oxidising environments and not reducing environments where the protective layer breaks down. Therefore corrosion resistance against strong acids is poor [41] and demonstrates why acids such as hydrofluoric acid are used to etch titanium during sample micropreparation. Aside from CP grades of titanium, higher strength α+β and β titanium alloys also exhibit strong corrosion resistance. It is interesting to note that alloy contents of more than 3% Mo and 8% Zr are extremely beneficial, but quantities of Al above 3% are actually detrimental [62]. Table 2.4 lists the repassivation potentials of select titanium alloys.

TABLE 2.4. REPASSIVATION POTENTIAL, OR CRITICAL PITTING POTENTIAL IN BOILING 5% SODIUM CHLORIDE SOLUTION OF VARIOUS TITANIUM ALLOYS IN THE ANNEALED CONDITION [62].

	CP-Ti Grade 2	Ti-6-4	Ti-15-3	B120VCA	Beta 21S	Beta C
Repassivation Potential (V) vs. Ag/AgCl	6.2	1.8	2.0	2.7	2.8	3.0

CP-Ti shows the highest value of 6.2 V which therefore means it exhibits the highest pitting corrosion resistance. As all the other alloys show repassive potentials of values higher than 1 V, then they are still considered to be resistant to pitting corrosion [41].

Crevice corrosion is frequently the serious mode of attack for titanium when exposed to highly acidic environments containing high concentration of chlorides at elevated temperatures [38, 63-68]. Figure 2.9 shows the combination of pH level and temperature at which crevice attack is observed for assorted titanium grades in NaCl [41].
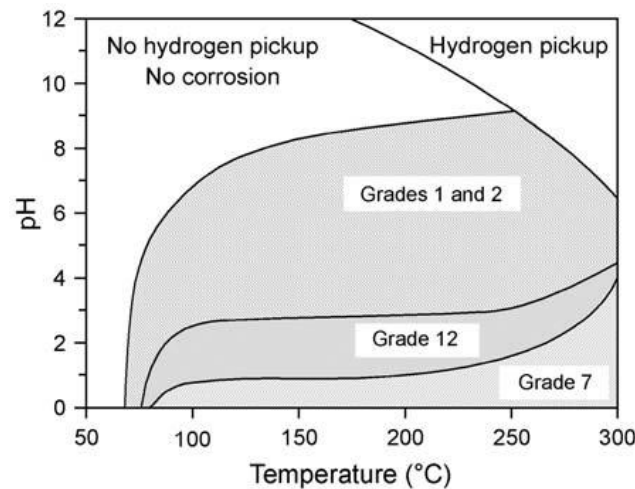
Figure 2.9. Temperature and pH limits for crevice corrosion of various titanium grades in NaCl [41].

It is important to see that the crevice corrosion resistance of Grade 2 CP-Ti can be strengthened by adding 0.3Mo+0.8Ni (Grade 12) or even further by adding Pd (Grade 7) [38]. Thorough research has been conducted on improving the stability of the surface oxide film of Ti by suitable alloying [69-75]. Nishimura found that the corrosion reaction resistance (R_t) for titanium alloys increased with addition of molybdenum as an alloying element [76]. Investigations into changes in chloride ion concentration, pH and potential were conducted within the crevice. This was done over long periods of time using microelectrodes. Figure

17

2.10a shows Nishimura's results of changes in crevice current of CP-Ti and 15%Mo-Ti in neutral 10% NaCl at 100°C as a function of time.
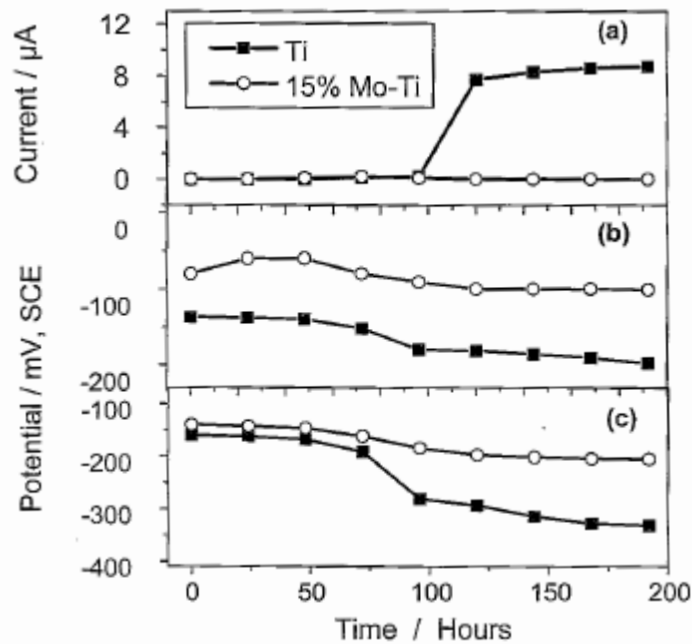
Figure 2.10. Change in (a) Crevice current; (b) Potential outside crevice and (c) Potential inside crevice [76].

For the first 96 h, there is no noticeable change in crevice current for both Ti and 15%Mo-Ti, but then there is a marked increase in current for Ti. Simultaneously, Figures 2.11b and c show a change of potential both inside and outside the crevice of Ti from -130 mV to -196 mV and -165 mV to -306 mV respectively. Importantly, these changes in potentials to a more active region reflected the decrease in stability of the passive film over the Ti surface which leads to an active dissolution reaction within the crevice [63, 65, 66, 76]. Conversely, the lack of changes for the above parameters for 15%Mo-Ti suggests that the integrity of the passive film of the alloy was preserved. Therefore, this alloy showed better resistance to corrosion than CP-Ti.

Figure 2.11 shows the changes within the crevice environment for both pH and chloride concentration inside the crevice of CP-Ti and 15%Mo-Ti in 10% NaCl at 100°C.
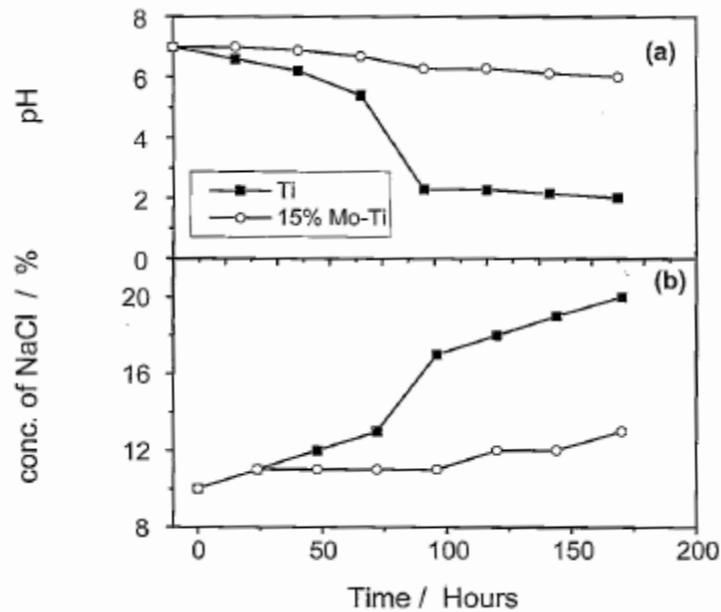
Figure 2.11. Changes within the crevice environment of (a) pH and (b) chloride concentration [76].

For CP-Ti after 96 h, the pH within the crevice had slowly moved towards lower values and settled on pH 2.3. This shows that the predominant dissolution reaction is happening within the crevice. Interestingly, this process results in producing Ti ions which subsequently undergo a hydrolysis reaction to produce H^+ ions which in turn, contribute to further decreasing the value of pH [66]. It can be seen for CP-Ti how the concentration of NaCl increases from 10% to 17% after 96 h and in order to maintain electro neutrality it follows that the acidity must also increase. This results in continuous propagation of crevice corrosion in CP-Ti after 96 h. Conversely, observing the same data for Ti-15%Mo shows only a marginal increase in chloride concentration. The behaviour of this alloy suggests that the Mo helps strengthen and preserve the passive film under high chloride concentrations and temperatures. The investigation to the effect of Mo alloying was taken further by monitoring the open circuit potential (OCP) in 20% NaCl at different pH values (Figure 2.12).
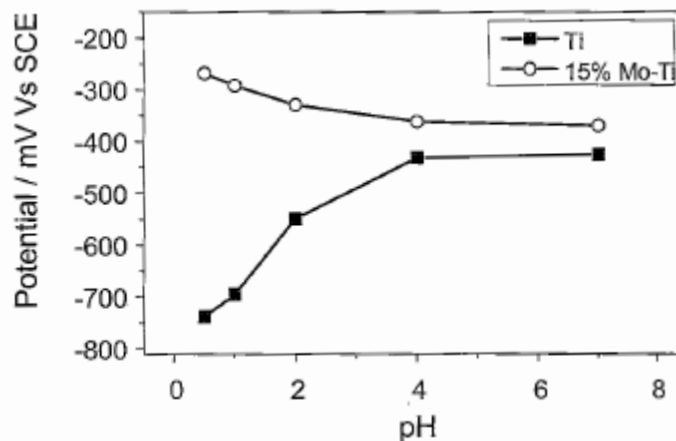
Figure 2.12. Open circuit potential (OCP) after 1 h immersion as a function of pH for Ti and Ti-15%Mo in 20% NaCl at 100°C [76].

The figure shows how CP-Ti is susceptible to crevice corrosion at pH levels < 4 as the OCP shifts to low values. However, the Ti-15%Mo alloy shows steady OCP levels and hence no crevice corrosion for the pH range 0.5-6.8 in a solution of 20% NaCl. The investigation has proved that alloying molybdenum with titanium increases the material's resistance to corrosion. Using microelectrode monitoring, potentiodyanmic polarisation measurements and electrochemical impedance spectroscopy, a molybdenum bearing titanium alloy can preserve a protective passive film under acidic conditions, high chloride concentrations and high temperatures [76].

Tomashov et al. [69] have looked at increasing the corrosion resistance of titanium in acids by alloying with Pd, Cr and Mo. They found that even small amounts of Pd (0.1%) were enough to considerably increase the corrosion resistance of titanium in acid. This is due to a shift in steady-state potential of the alloy by a decrease in hydrogen overvoltage to the region of values where Ti is passive. Secondly, they observed that alloying titanium with molybdenum c.f. Nishimura et al. [76] increased the resistance to corrosion as molybdenum inhibits the anodic dissolution reaction of the alloy and increases thermodynamic stability of the passive film. Interestingly though, alloying with chromium did not strengthen the corrosion resistance of the titanium, and in some cases it actually diminished it. In acid at a potential corresponding to the steady-state potential of titanium, chromium has a lesser tendency to passivate than titanium. However, ternary alloys such as Ti-Pd-Cr and Ti-Pd-Mo have a high corrosion resistance in acid. The work shows how alloying with palladium shifts the steady-state corrosion potentials of these alloys in the noble direction and alloying with

20

chromium and molybdenum leads to a concurrent reduction of the anodic dissolution current in the proximity of the steady-state potential [69].

Tomashov *et al.* [70] then took the work further by investigating passivation and corrosion behaviour of titanium and binary titanium alloys. They showed the structure effects of binaries and ternaries on the corrosion rate in 5% HCl solution at 100°C (Table 2.5) [77].

TABLE 2.5. THE EFFECT OF COMPOSITION AND STRUCTURE OF TITANIUM ALLOYS ON THE CORROSION RATE IN 5% HYDROCHLORIC ACID AT 100°C [77].

Alloy	Single phase		Two-phase	
	Structure	Corrosion rate $g/m^2.h$	Structure	Corrosion rate $g/m^2.h$
Ti	α	10.0	-	-
Ti-5Cr	α	10.0	α+γ	133.0
Ti-15Cr	β	28.6	α+γ	230.0
Ti-5Cr-5Ta	β	9.7	α+γ	79.0
Ti-5Cr-15Ta	β	5.8	α+γ	11.0

It can be seen that the two-phase alloys α+γ have a corrosion rate 2-10 times greater than the single phase alloys of the same composition. This is explained by a lowering of overvoltage of hydrogen evolution on the cathode for two-phase alloys in comparison with single-phase. This was observed by measuring the cathode polarisation curves. This process increases the rate of anodic dissolution. This is because the phase $TiCr_2$ or $(TiTa)Cr_2$ undergoes intense corrosion and leads to formation of structure defects [70]. It was also shown that the rate of alloy dissolution increases as chromium percentage in the alloy grows and the rate decreases as tantalum percentage increases.

Glass *et al.* [71] have looked at the transpassive behaviour of Ti-Mo alloys in acid. The time behaviour upon insertion into solution, E_{oc} for titanium and a selection of Ti-Mo alloys is shown in Figure 2.13.
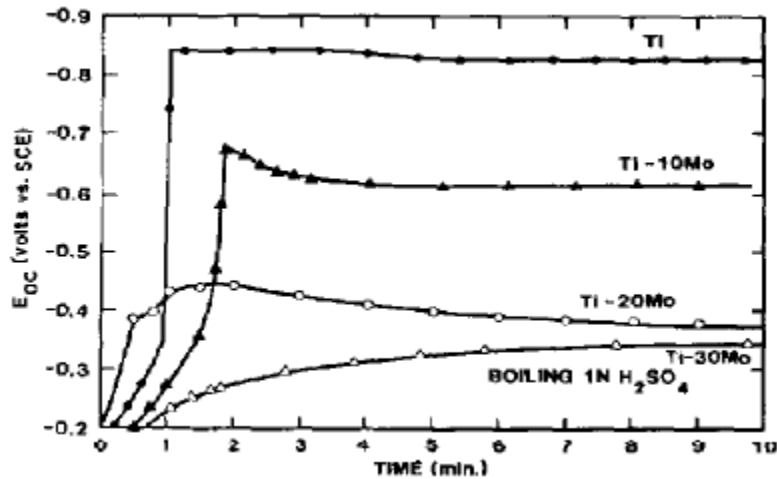
Figure 2.13. E_{oc} - time behaviour for CP-Ti and Ti-10, 20, 30Mo following immersion into solution [71].

It can be seen that CP-Ti rapidly activates upon immersion into acid attaining an active corrosion potential of -0.83 V. Ti-10Mo also exhibits active corrosion in this solution, however the value of E_{oc} is lower, and the time is longer. This is due to a lower hydrogen evolution overvoltage resulting from the molybdenum content [69]. The Ti alloys with the higher molybdenum content of 20% and 30% remain passive in this medium. The slow attainment of the steady-state E_{oc} for these alloys is due to readjustment of the Mo/Ti ratio within the oxide films and a film thickening process. Within the region of transpassivation with respect to molybdenum, the molybdenum/titanium ratio within at least the outermost layers of the oxide decreases as the potential of the binary alloys is made more positive. AES analysis shows that the outer layers of the oxide films become more protective and have a more defect-free structure *c.f.* TiO_2. This leads to a decrease in anodic currents.

2.5 Machining

The aim of any manufacturing process is to achieve a component of specified shape and material properties. A machining process involves removing surplus material from a workpiece to produce the desired shape. Generally, this surplus material is removed from the workpiece in the form of chips through interaction of the workpiece with the chosen tool [78]. Advances in machining are achieved by the ingenuity, not just of the metallurgist, but also of the machine tool operator, lubrication engineer and tool designer. With deeper knowledge of events at the cutting edge of the tool, the performance and life of tools; the machinability of metals and alloys; and the final qualities of the machined surface can all be increased [24].

22

It is important to understand and define the term 'machinability'. Trent quips "the machinability of an alloy is similar to the palatability of wine – easily appreciated but not readily measured in quantitative terms" [24]. Unfortunately, there is no single unified definition or parameter one can use or measure to determine the machinability of a material. A material may show desirable machinability according to one criterion, but poor machinability according to another. Furthermore, there are so many practitioners involved in the machining process that it becomes subjective. This includes the opinions of the engineer planning the cutting process using CADCAM to the machinist operating the rig on the shop floor. Relative machinability may change depending on which cutting process is used (turning vs. milling); tool material chosen (tungsten carbides, cubic boron nitrides); or even machining environment (cryogenic, room temperature). Despite the lack of solid definition, today machinability tends to be assessed by a combination of the following criteria: tool life; material rate of removal; cutting forces; surface finish; and chip shape [24].

Within the metal processing industry there are four fundamental machining processes: turning, milling, drilling and grinding. The principles of turning (orthogonal cutting) are discussed below. However, the latter processes are beyond the scope of this study and so the reader is advised to consult Trent and Wright [24].

2.5.1 Fundamentals of turning

Turning is the most frequently employed experimental technique in metal cutting. The workpiece is held in the chuck of the lathe and rotated at a pre-determined speed. The tool is held rigidly in a tool holder and moved at a constant rate along the axis of the workpiece, cutting away a layer of metal to form a profile (Figure 2.14).
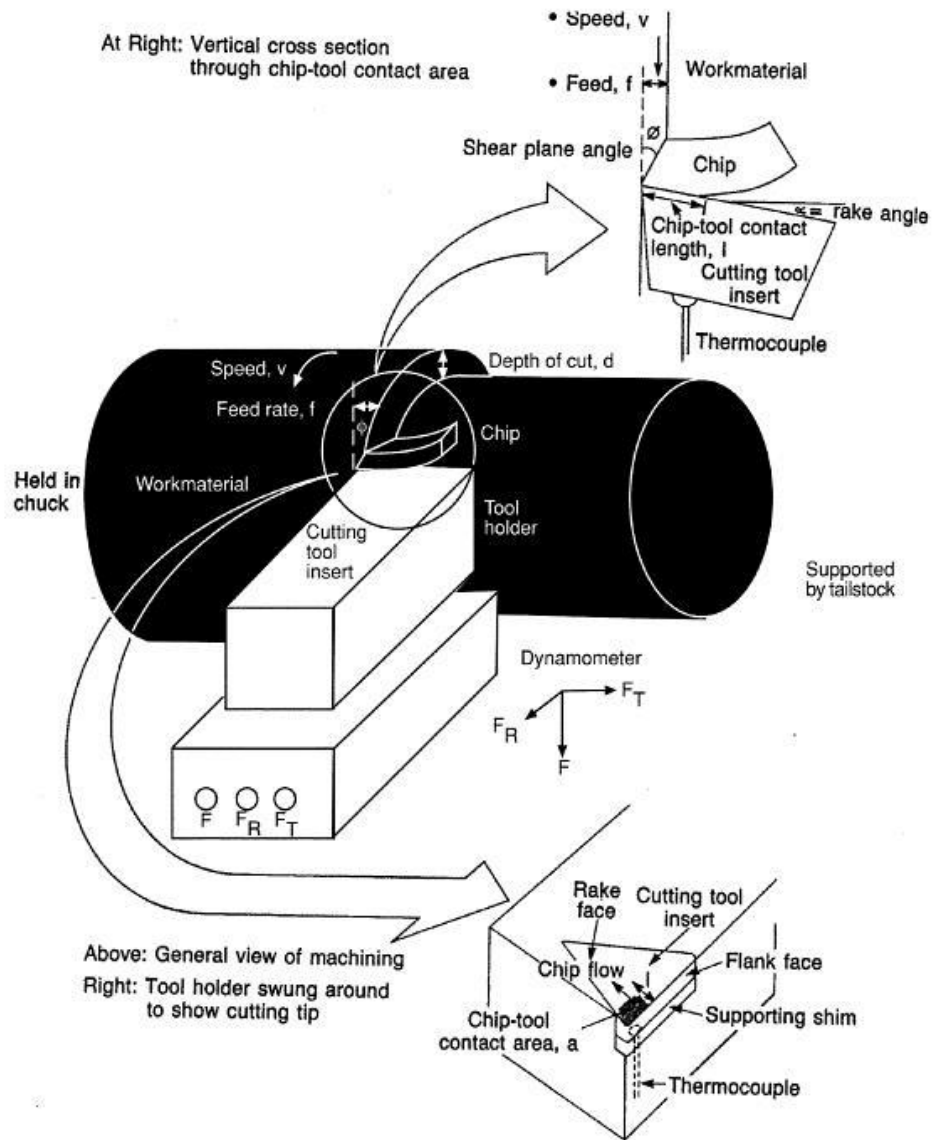
Figure 2.14. Lathe turning showing a vertical cross-section in top right and detail of insert geometry in bottom right [24].

The cutting speed, V_c is the rate at which the uncut surface of the work passes the cutting edge of the tool; it is usually expressed in units of m.min^{-1}. The feed, f is the distance moved by the tool as it advances against the workpiece, this is often expressed as mm.rev^{-1}. The depth of cut (DOC), w is the thickness of metal removed from the workpiece measured in a radial direction. This is the volume of workpiece which can be removed per unit time, often expressed in units of mm. Using the above parameters one can derive an expression for the rate of metal removal (Equation 2.1).

$$V_c f w = rate\ of\ removal \hspace{4cm} \text{Equation 2.1}$$

To achieve optimum cutting parameters, the cutting speed and feed are adjusted. Cutting speed is usually between 3 and 200 m.min^{-1}, and feed can be from as low as 0.0125 to 2.5 mm rev^{-1} for heavy cutting. Depth of cut can vary to over 25 mm. The main features of a turning tool can be seen in Figure 2.15.
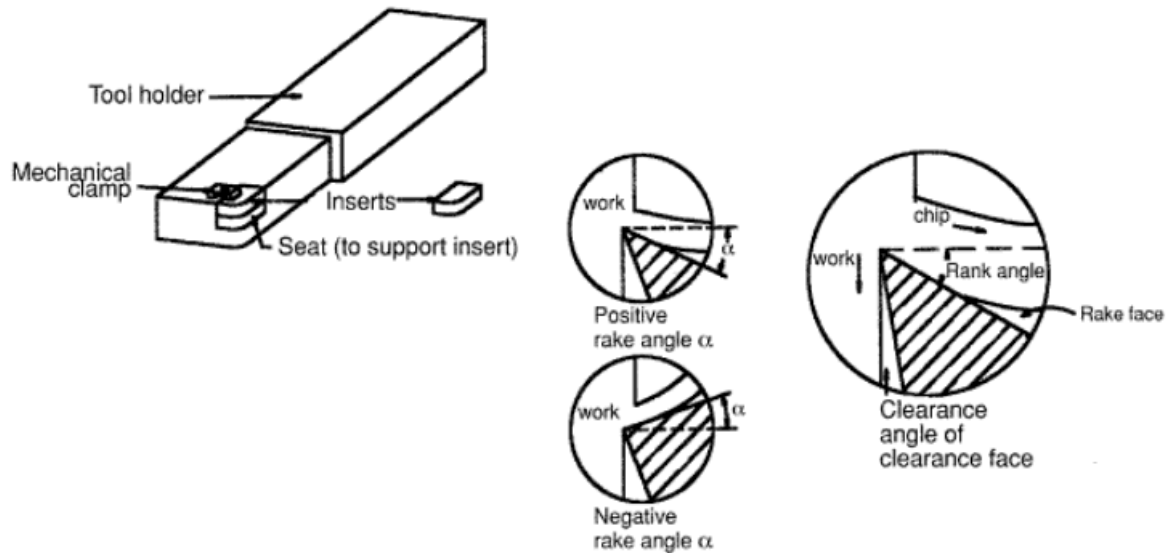
Figure 2.15. Cutting tool terminology [24].

The rake face is the surface of the tool over which the chip flows. The intersection of the rake face with the flank of the tool is called the cutting edge. The clearance angle is there to prevent the flank of the tool interacting with the freshly cut metal surface. The clearance angle is usually between 6 and 10°. The rake face is inclined at an angle which can be adjusted to achieve optimum cutting performance for particular materials. The rake angle is measured from a line parallel to the axis of rotation of the workpiece. A positive rake angle is one where the rake face dips below the line, and conversely, a negative rake angle is one where the rake face is above the line [24].

During a turning operation, cutting can be either orthogonal or oblique. During orthogonal cutting, the cutting angle is at 90° in respect to the direction of rotation of the workpiece. On the other hand, oblique cutting does not flow on the orthogonal plane. Machining operations usually consider orthogonal cutting as a useful, more manageable model [79]. The simplicity of orthogonal cutting is the main reason behind its frequent use in machining research. A simplified schematic of 2D orthogonal cutting is shown in Figure 2.16a.
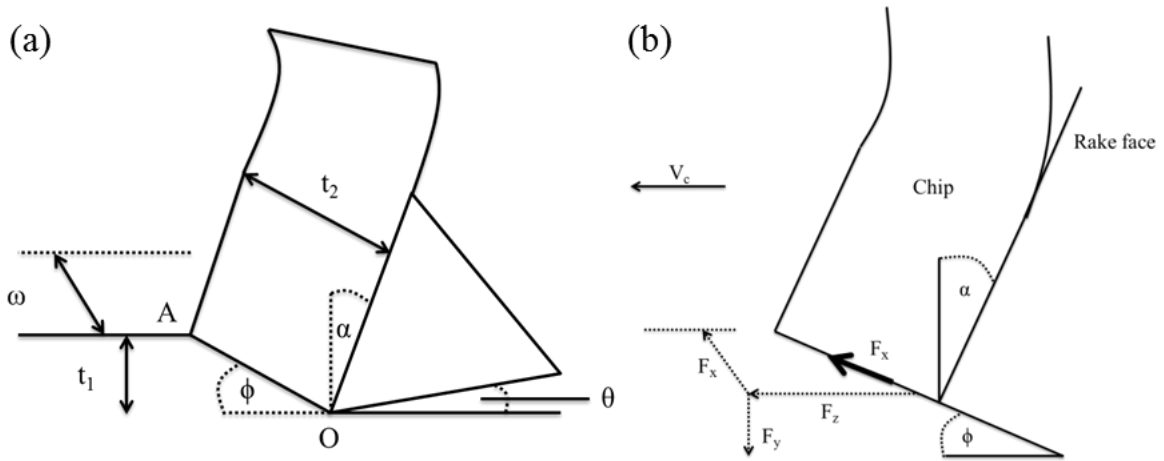
Figure 2.16. Schematics of simple two-dimensional orthogonal cutting showing (a) important dimensional parameters and (b) the ensuing force components in the system [80].

The tool is characterised by the rake angle, α and the clearance (or relief) angle, θ. The rake angle and clearance angle are controlled by the tool holder. In real machining, all machining trials are of course three-dimensional, therefore ω corresponds to the DOC / width of cutting material [43]. The cutting process creates intense forces upon the tool so that shearing of the workpiece occurs at the cutting zone. The chip thickness ratio, r = t_1 / t_2 can be calculated and is normally r ≈ 0.5. The formation of the chip subjects the workpiece to large plastic shear strains (γ = 2-4) where the strain rates are > 10^3 s^{-1}. Within the vicinity of AO there is a large region of localised shear which is inclined with a shear angle, ϕ [80].

Figure 2.16b shows the orthogonal cutting arrangement labelled with the resulting stress components. During a machining (orthogonal) trial, the resulting instantaneous cutting forces are defined as F_x, the force acting within the plane of the DOC normal direction normal force; F_y the feed direction thrust force; and F_z the force in the direction of cutting. Using these parameters with the known machining parameters, Merchant [81-83] has shown how to determine the friction coefficient, μ for the cutting environment, the resultant shear plane force, F_s and the average shear stress, τ of the material acting on the shear plane (Equations 2.2 to 2.4) [43].

The friction coefficient at the tool face, μ:

$$\mu = \frac{F_y + F_z \tan \alpha}{F_z - F_y \tan \alpha}$$

Equation 2.2

The resultant force resolved parallel and normal to the shear plane, F_s:

$$F_s = F_z \cos \phi - F_y \sin \phi$$

Equation 2.3

From the resultant shear plane force F_s, the average shear stress of the material, τ.

$$\tau = \frac{F_s + \sin\phi}{\omega t_1}$$
Equation 2.4

2.5.2 Titanium alloy machining

Titanium alloys are generally considered to be difficult to machine due to several inherent properties they possess. Firstly, titanium is a poor conductor of heat which makes it difficult for the high temperatures reached at the cutting zone to dissipate. This high concentration of heat at the cutting edge creates severe problems for both tool wear and workpiece surface integrity. Secondly, titanium alloys exhibit high chemical reactivity which is further promoted by the aforementioned high concentrations of heat at the cutting zone. The strong chemical reactivity can cause severe tool wear and even catastrophic tool failure. Thirdly, titanium alloys have a relatively low modulus of elasticity resulting in a low chatter stability limit. This leaves the system prone to chatter unless stable cutting parameters are identified. Lastly, the lower hardness of titanium alloys can lead to the possibility of galling the workpiece with the cutting tool [24, 39].

When machined, titanium alloys produce a signature segmented, or 'saw-tooth' chip formation (Figure 2.17).
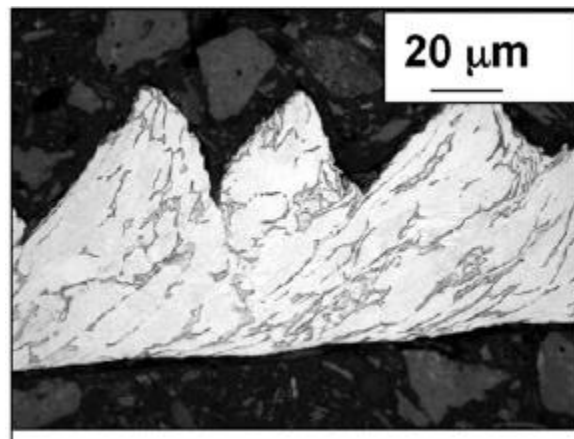
Figure 2.17. Typical 'saw-tooth' chip formation of a machined titanium alloy. This example shows Ti-64, after Arrazola *et al.* [84].

The titanium alloy chip formation is due to plastic instability during the cutting process resulting from the competition between the thermal softening and work hardening in the primary shear zone [85]. Titanium alloys exhibit these intense shear bands due to the materials low thermal conductivity. During the segmentation cycle, each course of thermoplastic shear is brief and relieves the stress. Following this, compressive strain

continues by dislocation movement until the next thermoplastic shear band is introduced. The chip is frequently found to be bonded to the cutting tool after the machining process due to forming strong diffusion bonds with the tool material. Whereas Figure 2.16 illustrated a schematic for continuous chip formation as observed when machining steels for example, Figure 2.18 shows a model for segmented chip formation as observed when machining Ti-64.
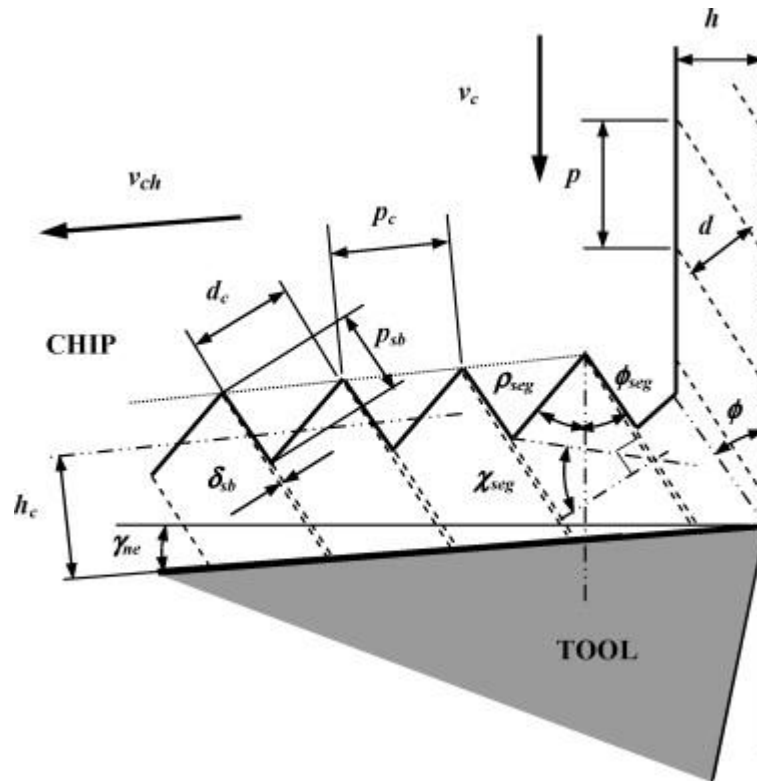
Figure 2.18. The geometry of chip segmentation when machining Ti-64 [86].

There are two stages to the process of segmented chip formation where at the tool-chip interface, the workpiece material experiences plastic deformation which causes it to bulge. As the amount of strain increases, it reaches a critical level where catastrophic failure occurs which results in the formation of a shear band extending from the tool tip to the workpiece surface. The chips result in exhibiting deformed chip segments separated by intense narrow shear bands [86].

Measuring chip cross-sections from experimental micrographs can give us the direction of localised shear, ϕ_{seg}. There could be variation of the instantaneous value of the shear angle, ϕ during the upsetting phase but for the catastrophic shear phase it reaches a value of ϕ_{seg}. This variation reduces at higher cutting speeds so we can assume $\phi \approx \phi_{seg}$, therefore the thickness of segment, $dc=d$ remains constant during the upsetting phase. This allows us to say that,

within each segment, the shear occurs along planes parallel to the adjacent shear bands. The angle, ρ_{seg} allows us to determine the critical shear to initiate shear band formation. This is where there is bulging of the workpiece at the end of the upsetting phase [86]. The shear within the segment is given by Equation 2.5 [87]:

$$\gamma_{seg} = tan\chi_{seg} = \frac{sin\rho_{seg}}{sin\phi_{seg}sin(\phi_{seg}+\rho_{seg})} \qquad \text{Equation 2.5}$$

As is generally the case when $\phi_{seg} \neq$ constant, the segment shear strain is given by Equation 2.6 [88]:

$$\gamma_{seg} = \frac{1}{\lambda_h sin\phi_{seg}}\sqrt{C} \qquad \text{Equation 2.6}$$

Where:

$$C = \lambda_h^2 - \frac{2\lambda_h cos(\rho_{seg})}{sin(\phi_{seg}+\rho_{seg})} + \frac{1}{sin^2(\phi_{seg}+\rho_{seg)})}$$

At higher cutting speeds, Equations 2.5 and 2.6 are identical where $\phi=\phi_{seg}$. The sum of the homogenous strain, γ_{seg} and the catastrophic shear strain, γ_c is equal to the shear strain within the shear band, γ_{sb}. The catastrophic shear strain is the ratio of the shear band projection, p_{sb} to the shear band thickness, δ_{sb} (Equation 2.7) [86].

$$\gamma_{sb} = \gamma_{seg} + \gamma_c \qquad \text{Equation 2.7}$$

Where:

$$\gamma_c = \frac{p_{sb}}{\delta_{sb}}$$

Sagapuram *et al.* [89] were able to capture shear band development when machining titanium alloys. Figure 2.19 shows an image sequence of shear band development in Ti-64.
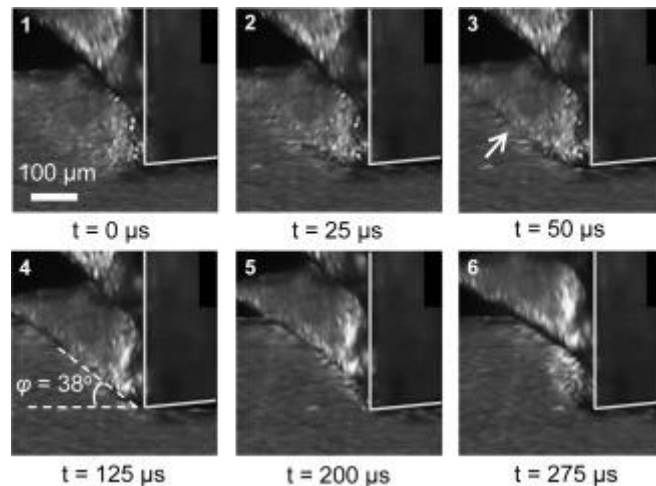
Figure 2.19. Shear band development in Ti-64. Frames 1-3 show initiation of a "weak path" (arrow), followed by shear (sliding) along this path in frames 4-6 [89].

Frames 1-3 show creation of a planar "weak path" which is the first step before subsequent localised flow. Frames 4-6 show the second step which is shear along the localised band with each side of the band sliding as a rigid body. This step reduces the load bearing area which contributes to flow softening. The team were also able to compute local strain by monitoring shear displacements during the cutting process (Figure 2.20).
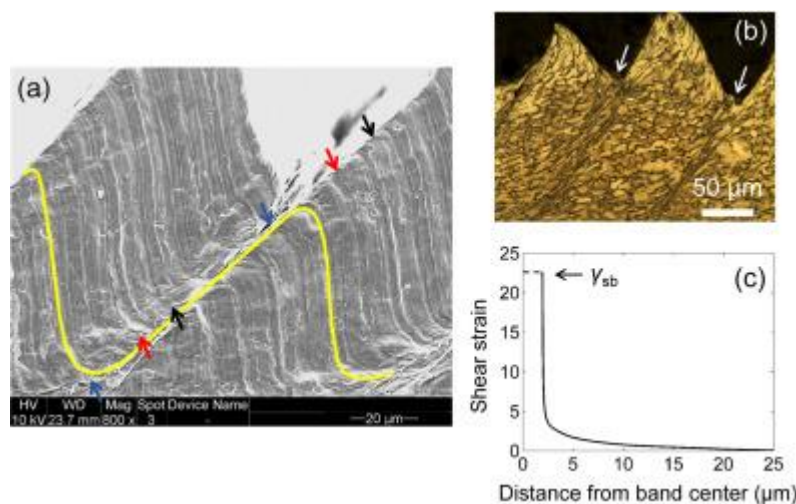
Figure 2.20. Shear band formation in Ti-64: (a) SEM micrograph showing displacements of specific markers (arrows) due to localised shear, (b) optical micrograph of chip microstructure, and (c) strain profile in band vicinity [89].

The marker displacements and segmented chip are due to localised flow in the bands. Figure 2.20a implies uniform straining along the band as the shear displacements were essentially equal. The strain profile obtained from local streak-line curvature is shown in Figure 2.20c. Figure 2.20b shows a highly deformed structure in the shear banded region and a less distorted region between the bands preserving the original grain structure. Figure 2.21 shows transmission electron microscopy (TEM) of the shear band which displays nanoscale

30

structures of grain size 50-100 nm which is a consequence of extreme deformation occurring in the shear band [89].
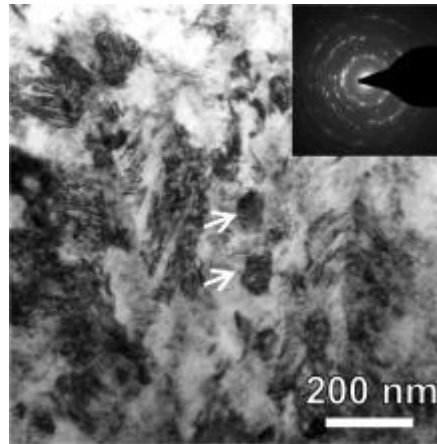
Figure 2.21. Bright field TEM micrograph and diffraction pattern showing nanocrystalline structure inside a Ti-64 shear band [89].

Shear localisation results in a cyclic variation of cutting forces with a marked variation in magnitude. The subsequent vibration or chatter in the machining process limits the material removal rate and severely affects tool wear [90]. The localised shearing corresponds with the generation of cyclic forces and acoustic emission. The frequency of the cyclic strain, load sensor and acoustic emission signals corresponds to the frequency of chip segmentation [91]. During the machining of titanium alloys, the force sensors are usually placed on the tool holder to record the dynamic changes in the cutting forces. These forces can be taken as indicative of the forces on the tool as a linear relationship exists between them [92]. An example of the relationship between the frequency of segmentation and measured cyclic force is shown in Figure 2.22.
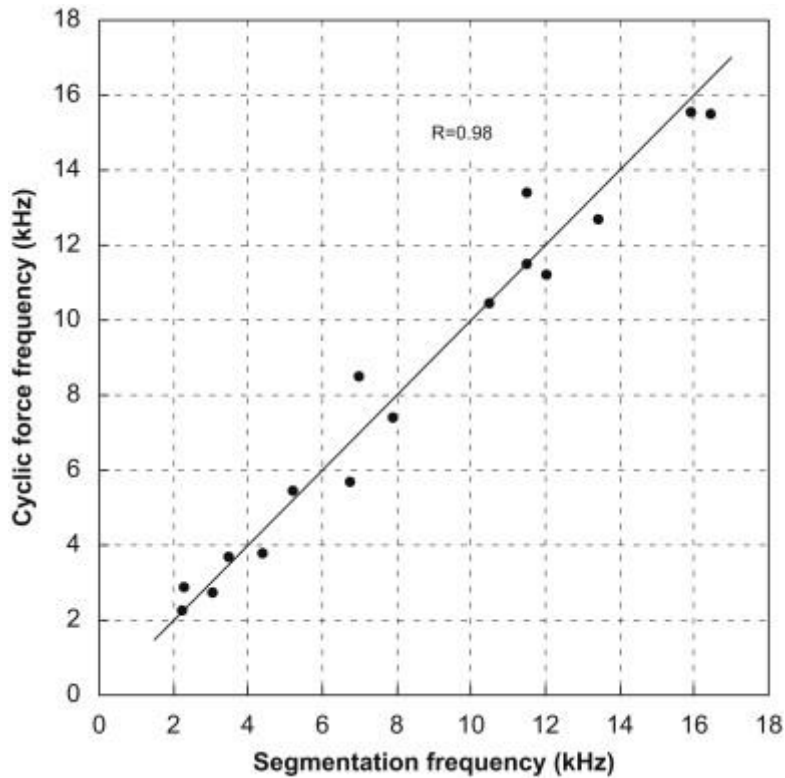
Figure 2.22. Correlation between cyclic force frequency and chip segmentation frequency for different cutting speeds and feeds, after Sun *et al.* [92].

The primary problem with machining titanium is that the tool life is so short which results in great expense for the aerospace manufacturing sector. This stems from the poor thermal conductivity where temperatures at the cutting zone can reach as high as 900°C at relatively low cutting speeds of 75 m.min^{-1} [93]. This promotes rapid chemical wear on the rake face which is a result of a diffusion mechanism. Figure 2.23 shows how high the cutting temperatures can reach for titanium alloys when compared with other materials such as steel.
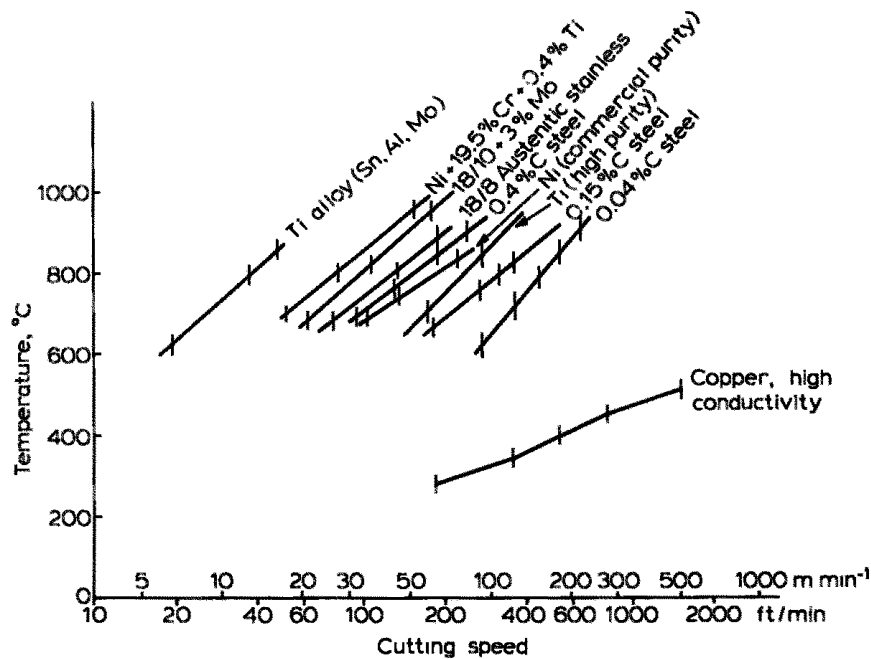
Figure 2.23. A comparison of tool-workpiece interface temperatures for a range of materials [24].

The centre of the high temperature zone is typically 0.5 mm away from the tool edge when cutting titanium. The heated region does not extend far along the rake face and the total contact length is short. This creates a high stress region at the tool edge at a very high temperature. Plastic deformation at the tool edge (amongst many other simultaneous tool wear mechanisms) ensues which leads to catastrophic failure of the tool.

When machining titanium alloys, the mechanical stresses occurring at the cutting zone are high. Konig [94] has shown that stresses on the tool are much higher when machining Ti-64 compared to nickel alloys (Nimonic 105) and steel (Ck 53N). Ezugwu and Wang [23] attribute this to the smaller chip-tool contact area for titanium alloys compared to steel for example. They also consider the high resistance to deformation at elevated temperatures for titanium alloys as a defining factor. However, during dry machining, temperatures can reach over 900°C [24] where the resistance to deformation would reduce considerably [23, 94].

As titanium alloys are often used in safety-critical components, the resulting surface integrity after machining is of great importance. Previous work [20, 95] has demonstrated that machining parameters can induce microstructural modifications at the surface of titanium alloys. Machining induced features e.g. slip bands and mechanical twins can initiate microcracking under dynamic loading conditions. Thus the mechanical twins and severely

33

plastically deformed 'swept' grains observed in Figures 2.24a to c are increasingly referred to as subsurface "damage".
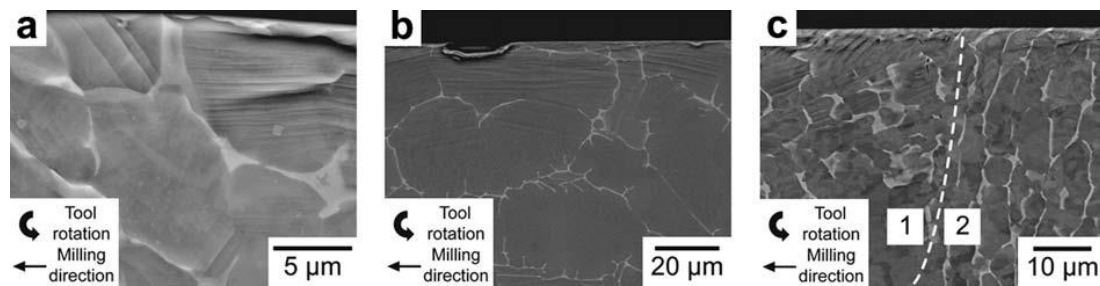
Figure 2.24. Backscattered electron micrographs showing deformation in the form of intense slip bands below the high-speed milled surface in (a) Ti–Al–4V and (b) Ti-834. (c) An example of the non-uniformity of deformation observed in Ti–6Al–4V, after Thomas *et al.* [95].

Care must be taken to avoid subsurface damage by selecting appropriate cutting parameters and tool geometry.

2.5.3 Tool wear
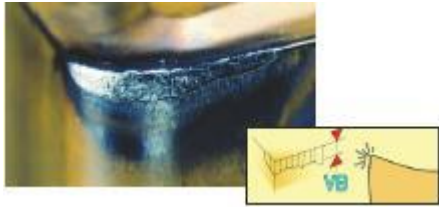
It has been discussed that one criterion for measuring the machinability of a material is tool life which is a direct result of tool wear. During a machining process, all cutting tools will gradually wear until they come to the end of their tool life. The tool life is often defined as the productive time available during which the cutting edge will machine components to an acceptable standard within predefined parameters. Industrial companies will often set their own tool life parameters which are often much shorter than what the tool manufacturer recommends. Rigorous surface integrity tests of machined components will aid companies in calculating their own tool life catalogues for different tool materials and their impending workpieces. Industry will also scrutinise surface texture, cutting accuracy, tool wear patterns and chip formation. The tool life criteria depend upon the type of process carried out i.e. finishing or roughing processes of a turning operation. For a careful finishing operation, tool life is often much shorter because it is a critical stage for final surface finish. On the other hand, tools will be used for much longer during a roughing operation as there are no surface texture limitations and therefore tools are changed much less frequently. It is obvious that the right tool must be selected for the right job, especially the choice of tool material and cutting geometry. However, in order to achieve maximum tool life, the machining conditions must be optimised. Reckless consideration of parameters such as cutting speed, depth of cut and feed rate will prematurely end many cutting edges [79]. Prolonging tool life is often seen as a

'black art' with numerous different aspects to consider and where expertise is required from many different disciplines.

Traditionally, there are three main categories to which tool wear can be broadly attributed: abrasive wear; diffusive/chemical wear; and fracture failure/mechanical wear. Abrasive wear is the plucking of particles which results from the tool sliding against the workpiece and chip which gives rise to flank wear. Diffusive wear is caused by chemical reaction between the tool material and workpiece. Diffusion of tool atoms into the workpiece and vice versa results in crater wear on the face of the tool. Finally, fracture failure stems from sudden failure of the tool which is the result of a thermomechanical combination of temperature fluctuations and cutting force variations [79].

Today, modern metal cutting research has extended the catalogue of tool wear mechanisms in an aim to help better understand and combat them. Table 2.6 lists seven wear mechanisms which fall into the above categories as well as also including adhesive and thermal classes [96].

TABLE 2.6. EXAMPLES OF WEAR ON CUTTING EDGES AFTER MACHINING OPERATIONS [96].

Wear category	Wear mechanism	Notes
Abrasive	Flank wear	The commonest wear type and preferred wear mechanism as it offers predictable and stable tool life
Chemical	Crater wear	Localised to the rake face, crater wear is due to a chemical reaction between the tool and workpiece. It is amplified by the high temperatures and pressures at the cutting zone
Adhesive	Built-up edge (BUE)	This wear is caused by pressure welding of the chip to the insert. Common when machining more ductile materials such as steels and aluminium
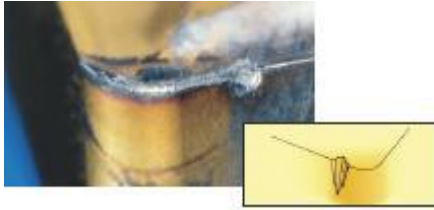
Adhesive		
	Notch wear	Found on both the rake face and flank, this wear is caused by localised damage at the depth of cut line
Thermal		
	Plastic deformation	This wear happens when the tool material is softened. Often occurs when the cutting temperature is too high for the tool material to handle
Thermal		
	Thermal cracks	These cracks may appear perpendicular to the cutting edge when the cutting temperature fluctuates. This is more commonly found during milling operations.
Mechanical		
	Edge chipping/breakage	This is due to an overload of mechanical tensile stresses. This is often due to inappropriate cutting parameters such as high feeds and depths of cut. However, this wear mechanism also arises after excessive wear on the insert or BUE.
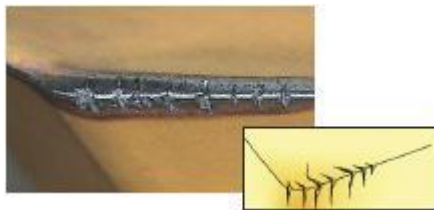
2.6 Tool materials

The evolution of tool materials has been one of the major contributing factors to helping shape the modern industrial world. It is crucial to match the most suited tool material (grade) and insert geometry with the workpiece material to be machined for an efficient cutting process. Different cutting tool materials provide different levels of hardness, toughness and wear resistance and are divided into numerous grades with specific properties. Typically, for a cutting material to be successful in its application, it should be: hard, to resist flank wear and deformation; tough, to resist bulk breakage; chemically and thermally stable; and non-reactive with the workpiece material [97]. In the modern world of metal cutting, cemented

carbides currently represent 80-90% of all cutting tool inserts [97]. Other materials include ceramics, cubic boron nitrides (CBN) and polycrystalline diamond (PCD). As they are the technologically most important group of cemented carbides, tungsten carbide-cobalt alloys (WC-Co) will be the focus of this discussion.

With the invention of tungsten carbide cutting tools in the early 1930s, machinists were able to cut many metals and alloys at much higher speeds and with much longer tool life than ever before. WC-Co tools consist of WC particles within a Co binder matrix (Figure 2.25). They are commercially available with Co contents between 4 and 12 wt.% and carbide grain size between 0.5 and 10 μm in diameter. Changing either of these parameters can drastically alter the tool's performance. For example, if the Co content or grain size is raised then the temperature at which the stress can be supported drops [98].
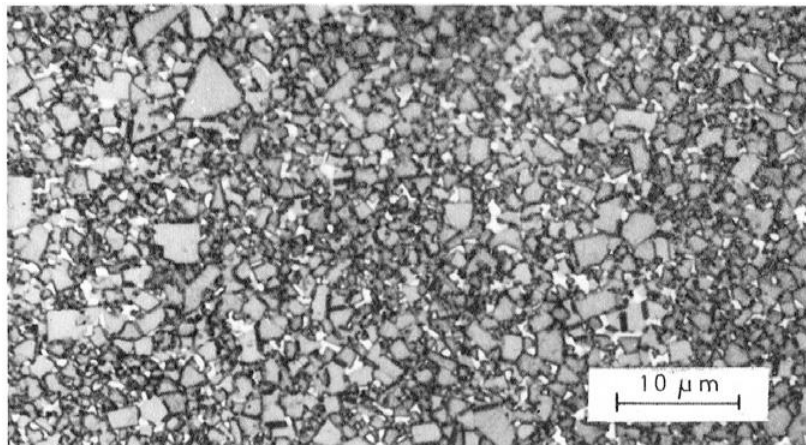
Figure 2.25. Micrograph of a WC-6%Co cutting tool with medium grain size [24].

The carbon content is also controlled very carefully. If the composition consists of too much carbon (free carbon) or too little (η-phase; Co_3W_3C), then the strength and performance of the tool will be compromised. For tungsten carbides, the coefficient of thermal expansion is low whereas the thermal conductivity is relatively high (100 W/mK). Oxidation resistance at elevated temperatures is poor and oxidation in air is rapid at temperatures above 900°C [24]. Machinists often use coolant to avoid this caveat during cutting.

2.6.1 Tool wear of WC-Co tools

§2.5.3 briefly overviewed the various forms and mechanisms of tool wear observed during machining. What follows below is a more specific account of tool wear observed for WC-Co tools.

2.6.1.1 Superficial plastic deformation by shear at high temperature

During a machining operation, the work material is seized to the WC-Co tool over most of the worn rake and flank surfaces when cutting titanium alloys at medium cutting speeds. A built-up edge is formed at the interface via an adhesive wear mechanism. However, as carbide tools exhibit a high hot-strength, they are protected from this wear mechanism due to superficial plastic deformation by shear at high temperature [24].

2.6.1.2 Plastic deformation under compressive stress

As speed and feed are raised when cutting, the rate of metal removal is often limited by deformation of the tool under compressive stress on the rake face. As tungsten carbides are relatively brittle, they can only withstand limited deformation before failure of the tool via microcrack propagation. Carbide tools with lower cobalt content are often used at higher feeds and speeds due to increased resistance to deformation [24].

2.6.1.3 Diffusion wear

When machining titanium alloys or steels at medium to high speeds, the WC-Co tool will suffer from rapid crater wear along the rake face which is a result of a chemical wear mechanism. Trent [24] describes this as "Metal and carbon atoms of the tool material diffuse into the work material that is seized on the rake face surface. These atoms are then carried away in the body chip." The high temperatures and pressures reached at the cutting zone during machining are ideal for considerable diffusion to take place in the solid state. The characteristics of crater wear are also consistent with a wear process based on solid phase diffusion. Figures 2.26 and 2.27 show crater wear along the rake face of a cutting tool after machining steel.
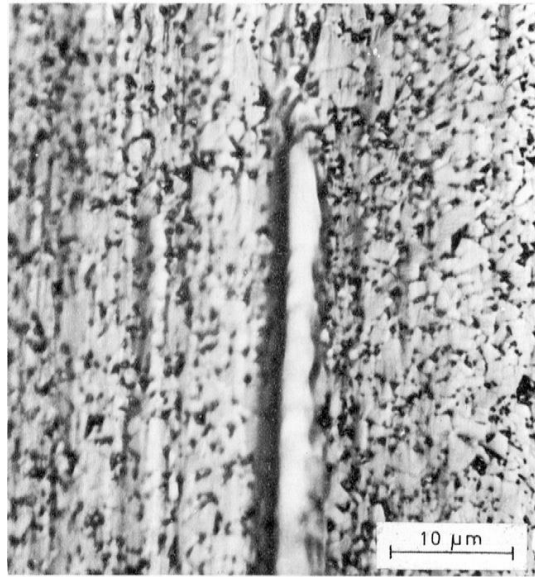
Figure 2.26. Crater wear along the rake face of a WC-Co tool after high speed machining of steel. The smooth surface with ridge is characteristic of diffusion wear [24].
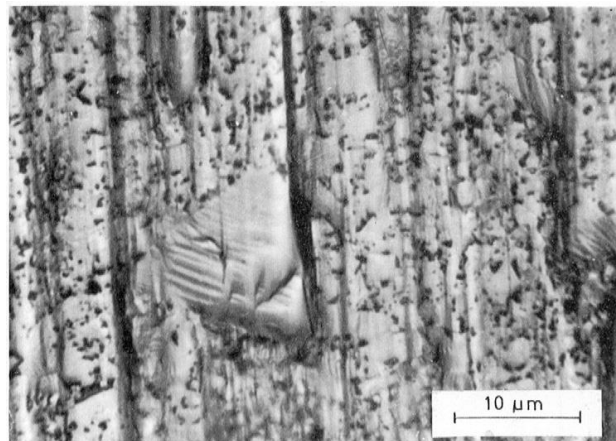
Figure 2.27. Worn crater on the rake face of a WC-Co tool showing a large WC grain which appears to have been etched via reaction with the steel workpiece at high temperature [24].

Kramer [99] has shown evidence that there is a higher concentration of dislocations in carbide grains at the interface than in the body of the tool. When subjected to high shear stress, this could further accelerate loss of metal and carbon atoms from the surface. For diffusion wear to take place during machining there must be some solubility. Different tool and workpiece combinations will show varying differences in diffusion wear rate. The chemical properties, rather than the mechanical strength or hardness of the tool dictates the rate of diffusion wear. Therefore, there is no improved resistance to diffusion wear for fine grained cemented carbides of higher hardness.

The rate at which atoms from the tool dissolve and diffuse into the work material determines the rate of diffusion wear. Trent [24] describes that when machining steel with WC-Co tools,

40

the most rapid diffuser is the cobalt binder atoms of the tool and the iron atoms of the workpiece. The carbide remains relatively unaffected as the diffused iron cements the carbide particles and plays the role of the lost cobalt. Hence for steel, the rate of diffusion wear is controlled by the rate of diffusion of tungsten and carbon atoms together into the workpiece. This is dependent upon temperature and rate of material flow at the tool-workpiece interface. Trent [98] shows that the rate of flank wear via a diffusion mechanism increases rapidly as the cutting speed is increased. Figure 2.28 plots flank wear for increasing cutting speeds when machining steel with WC-Co tools.
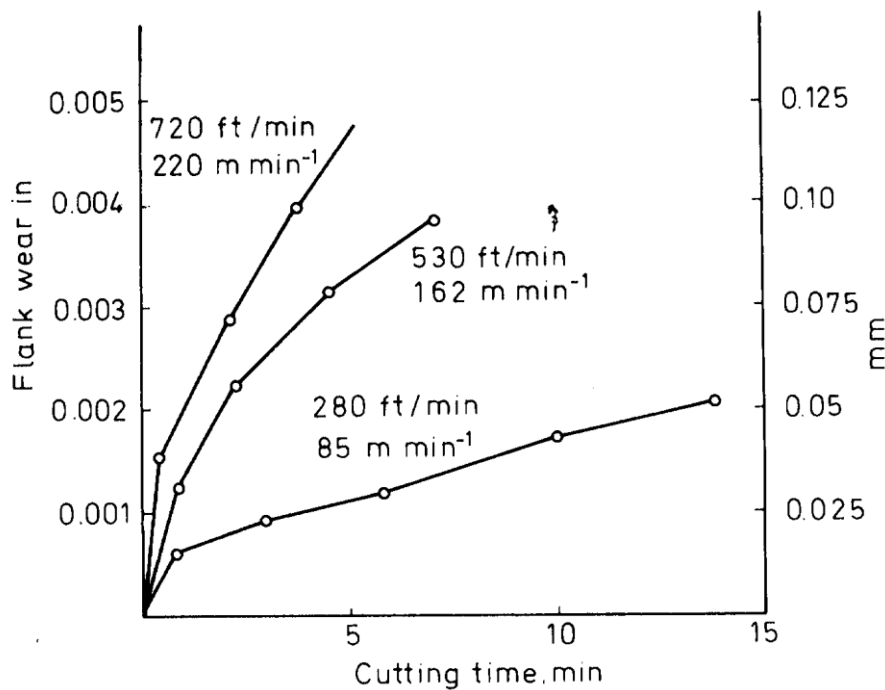
Figure 2.28. Flank wear (via a diffusion mechanism) vs time for increasing cutting speeds when machining steel with WC-Co tools [24].

WC-Co alloys with a greater quantity of cobalt show a higher rate of wear via diffusion. However, as WC-Co cutting tools for machining use a relatively small range of cobalt, the differences in rate of diffusion ware is small.

Diffusion wear with respect to machining of titanium alloys is discussed in more detail in §2.8.

2.6.1.4 Attrition wear and BUE
It has been seen how at high cutting speeds, crater wear on the flank face via a diffusion mechanism is the dominant wear mechanism. However, at lower speeds it is tool wear by

attrition which the dominant wear process. Attrition is otherwise known as an adhesive wear mechanism which represents BUE and notch wear.

A built-up edge is formed on the cutting edge of the tool and is formed by welding of the workpiece chip. A BUE often serves as a protective shield to tool wear. Formation of a BUE can also change the effective rake angle of the tool as it alters the shape of the cutting edge [100]. Contrary to forming a protective barrier, the BUE can result in wear on the cutting edge which could result in substandard surface integrity of the workpiece. This is due to pieces of the BUE being pulled under the leading edge of the tool [26, 101-104]. Owing to the inherent poor machinability of titanium alloys when compared to ferrous materials, most machinists would ironically admit that they are operating at very high cutting speeds even at the mildest of cutting conditions. Kramer has demonstrated [102] that when cutting titanium alloys, the formation of a carbide layer promotes the formation of a BUE, protects the tool from catastrophic failure. Without forming this stable BUE, it would very difficult to machine titanium alloys due to excessive tool wear. Figure 2.29 shows the relationship of flank wear vs cutting time via a wear curve.
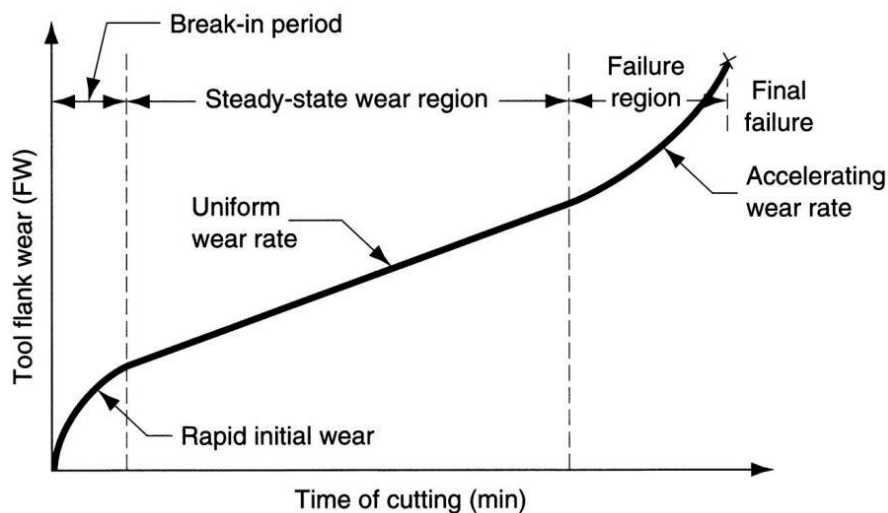
Figure 2.29. Wear profile of a cutting tool vs. cutting time. Important wear regions are identified [105].

The mechanism of flank wear begins with a break-in period. Here, there is fast, preliminary wear. Afterwards, there is a steady-state period of wear across the cutting edge of the tool followed by an abrupt failure region where the wear rate is rapidly accelerated. The mechanism of tool crater wear shadows a similar profile to that shown in Figure 2.29.

2.6.1.5 Taylor relationship of tool wear

Wear curves are a traditional approach to determining the machinability of a material with regards to tool wear. The machining time (tool life) is recorded when the wear limit (predetermined) has been attained for a range of cutting speeds. Taking this data and converting it into a log plot of time and speed results in the graph presented in Figure 2.30.
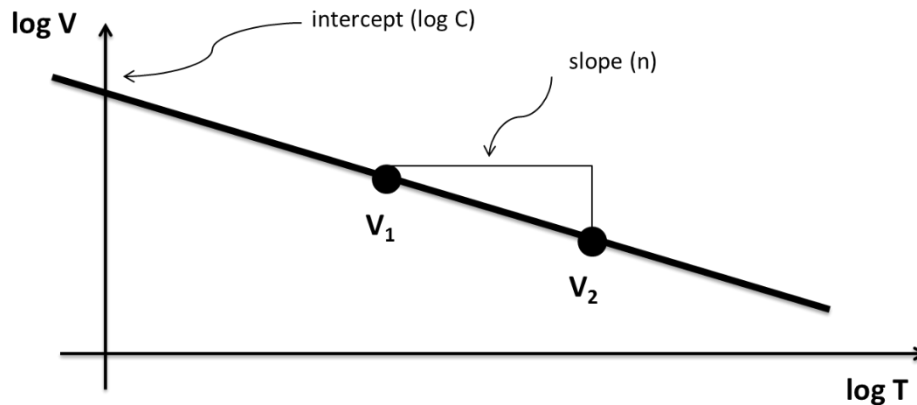
Figure 2.30. Taylor relationship of tool wear [105].

The Taylor equation, which allows for the estimate of tool life, can be calculated by using the constants from the plot in Figure 2.30. The Taylor relationship (Equation 2.8) shows how tool life, T is related to the cutting speed, V_c and the constants n and C that represent depth of cut, tooling and workpiece material as well as machining feed. This equation allows machinists to accurately predict tool life for a given machining speed. However, the equation assumes all other parameters are constant.

$$V_C T^n = C \hspace{6cm} \text{Equation 2.8}$$

Jaffrey *et al.* [106] have constructed a tool wear map after machining Ti-64 using WC-Co tools (Figure 2.31). Using orthogonal cutting trial data at a range of different feeds and speeds, the map classifies tool wear in regions of high, moderate and low wear. Maps like these have traditionally been constructed for machining of ferrous materials [107, 108] where they help machinists identify optimum cutting conditions.
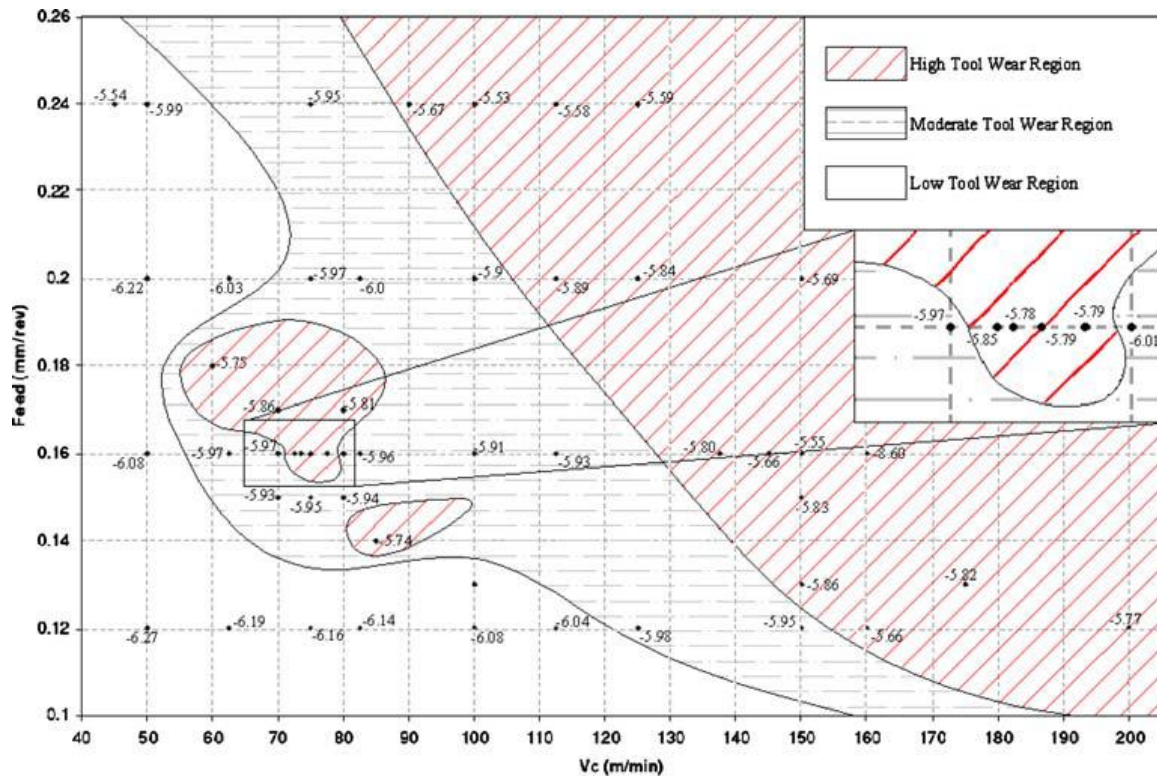
Figure 2.31. Ti-64 map of wear rate [106].

The wear map plots cutting speed on the abscissa and feed rate on the ordinate to determine the flank wear rate. It is interesting to note that the wear map does not contain a safety zone, contrary to those wear maps obtained for steels. Furthermore, the map shows areas of high tool wear within regions of moderate tool wear.

The key benefit of tool wear maps is that the machinist can get a rounded overview of the system. The wear map above for Ti-64 shows how sensitive tool integrity is to marginal changes in either feed or cutting speed. As discussed previously, the establishment of a BUE ahead of the tool can heavily influence tool wear dynamics, acting as a barrier to subsequent tool wear. Jaffrey *et al.* [106] were not able to carry out further research into the obscure regions of high tool wear within moderate tool wear zones but Crawforth [43] suggests that these high wear regions may be related to the chemical compositions of the tool and workpiece. He explains that the stability of the protective BUE is a direct result of the relative chemical stability between the two materials.

2.6.2 Tool coatings

Towards the end of the 1960s, one of the significant steps in the development of cutting tool materials was the introduction of various tool coatings. One of the very first coatings to be used successfully was titanium carbide (TiC). For machining ferrous materials, the coating

44

drastically improved tool life despite being only a few microns thick. When machining steel, the effect of the coating continues long after it has partly worn off which results in the reduction of crater wear. Higher feeds and speeds can be attained because higher temperatures can be tolerated. Generally, for cemented carbides wear resistance decreases as toughness increases; therefore, the introduction of coating technology was ground breaking in preventing any compromise in tool choice. Over the past half a century, the technology has continued to grow and progress to new levels. Today, more than 75% of turning operations, and more than 40% of milling trials on ferrous materials are performed with coated carbides [79]. Coated grades have also found wide application in drilling tools for cast-iron and steel machining. The most common coatings are titanium carbide (TiC), titanium nitride (TiN), aluminium oxide (Al_2O_3) and titanium carbon nitride (TiCN). TiC and Al_2O_3 coatings are generally used to act as a chemical and heat barrier at the tool-chip interface. This is because they are chemically inert thus providing extra protection to crater wear, for example. Although not as hard, TiN coatings offer a lower coefficient of friction to the cutting edge and improved cratering resistance. Another advantage of using TiN is that the coating can be applied a relatively low temperature, thus not effecting the tool substrate as much.

Recently, various combinations of multiple-coatings have been developed to extract the best properties from different coating materials. Coating combinations have been engineered to offer the broadest range of desirable properties for machining various materials. They generally offer high wear resistance, maintain hot-hardness and also lack chemical affinity with workpiece materials. Due to the lower thermal conductivity of the coating layer, less heat is transferred into the workpiece. This means that the addition of any coating does not affect the hot-hardness properties of the tool material. TiCN demonstrates excellent wear resistance as well as strong bonding properties which mean it can be used within multiple layers. Insert coatings are rarely thicker than 2-12 µm in total, otherwise negative tool performance can arise with excessive thickness [79]. Figures 2.32a to c show micrographs of single-layer; double-layer; and multiple-layer coatings respectively on WC-Co substrates.
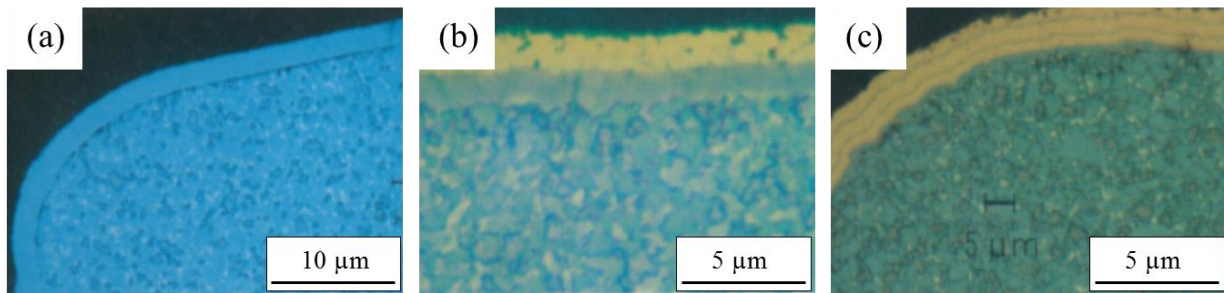
Figure 2.32. (a) single layer coating; (b) double-layer coating; and (c) multi-layer coating on a WC-Co substrate [79].

Despite the numerous advantages offered by coated tools for machining ferrous materials [109-112], it is widely believed that they offer little in improving titanium alloy machining. Dearnley *et al.* [93] evaluated the principal wear mechanisms of coated and uncoated cemented carbides when machining Ti-64. The primary conclusion of their study was that 'straight grade' WC-Co cemented carbides were the most suitable tool for machining titanium alloys. WC-Co tools which contained a cobalt content of 6 wt.% and a WC grain size of > 0.8 μm. Tools with a cobalt content > 6 wt.% gave rise to plastic deformation at the cutting edge. For all tool materials tested, they suffered from two rake and flank face wear mechanisms: diffusion and attrition. Diffusion wear predominated on the rake face of all uncoated cemented carbides. The study showed that coatings of TiN, TiC, Al_2O_3 and HfN suffered more rapid wear than uncoated WC-Co on both the rake and flank face. This was true for both diffusion and attrition wear mechanisms. As well as cemented carbides, the investigation looked at ceramic tools for machining Ti-64. They concluded that they were not suitable for turning titanium alloys as they suffered from severe notch wear. Although the coated cemented carbides performed poorly, CBN tools and TiB_2 coatings showed increased resistance to diffusion wear. They go on to suggest that borides are potential candidates for resisting chemical wear in machining titanium alloys.

Hong *et al.* [113] have investigated tool life improvement in cryogenic machining of Ti-64 and were quick to state that developments in tool coating technology do not help titanium alloy machining. They report that Al_2O_3 coatings prevent heat dissipation as the coating has a lower thermal conductivity than WC-Co substrates. They further state that TiC and TiN coatings show unfavourable chemical affinities with the Ti-64 workpiece.

Vigneau *et al.* [114] also mention that nitrides of zirconium and hafnium have been unsuccessful in increasing tool life for titanium alloy machining. They however go on to show that coatings of chrome nitride (NCr), titanium carbonitride (TiCN) and titanium

aluminium nitride (TiAlN) appear to offer some resistance to tool wear. López de lacalle *et al.* [115] investigated machining of Ti-64 with TiCN and NCr coated tools and found that the tools developed high flank wear as well as notch wear on the cutting edge.

Jawaid *et al.* [116] studied the wear mechanisms of coated carbide tools when face milling Ti-64. The team compared performances of coatings applied via physical vapour deposition (PVD) and chemical vapour deposition (CVD) and found that the CVD tools outperformed the PVD tools. The PVD-TiN and CVD-TiCN+Al_2O_3 coated tools were predominantly worn on the flank face before chipping and failing on the rake face. Plastic deformation was also found. Diffusion and attrition wear were the mechanisms responsible. It is also interesting to note that there was evidence of diffusion of cobalt and tungsten into the adhered workpiece (BUE) at the flank and rank faces of the tools.

Despite the negativity surrounding coated carbide tools for titanium alloy machining, Wang *et al.* [117] found that PVD-TiN and a multi-layer TiN/TiCN/TiN coated carbide tools are suitable for machining Ti-64. The coatings were found to minimise tool wear. Cadena *et al.* [118] investigated a heat-treated AlCrN coated carbide tool for machining Ti-64 and found favourable results for tool wear and workpiece surface integrity. The AlCrN coating showed low friction coefficients and wear rates. However, in this author's opinion, such novel coatings need further parametric investigation in comparison with uncoated WC-Co tools.

In recent work by Jaffery and Mativenga [119], the authors produced a table which lists the different conclusions drawn by various researchers on the performance of coated inserts and different tool materials in turning titanium alloys (Table 2.7).

TABLE 2.7. SUMMARY OF PERFORMANCE OF VARIOUS TOOL MATERIALS AND COATINGS CONSIDERED BY RESEARCHERS IN TURNING, ADAPTED FROM JAFFERY AND MATIVENGA [119].

Reference	Conclusion
Narutaki *et al.* [120]	TiN-coated cermet, TiC-coated carbide, ceramic aluminium oxide, and CBN tools were not recommended for machining titanium alloys. Natural diamond performed better than PCD and K10 tools, while PCD and K10 inserts showed similar performance.
Hartung *et al.* [26]	Of the tools considered, Al_2O_3 tools recording highest wear rate while only PCD tools recorded wear rates lower than uncoated carbide tools.
Dearnley *et al.* [121]	Only crystalline WB-coated carbide inserts showed better performance as compared with uncoated carbide inserts in terms of crater wear.
Cherukuri and Molian [122]	TiAlN-PVD and $AlMgB_{14}$-20%TiB_2-PLD-coated carbide inserts out performed uncoated carbide inserts in terms of tool life at V_c=61 m/min, f=0.15 mm/rev and a_p=0.76 mm while $AlMgB_{14}$-20%TiB_2-PLD-coated carbide inserts also out performed uncoated carbide inserts in terms of tool life at V_c=61 m/min, f=0.15 mm/rev and a_p=1.27 mm. TiAlN-PVD and $AlMgB_{14}$-20%TiB_2-PLD-coated carbide inserts showed similar tool life at V_c=61 m/min, f=0.15 mm/rev and a_p= 0.76 mm. It was also mentioned that $AlMgB_{14}$ is believed to have excellent thermal dissipative capability, resulting in reduced tool heating.
Fitzsimmons and Sarin [123]	After testing different types of WC/Co composite coatings were found to behave chemically similar to uncoated C2 tools, which were described as the most chemically wear resistant in titanium machining. Flank wear was said to have been dominated by the substrate properties and crater wear by the surface, or coating properties. Lower flank wear was observed by utilising SiAlON substrates, while crater wear was found to have reduced by utilising WC/Co composite coating.
Nabhani [11]	The presence of coated layers on the carbide tool was reported to have had no beneficial effect on their performance since these layers were rapidly removed leaving the tungsten carbide substrate vulnerable to tool wear. PCD tools were shown to have the highest tool life followed by CBN with multi-coated tools showing highest tool wear.
Ezugwu *et al.* [124]	Uncoated carbide tools performed better than CBN tools in terms of tool life as well as surface roughness at f=0.15 mm/rev, a_p=0.5 mm and V_c=150. Increase in CBN content reportedly caused greater notch wear, thus reducing tool life. Only CBN tools were

	tested at higher speeds. T1 having low thermal conductivity performed better than T2 and T3 at all cutting conditions tested.
Wang and Ezugwu [117]	Uncoated K20 inserts, was described better than P grades Single-coated tools performed better at higher feed rate (0.25 mm/rev) while the multi-coated tools showed higher tool life at low feed rate (0.13 mm/rev).
Ezugwu *et al.* [125]	TiN/TiCN/TiN multi-coated inserts were reported to have shown better tool life than TiN-coated inserts, at low feed rate (0.25 mm/rev) as compared with lower feed rate (0.13 mm/rev). A comparison with uncoated tools was not presented.
Kishawy *et al.* [126]	Uncoated rotary carbide inserts demonstrated higher tool life as compared with uncoated fixed tools as well as coated rotary inserts.
Corduan *et al.* [31]	PCD inserts showed best results at V_c=150 m/min, f=0.1 mm/rev and a_p=1 mm. TiB$_2$ inserts were recommended only for cutting speeds less than 100 m/min while CBN tools were only recommended for finishing cutting conditions. The authors also recommended further research in the quest for a coating having better thermal fatigue resistance as well as improvement in deposition methods for TiB$_2$ coatings.
Bhaumik *et al.* [127]	wBN–cBN composite tools showed a tool life of 80 min against 12 min for K20 carbide tools. The surface roughness was also reported to be superior for wBN– cBN tools after machining for 15 min at Ra=0.57 against a value of Ra=1.42 for K20 tools after machining for 2 min.

2.7 The importance of alloy chemistry in machining

It is well known in the machining community that high strength metastable β alloys such as Ti-5553 are more difficult to machine than α+β alloys such as Ti-64 [84, 128, 129]. As such there is a systematic trend towards a decrease in machinability with an increase in β stabilisers [130]. Contrasting alloys such as these are often selected for machinability trials to highlight any effect that additional alloying elements may have upon performance [84, 130]. Currently bucking the trend is TIMETAL® 54M (Ti-54M). TIMET have developed this alloy as a potential substitute for Ti-64 in applications such as intake valves and connecting rods. Ti-54M is also less expensive in manufacturing processes due to improved machinability over Ti-64. During early development of the alloy, Kosaka *et al.* [131] performed a number of drilling trials on Ti-5Al-4V-Mo/Fe base alloys and found that they showed increased drill performance when compared to Ti-64. Further experimental projects have gone on to report heightened machinability properties of Ti-54M over Ti-64. Armendia *et al.* [132] proved better machinability of Ti-54M over its counterpart following several analyses involving tool wear measurements, cutting forces, chip formation and SEM observation. They reported that, although there was no significant difference in machinability at low cutting speeds, improved tool integrity was found when machining at high speeds. The team speculate that differences in formation of BUE when machining both alloys is key to understanding why Ti-54M better performs. On the other hand, Rahim *et al.* [133] found Ti-64 to possess superior machinability over Ti-54M by way of increased tool life (lower flank wear) during drilling. Ugarte *et al.* [130] report on the poor machinability of Ti-5553 with regard to a "combination of high dynamic loads as a result from a higher chip segmentation frequency and higher cutting temperatures." Crawforth [43] considers that these conclusions do not offer the reader an insight into how the material could be adding to its machining performance from a metallurgical point of view. Upon comparing the machinability of Ti-5553 and Ti-64, Arrazola *et al.* [84] made an interesting observation where the formation of a BUE was observed in cutting trials of Ti-64. There was a decrease in BUE size with increasing cutting speed. Upon removal of the BUE, there was a significant increase in tool wear. The authors did not comment on whether this was observed for Ti-5553, however it does echo the observations made of Armendia *et al.* [132] where BUE was observed on the tool after machining Ti-54M and Ti-64.

Engineers are continually striving to improve the performance of titanium alloys and as such are always investigating new chemistries. More recently, TIMET have developed the novel

compositions of TIMETAL-575 (Ti-575) and TIMETAL-639 (Ti-639) which provide higher strength alternatives to Ti-6246 and Ti-64 respectively [134]. Ti-575 is an α+β alloy developed for fan disc forgings which provides increased static and low cycle fatigue strength. What is more, it does not compromise on density or ductility. Ti-639 is also an α+β alloy and was developed as an alternative material for solid or hollow fan blades. Another recent development alloy is TIMETAL-407 which was developed as a further alternative to Ti-64 [135]. It was designed primarily for improved ductility leading to enhanced low temperature forming and superior machinability [136].

2.8 Diffusion in titanium alloy machining

The topic of diffusion was initially discussed in §2.3 where various diffusivity data was considered for hcp and bcc titanium. Diffusion mechanisms in terms of BUE formation and chemical tool wear were then touched upon in §2.5.2. Diffusion wear in machining was then presented as primary category of tool wear in §2.5.3 where cause and effect was outlined. Finally, diffusion wear specific to WC-Co tools was examined in §2.6.1.2 before the work of Dearnley *et al.* [93] and Jawaid *et al.* [116] showed how diffusion-dissolution wear was the dominant wear mechanism in titanium alloy machining in §2.6.2.

During machining of titanium alloys, the intimate contact between the workpiece and tool at temperatures above 800°C provide a high thermodynamic driving force for diffusion of tool material atoms across the tool-workpiece interface. This theory is also valid for diffusion of workpiece atoms into the tool. Wang *et al.* [27] studied diffusion wear in milling Ti-64 and showed that as diffusion wear occurred, a carbon-rich layer was formed at the tool-workpiece interface while the tool material at the flank face was carbon depleted. They proposed a model of carbon diffusion for WC-Co tool wear after milling at high speeds (Figure 2.33).
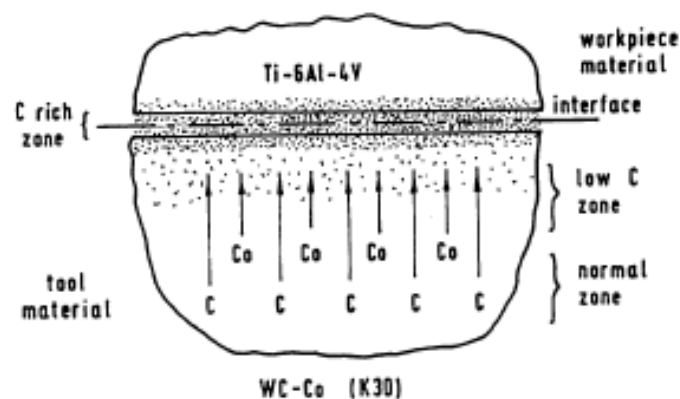
Figure 2.33. Wang model for WC-Co tool wear by carbon diffusion [27].

51

The study also found evidence of cobalt diffusion; however, they did not observe any diffusion of titanium or tungsten at the interface. The authors hypothesised that this was actually due to instrumental measurement limitations. This author agrees as the measurement techniques of wavelength dispersive spectroanalysis and Auger electron spectroscopy used in the study are outdated by today's standards. The study also concluded that as the carbon is redistributed at the boundary layer, the mechanical properties of the cemented carbide are affected. Diffusion wear by embrittlement and weakening of the surface causes the tool to wear.

Joshi *et al.* [28] report that a change in β-phase fraction in titanium alloys changes the shear band forming tendency and the corresponding segmentation frequency during machining. Consequently, they have shown how the mechanism of tool wear differs with a change in β-phase fraction. Turning trials using TiAlN coated WC-Co tools found that the dominant wear mechanisms were abrasion, abrasion with BUE, and plastic deformation of the α, α+β, and more β-rich α+β titanium alloys respectively. When machining the α alloy Ti-5.26Al-3.03Sn the tool face became rough after delamination of the coating material from abrasion with the workpiece (Figures 2.34a to c). It was concluded that the TiAlN coating failed to minimise tool wear when machining the α alloy. Despite no adherence of the chip, there was some evidence of diffusion from the workpiece as X-EDS analysis confirmed the presence of Sn on the cutting edge.
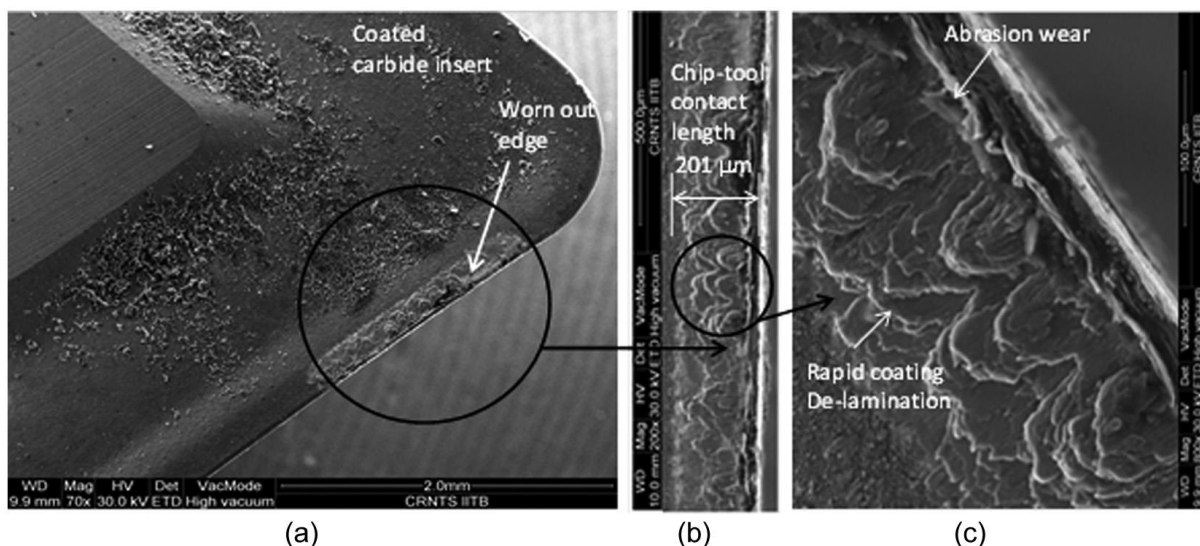
Figure 2.34. Electron micrograph of the cutting tool edge used to machine Ti-5.6Al-3.03Sn: (a) insert, (b) chip-tool contact length and (c) mechanism of tool wear [28].

When cutting the α+β alloy Ti-64, they observed formation of a BUE (Figure 2.35a to c) which encourages abrasion and diffusion of workpiece elements onto the tool surface. Joshi *et al.* believe that the pattern of tool wear observed for increasing β phase fraction is directly related to more rapid diffusion in β titanium.
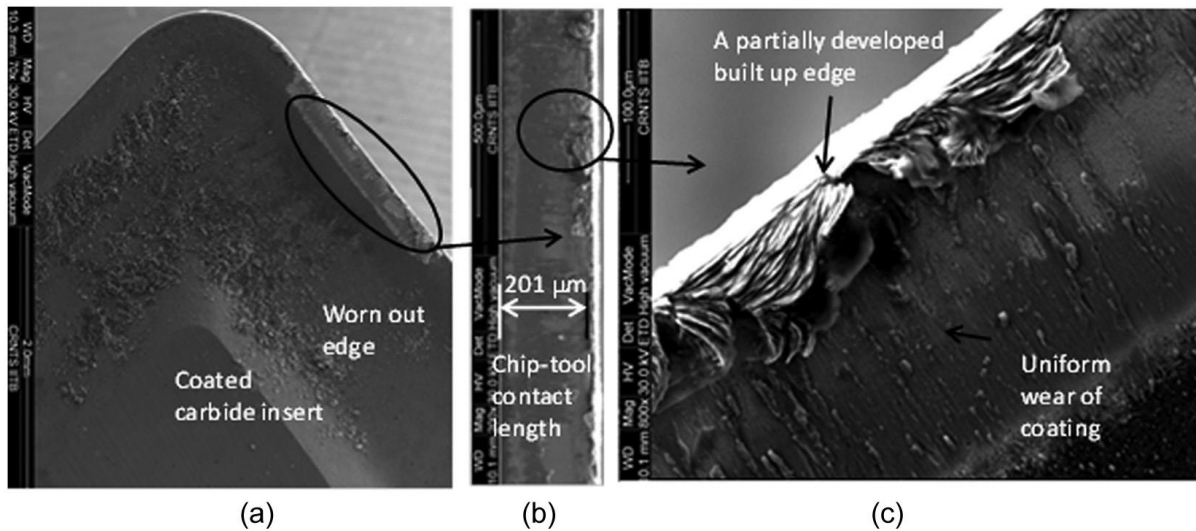
Figure 2.35. Electron micrograph of the cutting edge used to machine Ti-64: (a) insert, (b) chip-tool contact length, (c) BUE [28].

Presence of vanadium confirmed via X-EDS confirmed diffusion of the workpiece into the tool. Tool wear when cutting the more β rich α+β alloy Ti-4.16Al-3.26V3.89Mo was primarily via plastic deformation (Figure 2.36a to c). No adherence of work material on the face or cutting edge of the tool was observed. The study goes on to say that a change of colour along the width of the worn edge shows removal of the coating. However, the planer surface nearer the cutting edge indicates a slow rate of coating delamination showing potential benefits of using coated tools to machine more β-rich alloys. No sign of BUE was observed on this tool. Presence of molybdenum on the tool was confirmed via X-EDS analysis proving diffusion of workpiece into the tool.
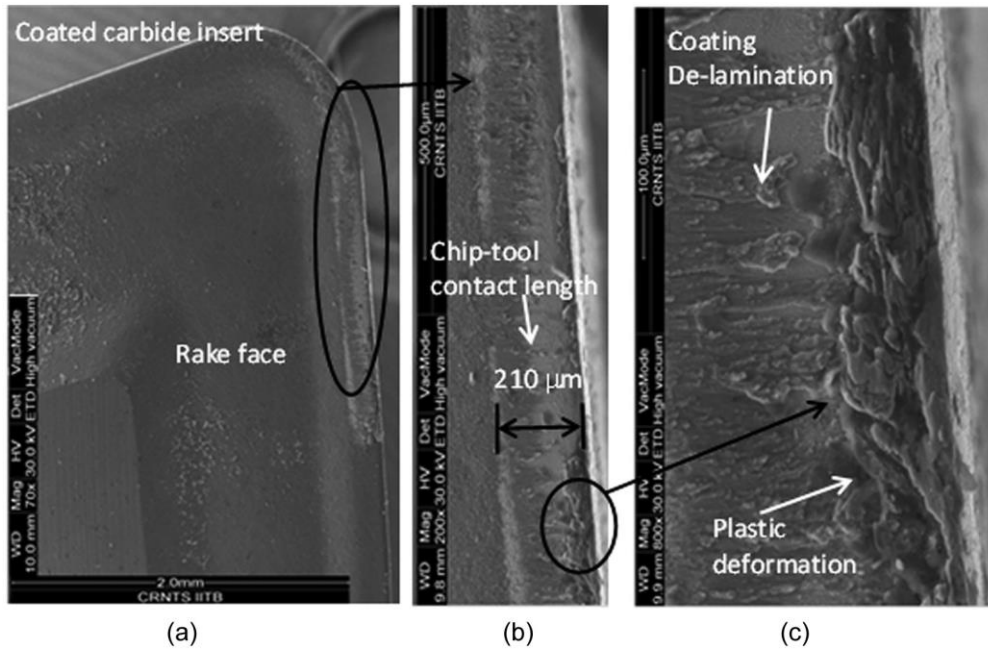
Figure 2.36. Electron micrograph of the cutting edge used to machine Ti-4.16Al-3.26V-3.89Mo): (a) insert, (b) chip-tool contact length and (c) mechanism of tool wear [28].

Zhang *et al.* [34] investigated diffusion wear during high-speed machining of Ti-64 with uncoated WC-Co tools. Firstly, the study theoretically proposed the diffusion analysis of the tool constituents towards the workpiece. To simplify the diffusion analysis of the tool-chip interface, it was assumed that the concentration gradient in the y-direction is small with respect to the gradient in the x-direction (Figure 2.37).
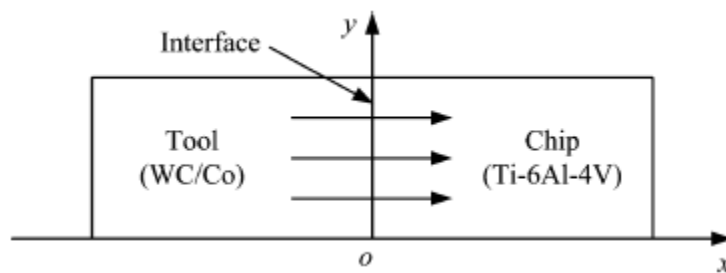
Figure 2.37. Zhang's schematic of the tool-chip diffusion interface [34].

When the concentration varies along only one direction, the concentration profiles for non-steady state diffusion can be expressed by Equation 2.9 below:

$$C(x,t) = \frac{C_0}{2}\left[1 - erf\left(\frac{x}{2\sqrt{Dt}}\right)\right]$$

Equation 2.9

Where $C(x.t)$ is the concentration at depth x after time t, and C_0 is the initial concentration of tungsten, carbon and cobalt in the tool material. The function *erf* is the Gauss error function

which is defined in Equation 2.10. For the full derivation of Equation 2.9, the reader should consult Zhang *et al.* [34].

$$\text{erf}(z) = \frac{2}{\sqrt{\pi}} \int_0^z e^{-\eta^2} d\eta \qquad \text{Equation 2.10}$$

Knowing the initial concentrations of the tool constituents and combining them with Equation 2.9, Zhang *et al.* were able to suggest that the final concentrations of tungsten and carbon are much higher than that of cobalt at the same cross-section of the workpiece after the same time. The diffusion theory was then verified firstly by a diffusion couple experiment, and then by a high-speed milling trial. There is minimal information concerning the diffusion couple experiment other than showing X-EDS analysis of tool constituents at two different depths in the workpiece. They were able to conclude that the diffusion layer is 'very thin' and 'very close' to the interface as they failed to detect much of a presence of tungsten, carbon or cobalt at a depth of 1.5 µm. During a diffusion couple experiment, there is no relative motion at the contact interface so they cannot entirely reflect the diffusion wear on the rake surface of the tool. Further verification of the diffusion model was therefore studied via a milling trial. The machining trial showed that cobalt diffusion led to the plucking of WC particles in the tool. The authors suggested that the plucking of WC particles due to cobalt diffusion dominated the crater wear mechanism as seen in Figures 2.38a and b.
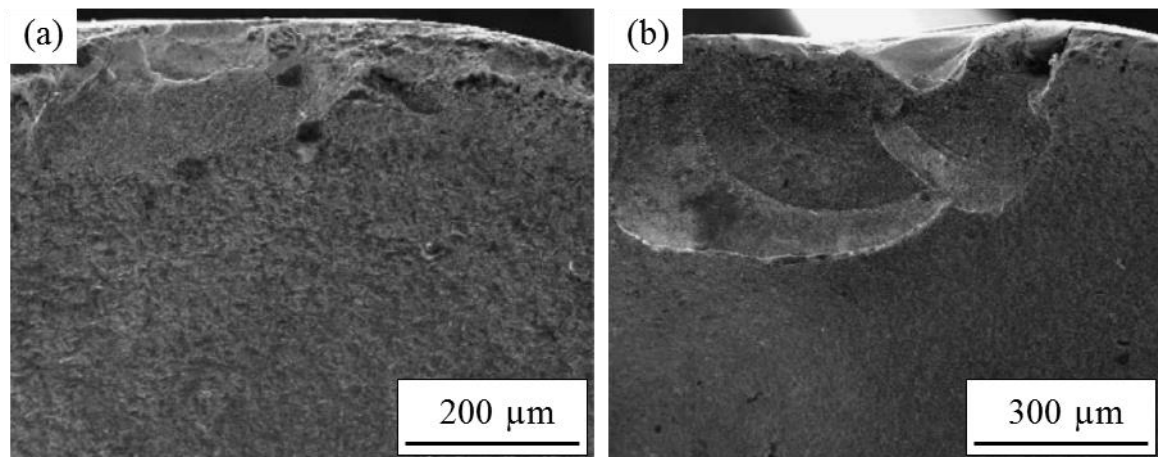
Figure 2.38. Electron micrographs of crater wear on rake face of tool after (a) 6 min milling and (b) 18 min milling, after Zhang *et al.* [34].

Hua *et al.* [30] also recognised the importance of cobalt diffusion initiating a crater wear mechanism and thus proposed a model to predict it. Figure 2.39 shows the model via a simple schematic: cobalt diffusion leads to the dislodging and breakaway of the WC grains and the formation of a crater on the rake face. It follows that larger WC grain size have a lower

surface area and consequently lower wear. However, this needs to be balanced against the lower toughness associated with larger grain size.

Tool substrate as a graded composite with WC grains in a Co matrix	During cutting process, cobalt diffuses into chip due to high temperature	Due to loss of cobalt, the relatively fragile WC breaks and is carried away by flowing chip
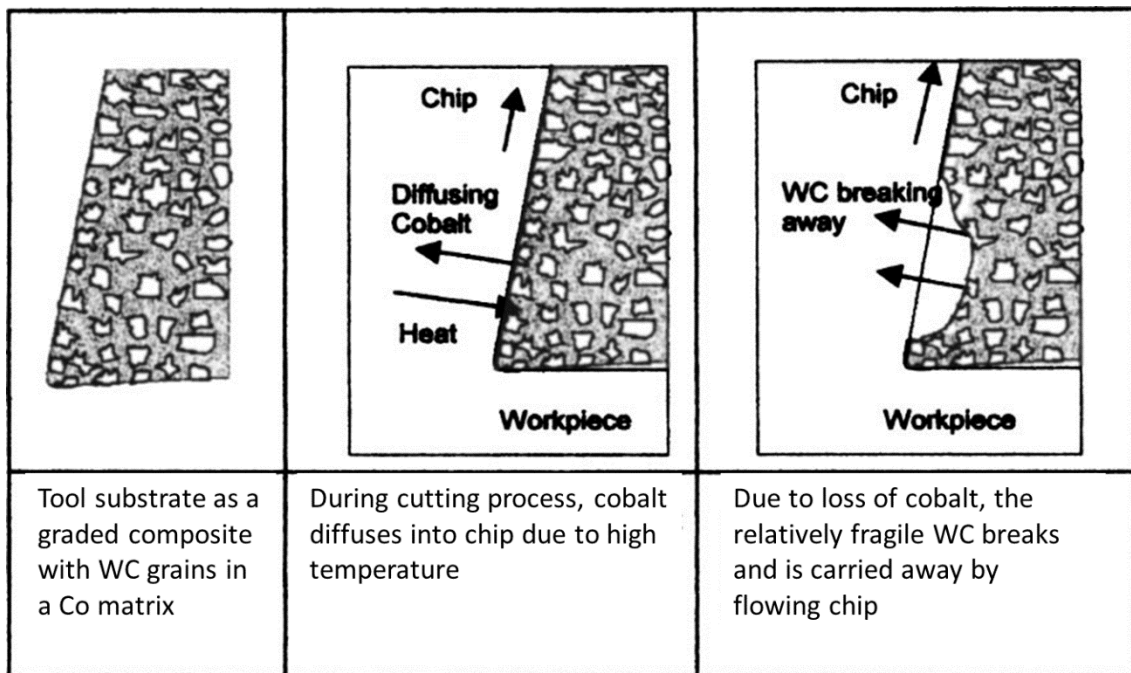
Figure 2.39. Diffusion mechanism in cutting titanium alloys with tungsten carbide tools, after Hua and Shivpuri [30].

The thermal diffusion based wear model for predicting crater wear rate was shown to be able to predict both crater wear depth and wear rate with reasonable accuracy when machining Ti-64. This was true for varying cobalt concentrations and for different cutting speeds and depths of cut. An example of this is shown in Figure 2.40 for a feed rate of 0.127 mm.rev^{-1}.
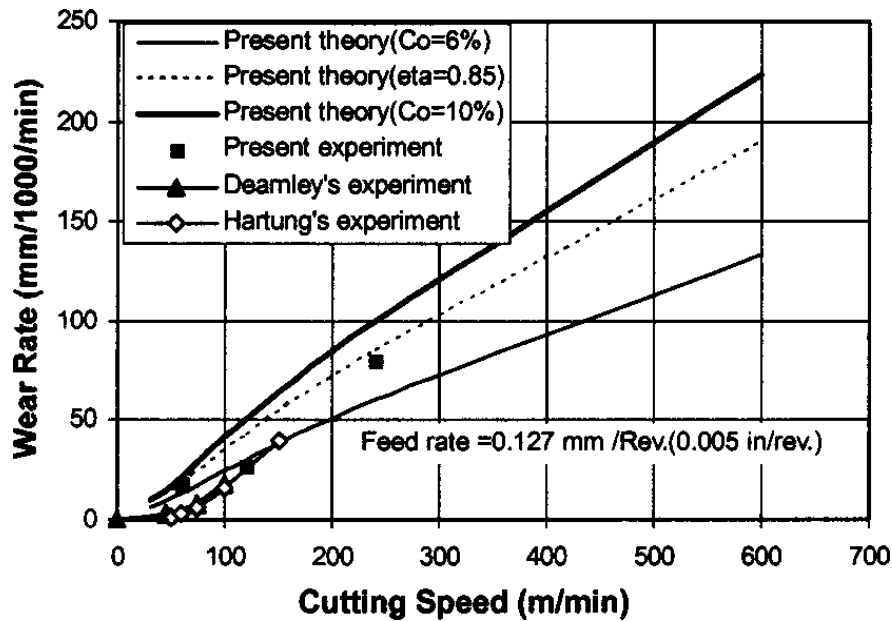
Figure 2.40. Comparison of predicted crater wear rate with experimental results for machining Ti-64 (Feed rate = 0.127 mm.rev[-1]), after Hua and Shivpuri [30]

The work also found that crater wear increases with cutting speed with the slope of the wear rate remaining constant after an initial change *c.f.* Figure 2.40. They found that crater wear doubles when the feed rate is doubled. However, they found that the wear rate was independent of cutting time which could not be explained by their diffusion model. Finally, the study found that the maximum depth of crater profile coincides with maximum temperature along the rake face.

Corduan *et al.* [31] write that turning of Ti-64 with carbide tools is mastered for cutting speeds of less than 60 m.min^{-1}. At speeds higher than this, chemical and mechanical properties of Ti-64 cause wear mechanisms such as adhesion and diffusion. The study looks at wear mechanism for new tool materials for machining of Ti-64: PCD, CBN and TiB_2 coated carbides. The wear patterns observed for all materials are strongly linked to chemical reactions and phase changes which occur in the PCD and CBN tools. Concerning the TiB_2 carbide tool, the coating originally protects the tool against diffusion and adhesion before severe delamination *c.f.* Joshi *et al.* [129]. The study calls for new coating technology which has better thermal fatigue resistance.

It was in 1980 when Kramer and Suh first proposed a quantitative understanding of tool wear by "solution" [25]. The work looked at the mechanism controlling the crater wear of single phase carbide cutting tool materials in the high speed cutting of steel. However, Kramer lets it be known that the work has broad application to other tool-work combinations. With

57

reference to Figure 2.41, Kramer and Suh show that the flux of tool material may be expressed as (Equation 2.11):

$$v_{wear} = K \left(-D \frac{dc}{dy} + C v_y \right)_{y=0}$$ Equation 2.11

Where v_{wear} is the wear rate of the tool material (cm.s^{-1}); K is the ratio of molar volumes of the tool material and workpiece material respectively; D is the diffusivity of the slowest diffusing tool constituent atom in the workpiece (cm^2.s^{-1}); c is the concentration of the tool material in the workpiece; C is the equilibrium concentration (solubility) of the tool material in the workpiece; and v_y is the bulk velocity of the chip material at the tool-chip interface perpendicular to the interface (cm.s^{-1}).
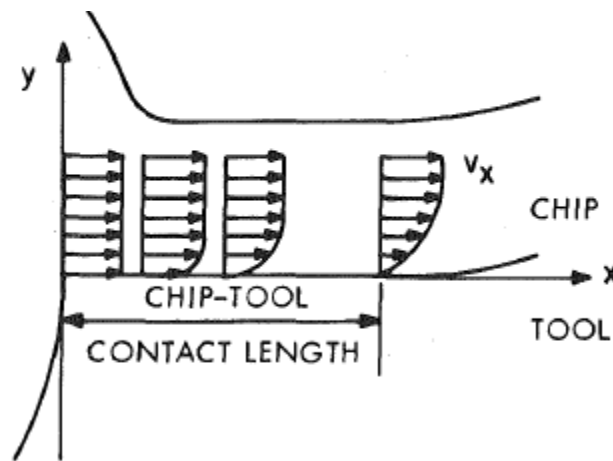
Figure 2.41. Schematic of the chip flow geometry, after Kramer and Suh [25].

The first term is the diffusion flux. The concentration gradient dc/dy (Equation 2.11), is the driving force for diffusion. The velocity profile within the chip strongly influences the concentration gradient. The chip flow is responsible for the second term in the equation, the flux due to the bulk flow of the chip material. Kramer showed that solution wear dominated the wear of carbides and postulated whether there is any potential for further improvement in the wear resistance of carbides.

Hartung and Kramer [26] took this work further by looking at diffusion wear in titanium alloy machining. Hartung suggests that tool wear is greatly reduced when adhesion occurs between the tool and chip. This is because it prevents relative sliding at the tool-chip interface. This adhesion which leads to BUE is promoted by chemical reaction at the interface. During a machining trial Hartung explains that, "the thickness of the reaction layer

58

is determined by the balance between the diffusion flux of tool constituents through the layer and the removal of tool constituents through chemical dissolution at the interface between the reaction layer and the titanium chip." So for given cutting conditions, or tool-workpiece pairings, a characteristic thickness of a reaction layer is maintained and the tool wear is limited by the rate of dissolution of the reaction layer into the titanium. Hartung demonstrates the existence of a stable reaction layer of TiC on both diamond and WC based tools when machining Ti-64 and that the estimated diffusion flux correlates well with the observed rate of tool wear. Hartung contemplates that there may be no potential tool materials in existence that are sufficiently chemically stable with respect to titanium to exhibit low ware rates by virtue of their low solubility in titanium. It is put plainly that to maximise tool life, relative sliding between the tool and chip must be eliminated. Formation of a BUE as a "boundary layer" on the tool face can limit the diffusion rate of tool constituents through this layer.

It is assumed that, since crater wear is the dominant form of tool wear in titanium alloy machining, that tool wear can be explained by chemical dissolution of the tool material in titanium *c.f.* Kramer and Suh [25]. It can be assumed that the mechanics of chip flow are similar for different tool materials cutting under the same conditions. Therefore, the relative wear rates of the tool materials may be taken as the ratio of the products of the solubility and the molar volume for each material (Equation 2.12).

$$Relative\ wear\ rate = \frac{v_{wear\,1}}{v_{wear\,2}} = \frac{v_1 C_1}{v_2 C_2}$$
<div align="right">Equation 2.12</div>

Where $v_{wear\,1}$ is the wear rate of 'tool material 1'; v_1 is the molar volume of 'tool material 1'; and C_1 is the equilibrium concentration (solubility) of 'tool material 1' in the workpiece at cutting temperature. Table 2.8 shows estimated solubilities of tool materials in titanium at various temperatures. It is assumed that the solubility of the tool material in titanium will be no greater than the solubility of its least soluble component. For example, if the tool material is WC, it may be assumed that the solubility of WC will be no greater than the solubility of carbon since the solubility of tungsten in titanium is much greater than that of carbon.

TABLE 2.8. ESTIMATED SOLUBILITIES OF TOOL MATERIALS IN TITANIUM AT
VARIOUS TEMPERATURES. * INDICATES CHEMICAL REACTION OCCURS.
AFTER HARTUNG AND KRAMER [26].

Tool material	Solubility (mole fraction)		
	1300 K	1400 K	1500 K
HfC	1.27	1.41	1.53
NbC	23.70	20.73	18.45
SiC	*	*	*
TaC	16.03	14.32	13.02
TiC	7.75	7.75	7.75
VC	*	*	*
WC	*	*	*
ZrC	4.23	4.42	4.58
BN	*	*	*
HfN	10.92	12.80	13.35
Si_3N_4	*	*	*
TiN	48.58	48.48	48.17
Al_2O_3	*	*	*
HfO_2	7.85	14.67	29.46
ZrO_2	10.47	21.58	39.50
La_2O_3	0.033	0.076	0.16
TiB_2	*	*	*

Table 2.9 shows the solubilities of tool constituents in titanium obtained from phase diagrams
[137-140]. Comparing Tables 2.8 and 2.9 shows that all tool materials save HfN, HfO_2 and
La_2O_3 have predicted solubilities in titanium that are greater than that of at least one of their
constituents. Here, the solubility of the tool material can be approximated by the solubility of
the least soluble component divided by the number of atoms of that component per molecule
of tool material.

TABLE 2.9. REPORTED SOLUBILITIES OF TOOL CONSTITUENTS IN TITANIUM AT VARIOUS TEMPERATURES. * INDICATES CONSTITUENTS THAT ARE SOLUBLE OVER A WIDE RANGE OF TEMPERATURES AND CONCENTRATIONS. AFTER HARTUNG AND KRAMER [26].

Tool constituent	Solubility (at%)		
	1300 K	1400 K	1500 K
Al	15.0	19.0	28.0
B	1.0	1.0	1.0
C	0.6	0.6	0.6
Hf	*	*	*
La	1.0	1.0	1.0
N	23.6	23.5	23.2
Nb	*	*	*
O	34.0	34.0	34.0
Si	2.2	3.0	4.0
Ta	*	*	*
Ti	100.0	100.0	100.0
V	*	*	*
W	*	*	*
Zr	*	*	*

A model by Cook and Nayak [141] yields an upper bound for the wear rate of tool materials in the machining of titanium alloys due to diffusion. Equation 2.13 shows the predicted wear rate in the centre of the crater.

$$v_{wear} = -KC \left(\frac{D}{\pi t}\right)^{1/2} \hspace{4cm} \text{Equation 2.13}$$

Where v_{wear} is the wear rate of the tool material; K is the ratio of molar volumes of the tool material and chip material; C is the equilibrium concentration of the tool material in the chip; D is the diffusion coefficient of the slowest diffusing tool constituent in the chip; and t is the time it takes for the chip to move from the edge of the tool to the centre of the crater. The predicted ware rates of various tool materials (at 1400 K) using Equation 2.13 were found to overestimate the wear rates when compared to actual measured wear rates. The model also failed to properly rank the materials in order of their wear resistance. However, an improved model by Hartung for calculating the wear rate of PCD and WC tools in titanium machining showed good agreement with actual measured wear results (Equation 2.14).

$$v_{wear} = \frac{v_t D}{C_t t} \left(\frac{C_b}{V_b} - \frac{C_0}{V_0}\right) \hspace{4cm} \text{Equation 2.14}$$

Where v_t is the molar volume of the tool material (cm^3.mol^{-1}); C_t is the concentration of carbon in the tool material (mol); D is the diffusion coefficient of carbon in the TiC reaction layer (cm^2.s^{-1}); C_b is the concentration of carbon at the reaction layer/chip boundary; C_o is the concentration of carbon at the reaction layer/tool boundary; t is the thickness of the TiC reaction layer; V_b is the molar volume as above; and V_o is the molar volume as above.

Like Zhang *et al.* [34], the chemical solubility of tool materials in titanium alloys was investigated via a diffusion couple technique by Bhat *et al.* [32]. The team compared the chemical wear behaviour of WC-Co tools and a novel AlMgB$_{14}$ ceramic with both CP-Ti and Ti-64. Using the equilibrium solubility equation by Kramer *et al.* [142] (Equation 2.15) to first determine the solubility of AlMgB$_{14}$ in titanium; and then the relative wear rate equation from Kramer and Suh [25] (Equation 2.12), they were able to show that a tungsten carbide tool will wear ~13 times faster than a AlMgB$_{14}$ tool. However, despite its high hardness and favourable fracture toughness, the material is far too brittle to use as a cutting insert.

$$C_{A_xB_y} = exp\left(\frac{\Delta G_{A_xB_y} - x\Delta G_A^{xs} - y\Delta G_B^{xs} - xRT\ln x - yRT\ln y}{(x+y)RT}\right) \qquad \text{Equation 2.15}$$

Where:
$C_{A_xB_y}$ = Chemical solubility of A_xB_y moles/mole of Ti
$\Delta G_{A_xB_y}$ = Free energy of formation of A_xB_y (cal/mol)
ΔG_A^{xs} = Excess free energy of solution of element A in Ti (cal/mol)
ΔG_B^{xs} = Excess free energy of solution of element B in Ti (cal/mol)

The study also used the model of Cook and Nayak [141] (Equation 2.13) to predict the crater wear rate of AlMgB$_{14}$. They write that it is predicted to be one fourth that of WC-Co despite Hartung and Kramer's critique [26] of the model's accuracy. The static diffusion couple tests were assembled in a sandwich fashion consisting of the tool between two workpiece alloys (Figure 2.42).
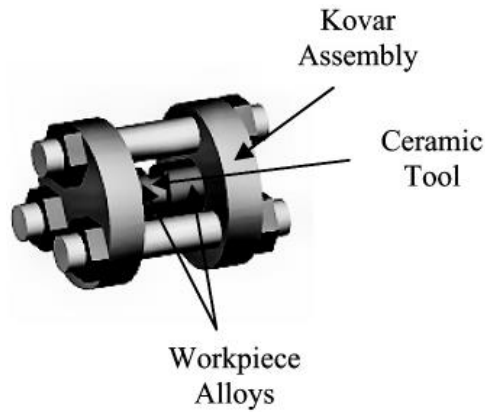
Figure 2.42. Diffusion couple setup known as the Kovar™ assembly [32].

The diffusion couples were heated in an argon furnace at 1000°C for 120 h. The high temperature was to mimic the tool-work interface in machining and the exaggerated time was to promote chemical activity. After heat treatment, the diffusion couples were analysed via SEM and electron probe microanalysis (EPMA). Figure 2.43 shows the reaction interface between CP-Ti and WC-Co.
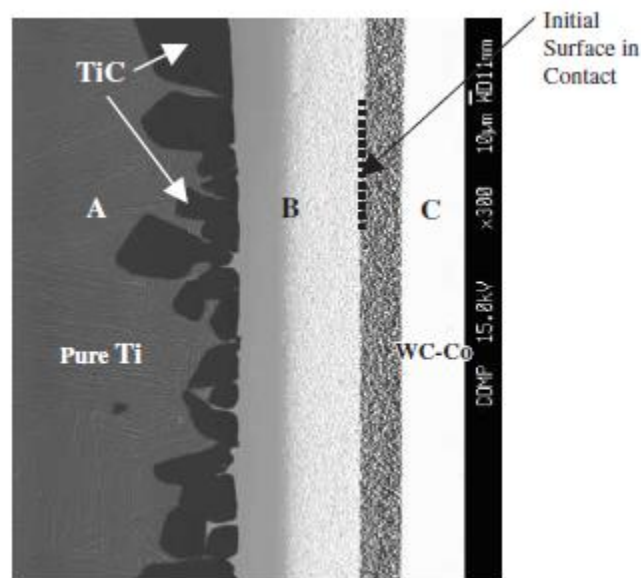
Figure 2.43. Electron micrograph of the reaction interface between CP-Ti and WC-Co after 120 h at 1000°C [32].

The micrograph shows discrete islands of TiC within the Ti bulk which were formed along the interface in a regular manner. Region B confirms the formation of TiC as there is a depletion of Ti and an enrichment of carbon. The authors suggest that the strong chemical reactivity of Ti leads to decomposition of WC. The brighter grey region in B indicates W enrichment with consequent depletion in titanium. Conversely, titanium enrichment and

tungsten depletion is observed within the tool side of the diffusion zone (dark grey next to region C). The width of the diffusion zone was estimated to be 250 μm.

Figure 2.44 shows the interface of the diffusion couple between CP-Ti and AlMgB$_{14}$.
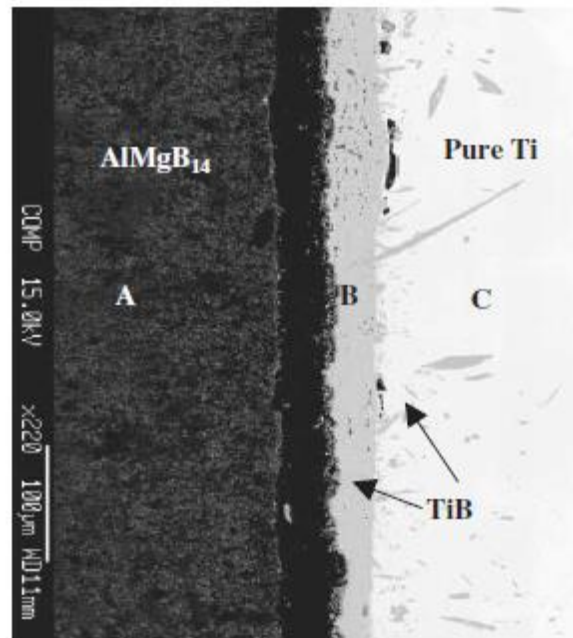
Figure 2.44. Electron micrograph of the reaction interface between CP-Ti and AlMgB$_{14}$ after 120 h at 1000°C [32].

This diffusion couple did not form a strong bond with the CP-Ti like the WC-Co did. However, it was strong enough to preserve and analyse. No diffusion was observed in the tool side but the workpiece side showed significant diffusion. Zone B shows a strong presence of titanium and boron which suggests titanium boride. The morphology of these borides shows evidence of preferential diffusion of boron from the tool along the grain boundaries of the titanium. The width of the diffusion interface was estimated to be 40 μm i.e. considerably less than that for WC-Co.

Jianxin *et al.* [33] investigated diffusion wear between Ti-64 and WC-Co tools, firstly with static diffusion couples and then with dry cutting. The diffusion couples (Figure 2.45) were subjected to a pressure of 10 MPa to obtain intimate contact between the tool and workpiece before being heat treated in an air atmosphere for 90 min at temperatures of 400°C, 600°C and 800°C respectively.
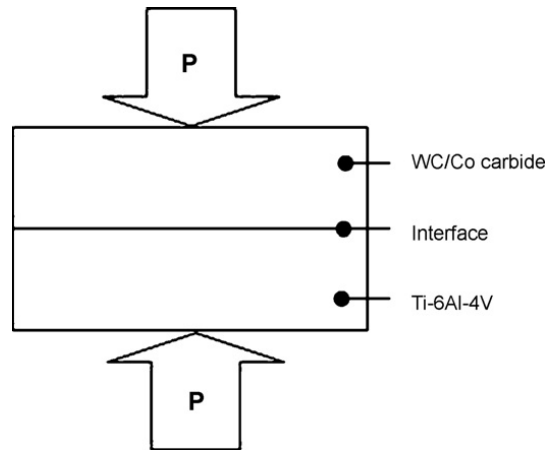
Figure 2.45. Schematic of diffusion couple setup [33].

Analysis of the diffusion couples was done using X-ray diffraction (XRD) to identify crystal phases; EPMA to analyse elemental diffusion; and Vickers hardness tests with a load of 10 N and 2 N for the WC-Co and Ti-64 respectively. XRD results showed that no oxidation took place at 400°C; a TiAlN phase formed at 600°C; while TiO_2 and Ti_4N_3 phases were detected at 800°C. This is to be expected as the titanium reacts with the oxygen and nitrogen in the air atmosphere. Figure 2.46a shows the oxidised surface of the WC-Co after heating in air atmosphere at 800°C where large cracks can be observed. The authors write that this is due to a large thermal expansion coefficient mismatch amongst WO_3, Co_3O_4 and WC phases during cooling. Figure 2.46b shows the oxidised layer on the surface of the WC-Co tool of thickness 16 µm.
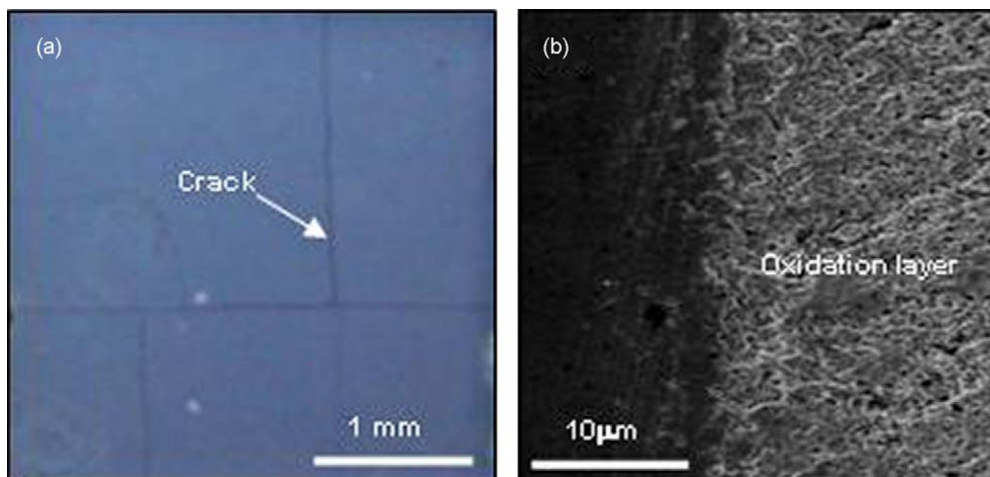
Figure 2.46. Micrographs of (a) cracks in oxidised surface and (b) cross-sectional view of the carbide after heating in an air atmosphere for 90 min at 800C° [33].

Figure 2.47 shows the interfaces of the diffusion couples after being heated to (a) 400°C and (b) 600°C. The increased depth to which the tungsten and cobalt diffuse into the Ti-64 can be observed at 600°C.
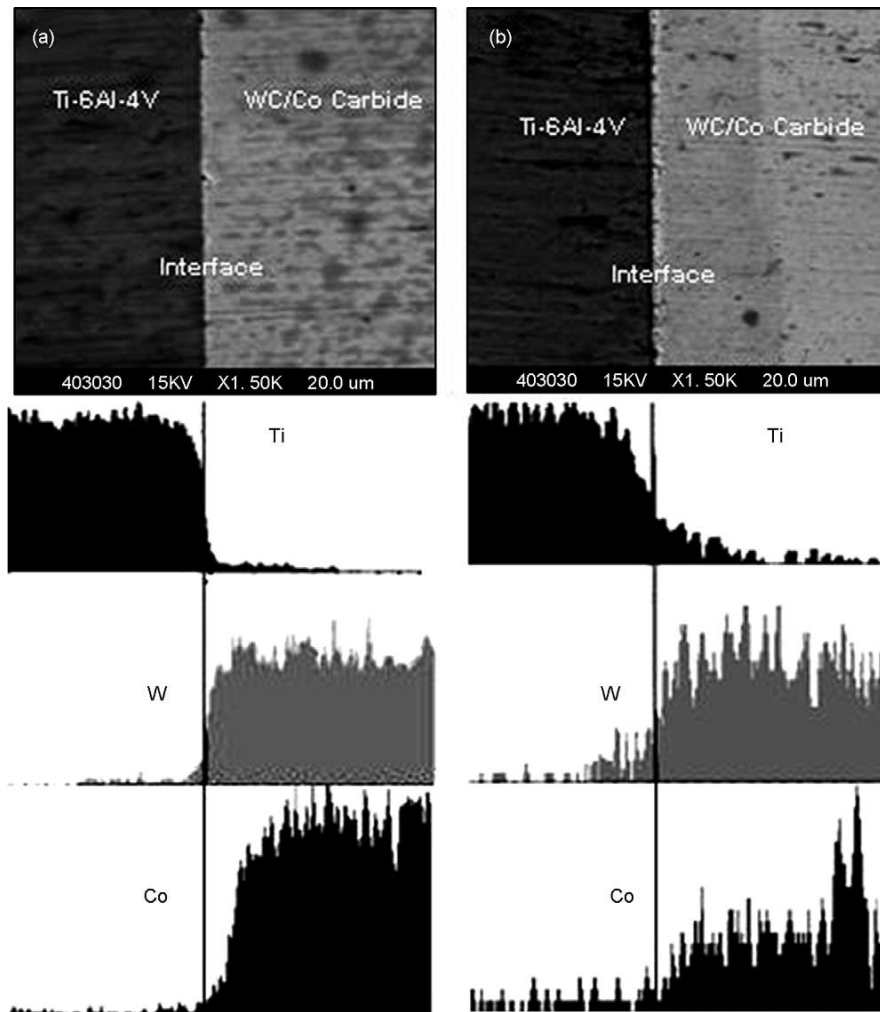
Figure 2.47. Elemental diffusion across the interface of a Ti-64 / WC-Co diffusion couple after heating in air atmosphere for 90 min at (a) 400°C and (b) 600°C [33].

Figure 2.48a to b shows the diffusion couple before and after heat treatment for 90 min at 800°C. In Figure 2.48b, a ~20 μm thick layer of different composition can be observed in the Ti-64 alloy near the interface. EPMA analysis confirms the presence of tungsten and cobalt in this region.
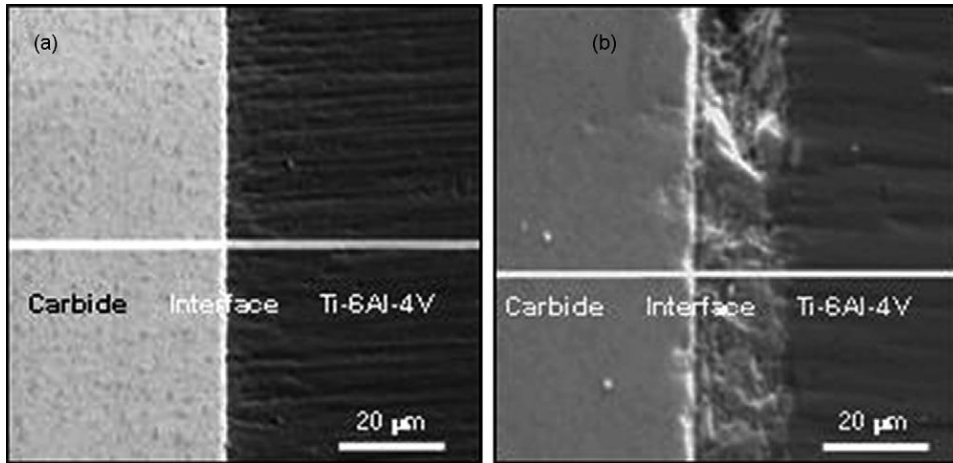
Figure 2.48. SEM micrographs of the diffusion couple (a) before and (b) after heating in air atmosphere for 90 min at 800°C [33].

Vickers hardness values were obtained across the interface of the diffusion couple after heating at 600°C. Figures 2.49a and b show how the hardness values are lower nearer the interface. The authors believe that this is due to elemental diffusion.
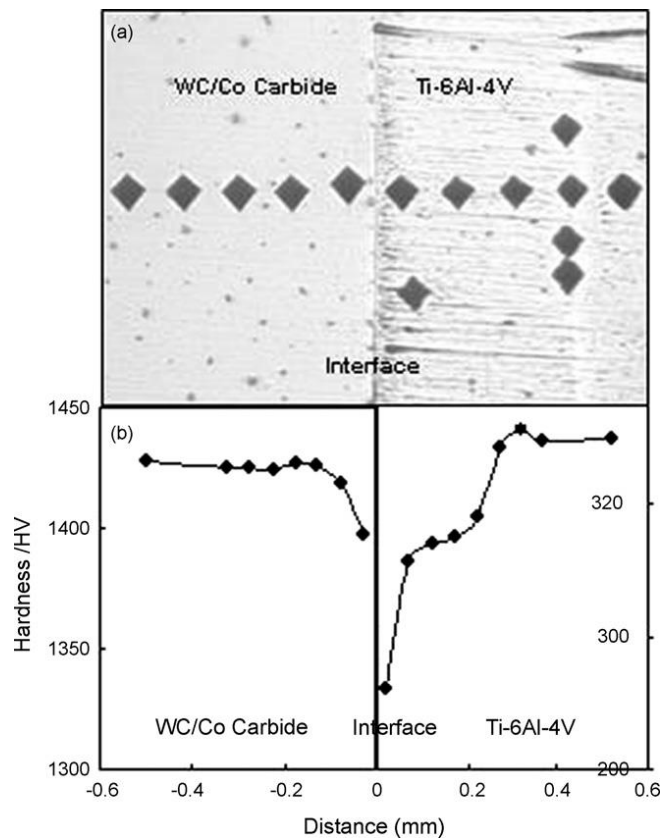
Figure 2.49. Hardness values along the interface of the diffusion couple after heating in air atmosphere for 90 min at 600°C [33].

The machining trials showed evidence of elemental diffusion from the workpiece onto the rake face of the tool for cutting speeds of 60 and 120 m.min^{-1}. However, evidence of workpiece elements (Ti, Al, V) were not found on the rake face after machining at a cutting

speed of 20 m.min^{-1}. The team measured cutting forces during dry cutting of Ti-64 with WC-Co tools and observed a sharp increase in force on F_z, F_y, and F_x after a distance of 600 m. However, the writers do not elaborate on why this may be the case. The forces were relatively stable at cutting distances less than 600 m. The sudden increase in cutting forces is probably due to a change in the tool wear mechanism. Formation of BUE on the cutting edge of the tool causes sliding at the cutting interface which eventually leads to tool failure. The work also fails to look at the microstructure of the titanium alloy. Any indication of change in the phase morphology at the subsurface of the titanium alloy could provide strong evidence of elemental diffusion.

Preliminary diffusion couple tests using titanium alloys and conventional carbide tools has not been taken any further in the current literature than already discussed here [32-34]. However, there has been some excellent work conducted by Palcut *et al.* [143, 144] who have looked at solid state reactions between lanthanum and manganese oxides using diffusion couples. Figure 2.50 shows a micrograph of the diffusion couple between La_2O_3 (left) and Mn_3O_4 (right) where a layer of $LaMnO_3$ can be observed at the interface.
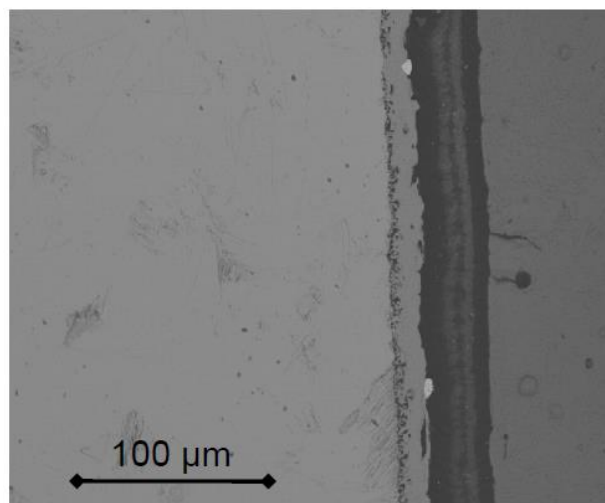
Figure 2.50. Cross section of a diffusion couple annealed at 1478 K for 60 h, after Palcut [144].

The study was able to conclude that the solid state reaction kinetics were predominantly governed by diffusion of Mn^{3+} through the $LaMnO_3$ reaction layer. It is important to draw parallels from this work with respect to the work of Nishimura [76] who looked at the corrosion of titanium alloys where on production of titanium ions, the system subsequently underwent a hydrolysis reaction to produce hydrogen ions which then lowered the pH value of the system. The work also correlates to that of Hartung and Kramer [26] where they

68

discuss how the reaction layer on the tool face can limit the diffusion rate of tool constituents through the layer.

Palcut also measured the thickness of the reaction layer as a function of time and temperature as shown in Figure 2.51. They conclude that the growth of the reaction layer obeys the parabolic rate law (Equation 2.16), and the reaction is therefore not controlled by the interfacial reactions at the two heterophase interfaces.

$$x^2 = 2k_p t$$ Equation 2.16

Where x is the thickness; t is the time; and k_p is the parabolic rate constant. The reaction layer grows towards the La_2O_3 side of the diffusion couple where La_2O_3 changes to $LaMnO_3$ forming vacancies at the Mn and O sites.
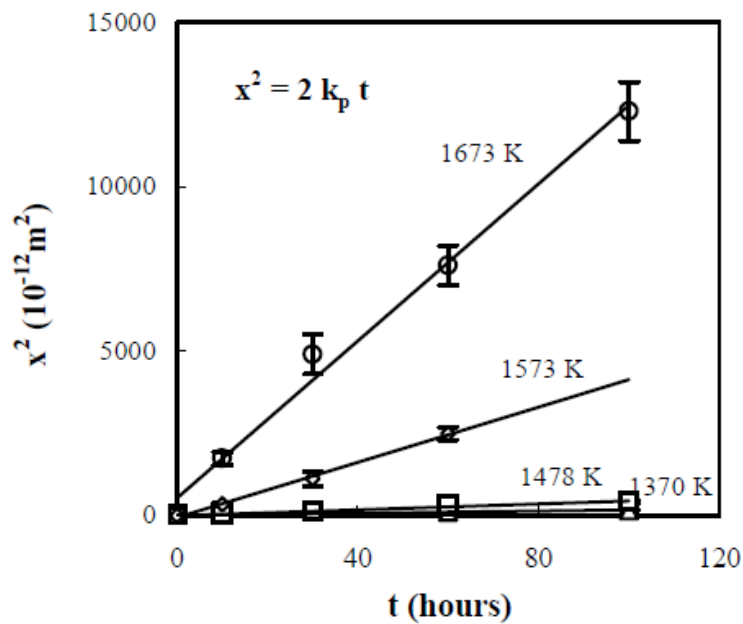
Figure 2.51. The thickness of the product layer as a function of time and temperature [144].

2.9 Chapter summary

This literature review has outlined the fundamentals behind the proposed work, following the metallurgical background of titanium which included: applications; alloy classification; thermomechanical processing; diffusion; corrosion; and oxidation. The mechanics of machining were then touched upon before detailing orthogonal cutting and the principles of tool wear. A discussion of modern tool materials used for machining was then presented followed by considering the importance of alloy chemistry. Finally, the current literature on diffusion in titanium alloy machining was analysed.

Currently there remains a significant knowledge gap in the understanding of the effect of chemistry and microstructure condition on the mechanisms of subsurface damage and tool wear behaviour in titanium alloy machining. This is particularly apparent in that tool manufacturers offer the same tool irrespective of which alloy is to be machined. This is despite the fact that the literature has shown how phase morphology of titanium alloys significantly affects their machinability.

Consequently, this study will aim to investigate tool wear via diffusion mechanisms in the machining of titanium alloys. This investigation will comprise of an experimental approach incorporating a range of diffusion bonding strategies coupled with thermodynamic modelling which will be directly validated by machining trials. Such an approach can provide a strong indication of the complex reaction mechanisms at the cutting zone. This will help to enhance tool grade development for increased efficiency in titanium alloy machining. This work will help the machining community to understand tool wear mechanisms at new levels of detail.

Chapter 3 - Experimental procedures and thermodynamic modelling approach

3.1 Introduction

This chapter will outline the common experimental procedures which were used during the investigation. These include metallographic sample preparation techniques, optical microscopy, scanning electron microscopy (SEM), transmission electron microscopy (TEM), focused ion beam (FIB) milling and X-ray energy dispersive spectroscopy (X-EDS). This chapter also introduces the thermodynamic modelling framework when using the software module, DICTRA. Any bespoke experimental methodologies are outlined in more detail along with the corresponding results and discussion.

3.2 Titanium alloys

Six different titanium alloys were used throughout this study in order to represent the α to near β spectrum. Typical applications of these alloys were first mentioned in §2.1 before a detailed account of their properties was examined in §2.2. They are presented below in order of increasing β phase quantity in Table 3.1.

TABLE 3.1. CHEMISTRY OF TITANIUM ALLOYS USED ALONG WITH THE INFORMAL NAMES AND ALLOY TYPE.

Nominal alloy chemistry	Informal name	Alloy type
CP-Ti (Grade 2)	CP-Ti	α
Ti-5.8Al-4Sn-3.5Zr-0.7Nb-0.5Mo-0.35Si-0.06C	Ti-834	Near α
Ti-6Al-4V	Ti-64	$\alpha+\beta$
Ti-5Al-4V-0.8Mo-0.5Fe	Ti-54M	$\alpha+\beta$
Ti-6Al-2Sn-4Zr-6Mo	Ti-6246	$\alpha+\beta$ / Near β
Ti-5Al-5Mo-5V-3Cr-0.6Fe	Ti-5553	Near β

Figure 3.1a to f shows the typical microstructures of the alloys listed in Table 3.1.
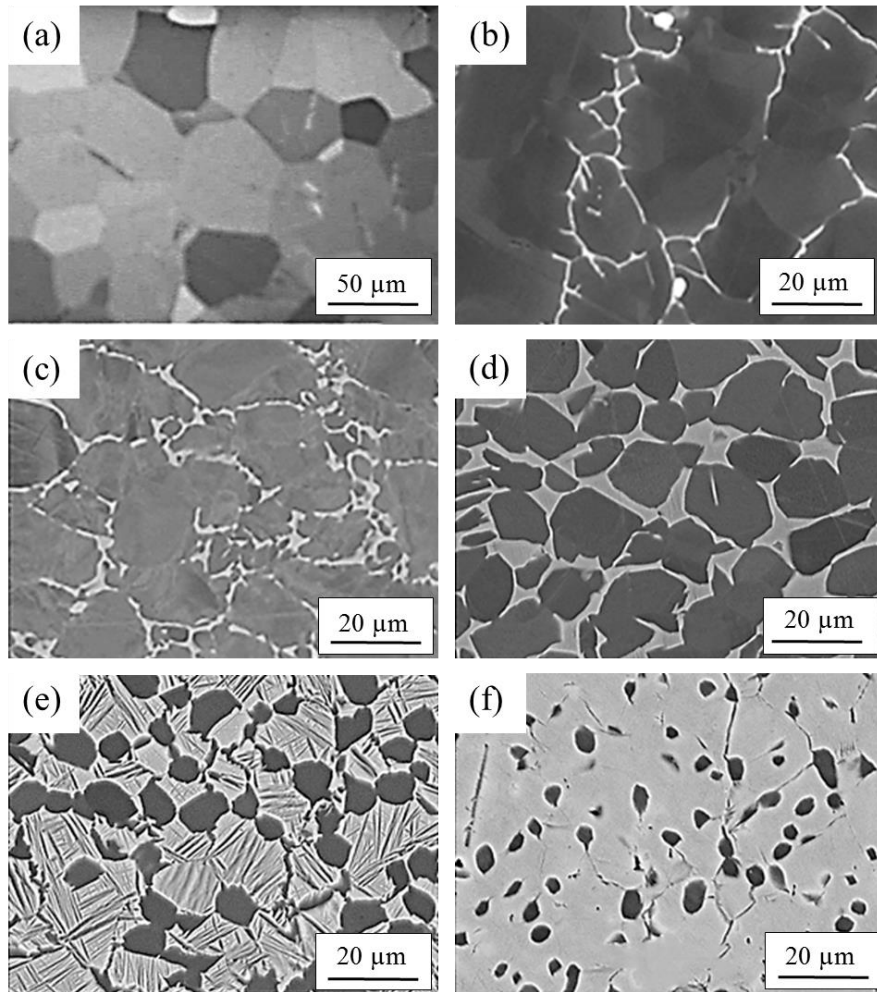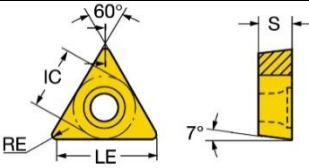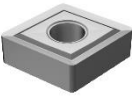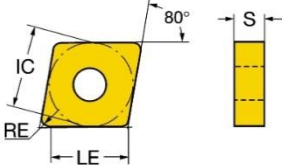
Figure 3.1. Light micrograph of (a) CP-Ti and electron micrographs of (b) Ti-834, (c) Ti-64, (d) Ti-54M, (e) Ti-6246 and (f) Ti-5553.

3.3 Tools

For the machining trials and diffusion couple experiments, uncoated Sandvik Coromant H13A grade cutting tool inserts were used. This grade comprises of tungsten carbide grains with 6 wt.% cobalt as binder (WC-6%Co). Table 3.2 gives more information on all tools used in this study.

TABLE 3.2. TOOL INSERT INFORMATION OF THOSE USED THROUGHOUT THE INVESTIGATION. IC = INSCRIBED CIRCLE DIAMETER; RE = CORNER RADIUS; LE = CUTTING EDGE LENGTH; S = INSERT THICKNESS [97].

Number	Grade	Image	Dimensions	Substrate	Coating
1	H13A			WC-6%Co	Uncoated
2	H13A			WC-6%Co	Uncoated

3.4 Metallographic preparation

Samples were prepared via the same procedure for all diffusion couple tests outlined in Chapters 4 and 7. All alloys listed in Table 3.1 were received as a billet in the as forged condition from TIMET UK. However, Ti-5553 was provided by Safran Landing Systems. The large billets were first cut into smaller, more manageable sizes using electrical discharge machining (EDM). Subsequently, samples were then precision sectioned into 20x20x5 mm coupons using a Struers Secotom-50 fitted with a MetPrep Type T5 abrasive cutting wheel. In order to prepare for diffusion tests each sample was first mounted in a 32 mm diameter Bakelite resin before being ground and polished to a mirror finish via the procedure outlined below in Table 3.3.

TABLE 3.3. METALLOGRAPHIC PREPARATION SUMMARY OUTLINING THE GRINDING AND POLISHING REGIMEN.

Step	Grit paper / polishing pad	Dosage	Time
1. Grinding	P400 grit SiC grinding paper	Constant water cooling	1 min Until planar with homogenous profile
	P800 grit SiC grinding paper	Constant water cooling	1 min Until planar with homogenous profile
	P1200 grit SiC grinding paper	Constant water cooling	1 min Until planar with homogenous profile
2. Primary polish	Struers MD-Largo polishing pad	Water based 9 μm diamond suspension (MetPrep)	6 min Ensure disc is suitably lubricated for duration Until planar with homogenous profile
3. Final polish	Struers MD-Chem porous neoprene disc	Silco solution - 90% 0.05 μm colloidal silica suspension and 10% laboratory reagent grade H_2O_2 (30% w/v) Rinse with water	5 min just water 5 min Silco with slow drip of water 1 min rinse with water 5 min Silco with slow drip of water 5 min rinse with water

All stages were completed using a Buehler Automet 250 set with a complimentary plate rotation speed of 249 rpm; a head speed of 50 rpm; and a constant of force of 30 N.

3.5 Imaging and analysis

3.5.1 Light optical microscopy

After grinding and polishing, the microstructures can be realised via light optical microscopy. For this investigation a Nikon Eclipse LV150 optical microscope was used with cross-

polarised light filters. Buehler OmniMet software was used for digital image acquisition and quantitative analysis.

3.5.2 SEM and X-EDS
To study microstructures at higher magnifications, a Zeiss EVO LS25 scanning electron microscope was used. Typical operating parameters are outlined below in Table 3.4. To help enhance the contrast between α and β phases as well as interface reaction species, the backscatter detector was most commonly employed.

TABLE 3.4. OPERATING PARAMETERS FOR THE SEM.

Parameter	Typical value
Accelerating voltage	20 keV
Spot size	3
Working distance	9-13 mm
Detector	Backscatter and secondary electron

Attached to the SEM was an X-EDS device from Oxford Instruments which was employed throughout the study for quantitative elemental analysis.

3.5.3 FIB and TEM
In order to study the microstructure of various cutting inserts at high magnification, a FIB lift out technique (FEI Quanta 3D SEM/FIB) was used to prepare samples for TEM analysis. After first locating the tool wear zone on the rake face (Fig.3.2a and b), a carbon strap is deposited on to the region of interest using an i-beam current of 0.3 nA. This $15x2x2 \ \mu m^3$ strap helps protect the foil sample during lift out. Subsequent trenches were then milled either side of the carbon strap measuring $20x8x4 \ \mu m^3$ using an i-beam current of 5 nA (Fig.3.2c). After the trenches are milled, the sample foil is milled out from the bulk ready for lift out (Fig.3.2d). Next, the sample foil is attached to an OmniProbe 200 (Oxford Instruments) using carbon deposition before final milling (0.5 nA) to release the foil (Fig.3.2e). The sample is then attached to a copper TEM grid using carbon deposition (0.3 nA) (Fig.3.2f) before retracting the omniprobe ready for final thinning (Fig.3.2g). Final thinning of the sample foil is achieved using the steps in Table 3.5 to achieve a foil thickness of < 100 nm (Fig.3.2h).
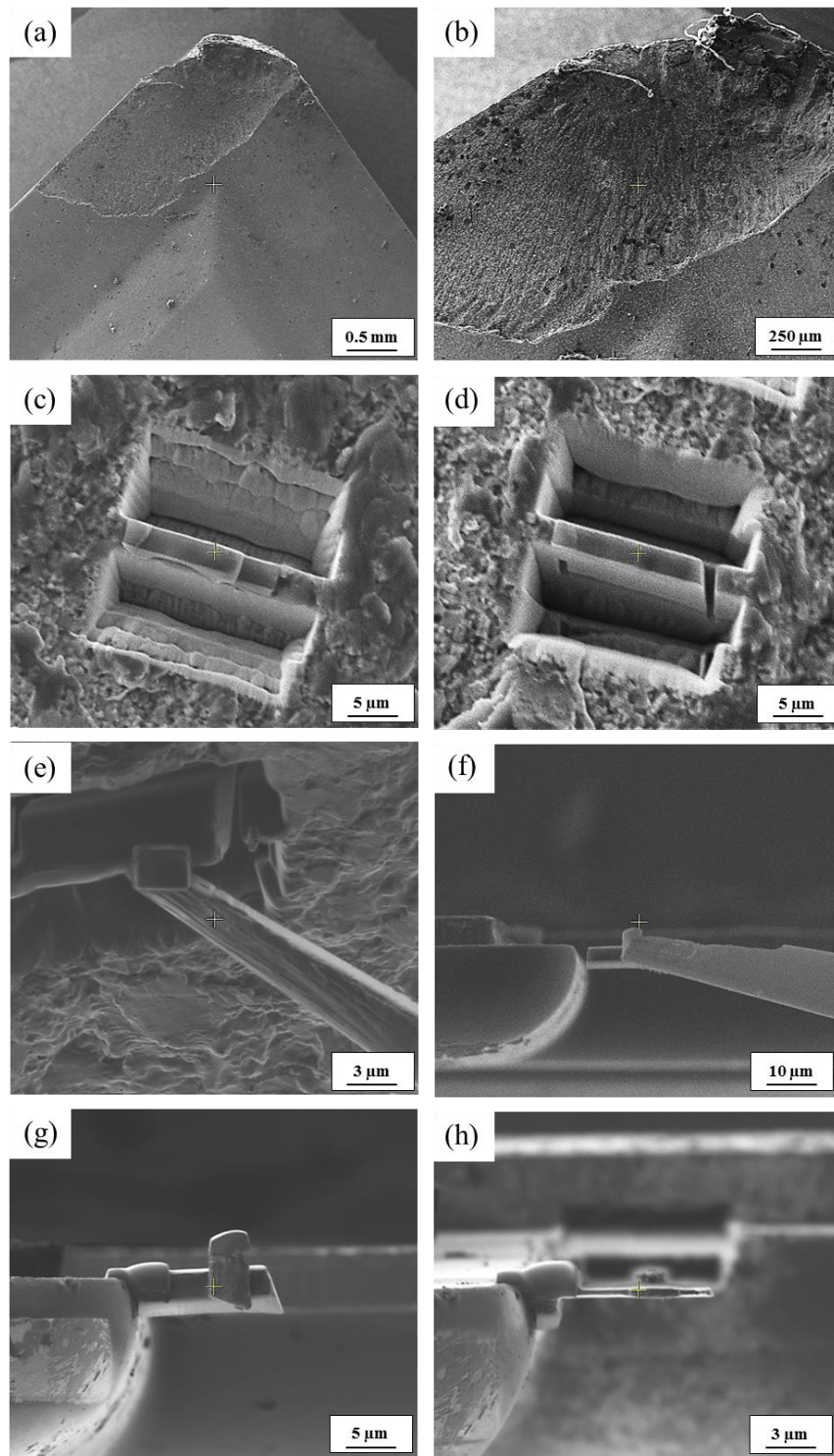
Figure 3.2. Electron micrographs of the stages of FIB lift out and attachment to the TEM copper grid. (a) Locating the wear zone on the rake face of the tool; (b) Finding suitable location to successfully ion mill; (c) deposition of carbon strap and subsequent milling of trenches either side; (d) milling the sample foil free from the trench; (e) attachment of omniprobe to sample foil using carbon deposition; (f) attachment of sample foil to copper TEM grid using omniprobe; (g) retraction of omniprobe to reveal successful attachment of sample foil to TEM grid and (h) final thinning of sample foil.

TABLE 3.5. STEPS FOR FINAL THINNING OF A TEM SAMPLE FOIL USING FIB.

Step	FIB current	Milling side	Stage tilt	Typical thickness after milling (nm)
1	0.5 nA	Back	50.8°	-
2	0.5 nA	Front	53.2°	500
3	100 pA	Back	51°	-
4	100 pA	Front	53°	150
5	30 pA	Back	51.5°	-
6	30 pA	front	52.5°	<100

After achieving a sample thickness of <100 nm, the microstructure can be revealed using TEM. During this study an FEI Tecnai 20 TEM was used which is a 200 kV fully computerised TEM with 0.24 nm resolution and probe size down to 1 nm in diameter. All micrographs are bright field (BF) TEM micrographs and were obtained using a single tilt beryllium holder.

3.6 Thermo-Calc DICTRA thermodynamic modelling software

Thermodynamic modelling plays a crucial role in this investigation with the aim of predicting elemental diffusion as well as interfacial reaction species formation. It is used to support experimental results obtained from diffusion couple tests discussed in Chapter 4. Thermo-Calc was the base software package used which allows for the calculation of thermodynamic and phase equilibria. By selecting a suitable thermodynamic database (assessed using CALPHAD), Thermo-Calc can be used to calculate phase diagrams, thermochemical data, and amounts of phases and their compositions as a function of temperature and chemistry. DICTRA is an add-on module to Thermo-Calc which can accurately simulate diffusion controlled reactions in multicomponent alloy systems. DICTRA is based on the numerical solution of the multicomponent diffusion equations and the CALPHAD approach. A basic calculation procedure consists of a numerical finite difference scheme for solving a system of coupled parabolic partial differential equations (Figure 3.3). All simulations depend on assessed kinetic and thermodynamic data which are stored in databases.
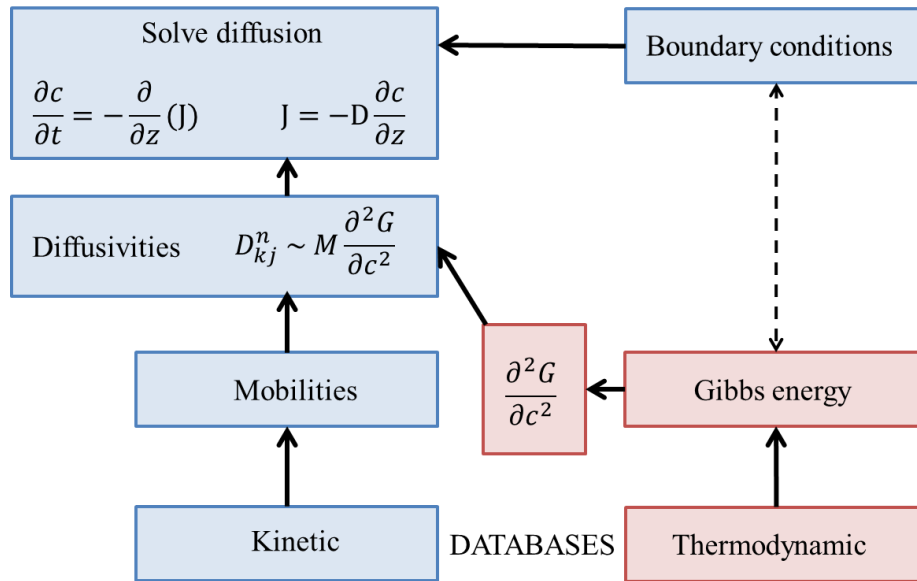
Figure 3.3. Basic calculation procedure for DICTRA. Data is needed from both kinetic and thermodynamic databases. G = Gibbs energy; c = concentration; D = diffusion coefficient; M = mobility; $\partial c/\partial z$ = slope of molar concentration [145].

To ensure reliable results, the choice of thermodynamic and kinetic database used in the simulation is of paramount importance. The databases are created via thermodynamic optimisation and equilibrium calculations (Figures 3.4 to 3.5).
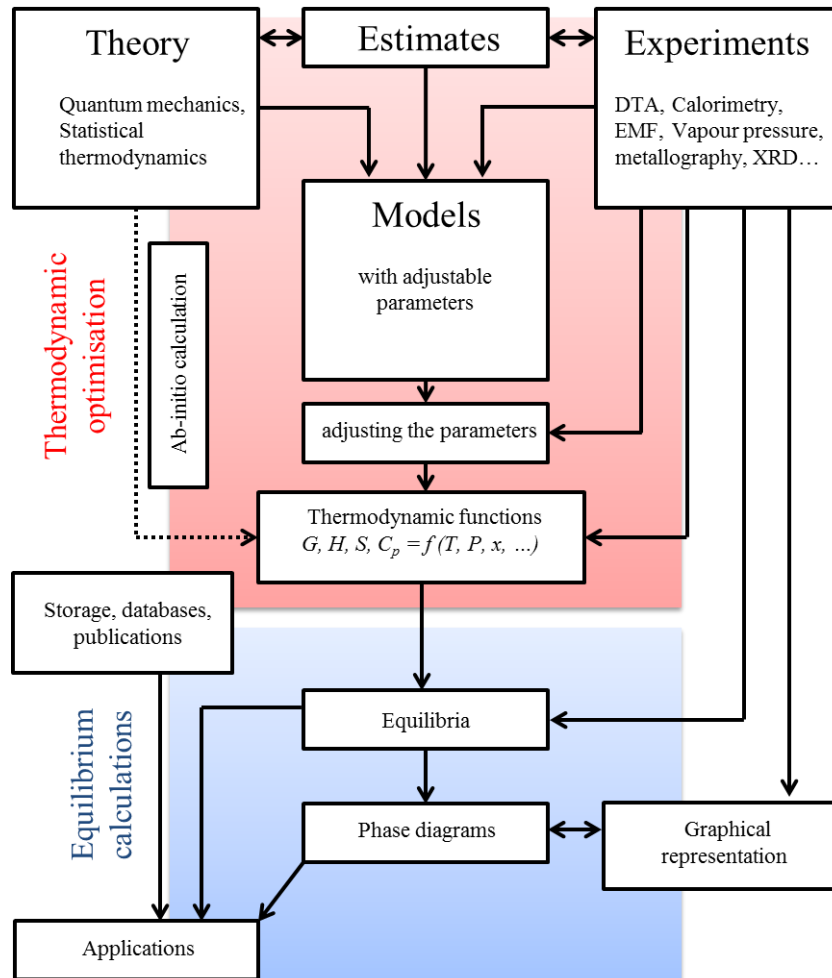
Figure 3.4. Schematic of how thermodynamic databases are collated via a CALPHAD approach in Thermo-Calc [145].
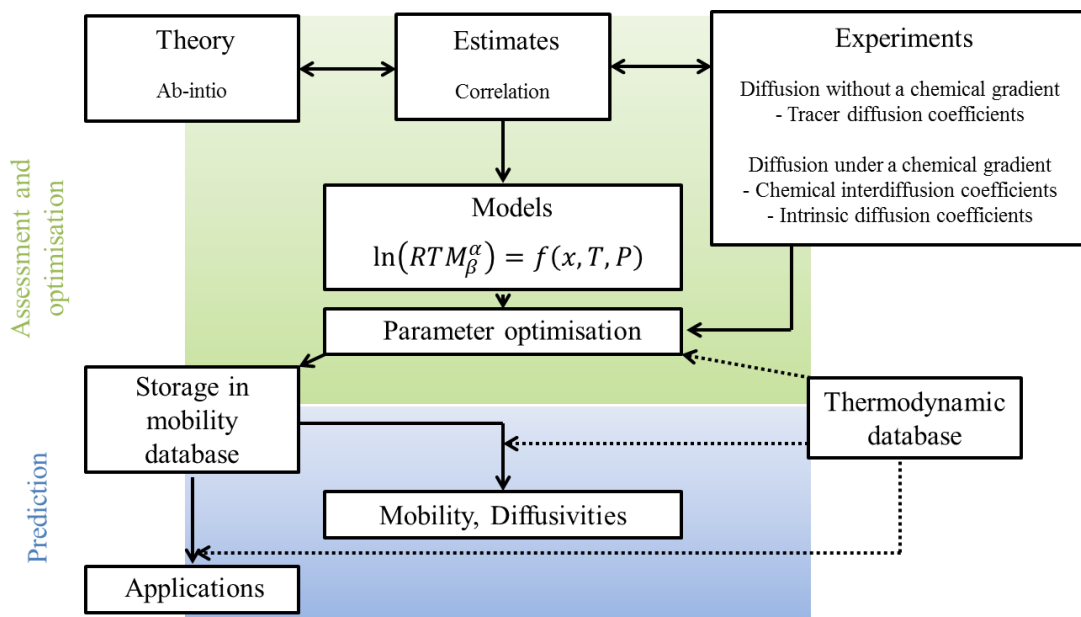
Figure 3.5. Schematic of how kinetic databases are collated in a CALPHAD fashion in DICTRA [145].

DICTRA counts a range of application types in its arsenal including diffusion in single phase systems; diffusion with moving interfaces; cell calculations (particle distributions, immobile interfaces etc.); diffusion in dispersed systems; homogenisation modelling and coarsening amongst others. For this investigation, the homogenisation model [146, 147] was used for all simulations as this approach allows for diffusion in more than one phase. To perform multiphase simulations in 1D, it is assumed that the equilibrium holds locally whereby in a small volume element, the chemical potentials, phase compositions and phase fractions are given by the equilibrium corresponding to the local temperature, pressure and composition. This assumption of local equilibrium is essentially the same for all 1D multiphase simulations.

To successfully run a simulation in DICTRA, one must first define a 'region' (Figure 3.6). This is essentially a 'box' with an arbitrary name and represents the system in which diffusion will take place.
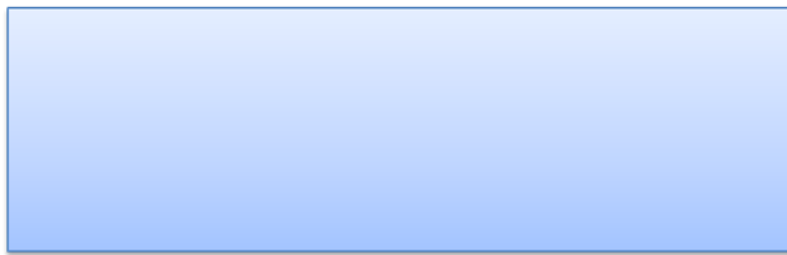
Figure 3.6. The 'region' in DICTRA represented by a box where the diffusion will take place.

Within the region, a 'grid' must be defined. This corresponds to the distribution of node points for numerical calculations (Figure 3.7).

Figure 3.7. The 'grid' in DICTRA showing a typical distribution of discrete node points for numerical calculations.

The distribution of node points can be linear i.e. equally spaced grid; geometric i.e. varying density of grid points in the region; or double geometric which makes it possible to have a high number of grid points in the middle or at both ends of a region. For both geometric and double geometric grids, a geometrical factor of R has to be defined which determines the

distribution of nodes in the region. If $R > 1$, this will yield a higher density of grid points at the lower (left) end of the region. Conversely, if $R < 1$, this will yield a higher density of grid points at the upper (right) end of the region. All simulations in this investigation were done using the double geometric grid. This is because it allows for a higher density of grid points in the middle of the region, and a lower density at the lower and upper ends of the region. This corresponds to more calculations at the interface between the two bodies where diffusion is taking place. Less information is needed toward the bulk of the bodies where diffusion is not experimentally apparent. Figure 3.8 shows a typical nodal distribution for a double geometric grid in DICTRA.

Figure 3.8. The typical nodal distribution for a double geometric grid in DICTRA where R is the geometrical factor.

The concentration profile for DICTRA calculations is illustrated in Figure 3.9 whereby the concentration, C_k of an element is a function of the distance, z.
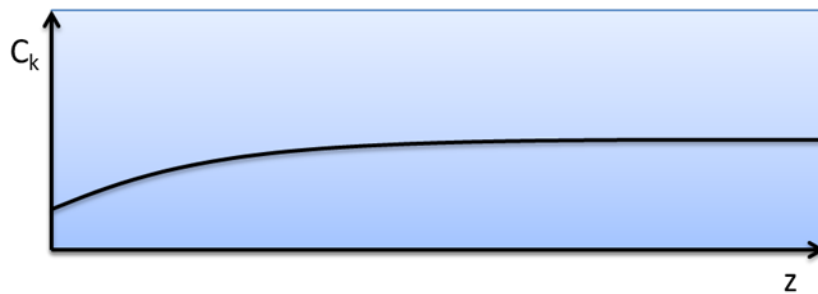
Figure 3.9. The concentration profile of an element, C_k as a function of distance, z.

For all simulations in this investigation, global conditions were used. This ensures that conditions e.g. temperature and pressure are valid for the entire system. Initial concentrations of the species concerned can be input as a function of distance (Figure 3.8), or special functions can be used such as 'Heaviside step functions'. Named after the British mathematician Oliver Heaviside, Heaviside functions are a simple way to enter sharp, step-like concentration profiles. They have been used for all simulations in this investigation. Figure 3.10 shows how a concentration profile for carbon between two different steels can be calculated using the Heaviside step function.
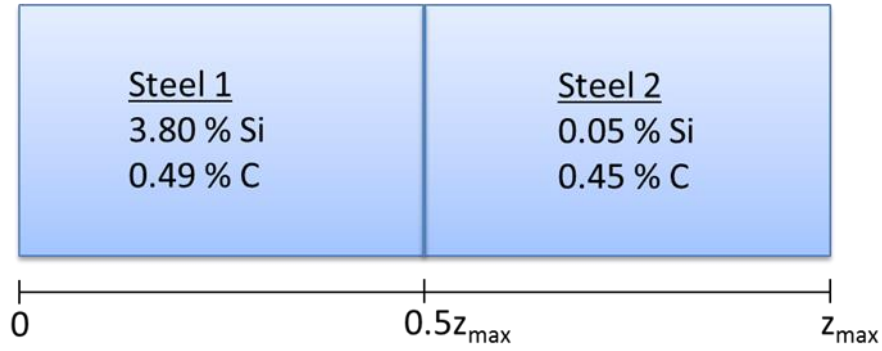
Figure 3.10. An example of how a concentration profile for carbon can be calculated between two different steels in combination with Equation 3.1.

Where z is the distance coordinate, c is the concentration and HS is the Heaviside function, we can write a typical concentration profile for carbon as:

$$C = c1 - (c1 - c2) * HS(z - 0.5z_{max})$$ Equation 3.1

When using the homogenisation model there are three basic groups of homogenisation functions which can be implemented: Wiener bounds, Hashin-Shtrikman bounds, and the 'Labyrinth factor' [146]. When choosing a homogenisation function in order to run a successful simulation in DICTRA, prior knowledge of the microstructure and the phase constitution of the considered system should be used in conjunction with the geometrical interpretations of the homogenisation functions. If diffusion data is available for all phases present, the Hashin-Shtrikman bounds should be used. If it assumed that phases are present as continuous layers, then the Wiener bounds should be used. The Labyrinth factor homogenisation function is identical to the upper Wiener bound where long range diffusion is assumed to occur in one phase only [146]. All simulations in this investigation utilise the upper Wiener bound for the homogenisation function. The Wiener bounds [148] are given by Equations 3.2 and 3.3:

$$\Gamma_k^* = \sum_\phi f^\phi \, \Gamma_k^\phi$$ Equation 3.2

For the upper bound and:

$$\Gamma_k^* = \left[\sum_\phi \frac{f^\phi}{\Gamma_k^\phi} \right]^{-1}$$ Equation 3.3

For the lower bound.

Where f^ϕ is the volume fraction of phase and $\Gamma_k^\phi = M_k^\phi u_k^\phi$.

82

M_k^ϕ is the mobility of component k and the u-fraction, $u_k = \frac{x_k}{\Sigma_{j\epsilon S}\, x_j}$.

x_k is the mole fraction of component k and $j \epsilon S$ means that the summation is to be taken over the substitutional elements only. Summations are taken over all phases, ϕ. For full justification, the reader should consult Larsson and Höglund [146].

These bounds correspond geometrically to continuous layers either parallel with (upper bound) or orthogonal to (lower bound) the direction of diffusion. For a rigorous discussion of the Hashin-Shtrikman bounds and Labyrinth factor, the reader is advised to consult [149, 150].

Table 3.6 summarises the fundamental models and functions used for all DICTRA simulations in this work. It is often a trade-off between the high resolution of results and sensible simulation times. Choice of database for both thermodynamic and kinetic data is stated in the corresponding results chapters together with the simulation plots.

TABLE 3.6. THE COMMON FUNDAMENTAL INPUTS FOR ALL DICTRA
SIMULATIONS USED IN THIS STUDY.

DICTRA prompt	Input	Notes
Reference component	Carbon	Reference state: graphite
Boundary conditions	Global	
Temperature (K)	1273.15	Value corresponds to actual temperature used in experimental
Width of region	200 μm	Wider than a typical X-EDS line scan in experimental results (~70 μm). To increase the resolution by decreasing the width of the region, the time step would have to decrease (inverse square) and therefore simulations would take many weeks to complete.
Grid type	Double geometric	
Number of nodes	60	
Value of R in lower part of region	0.95	
Value of R in upper part of region	1.05	
Composition type	Weight fraction	
Concentration profile function	Heaviside function	When $x < 100$ μm: HS$\rightarrow$0 When $x > 100$ μm: HS$\rightarrow$1
Use equilibrium value of phase	Yes	
Application type	Homogenisation model	
Homogenisation function	Upper Wiener bound	Rule of mixtures with excluded phases
Vary potentials or activities	Activities	Vary activities as the content of one or more of the components becomes very low. Activity will approach 0 which is easier to simulate than a potential which approaches ∞
Always calculate stiffness matrix in muldif	Yes	Ensures calculation of the diffusion coefficient matrix, yielding the stiffness matrix, at each iteration
Simulation time (s)	600	
Max. time step during integration (s)	60	
Initial time step (s)	1×10^{-7}	
Smallest acceptable time step (s)	1×10^{-15}	

3.7 Chapter summary

This chapter has explained the common experimental procedures, operating techniques and instrumental settings used throughout this research project. An outline of the fundamental models and processes used within DICTRA was then discussed. The following chapters make use of these techniques while investigating the diffusion wear behaviour of titanium alloys and their cutting tools. More specific exacting experimental procedures are outlined in greater detail in the corresponding chapters which follow.

Chapter 4 - Tool-workpiece diffusion couple investigations

4.1 Introduction

This chapter compares two novel diffusion couple techniques with the aim of replicating diffusion tool wear mechanisms observed in titanium alloy machining. The diffusion couple tests are modelled on the sticking or seizure region at the tool-chip interface. Figure 4.1 illustrates the location of this region with respect to the sliding region (not to scale) *c.f.* Figure 2.18.
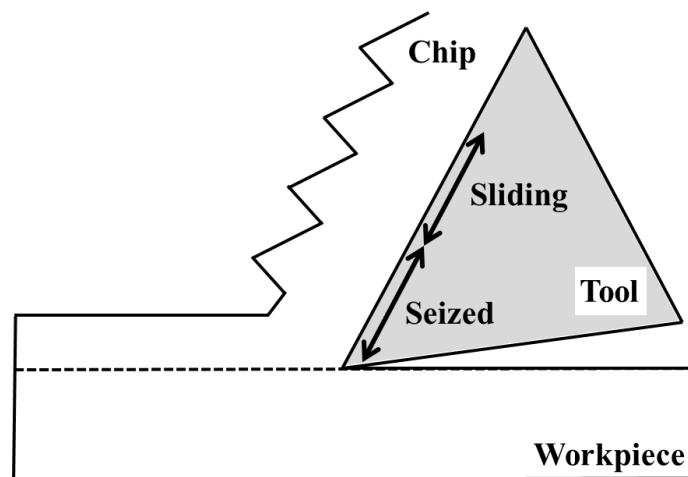
Figure 4.1. 2D schematic for orthogonal cutting of a titanium alloy [151]. The seized region is the area of the tool-workpiece interface which the diffusion couples intend to imitate.

The seized region exists where the stress is constant and the sliding region exists where the coefficient of friction is constant [152]. These two regions exist simultaneously on the rake face of the tool. The contact temperature and work material flow rate at the seized surface control the level of diffusion [153]. All six titanium alloys are subject to both diffusion couple methods described below. The results are presented and analysed via SEM and X-EDS techniques.

4.2 Experimental methods

The work presented in this chapter followed the experimental methods below. This is in addition to the common material analysis procedures outlined in Chapter 3.

4.2.1 Vacuum weight diffusion couple method

The vacuum weight (VW) diffusion couple method consists of placing a 20x20x5 mm coupon of the titanium alloy in contact with the cutting tool. An Inconel weight is then placed on top of the diffusion couple in order to promote intimate contact. The sample is then placed on a ceramic stage inside a vacuum furnace for heat treatment. The coupons are first ground

and polished to a mirror finish using conventional methods before being ultrasonically cleaned in isopropanol. The cutting tools used are Sandvik Coromant grade H13A which consists of a WC substrate with 6 wt.% cobalt as binder phase. The tool inserts are uncoated as per Table 3.2. The furnace used is an Elite TSH 12-5-300 which is attached to an Edwards T-Station 75 vacuum pump. The pressure inside the chamber is 10^{-5} mbar as the samples are heated to 1000 °C and held for 2 h. The samples are then allowed to cool down to room temperature inside the furnace under vacuum (Figure 4.2).
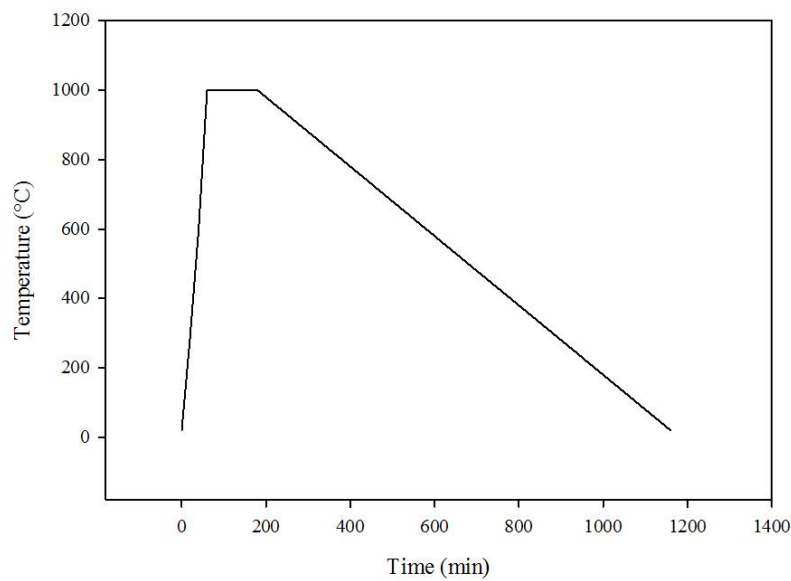
Figure 4.2. Heat treatment profile for all diffusion couple experiments. A heating rate of 16°C.min^{-1}, followed by a hold for 2 h, and then a cooling rate of 1°C.min^{-1}.

The temperature was selected as this is representative of temperatures reached during titanium alloy machining [24]. The length of time was chosen to help promote chemical reactivity. A schematic of this setup can be seen in Figure 4.3b.
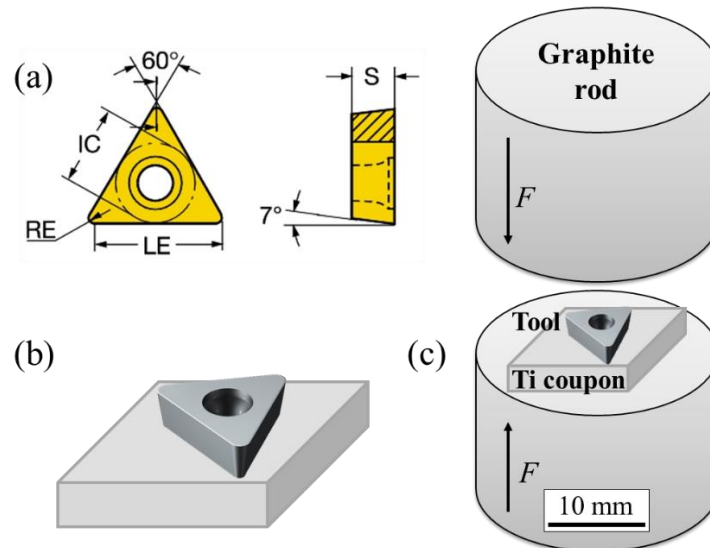
Figure 4.3. (a) Dimensions of tool: corner radius, RE = 0.79 mm; circle diameter, IC = 9.53 mm; cutting edge length, LE = 15.70 mm; thickness, S = 3.67 mm; clearance angle = 7°. (b) Experimental setup of VW and (c) VCR methods. Schematics of tools from [97].

4.2.2 Vacuum compression rig

The vacuum compression rig (VCR) diffusion couple method (Figure 4.3c) consists of two 20x20x5 mm coupons (allowing two alloys to be tested simultaneously) sandwiching a cutting tool. The coupons and cutting tool are the same as described above. The sample is secured via two graphite rods inside a vacuum furnace (10^{-5} mbar) and held with a constant load of 150 N. The sample is subjected to a temperature of 1000°C for 2 h before being furnace cooled to room temperature. This time and temperature was selected for the same reasons as outlined in §4.2.1. After heat treatment, all samples were carefully sectioned before being prepared for metallography using standard methods.

4.3 Results and discussion

Figures 4.4a to l show the diffusion interface between the WC-6%Co tool and CP-Ti, Ti-834, Ti-64, Ti-54M, Ti-6246 and Ti-5553 respectively. The left hand side column shows the VW method and the right hand side column shows the VCR method.
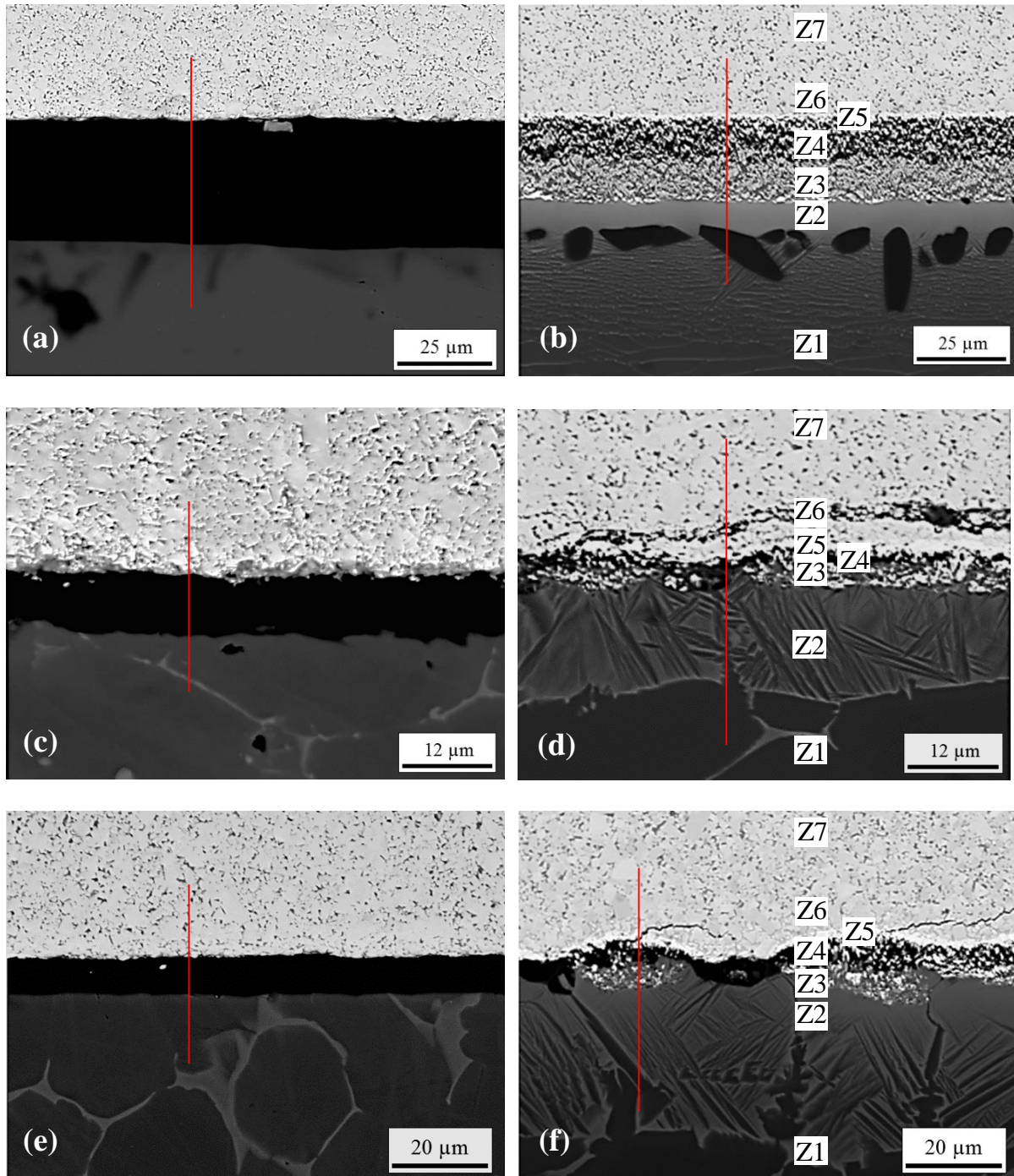
Figure 4.4. Backscatter electron micrographs of the VW diffusion interface between the WC-6%Co tool and (a) CP-Ti, (c) Ti-834 and (e) Ti-64. Backscatter electron micrographs of the VCR diffusion interface between the H13A cutting tool and (b) CP-Ti, (d) Ti-834 and (f) Ti-64. Red line indicates approximate position of the X-EDS line scan.
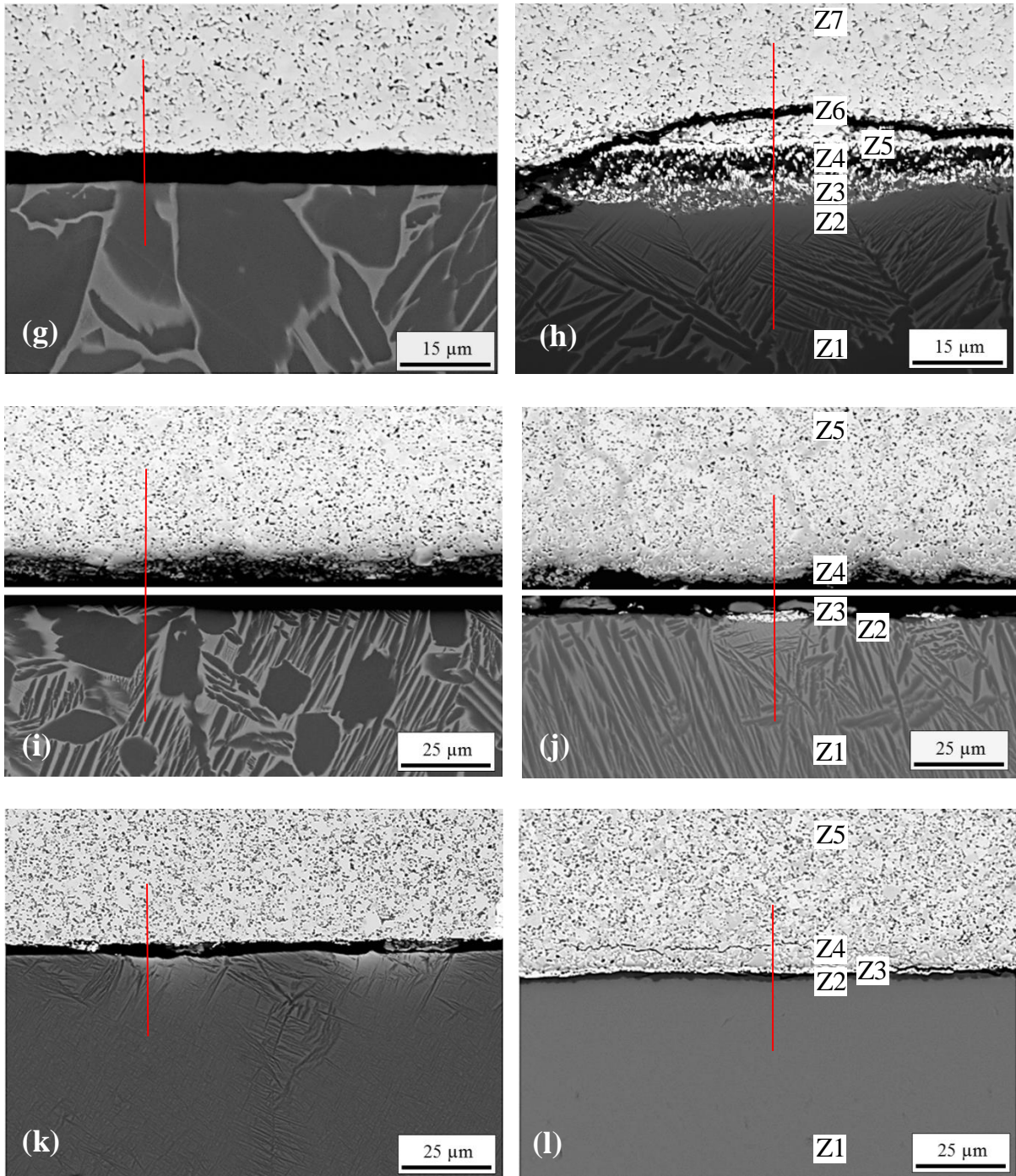
Figure 4.4. Backscatter electron micrographs of the VW diffusion interface between the WC-6%Co tool and (g) Ti-54M, (i) Ti-6246 and (k) Ti-5553. Backscatter electron micrographs of the VCR diffusion interface between the H13A cutting tool and (h) Ti-54M, (j) Ti-6246 and (l) Ti-5553. Red line indicates approximate position of the X-EDS line scan.

For CP-Ti, both diffusion couple methods yielded a strong diffusion bond between the titanium alloy and WC-6%Co tool (Figure 4.4a and b). The VW diffusion couple shows the largest interface of 28.7 μm in length. Figure 4.5 shows the X-EDS plot of the line scan shown in Figure 4.4a.

90
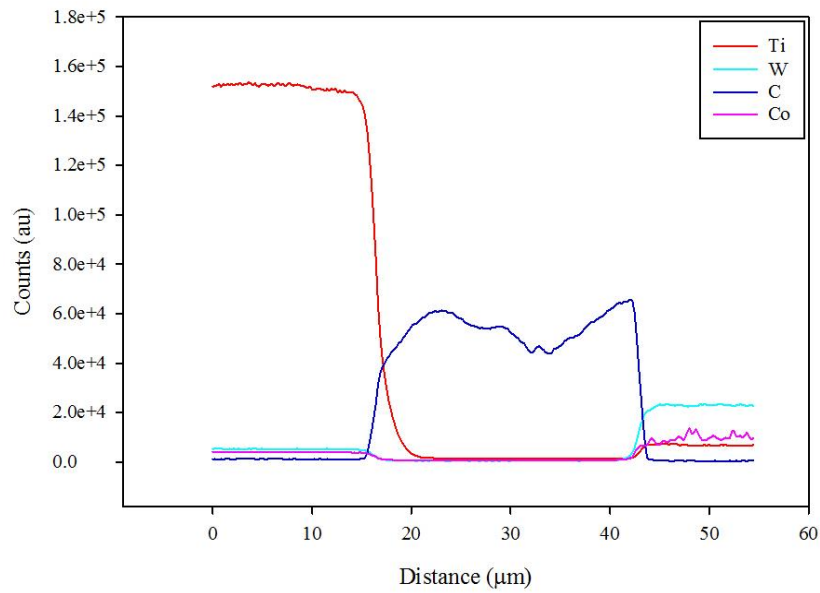
Figure 4.5. X-EDS plot of the VW diffusion interface between CP-Ti and WC-6%Co tool. Location of line scan shown in Figure 4.4a.

The interface is shown to comprise primarily of TiC with greater concentrations at the subsurface of the tool and CP-Ti. The VCR method however, shows a more complex interface where multiple diffusion zones can be observed. Figure 4.6 shows the X-EDS plot of the line scan shown in Figure 4.4b.
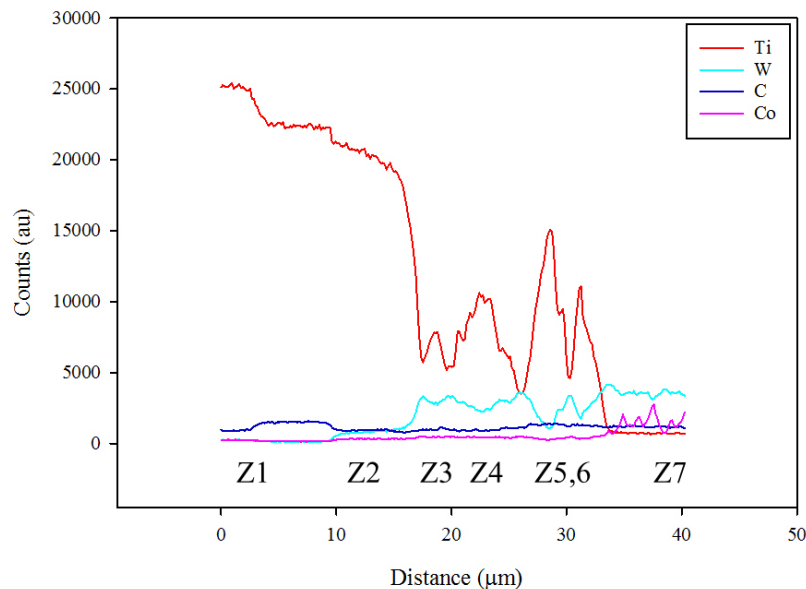
Figure 4.6. X-EDS plot of the VCR diffusion interface between CP-Ti and WC-6%Co tool. Location of line scan shown in Figure 4.4b.

Toward the bottom of the micrograph in Figure 4.4b (Zone 1, Z1), fine lamellae of strengthened β phase can be observed. This graduates towards a marked band of strengthened

91

β phase at the subsurface of the CP-Ti (Z2). The X-EDS data shows areas of increased tungsten and cobalt at the subsurface of the CP-Ti which are both β stabilisers.

The X-EDS data together with observations at the subsurface of the CP-Ti indicate that this phase is composed of $Ti_2Co+\beta$. Figure 4.7 shows the binary phase diagram of the titanium-cobalt system [154].
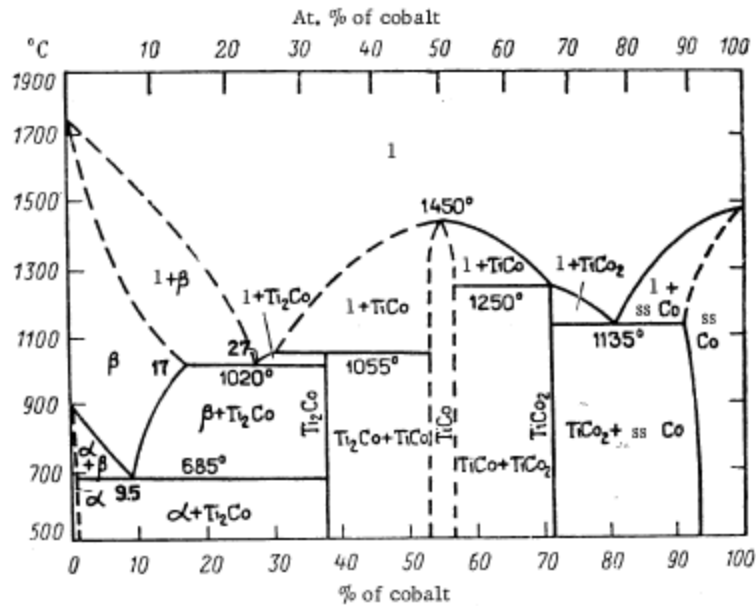
Figure 4.7. Binary phase diagram of the Ti-Co system, after Molchanova [154].

The phase diagram actually shows $Ti_2Co+\alpha$. Due to the β phase being highly unstable at temperatures below 685°C, it converts back to α phase. Within the band of $Ti_2Co+\beta$, dark laths of TiC formation can also be observed at regular intervals. This is confirmed via in the increase in carbon content observed in the X-EDS data. This formation of TiC within the subsurface of the CP-Ti can also be observed for the VW method. At the subsurface of the tool, a solid solution of TiC (dark) with WC (bright) and a small quantity of cobalt binder can be observed (Z3). The darker diffusion zone above this (Z4) is highly enriched in TiC due to carbon favouring this bond over that with tungsten (TiC ΔG = -170 kJ.mol^{-1}, W_2C ΔG = -38 kJ.mol^{-1} at 1000°C) [155]. The brighter phase in Z4 consists of a highly enriched solid solution of β(Ti,W) and WC. The bright band above this zone (Z5) corresponds to an $M_{12}C$ phase (Co_6W_6C) which is an η-phase [156]. It has been shown [157] that in the temperature range 760-980°C, M_6C carbides decompose to form $M_{12}C$ carbides which can be maintained with slow cooling processes, as seen here. In addition to the β strengthened subsurface of the CP-Ti, this shows further evidence of how the cobalt binder is drawn from the tool towards the interface. The same is true for tungsten. This cobalt diffusion coupled with the high

concentrations of carbon in the areas of high TiC concentration leaves a markedly brittle region at the subsurface of the tool (Z6). Here, at the deficit of carbon, an M_6C phase is formed consisting of $Co_3W_3C_y$ (W_2C), also an η-phase. Due to the depleted carbon and cobalt in this region, it can become brittle and prone to fracturing. Towards the top of the micrograph (Z7) is the bulk of the WC-6%Co tool which is unaffected by chemical interaction with the CP-Ti substrate.

With Ti-834, both methods yielded a strong diffusion bond between the alloy and tool. For the VW diffusion couple (Figure 4.4c), a sizeable interface of 8.6 µm can be observed. However, the micrograph does not reveal any marked diffusion zones at the interface. Figure 4.8 shows the X-EDS plot of the line scan shown in Figure 4.4c.
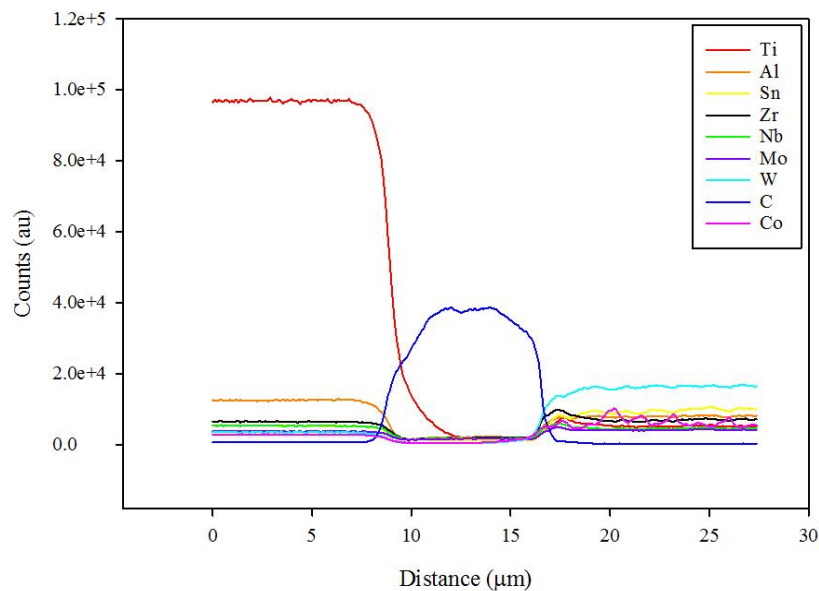
Figure 4.8. X-EDS plot of the VW diffusion interface between Ti-834 and WC-6%Co tool. Location of line scan shown in Figure 4.4c.

The profile is similar to that of CP-Ti where the interface comprises predominantly of TiC which preferentially forms at the subsurface of the Ti-834. The formation of reaction species and resultant diffusion zones are much more apparent for the VCR diffusion couple method (Figure 4.4d). Starting with the bulk of the Ti-834 substrate (Z1) we can observe that it is unaffected by diffusion mechanisms before a 15 µm deep layer of $Ti_2Co+β$ is apparent at the subsurface of the titanium alloy (Z2). Figures 4.9a and b show the X-EDS data of the line scan shown in Figure 4.4d in order to help identify the various diffusion zones observed.
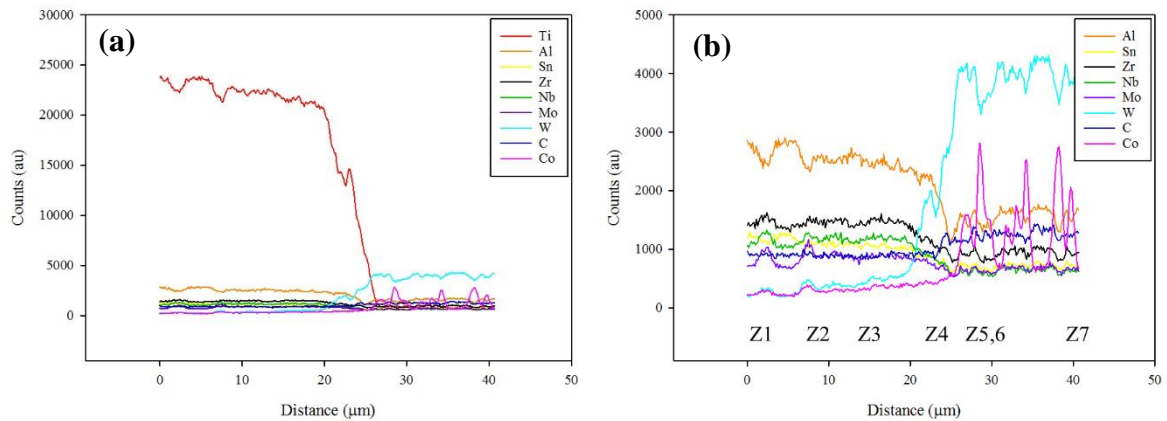
Figure 4.9. (a) X-EDS plot of the VCR diffusion interface between Ti-834 and WC-6%Co tool; (b) shows the same data with the Ti removed for clarity. Location of line scan shown in Figure 4.4c.

At the subsurface of the tool, a mixture of TiC, WC and cobalt co-exists with the $Ti_2Co+\beta$ phase (Z3). As seen with CP-Ti, although narrower, a diffusion band of enriched TiC with $\beta(Ti,W)$ and WC appears adjacently (Z4). The bright band of the $M_{12}C$ η-phase (Z5) follows before the M_6C η-phase at the subsurface of the tool (Z6). Prominent fractures can be observed here as the cobalt and tungsten are lost to the interface. Z7 shows the bulk of the WC-6%Co tool which is unaffected by chemical interaction with the Ti-834 substrate.

With Ti-64, both methods yielded a strong diffusion bond between the titanium alloy and WC-6%Co tool. Looking first at the VW diffusion couple (Figure 4.4e), X-EDS data in Figure 4.10 shows how formation of TiC at the interface forms in a similar manner to the CP-Ti and Ti-834 samples. The size of the interface is slightly shorter in length, measuring 5.3 μm.

94
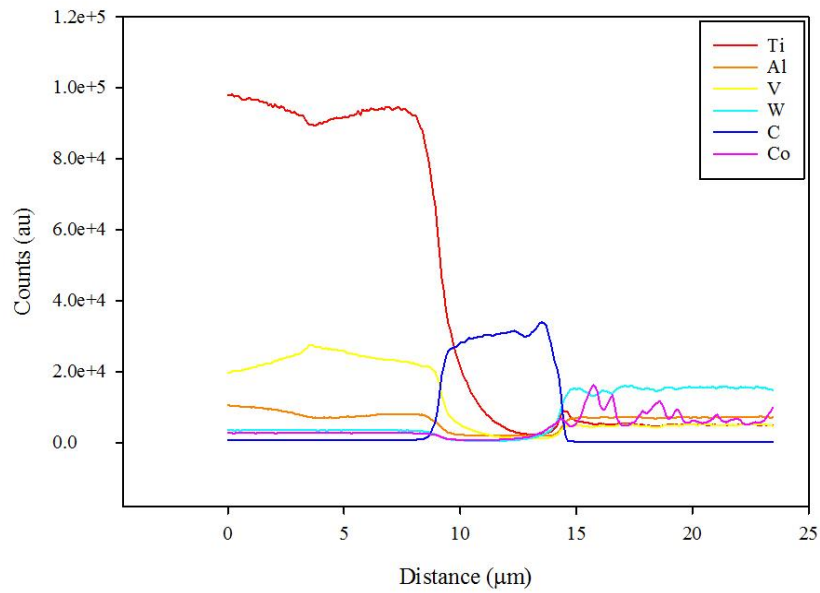
Figure 4.10. X-EDS plot of the VW diffusion interface between Ti-64 and WC-6%Co tool. Location of line scan shown in Figure 4.4e.

For the VCR diffusion couple (Figure 4.4f) the same seven diffusion zones can be observed as discussed for both CP-Ti and Ti-834. Firstly, the bulk of the Ti-64 (Z1); before the presence of $Ti_2Co+\beta$ in the region of enhanced β phase at the subsurface of the alloy (Z2); followed by TiC+WC+Co (Z3); then a band of β(Ti,W) and WC (Z4); before both $M_{12}C$ (Z5) and M_6C (Z6) η-phases. Hairline fractures can be seen in the latter η-phase. Z7 shows the bulk of the WC-6%Co which is unaffected by chemical interaction with the Ti-64 substrate. Figures 4.11a and b show the X-EDS data for the line scan shown in Figure 4.4f.
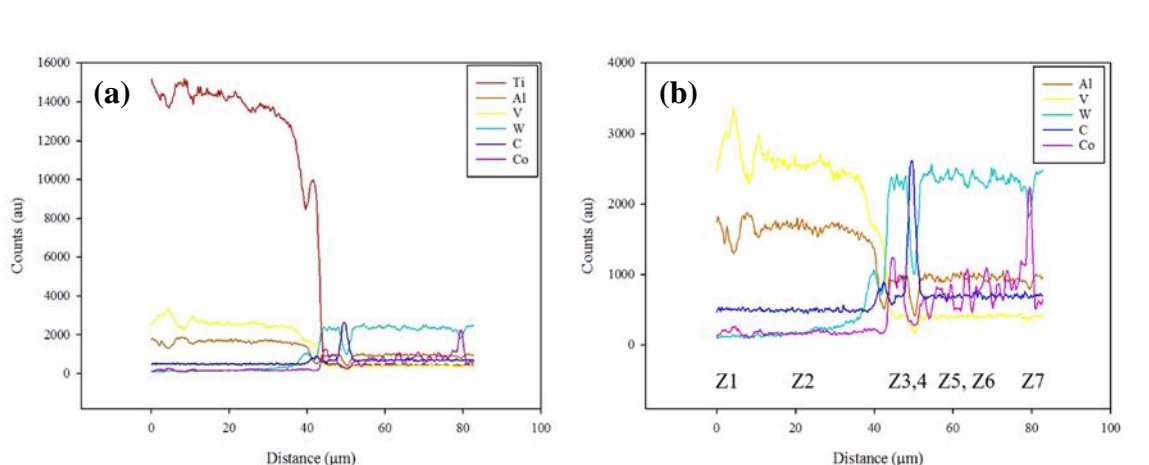
Figure 4.11. (a) X-EDS plot of the VCR diffusion interface between Ti-64 and WC-6%Co tool; (b) shows the same data with the Ti removed for clarity. Location of line scan shown in Figure 4.4f.

95

Figures 4.4g and h show the diffusion interface between Ti-54M and the WC-6%Co tool. Both methods yielded a strong diffusion bond. The VW method shows the same TiC interface as the previous three alloys albeit slightly more narrow at 4.2 μm. Figure 4.12 shows the X-EDS plot of the line scan shown in Figure 4.4g.
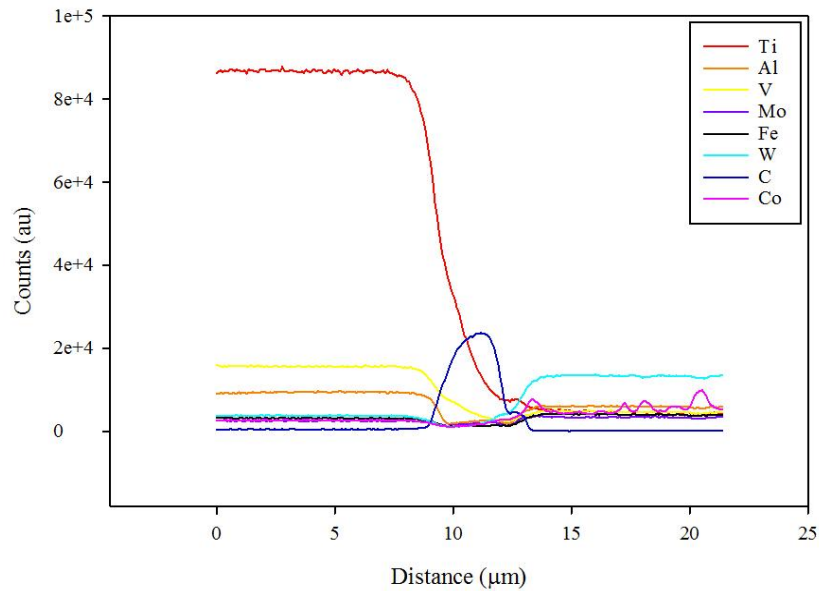
Figure 4.12. X-EDS plot of the VW diffusion interface between Ti-54M and WC-6%Co tool. Location of line scan shown in Figure 4.4g.

Figure 4.4h shows the diffusion interface for the VCR method. First observations show a similar interface to the previous three alloys. The X-EDS line scan is shown in Figure 4.13.
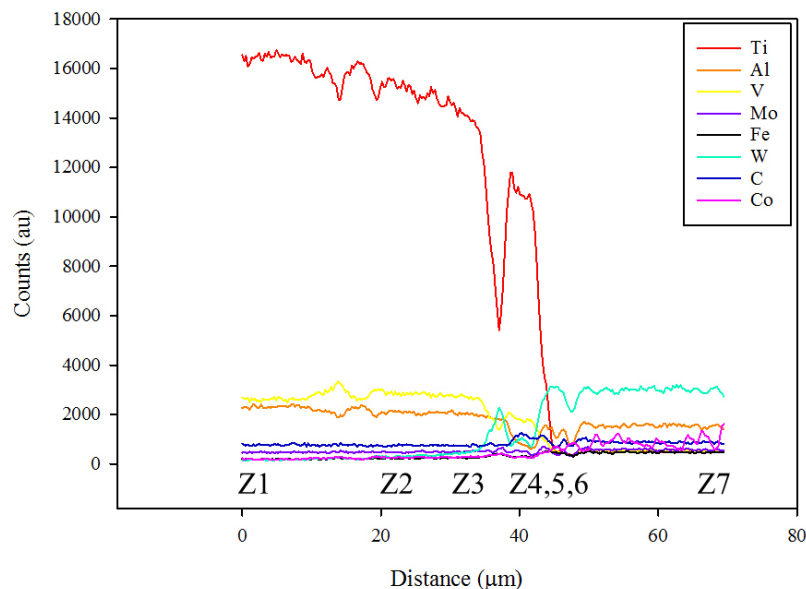
Figure 4.13. X-EDS plot of the VCR diffusion interface between Ti-54M and WC-6%Co tool. Location of line scan shown in Figure 4.4h

The same diffusion zones can be observed as discussed for CP-Ti, Ti-834 and Ti-64. Firstly, the bulk of the Ti-54M (Z1); followed by the presence of $Ti_2Co+\beta$ in the region of enhanced β phase at the subsurface of the alloy (Z2); followed by TiC+WC+Co (Z3); then β(Ti,W) and WC (Z4); before both $M_{12}C$ (Z5) and M_6C η-phases (Z6). Hairline fractures can be seen in the latter η-phase. Z7 shows the bulk of the WC-6%Co tool which is unaffected by chemical interaction with the Ti-54M substrate.

Figures 4.4i and j show the diffusion interface between Ti-6246 and the WC-6%Co tool. Contrary to the previous titanium alloys tested, neither method yielded a diffusion bond. First observations of the VW method show evidence of wear at the subsurface of the tool, however there are no visible differences along the surface of the Ti-6246 which appears uniform throughout the bulk. The X-EDS data for the VW method is shown in Figures 4.14a and b.
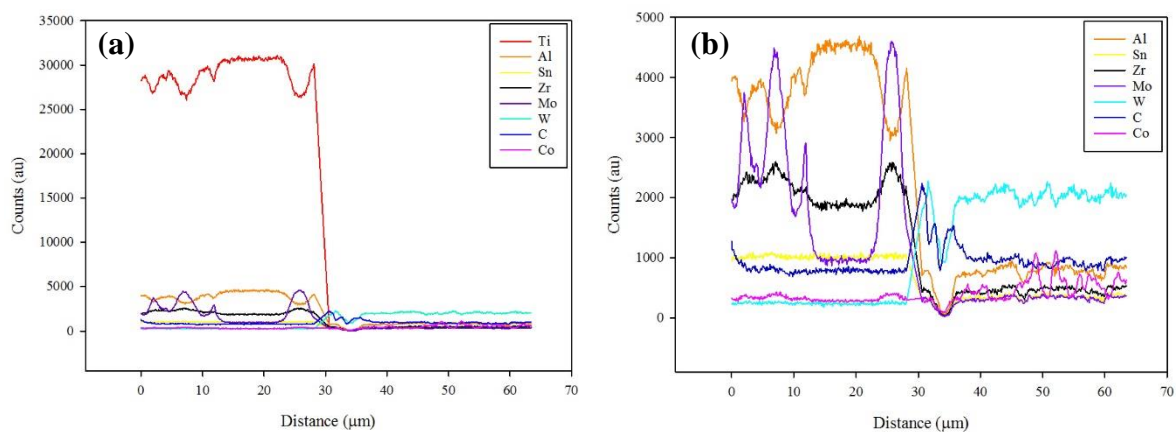
Figure 4.14. (a) X-EDS plot of the VW diffusion interface between Ti-6246 and WC-6%Co tool; (b) shows the same data with the Ti removed for clarity. Location of line scan shown in Figure 4.4i.

Looking first at the Ti-6246 substrate, there is no evidence of tool constituent diffusion. The only fluctuations in the X-EDS data are troughs for titanium and aluminium with corresponding peaks for molybdenum as the scan passes over α and β grains respectively. Looking at the subsurface of the tool, the X-EDS data shows a concentration of workpiece elements (Ti, Al, Sn, Zr, Mo) which peak together with the tool constituents (at ~32 µm, Figure 4.14b), there is then a noticeable drop which shows how the elements have diffused towards the interface (~34 µm, Figure 4.14b). Figures 4.15a and b show the VCR X-EDS data.
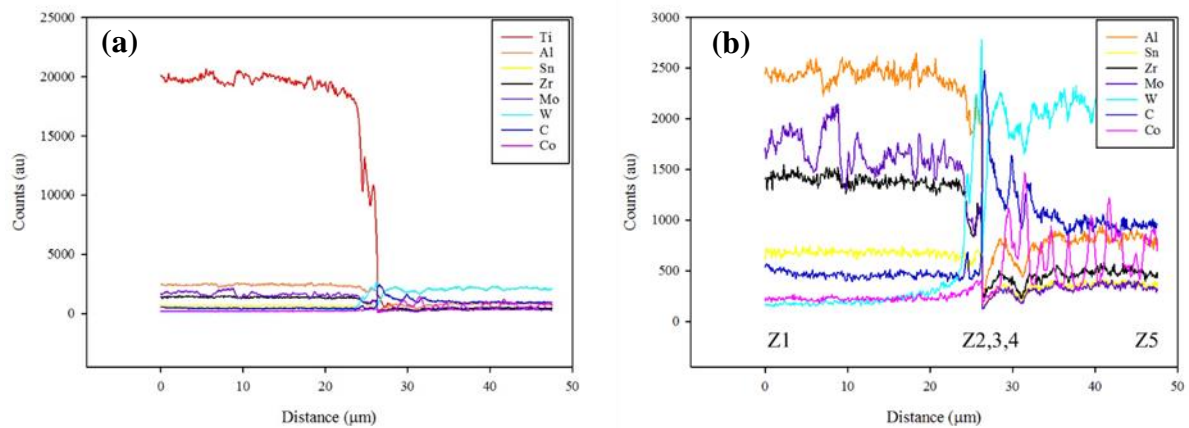
Figure 4.15. (a) X-EDS plot of the VCR diffusion interface between Ti-6246 and WC-6%Co tool; (b) shows the same data with the Ti removed for clarity. Location of line scan shown in Figure 4.4j.

Similar to the results for the Ti-54M diffusion couples, the micrographs for the VCR method yield more points of interest. The microstructure of the Ti-6246 bulk (Z1) consists of a fully lamellar microstructure with obvious strengthening of the β phase (Z2) in areas where small quantities of tool constituents have bonded to the surface of the alloy (Z3). This is the same $Ti_2Co+β$ phase as seen in the Ti-54M diffusion couples. These observations are supported by the X-EDS data which shows increased quantities of tungsten, carbon and cobalt at the surface of the Ti-6246. There is only a negligible trace of TiC formation observed and no indication of the $M_{12}C$ η-phase as seen in the Ti-54M diffusion couple. However, similarly to the Ti-54M sample, a narrow band of the M_6C η-phase can be observed at the subsurface of the tool (Z4) which is also the location of severe tool wear. Notching and edge chipping can be observed here. Z5 is the bulk of the WC-6%Co tool which is unaffected by chemical interaction with the Ti-6246.

Figures 4.4k and l show the diffusion interface between Ti-5553 and the WC-6%Co tool. Both methods yielded a diffusion bond. For the VW diffusion couple, only a very small quantity of TiC is formed at the interface which is confirmed by the X-EDS data in Figure 4.16a and b. Strengthening of the β phase is also observed at the subsurface of the Ti-5553 with formation of $Ti_2Co+β$. The M_6C and $M_{12}C$ η-phases are not apparent in the micrograph however the X-EDS data does confirm increased cobalt content towards the subsurface of the tool.
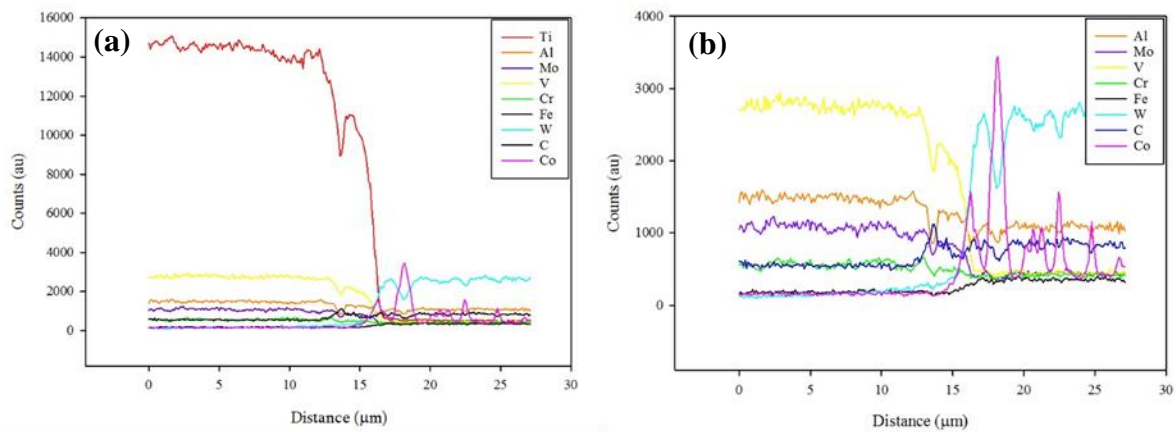
Figure 4.16. (a) X-EDS plot of the VW diffusion interface between Ti-5553 and WC-6%Co tool; (b) shows the same data with the Ti removed for clarity. Location of line scan shown in Figure 4.4k.

The VCR diffusion couple method exhibits a microstructure which is more similar in appearance to the unbonded Ti-6246 sample rather than the bonded samples of CP-Ti, Ti-834, Ti-64 and Ti-54M. The micrograph does not reveal much detail in the microstructure of the Ti-5553 (Z1). There is an absence of clear, banded diffusion zones save for a fine layer of TiC at the subsurface of the titanium alloy substrate (Z2). There is a fine band of $M_{12}C$ η-phase which can be observed at the subsurface of the tool (Z3). Hairline fractures can be seen adjacent to this which indicates presence of the brittle M_6C η-phase (Z4). This is supported by the X-EDS data in Figures 4.17a and b. These plots also confirm evidence of the small quantity of TiC formation as the quantity of carbon increases towards the interface. Z5 is the bulk of the WC-6%Co tool which is unaffected by chemical interaction with the Ti-5553.
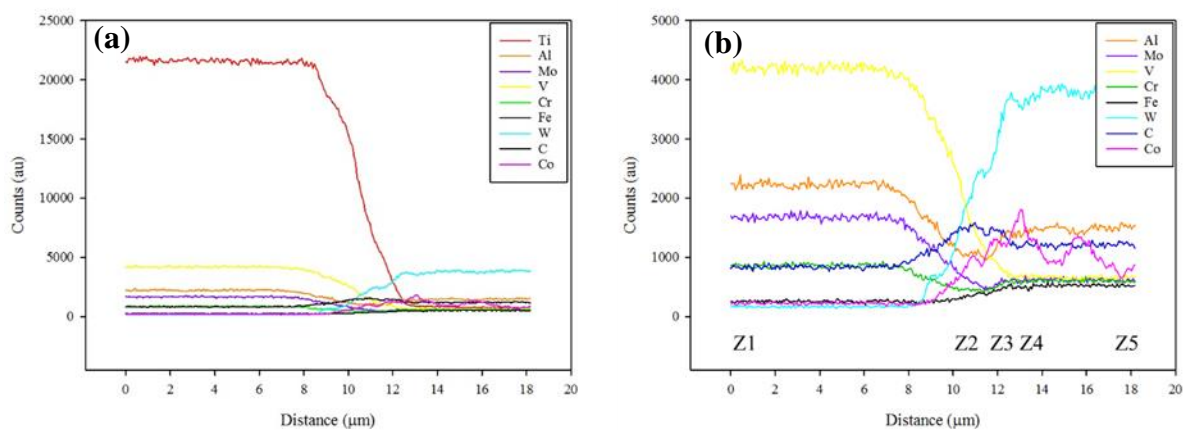
Figure 4.17. (a) X-EDS plot of the VCR diffusion interface between Ti-5553 and WC-6%Co tool; (b) shows the same data with the Ti removed for clarity. Location of line scan shown in Figure 4.4l.

All titanium alloys used in this study formed a strong diffusion bond with the WC-6%Co tool with the exception of Ti-6246. Also of note is the similarity in behaviour of Ti-5553 to Ti-6246 despite forming a bond with the tool. To understand the difference in diffusion behaviour, one has to consider the chemistry of the alloys. This is the only difference between the diffusion couple tests as all other variables were kept constant. It is important to realise that Ti-6246 possesses a higher Mo_{eq} value than CP-Ti, Ti-834, Ti-64 and Ti-54M. This means that Ti-6246 is more β rich and therefore more difficult to machine. The high Mo_{eq} value of Ti-6246 is primarily due to its high molybdenum content of 6 wt.%. Nishimura [76] found that the corrosion reaction resistance of titanium alloys increased with the addition of molybdenum as an alloying element. Investigations into corrosion at high temperature found that molybdenum helped strengthen and preserve a passive oxide film which served as protective layer. Tomashov *et al.*[69] observed that alloying titanium with molybdenum also increased the resistance to corrosion as molybdenum inhibits the anodic dissolution reaction of the alloy and increases thermodynamic stability of the passive oxide film. Electrochemistry work by Glass *et al.* [71] looked at the transpassive behaviour of titanium-molybdenum alloys in acidic conditions. They found that oxide films become more protective and have a more defect-free structure as molybdenum content increases. Fox [158] looked at modelling the reaction layer growth rate in Ti/SiC metal matrix composites. It was shown that matrix alloying elements such as molybdenum in metastable β alloys affect the equilibrium compositions and diffusivites in the matrix. A number of factors were shown to affect the growth rate of the TiC reaction layer including the effect of alloying elements on the interfacial carbon levels. TIMETAL 21S was used in the investigation which has 15 wt.% molybdenum content. It was shown that with titanium alloys possessing a high molybdenum content, the TiC reaction layer growth rates are significantly reduced. This is likely due to the molybdenum preserving the protective oxide layer. Fox also offers an insight into why the Ti-5553 behaves similarly to Ti-6246 (despite bonding, no clear diffusion zones observed) as the presence of 3 wt.% chromium which is a strong carbide former causes partitioning in the reaction matrix and changes interfacial carbon concentrations. Hartung and Kramer [26] summarised that due to chemical reaction, a reaction layer forms of thickness determined by the balance between the diffusion rate of tool material through the layer and the rate of dissolution of the reaction layer in the workpiece. The wear rate of tool materials which maintain a stable reaction layer (as seen here for CP-Ti, Ti-834, Ti-64 and Ti-54M) is limited by the diffusion rate of tool constituents from the tool-chip interface. Those tools which can form a stable reaction layer are the most wear resistant materials.

4.4 Conclusions and chapter summary

An investigation was carried out to compare two novel diffusion couple techniques in order to replicate diffusion tool wear mechanisms observed in titanium alloy machining. The diffusion couple tests were modelled on the sticking or seizure region at the tool-chip interface. For both the VW and VCR diffusion couple techniques; strong diffusion bonds were observed between the WC-6%Co tool and CP-Ti, Ti-834, Ti-64, Ti-54M and Ti-5553. However, diffusion couple tests with Ti-6246 did not result in bonding with the tool. Including the bulk of both the titanium alloy and WC-6%Co tool, up to seven different phases and/or reaction species were identified for all bonding samples offering, for the first time, an insight into the mechanisms of tool wear by diffusion. This includes the formation of $Ti_2Co+\beta$ which is hypothesised to experience a rapidly accelerating diffusion rate acting as a driving force for further diffusion, phase changes, and reaction species formation. In addition to this, diffusion zones of TiC+WC+Co; $\beta(Ti,W)$+WC; $M_{12}C$ (Co_6W_6C); and M_6C ($Co_3W_3C_y$, (W_2C)) were observed. These observations have been supported by key literature outlining how a titanium alloy bearing a high content of molybdenum are less susceptible to TiC formation when machined with WC-6%Co tools. This was observed in the diffusion couple tests.

The VW diffusion couple technique is successful in offering some insight into the diffusion mechanisms at the tool-workpiece interface for titanium alloy machining. Firstly, it shows whether the tool material and titanium alloy have a propensity to form a bond. Whilst not offering the high resolution of various diffusion zones and reaction species formation, this technique does yield reaction interfaces of different sizes for different alloys. A trend can be observed whereby the more β rich the titanium alloy is, the smaller the resulting reaction interface. Table 4.1 summarises the diffusion couple results in terms of their bonding characteristics and relative TiC reaction layer at the interface.

TABLE 4.1 SUMMARY TABLE LISTING BONDING CHARACTERISTICS AND RELATIVE TiC REACTION LAYER THICKNESS.

Titanium alloy	Bonding / Non-bonding	TiC layer thickness (µm)
CP	Bonding	28.7
834	Bonding	8.6
64	Bonding	5.3
54M	Bonding	4.2
6246	Non-bonding	trace
5553	Bonding	trace

The VCR method on the other hand, offers much more information to the observer. This includes clear, banded diffusion zones and locations of fracture along the subsurface of the tool. For the unbonded Ti-6246 samples, the force applied via the VCR method shows slight bonding of tool constituents and corresponding strengthening of the β phase at the subsurface of the alloy. This offers an insight into the resistance of Ti-6246 towards bonding with the tool even under the force applied via this method. It can be seen how the VCR method offers more information over the VW method into the mechanisms of tool wear via diffusion in titanium alloy machining. However, this must be balanced against the cost and complexity of the VCR technique. A reliable vacuum furnace is all that is required for the VW method. This will offer information on reaction species formation such as thickness of the reaction layer at the interface. X-EDS data will also show evidence of the diffusion zones described above. However, these would be hard to successfully evaluate without the extra resolution offered by the VCR method. The VCR method also crucially, shows failure of the tool via diffusion mechanisms with hairline fractures along the tool's subsurface.

To see whether the results in this chapter are accurate in predicting tool wear by diffusion mechanisms in titanium alloy machining, the next chapter compares two of these alloys, Ti-54M (bonding) and Ti-6246 (non-bonding) via precision outer diameter (OD) turning trials.

Chapter 5 - Turning study of alloys Ti-54M and Ti-6246

5.1 Introduction

Following on from the findings discussed in Chapter 4 where two novel diffusion couple techniques were used to replicate the diffusion tool wear mechanisms observed in titanium alloy machining. The objective of this chapter is to verify those results by conducting OD turning trials on Ti-54M and Ti-6246. These alloys were chosen as they represent the two different behaviours observed in the diffusion couple tests. Ti-54M bonded with the WC-6%Co tool whereas Ti-6246 did not bond with the WC-6%Co tool.

5.2 Experimental methods

The work presented in this chapter followed the experimental methods below. This is in addition to the common material analysis procedures outlined in Chapter 3.

5.2.1 As received material

Two TIMET α+β titanium alloys in the as-forged condition were chosen for this investigation: Ti-54M (nominal composition in wt.% is 5 Al, 4 V, 0.8 Mo, 0.5 Fe, bal. Ti) and Ti-6246 (6 Al, 2 Sn, 4 Zr, 6 Mo, bal. Ti). The α+β morphology for Ti-54M is shown in Figure 5.1a. Approximately 70% α phase volume fraction can be observed. Each primary α grain is surrounded at the grain boundary by residual β phase. The α+β morphology for Ti-6246 is shown in Figure 5.1b which shows an equiaxed structure of both α lamellae and α platelets in a transformed β matrix. The cutting tools used in the machining trials were uncoated cemented carbide WC-6%Co from Sandvik Coromant. The CNMG 12 04 08-23 H13A grade tools were rhombic in shape with a chip breaker. The inserts were mounted in a CoroTurn RC DCLNL 2020 tool holder which provided an effective rake and flank angle of 6°. A fresh cutting edge was used for each test.
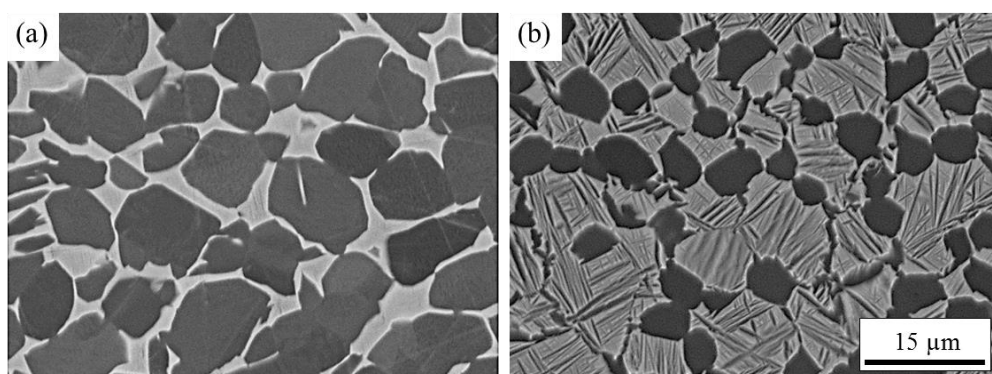
Figure 5.1. Backscatter electron micrographs of the as-forged microstructures of (a) Ti-54M and (b) Ti-6246.

5.2.2 Machining trials

Outer diameter (OD) turning trials were conducted on a MAG Cincinnati Hawk 250 lathe connected to a Kistler dynamometer to record cutting forces. Figure 5.2 shows the experimental setup.
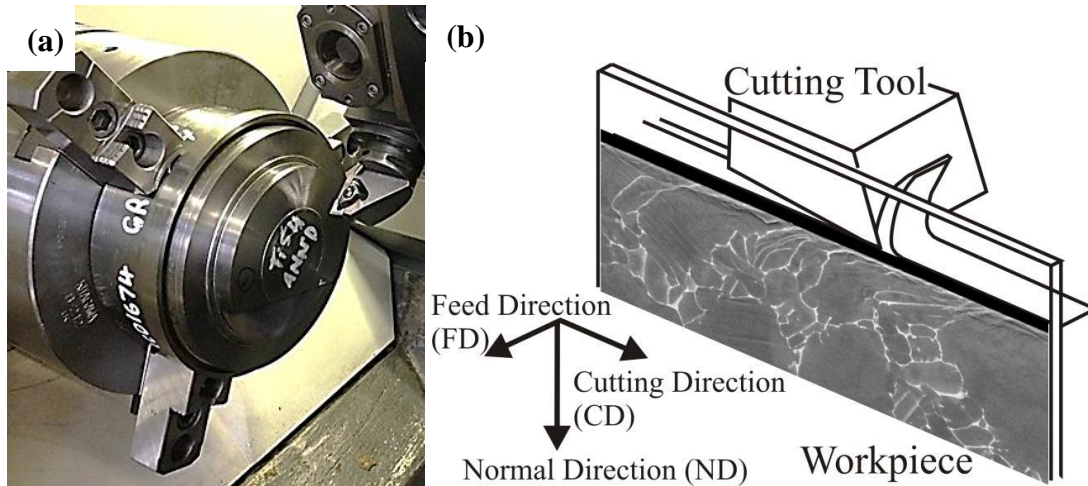
Figure 5.2. (a) Machining trial setup with the Ti-54M billet loaded in the chuck and (b) Schematic of the cutting process together with example subsurface microstructure deformation, after Crawforth [43].

A constant exaggerated cutting speed of 120 m.min^{-1} was used in order to increase the reaction kinetics and intensify chemical reactivity at the tool-workpiece interface. It is recognised however that in reality, cutting speeds do not normally exceed 45 m.min^{-1} for $\alpha+\beta$ titanium alloy machining [93]. A constant feed rate of 0.1 mm.rev^{-1} and a 1 mm depth of cut was used. The water based coolant used was Houghton Hocut 795B controlled at a concentration of 5%. It was used at a rate of 13 L.min^{-1}. 14 OD turning trials were conducted in total: seven using Ti-54M and seven using Ti-6246. Table 5.1 lists the machining trials together with a corresponding code. N.B. a length of cut of '0 s' is included in the table for both titanium alloy workpieces. This is for matters of completeness and to avoid labelling confusion with Figures 5.5a and 5.6a where images of new tools are included, effectively after 0 s of machining time.

Table 5.1. DURATION OF CUTTING FOR MACHINING TRIALS CONDUCTED AT 120 M.MIN^{-1} WITH A FEED RATE OF 0.1 MM.REV^{-1} AND A DEPTH OF CUT OF 1 MM.

Machining trial code	Duration of cut (s)
Ti-54M	
1A	0
1B	30
1C	60
1D	90
1E	120
1F	150
1G	180
1H	210
Ti-6246	
2A	0
2B	30
2C	60
2D	90
2E	120
2F	150
2G	180
2H	210

The aim of the interrupted cuts at various times allows for the tool and workpiece to be analysed as 'snapshots through time' of the longer turning trial which ran the length of each billet.

5.2.3 Tool wear

Due to the tool's position relative to the workpiece during OD turning, it is subjected to non-uniform contact at the cutting edge (Figure 5.3a). Figure 5.3b shows a cutting insert illustrating the location of the leading edge and nose of the tool. Each has a respective rake face and flank face. As the depth of cut is fixed for all turning trials, the length of wear along the leading edge is fixed. The uncut chip thickness (feed rate) determines the size of the contact area of the tool with the workpiece. Only the rake and flank edges of the nose of the tool were subject to analysis in this investigation as this region has substantial impact on workpiece surface integrity.
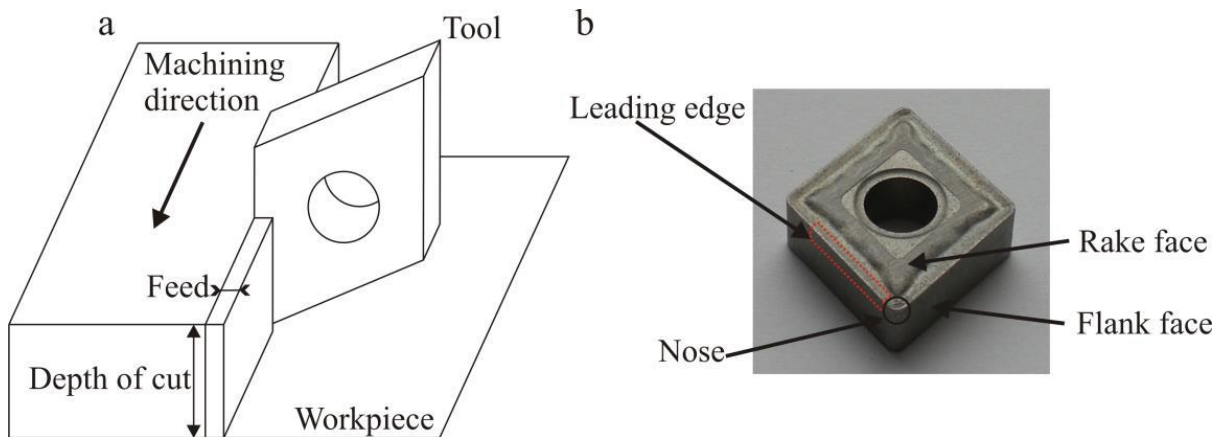
Figure 5.3. (a) Schematic showing the orientation of the tool relative to the workpiece during OD turning. (b) Photograph of a tool insert, grade CNMG 120408-23 H13A (Sandvik Coromant) showing the location of the rake face, flank face, nose and leading edge, after Crawforth [43].

An Alicona InfiniteFocus instrument (Figure 5.4) was used to image and quantify the wear on the flank face and rake face at the nose of each tool. An industrially accepted tool wear (VB) criterion developed by Sandvik Coromant outlines the average and maximum acceptable tool wear limits for flank wear as VB = 0.25 mm and VB_{max} = 0.5 mm. However, since the titanium alloy workpieces are being machined at cutting speeds higher than those recommended (for reasons outlined previously), VB and VB_{max} values will promptly be surpassed. For this reason, VB and VB_{max} values will not be measured. For quantitative tool wear measurement, Alicona measurements of valleys below the reference surface (an unused tool) will be compared as this gives an indication of material removal from the rake and flank faces of the tool.
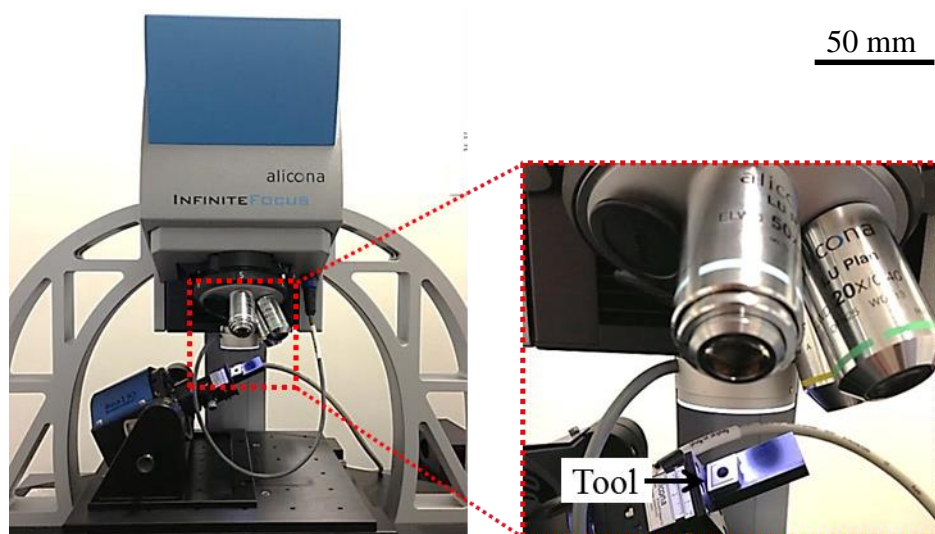
Figure 5.4. Alicona setup with the tool insert magnetically fixed to stage.

5.2.4 Microstructural analysis

In order to analyse the workpiece, the billet was first grooved and then parted into 15 mm thick rings. The grooving tool used was grade N123H2-0400-0002-GF 1105, and the parting tool used was grade NE123E2-0200-RO S05F (both Sandvik Coromant). The tools were mounted in a 570-32R123E15B tool holder (Sandvik Coromant). The rings were then sectioned using wire-electrical discharge machining (EDM) before being ground and polished ready for microstructural analysis. This was performed by using the methods outlined in §3.4.

5.3 Results and discussion

5.3.1 Tool wear

Figure 5.5a to h shows Alicona scans of the cutting edge of each tool insert used in the OD turning trials of Ti-54M.
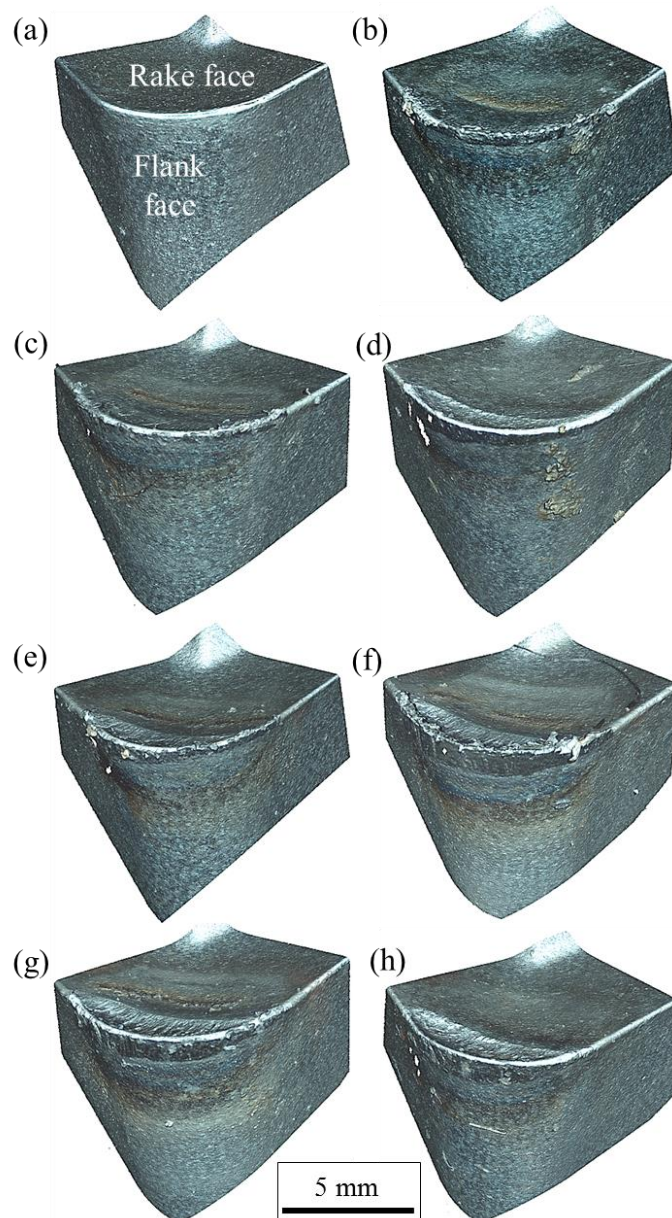
Figure 5.5. Alicona scans of the tool inserts used in OD turning of Ti-54M presented in order of increasing machining time: (a) 0; (b) 30; (c) 60; (d) 90; (e) 120; (f) 150; (g) 180; (h) 210 s.

It can be seen how the dominant wear mechanism is crater wear which is localised on the rake face of the tool. As machining time increases, as does the severity of the crater wear scar. This is due to a chemical reaction between the workpiece and tool which is amplified by the high cutting speed. Excessive crater wear weakens the cutting edge and can lead to fracture. There is also evidence of flank wear as the flank face remains in sliding contact with

the workpiece. This is less severe than crater wear as there is no corresponding seized region as seen on the rake face. Flank wear occurs due to abrasion which is caused by hard constituents in the workpiece material.

Figure 5.6a to h shows Alicona scans of the cutting edge of each tool insert used in the OD turning trials of Ti-6246.
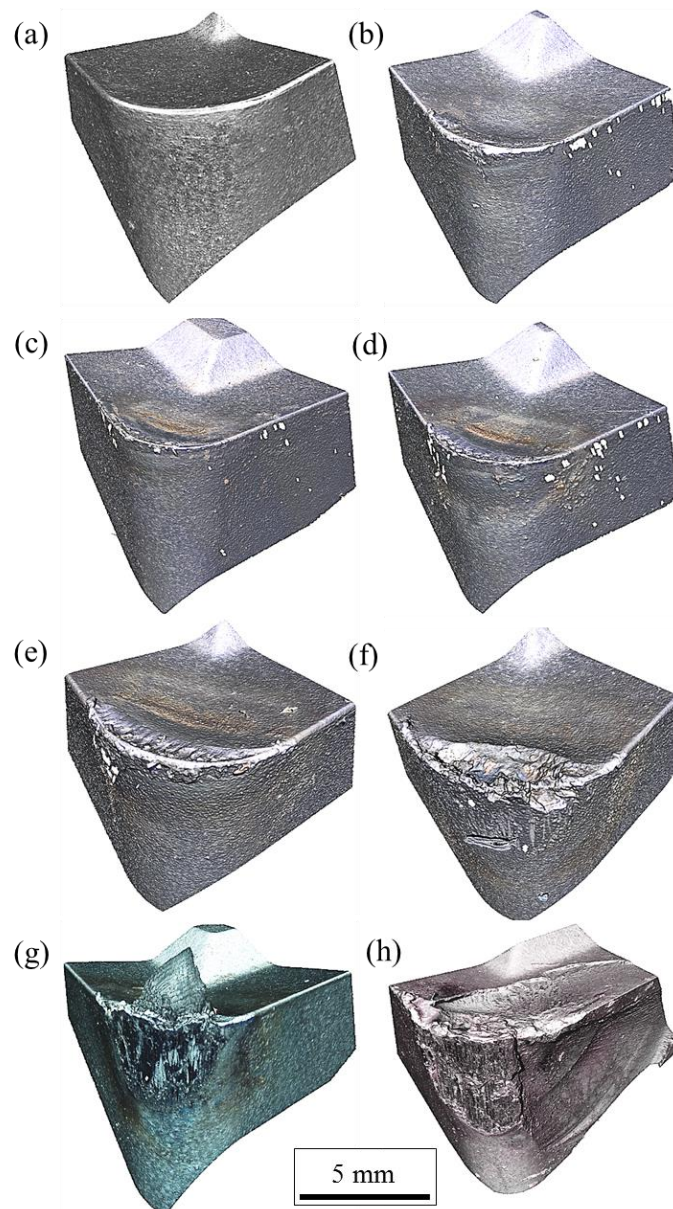
Figure 5.6. Alicona scans of the tool inserts used in OD turning of Ti-6246 presented in order of increasing machining time: (a) 0; (b) 30; (c) 60; (d) 90; (e) 120; (f) 150; (g) 180; (h) 210 s.

It is immediately apparent that the machining of Ti-6246 has resulted in much greater tool wear than Ti-54M. A similar crater tool wear pattern to Ti-54M is observed in Figure 5.6a to e before catastrophic tool wear consumes the nose of the tool. Figure 5.6f shows severe flank

wear and plastic deformation as the tool material softens due to the high temperatures at the tool chip interface. Figure 5.6g shows a pronounced built-up edge (BUE) which is caused by pressure welding of the chip to the tool insert. Figure 5.6h shows catastrophic tool failure via severe chipping which is the results of mechanical tensile stresses. Diffusion of cobalt binder phase from the tool to the chip and workpiece weakens the tool substrate and allows for carbide grains to be stripped from the surface. This mechanism is observed in the diffusion couple experiments discussed in Chapter 4. Figure 5.7a and b show plots of tool wear versus machining time for both Ti-54M and Ti-6246.
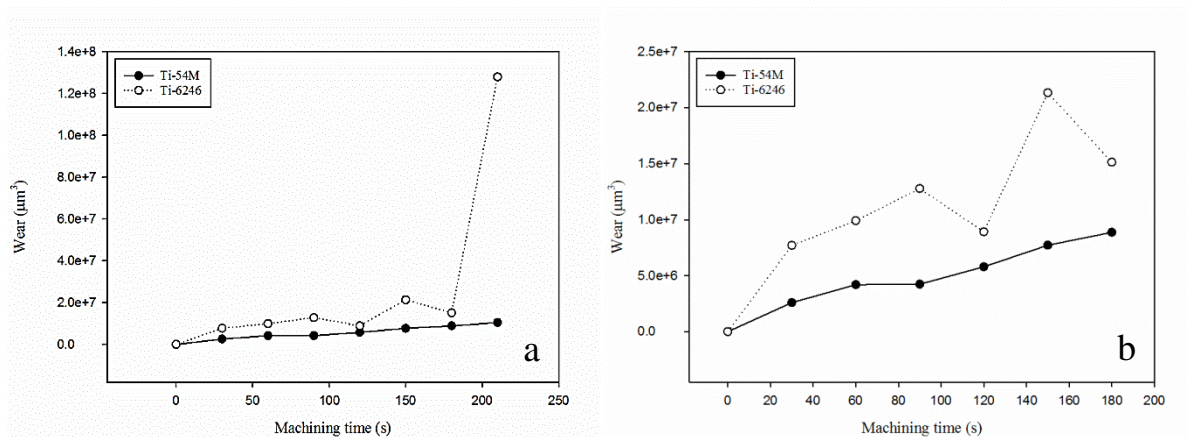
Figure 5.7. (a) Tool wear vs. machining time for Ti-54M and Ti-6246; (b) shows same plot with final data point removed for clarity.

It can be observed that tool wear for machining Ti-6246 is more severe than Ti-54M during the entire length of cut. Furthermore, the Ti-54M tool wear profile is more consistent (more constant slope) than that of Ti-6246.

Figure 5.8a and b show the worn rake face of the tools used to machine Ti-54M and Ti-6246 respectively. The rake face of the Ti-54M tool is coated with a homogenous and uniform layer of TiC. X-EDS data reveals high quantities of workpiece material (87 wt.% Ti; 5 Al; 4 V; 1 Mo; 1 Fe) as well as retained carbon (1.5 wt.%). The other tool constituents; tungsten and cobalt are relatively depleted (0.5 wt.%W; 0.2 Co) which agrees with the results observed in the Ti-54M diffusion couple (Figure 4.4h) where a high quantity of TiC is observed in Z3 and Z4. The same TiC formation is observed on the rake face of the Ti-6246 tool; however, it is much sparser and intermittent in appearance. Spot 1 in Figure 5.8b shows evidence of workpiece material (74 wt.% Ti; 6 Al; 2 Sn; 5 Zr; 6 Mo) and a retained quantity of carbon (6 wt.%). Conversely, Spot 2 shows the presence of tool constituents (78 wt.%W; 8 C; 6 Co) in high quantity and only negligible values of workpiece constituents (4 wt.% Ti; 0.3 Al; 0.7 Sn; 1.4 Zr; 1 Mo). The lack of TiC formation observed on the Ti-6246 tool

compared to the Ti-54M tool during dynamic OD turning trials agrees with the results seen in the static vacuum diffusion couple experiments in Chapter 4.
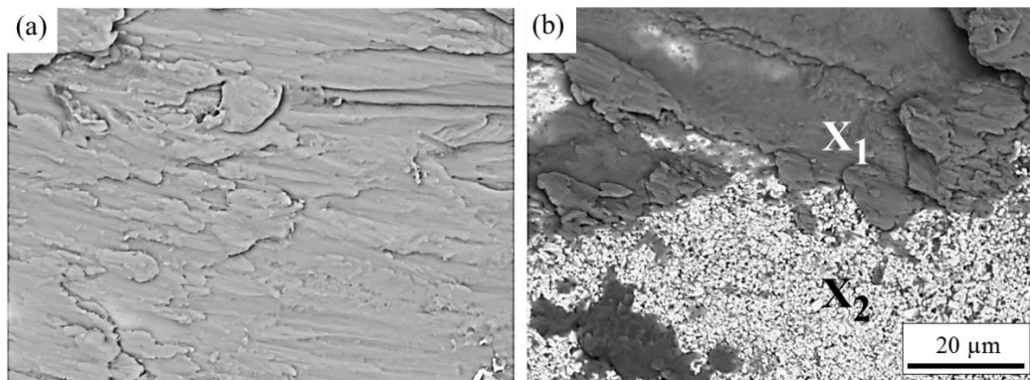
Figure 5.8. Backscattered electron micrographs of the rake face of the tool insert used to machine (a) Ti-54M and (b) Ti-6246 respectively.

Figure 5.9a shows a bright field (BF) transmission electron micrograph of the rake face of a new, unused WC-6%Co tool insert. Figures 5.9b and c show BF TEM micrographs of the worn rake face of the tool insert after machining the Ti-54M billet for 30 and 210 s respectively. The sample foils were lifted from the crater worn rake face as per §3.5.3. Moving from 0 to 30 to 120 s of machining time, there is a marked change in structural integrity of the tool insert. With an increase in machining time comes an increase of glissile dislocations and stacking faults. The applied load of the turning operation results in redistribution of the WC grains associated with plastic deformation. This redistribution leads to formation of intergranular binder phase lamellae. Shifting from 30 s to 210 s of machining time, Figures 5.9b and c show how the binder phase has infiltrated the broken grain boundaries. The small arrows mark where the cobalt binder phase has formed thin lamellae between the WC grains. Interestingly, these lamellae of binder phase run parallel to the direction of the resulting force from the machining operation (large arrow, marked *F*). This results in a fully banded WC grain structure with cobalt lamellae at the grain boundaries after 210 s of turning. It has been shown previously [159, 160] that cobalt segregates at the grain boundaries of tungsten carbide in WC-Co materials.
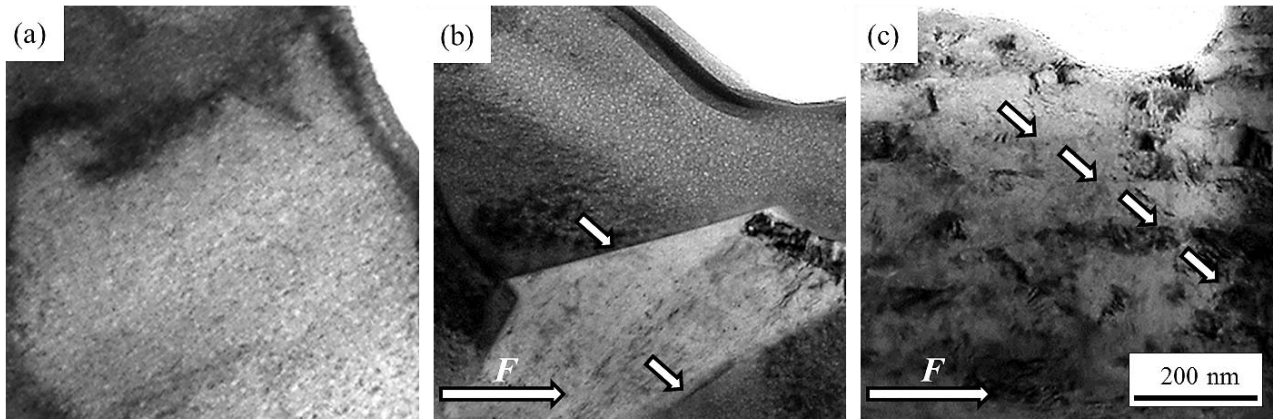
Figure 5.9. Bright field transmission electron micrographs of the rake face of the tool insert after (a) 0, (b) 30 and (c) 210 s machining time of the Ti-54M billet. Small arrows indicate cobalt binder lamellae. Large arrows indicate the resulting force direction from machining operation.

Figure 5.10a shows a bright field (BF) transmission electron micrograph of the rake face of a new, unused WC-6%Co tool insert. Figures 5.10b and c show BF TEM micrographs of the worn rake face of the tool insert after machining the Ti-6246 billet for 30 and 210 s respectively. The sample foils were lifted from the crater worn rake face as per §3.5.3.
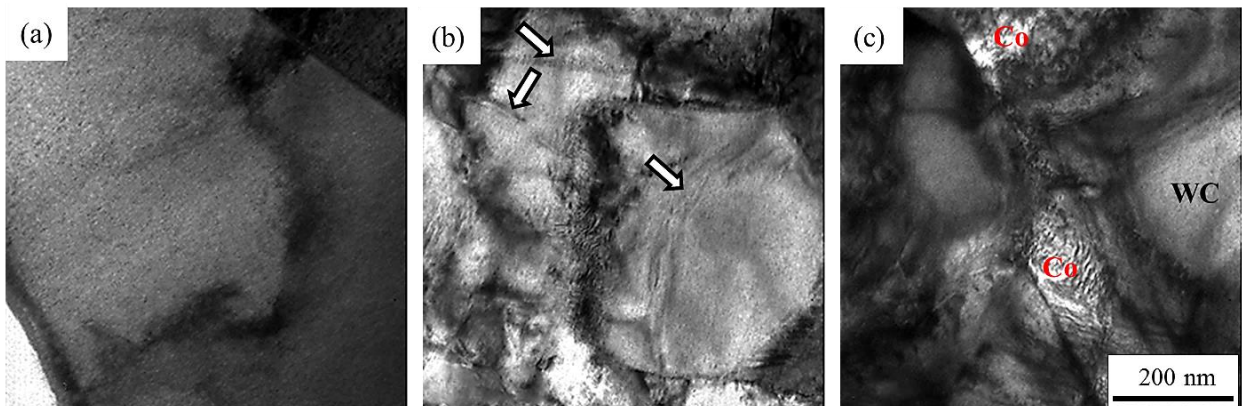
Figure 5.10. Bright field transmission electron micrographs of the rake face of the tool insert after (a) 0, (b) 30 and (c) 210 s machining time of the Ti-6246 billet. Small arrows indicate dislocations.

First observations of the microstructure of the WC-6%Co after machining Ti-6246 reveal marked differences in structure. Figure 5.10b shows how after only 30 s of turning, the WC grains are severely plastically deformed with a high density of dislocations (marked with arrows). Figure 5.10c is similar in appearance to Figure 5.10b indicating that lack of TiC formation fails to protect the cutting edge from crater wear. The banded structure of the WC grains as seen in machining Ti-54M is not observed for Ti-6246. Cobalt binder phase can be seen at the WC grain boundaries but it is not uniform which results in small pools of binder phase intersecting the separated grain boundary (Figure 5.10c). Östberg and Andrén [161]

explain that the presence of binder lamellae at grain boundaries indicates that interfacial energies are integral to deformation resistance. Figure 5.11 shows how the grains are forced apart by a locally induced tensile force with simultaneous grain boundary sliding due to induced shear stresses. It has been shown [162] that the formation of two Co/WC phase boundaries is energetically favourable when a tungsten carbide grain boundary is exposed to high tensile force in a WC-Co system.
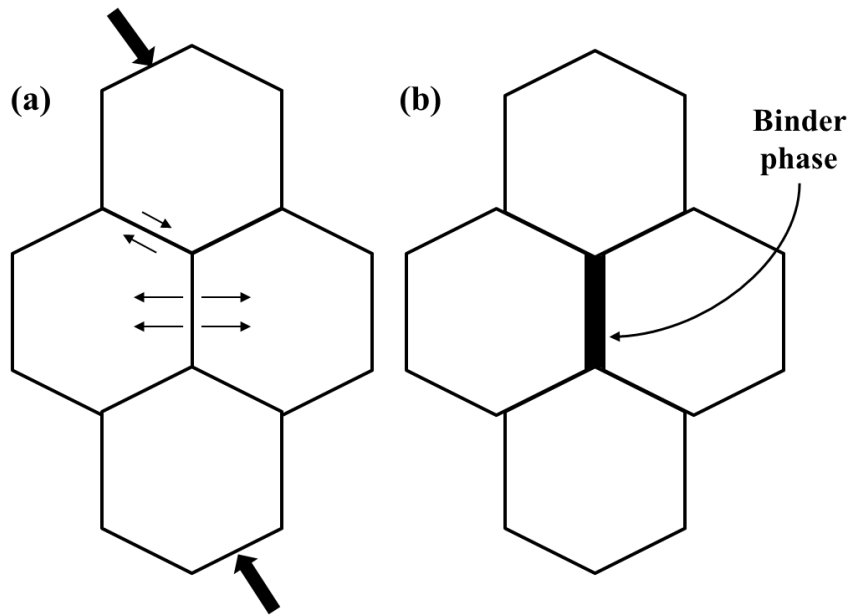
Figure 5.11. A schematic showing for the formation of binder phase lamellae. (a) Macroscopic compressive force (large arrows) may induce local tensile or shear forces (small arrows) between grains (orientation depending). (b) At the shearing forces, grain boundary sliding occurs. With the tensile stresses, the grains are separated with simultaneous diffusion of cobalt into the grain boundary, from Östberg and Andrén [161].

5.3.2 Workpiece material microstructure

Figure 5.12 shows the workpiece material microstructure of the machined Ti-54M (a to d) and Ti-6246 (e to h). The delineated lines separate the regions of bulk material; plastically deformed material and severely deformed tertiary shear material. Previous work [20, 95] has demonstrated that machining parameters can induce microstructural modifications at the surface of titanium alloys. Machining induced features such as mechanical twins and intense slip bands can initiate microcracking under dynamic loading conditions. Thus the mechanical twins and severely plastically deformed 'swept' grains observed in Figure 5.12 are increasingly referred to as subsurface "damage". Interestingly, the maximum damage depth observed within the surface layer is greater for Ti-54M (40 μm, Figure 5.12d) than Ti-6246 (12 μm, Figure 5.12h) even though Ti-6246 degrades the tool more rapidly than Ti-54M (Figures 5.5 and 5.6). It is hypothesised that less damage is observed in Ti-6246 due to the higher volume fraction of ductile β phase at the machining interface temperature. As the machining time, and therefore tool wear increases, there is corresponding increase in depth of subsurface damage for Ti-54M. This is true for both the plastically deformed, and severely plastically deformed regions. Although the maximum damage depth is lower for Ti-6246, the same trend can be observed whereby the depth of damage to the workpiece subsurface grows larger as machining time and tool wear increases. There is no severely deformed tertiary

shear zone for Ti-6246 and therefore only one delineated line to separate the bulk material from the plastically deformed material.
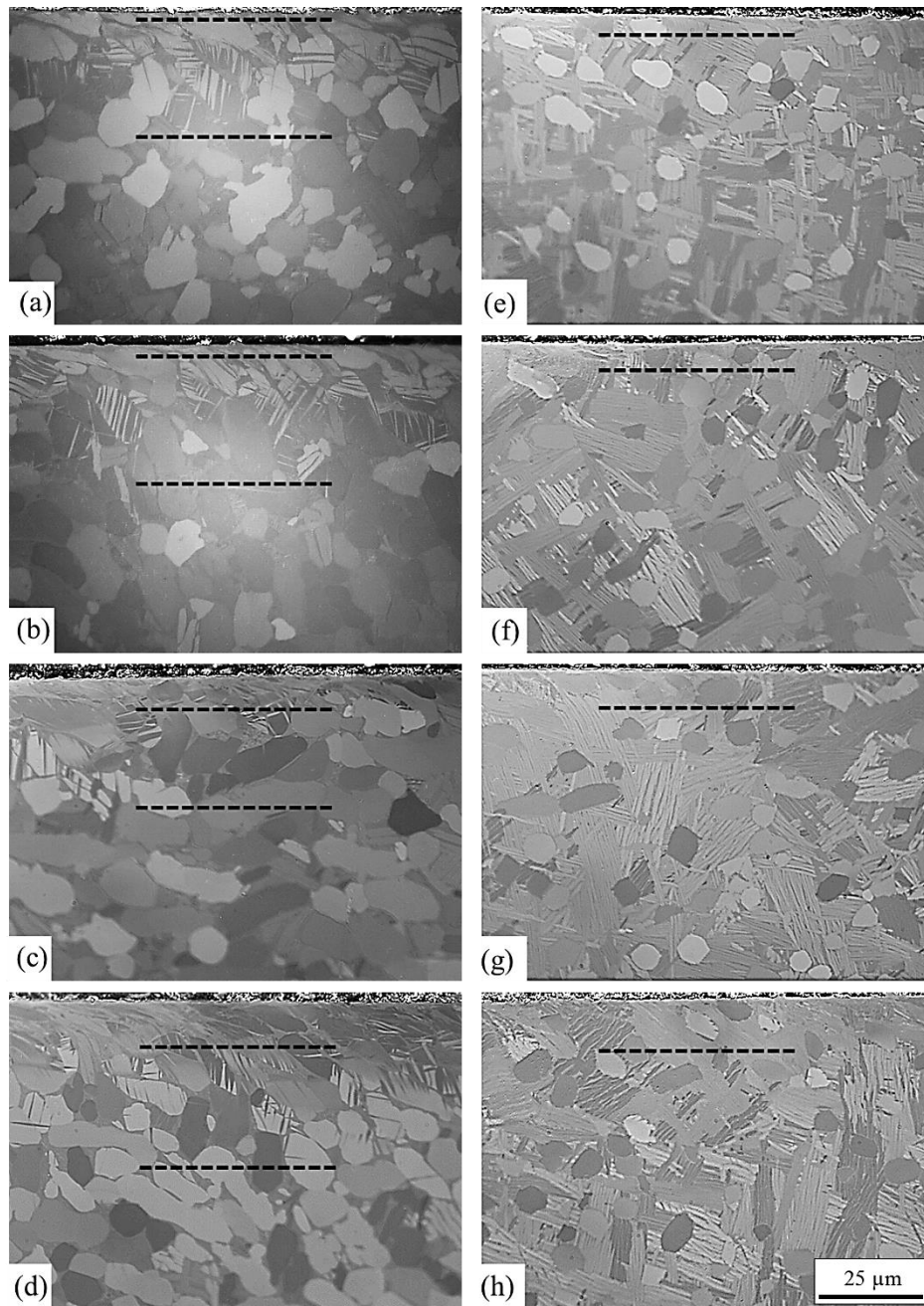
Figure 5.12. Left column shows light micrographs of the machined Ti-54M workpiece after (a) 45, (b) 90, (c) 135 and (d) 180 s turning. The delineated lines separate the regions of bulk material; plastically deformed material and severely deformed tertiary shear material. Right column shows light micrographs of the machined Ti-6246 workpiece after (e) 52, (f) 105, (g) 157 and (h) 210 s turning. The delineated line separates the bulk material from the plastically deformed material.

5.3.3 Chip morphology

Figure 5.13 shows photographs of the machined swarf from the OD turning trials of Ti-54M (blue) and Ti-6246 (red). For both titanium alloys, as the machining time, and hence the tool

wear increases, the chip becomes more irregular in shape and less coiled. This is due to the decreasing conformity of cutting edge of the tool insert which results in less effective contact with the workpiece. The Ti-6246 chip shows more severe irregularity in shape and form which corresponds with the increased tool wear observed in Figure 5.6.
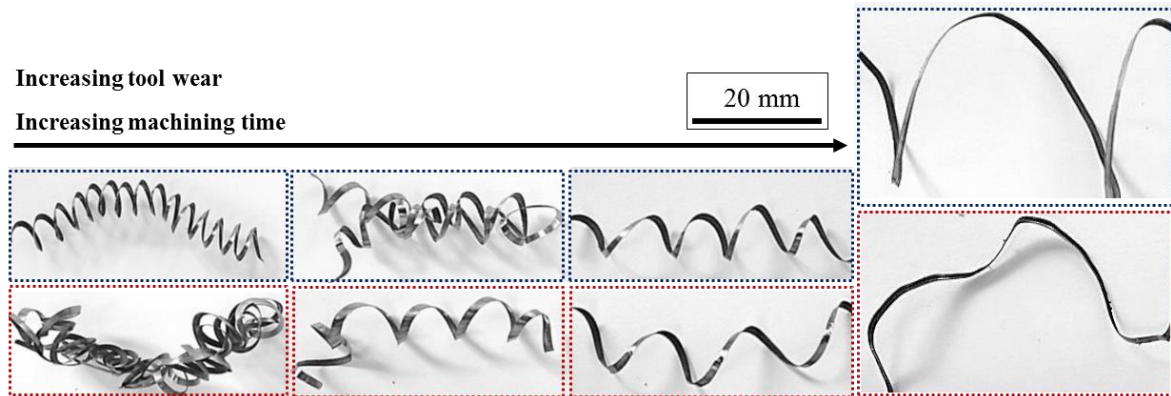
Figure 5.13. Photographs of the machined chip from Ti-54M (blue) and Ti-6246 (red).

Figure 5.14 shows the microstructure of the machined chip for Ti-54M (a to d) and Ti-6246 (e to h). Both materials display the trademark segmented chip formation typical of machined titanium alloys. As expected from the more severely worn tool observed with Ti-6246, the chip displays wider pitch, greater peaks, and deeper valleys than the Ti-54M chip.
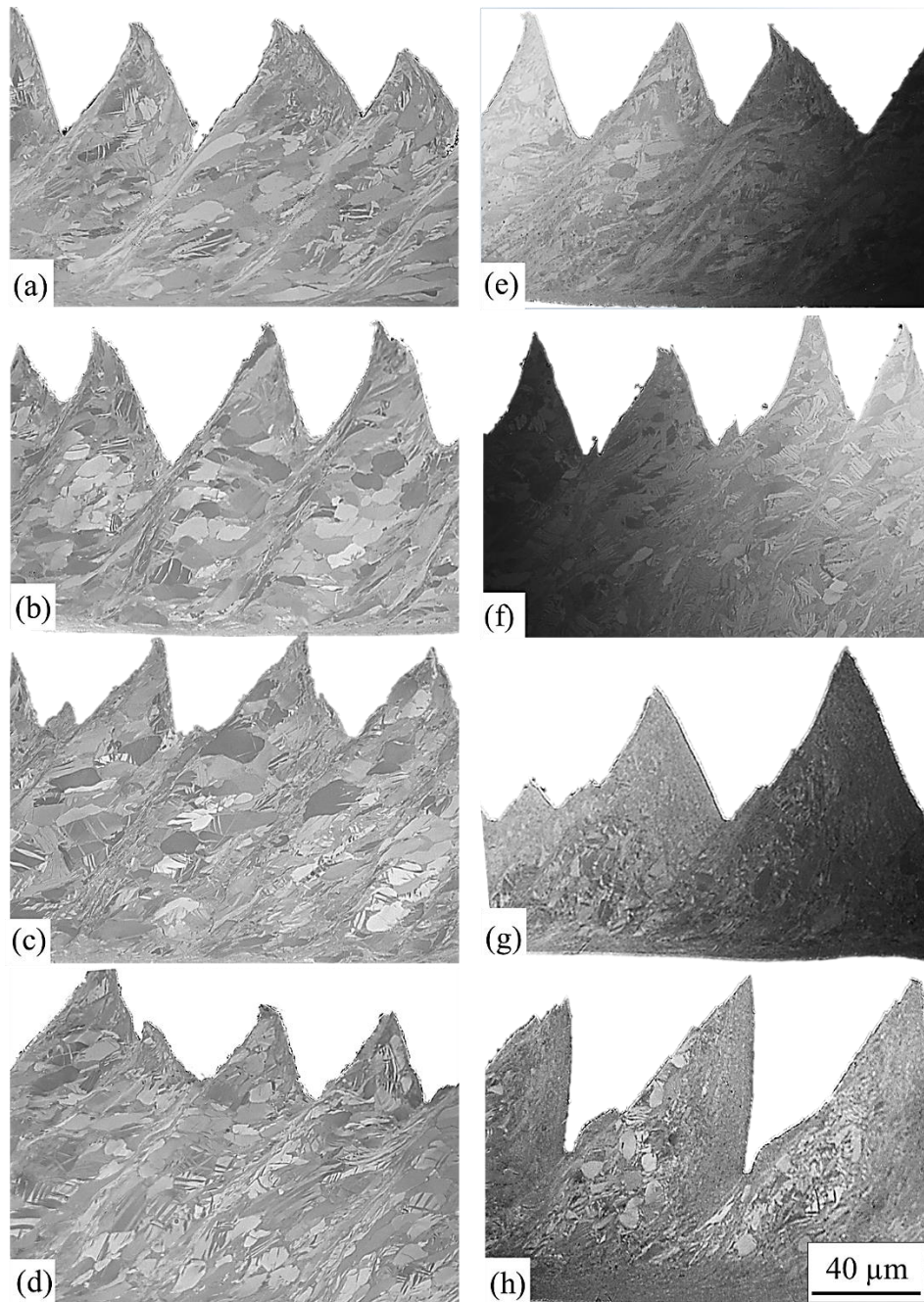
Figure 5.14. Left column shows light micrographs of the Ti-54M chip after (a) 52, (b) 105, (c) 157 and (d) 210 s turning. Right column shows light micrographs of the Ti-6246 chip after (e) 52, (f) 105, (g) 157 and (h) 210 s turning.

X-EDS data recorded at the subsurface of the Ti-54M workpiece shows high quantities of titanium (77 wt.%) and carbon (12 wt.%) indicating a strong presence of TiC. A similar trend can be observed in the chip at higher quantities, (79 wt.% Ti; 13 C). Ti-6246 also shows evidence of TiC at the workpiece subsurface (81 wt.% Ti; 5 C) and chip (76 wt.%; 7 C) however in much lower quantities than Ti-54M. This strongly agrees with experimental observations on the tool rake face which showed a homogenous layer of TiC for Ti-54M (Figure 5.8a) and a sparse intermittent layer of TiC for Ti-6246 (Figure 5.8b).

117

5.3.4 Cutting forces

Below are the cutting forces recorded for the OD turning of Ti-54M and Ti-6246. The x force is the normal force i.e. towards the centre of the billet, a resultant force by virtue of the depth of cut. The y force is the feed force i.e. as the tool moves along the outside of the billet. The z force is the cutting force i.e. with the rotation of the workpiece. Figure 5.15 shows the cutting forces for Ti-54M and can be identified via the following regions within the cutting cycle: start, contact, steady state, and finish. The start region shows that data acquisition has begun as the signal fluctuates around 0 ± 5 N before cutting begins. The contact region is represented by the sharp increase in force once the tool comes into contact with the workpiece. After the sharp increase in force, a steady state is reached after two to five initial revolutions. Here, the forces are subject to change as the tool wears which gradually affects the tool edge geometry and therefore contact with the workpiece. The finish occurs when the tool is withdrawn from the workpiece and the force reverts to zero.
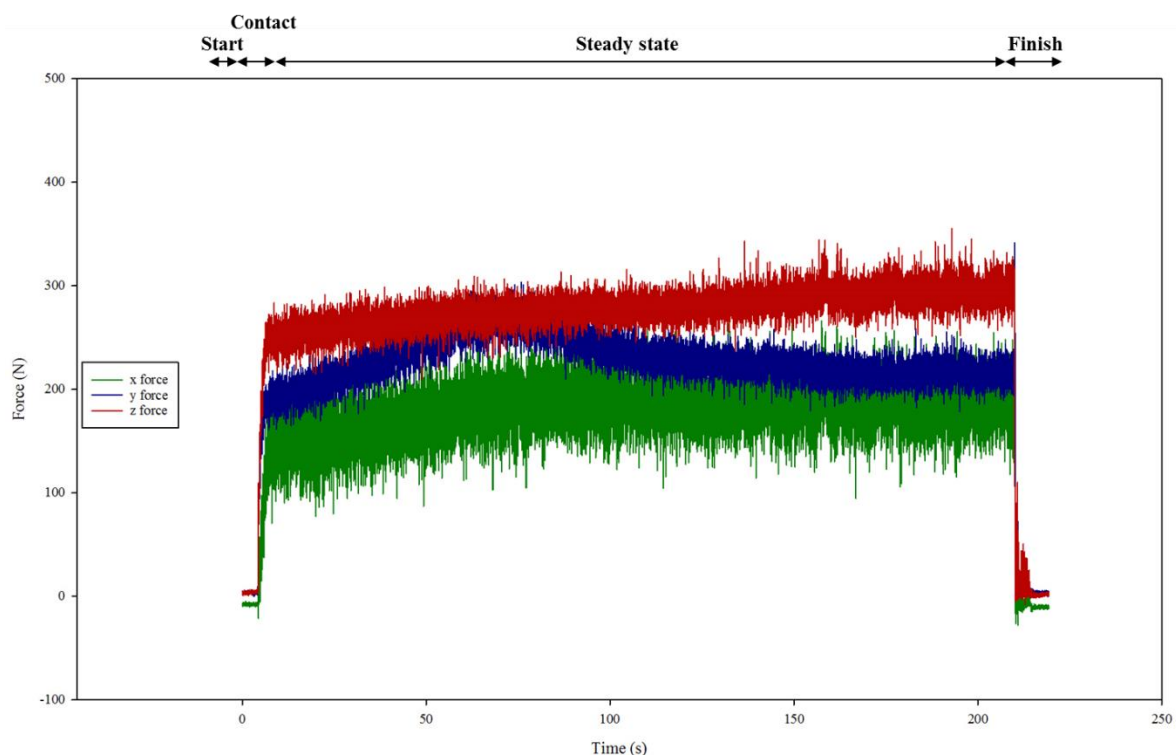
Figure 5.15. Cutting forces during the turning of Ti-54M for 210 s. Green = x force; blue = y force and red = z force.

Figure 5.16 shows the cutting forces for Ti-6246. The plot shows the same regions of the cutting force regimen to Ti-54M but also shows an extra region: tool failure. After a period of steady state, there is a sharp increase in cutting forces (~125 s) as the tool suffers catastrophic failure which prevents the workpiece from being cut efficiently. Figures 5.6e and f show how

the shape and structure of the nose of the tool has changed dramatically which corresponds to the time of cut where large force responses are recorded.
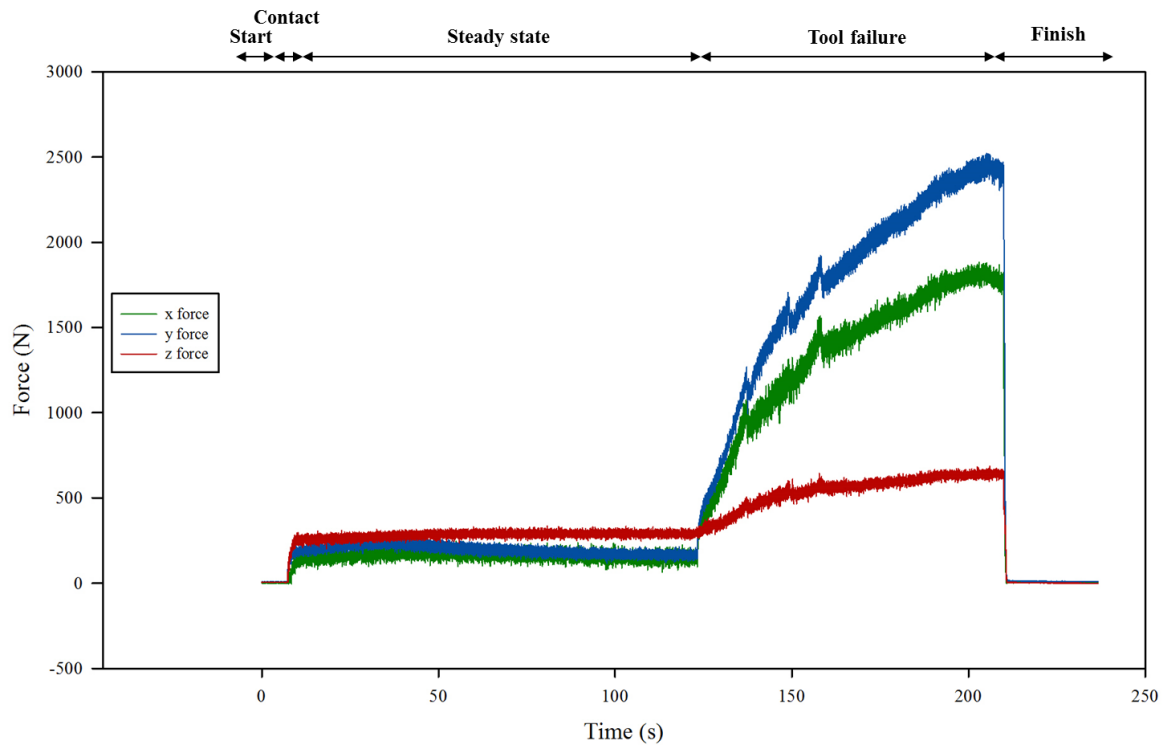
Figure 5.16. Cutting forces during the turning of Ti-6246 for 210 s. Green = x force; blue = y force and red = z force.

It is interesting to note that both materials showed similar cutting forces in steady state for the first 120 s of cutting. For Ti-54M, the x, y and z forces are shown to be approximately 150, 200 and 280 N respectively. For Ti-6246, the x, y and z forces are shown to be approximately 150, 200 and 300 N respectively.

5.4 Conclusions and chapter summary

Figure 5.17 shows a collated image of the tool, tool rake face, workpiece and chip for Ti-54M and Ti-6246 for direct comparison.
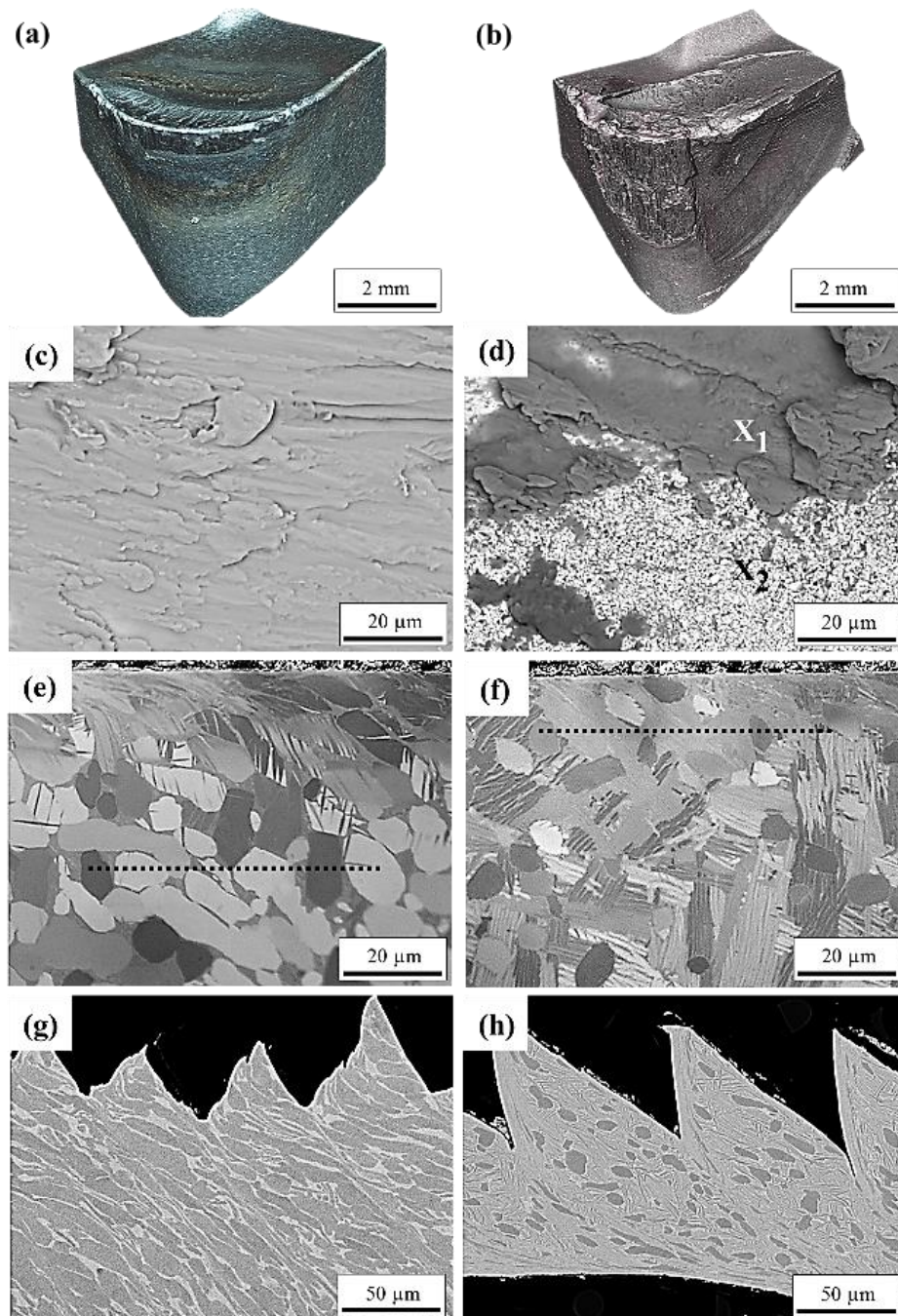
Figure 5.17. Alicona scans of tools used to machine (a) Ti-54M and (b) Ti-6246. Backscattered electron micrographs of the tool rake faces used to machine (c) Ti-54M and (d) Ti-6246 with the corresponding light micrographs of the workpiece material microstructure of (e) Ti-54M and (f) Ti-6246. Backscattered electron micrographs showing the machined chip microstructure of (g) Ti-54M and (h) Ti-6246 after 210 s turning. Crosses indicate position of X-EDS spot scan; delineated line indicates approximate damage depth.

For Ti-54M, smooth crater wear is observed on the rake face of the nose of the tool (Figure 5.17a) which corresponds to a homogenous coating of TiC on the rake face (Figure 5.17c). A 40 µm depth of damage is observed at the subsurface of the workpiece (Figure 5.17e) and the chip shows defined shear bands after 210 s of machining time (Figure 5.17g). For Ti-6246, more severe tool wear is observed (Figure 5.17b) which corresponds to the intermittent content of TiC on the rake face (Figure 5.17d). However, the level of subsurface damage to the Ti-6246 workpiece (Figure 5.17f) is approximately 12 µm which is not as deep as the damage observed for Ti-54M. The chip in Figure 5.17h shows less defined shear bands than the Ti-54M chip along with a wider pitch, greater peaks and deeper valleys. The results of the OD turning trials of Ti-54M and Ti-6246 show strong agreement with the diffusion couple experiments discussed in Chapter 4. For Ti-54M where diffusion bonding is observed, a high quantity of TiC formation occurs on the rake face of the tool insert. For Ti-6246 where diffusion bonding did not occur, only a negligible amount of TiC is observed on the rake face of the tool insert. This corresponds to the more severe tool wear observed for machining Ti-6246 compared with Ti-54M.

Chapter 6 - Thermodynamic modelling of tool-titanium alloy diffusion couples

6.1 Introduction

With the continued aim of predicting the machinability of titanium alloys before the occurrence of costly machining trials, this chapter investigates the use of DICTRA [163], the Diffusion Module of Thermo-Calc software [145]. The objective of this chapter is to develop a reliable model for the simulation of elemental diffusion between the tool and workpiece during titanium alloy machining. Furthermore, the intention is to explore whether such a model can predict the formation of reaction species and phase changes at the tool-workpiece interface. The results of the model are directly compared with the experimental findings from both the diffusion couple experiments in Chapter 4 and the OD turning trials in Chapter 5.

6.2 Experimental methods

All simulations presented in this chapter are a result of the experimental methods followed below. A detailed account of the principles behind DICTRA and what influences the choice of key functions is outlined in §3.6.

For the majority of simulations, the thermodynamic database TCFE8 [164] was used in tandem with the mobility database MOBFE3 [165]. Both are steel and iron alloy databases which are not necessarily the most accurate for simulations concerning titanium alloys. However, they are the most suitable databases with respect to tungsten carbides i.e. the tool insert material. It is generally a balancing act, with no perfect solution in regards to choice of database for reliable simulations. For simulations involving titanium alloys Ti-834 (Ti-5.8Al-4Sn-3.5Zr-0.7Nb-0.5Mo-0.35Si-0.06C) and Ti-6246 (Ti-6Al-2Sn-4Zr-6Mo), the thermodynamic database SSOL4 [166] was used in tandem with the mobility database MOB2 [167]. This is because TCFE8 and MOBFE3 are not capable of assessing systems with tin content. SSOL4 is a solutions thermodynamic database which is capable of assessing many binary, ternary and higher-order systems. MOB2 is a steel and iron alloy mobility database like MOBFE3 but is capable of assessing systems involving tin. Table 6.1 summarises the choice of each database with the corresponding system.

TABLE 6.1. CHOICE OF THERMODYNAMIC AND MOBILITY DATABASES FOR
EACH SYSTEM.

Nominal alloy chemistry	Informal name	Tool	Thermo- dynamic database	Mobility database
CP-Ti (Grade 2)	CP-Ti	WC-6%Co	TCFE8	MOBFE3
Ti-5.8Al-4Sn-3.5Zr-0.7Nb-0.5Mo-0.35Si-0.06C	Ti-834	WC-6%Co	SSOL4	MOB2
Ti-6Al-4V	Ti-64	WC-6%Co	TCFE8	MOBFE3
Ti-5Al-4V-0.8Mo-0.5Fe	Ti-54M	WC-6%Co	TCFE8	MOBFE3
Ti-6Al-2Sn-4Zr-6Mo	Ti-6246	WC-6%Co	SSOL4	MOB2
Ti-5Al-5Mo-5V-3Cr	Ti-5553	WC-6%Co	TCFE8	MOBFE3

As the purpose of the simulation was to try and replicate the results observed in both the diffusion couple experiments and OD turning trials, the DICTRA model was designed to mirror those experimental conditions as close as realistically possible. However, in order to achieve sensible simulation times, the theoretical time of heat treatment was set to 600 s with a grid size of 200 μm. For the results outlined below, a typical DICTRA simulation can take between three to seven days to complete when using a computational processor of 4 GHz.

6.3 Results and discussion

Below are composite plots of elemental diffusion and interfacial reaction species formation, together with the corresponding DICTRA simulation profiles. The X-EDS plot refers to the data acquired from the X-EDS instrument during SEM analysis. These are the same X-EDS plots as found in Chapter 4 for the corresponding diffusion couples. There are two DICTRA plots per graph: one for weight per cent (wt.%); and one for mole fraction (χ). The different plots are clearly defined in each figure. The alloys are presented in the same order as Chapter 4: CP-Ti, Ti-834, Ti-64, Ti-54M, Ti-6246, and Ti-5553. An increase in β phase stability at room temperature.

6.3.1 α titanium alloy: CP-Ti and WC-6%Co

Figures 6.1a to d show the individual elemental diffusion profiles for the CP-Ti and WC-6%Co diffusion couple. Figure 6.1e shows the DICTRA simulation plot of TiC and $M_{12}C$ formation at the theoretical diffusion couple interface.

Figure 6.1. DICTRA plots and X-EDS data for the CP-Ti and WC-6%Co diffusion couple showing (a) titanium, (b) tungsten, (c) carbon and (d) cobalt. DICTRA predictions of (e) TiC and $M_{12}C$.

The DICTRA profiles for titanium diffusion (Figure 6.1a) from the workpiece to the tool loosely follow the X-EDS plot. DICTRA is successful in calculating the position of the interface and also shows a gradual slope as the titanium diffuses into the tool-workpiece

interface. However, DICTRA does not predict any titanium to be present in the subsurface of the tool which contradicts the X-EDS plot where formation of TiC is detected. It is important to note that the DICTRA profiles for titanium at the interface are not perpendicular to the abscissa. Titanium is present at the interface in small quantities (~16 μm, Figure 6.1a). The difference between the wt.% and mole fraction profiles is only negligible as the wt.% profile shows a more gradual diffusion of titanium into the interface.

The DICTRA profiles for tungsten diffusion (Figure 6.1b) are slightly more accurate in following the X-EDS plot. Small quantities of tungsten are predicted to diffuse into the interface and there is an additional gradient of tungsten into the CP-Ti substrate which is representational of the WC found in the subsurface of the CP-Ti in the diffusion couple (Figure 4.4b, Z3 and Z4). As with titanium, there is only a negligible difference between the DICTRA profiles of wt.% and mole fraction. The DICTRA profiles for carbon (Figure 6.1c) show poor representations of the experimental X-EDS data. Almost no carbon is predicted to diffuse into the CP-Ti substrate in a location where the X-EDS plot shows the highest peak (6 μm). The DICTRA profiles for the remaining tool element, cobalt (Figure 6.1d) also show poor agreement with the X-EDS data. However, there is a gradient of cobalt diffusion from the tool to the workpiece which does agree with the $Ti_2Co+\beta$ diffusion zone found in the diffusion couple. In reality, the X-EDS plot for cobalt shows alternating peaks and troughs as the line scan passes over the corresponding binder and WC particles respectively.

Figure 6.1e shows the DICTRA predictions for the formation of TiC (red) and $M_{12}C$ (blue) at the tool-workpiece interface. TiC is predicted to form at the interface with a mole fraction of 0.2, and $M_{12}C$ with a mole fraction of 0.19. Both reaction phases are present in the CP-Ti diffusion couple. In Figure 4.4b, TiC is found at the interface and $M_{12}C$ at the subsurface of the tool. DICTRA predicts both phases to be present at the centre of the interface.

It appears that the lack of activity predicted by DICTRA for the case of CP-Ti is due to the diffusion between the titanium and the cemented carbide stopping completely after an initial precipitation of carbides at the interface. Figure 6.2 shows how the fraction of carbides at the interface has reached one ($\chi = 1$) after only 1 s. This results in the diffusion stopping completely. The sum of carbides includes TiC, $M_{12}C$ and WC.
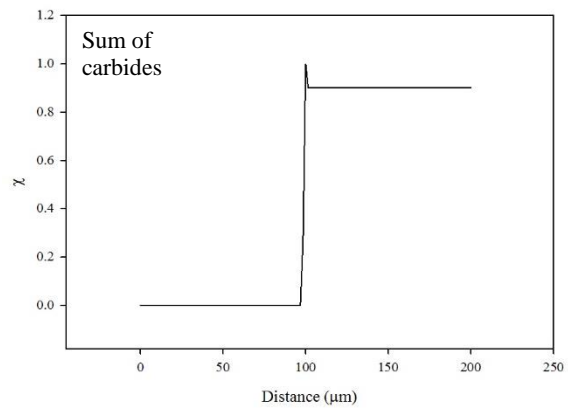
Figure 6.2. DICTRA prediction of the sum of carbides at the interface after 1 s.

6.3.2 Near α titanium alloy: Ti-834 and WC-6%Co

Figures 6.3a to i show the individual elemental diffusion profiles for the Ti-834 and WC-6%Co diffusion couple. Figure 6.3j shows the DICTRA simulation plot of TiC and $M_{12}C$ formation at the theoretical diffusion couple interface.

Figure 6.3. DICTRA plots and X-EDS data for the Ti-834 and WC-6%Co diffusion couple showing (a) titanium, (b) aluminium, (c) tin, (d) zirconium, (e) niobium and (f) molybdenum.

Figure 6.3. DICTRA plots and X-EDS data for the Ti-834 and WC-6%Co diffusion couple showing (g) tungsten, (h) carbon and (i) cobalt. DICTRA predictions of (j) TiC and $M_{12}C$.

The DICTRA profiles for titanium diffusion (Figure 6.3a) show some agreement with the X-EDS profile. There is a slight gradient as the titanium diffuses from the workpiece to the tool which increases towards to the tool substrate (~21 μm). The DICTRA simulation however, is unable to predict the high quantity of titanium at the interface which is shown as a peak in the X-EDS data at 24 μm along with a more gradual slope in the X-EDS profile. The DICTRA predictions for aluminium diffusion (Figure 6.3b) are quite interesting as a large peak is observed at the interface (22 μm) for aluminium mole fraction. However, this trend is not observed experimentally in the diffusion couples and corresponding X-EDS (Figures 4.9a and b). Instead, the diffusion couple shows a more gradual diffusion of aluminium in low quantities. An aluminium carbide (Al_4C_3) species is not detected experimentally nor in the DICTRA simulations. The DICTRA plots for the alloying elements tin, zirconium, niobium and molybdenum (Figures 6.3c to f) all share a similar profile. There is only a slight gradient at the interface for these elements and negligible quantity is shown to diffuse into the tool. The mole fraction plots are arguably more in agreement with the X-EDS data than the wt.% plots. The X-EDS data from the diffusion couple show only a slight decrease in tin, zirconium, niobium and molybdenum quantity between the workpiece and tool.

128

The DICTRA simulation for tungsten (Figure 6.3g) mirrors that of titanium. There is good agreement with the X-EDS diffusion profile which shows quantities of tungsten at the interface and tool subsurface which corresponds to Z3 and Z4 in the diffusion couple in Figure 4.4d. For carbon diffusion (Figure 6.3h), DICTRA shows a large peak in mole fraction at the interface of the diffusion couple (~25μm). There are also quantities of carbon predicted at the subsurface of the tool. This corresponds to a number of phases observed experimentally including TiC, WC, M_6C and $M_{12}C$. Good agreement is found with the X-EDS data for carbon diffusion. The peak at the surface of the tool (25 μm) before a trough (23 μm) which is also observed in the DICTRA profiles. Also interesting to note is that DICTRA predicts the mole fraction of carbon to be close to zero either side of the interface which indicates diffusion of carbon. The mole fraction of carbon returns to above zero moving away from the interface. DICTRA also predicts cobalt (Figure 6.3i) to diffuse to the interface as a strong peak in wt.% is observed at 27 μm. As observed with CP-Ti, there is also a slight gradient as cobalt diffuses from the tool to the interface corresponding to the $Ti_2Co+\beta$ phase observed in the diffusion couple experiment.

Figure 6.3j shows the DICTRA prediction for the formation of TiC and $M_{12}C$ at the tool-workpiece interface. Both species are observed experimentally in the diffusion couple for Ti-834. TiC is predicted to be at the centre of the reaction interface which corresponds to Z3 and Z4 in Figure 4.4d. $M_{12}C$ is observed adjacent to the TiC peak which corresponds to Z5 in Figure 4.4d. As well as successfully predicting the formation of these species, DICTRA also plots them in the correct 'order': TiC at the interface, and $M_{12}C$ at the subsurface of the tool. However, DICTRA predicts that the $M_{12}C$ phase continues into the bulk of the tool which is not observed experimentally.

6.3.3 α+β titanium alloy: Ti-64 and WC-6%Co
Figures 6.4a to f show the individual elemental diffusion profiles for the Ti-64 and WC-6%Co diffusion couple. Figure 6.4g shows the DICTRA simulation plot of TiC, M_6C and $M_{12}C$ formation at the theoretical diffusion couple interface.

Figure 6.4. DICTRA plots and X-EDS data for the Ti-64 and WC-6%Co diffusion couple showing (a) titanium, (b) aluminium, (c) vanadium, (d) tungsten, (e) carbon and (f) cobalt. DICTRA predictions of (g) TiC, M₆C and M12C.

The DICTRA profiles for titanium diffusion (Figure 6.4a) show good agreement with the X-EDS data. There is an increase in titanium concentration towards the interface which is represented by a slight hump in the DICTRA plots at 38 µm. The X-EDS plot shows a peak in titanium concentration at 42 µm which corresponds to TiC formation. The DICTRA profiles for aluminium diffusion (Figure 6.4b) also show good agreement with the X-EDS data. There is a strong peak towards the interface (40 µm) followed by a smaller peak at the tool substrate (42 µm). However, DICTRA does not predict aluminium to be present past the subsurface of the tool which is observed experimentally. The X-EDS data for vanadium (Figure 6.4c) shows two strong peaks at the interface at 18 and 22 µm. These are also predicted by DICTRA which shows two strong peaks at the interface for both wt.% and mole fraction.

The DICTRA profiles for tungsten (Figure 6.4d) are equally accurate at modelling the X-EDS data. There is a peak as the tungsten diffuses toward the interface, and a gradual slope towards the tool which corresponds with the tungsten bearing species observed at the interface such as WC and β(Ti,W) in the Ti-64 and WC-6%Co diffusion couple (Figure 4.4f). The DICTRA profiles for carbon diffusion (Figure 6.4e) appear to be the most accurate at following the X-EDS plot from the diffusion couple. There are two prominent peaks of carbon concentration at the interface which correspond to Z3 and Z4 in Figure 4.4f. Finally, the DICTRA profiles for cobalt diffusion (Figure 6.4f) also show good agreement with the X-EDS data as the cobalt is shown to diffuse towards the tool-workpiece interface. This corresponds to the area of strengthened β-phase observed at the subsurface of the titanium alloy substrate, $Ti_2Co+\beta$ (Z2, Figure 4.4f).

Figure 6.4g shows the DICTRA prediction for the formation of TiC, M_6C and $M_{12}C$ at the tool-workpiece interface for the diffusion couple of Ti-64 and WC-6%Co. This is the only diffusion couple where DICTRA predicts the formation of an M_6C species which is observed experimentally (Figure 4.4f, Z6). This M_6C phase is important in the understanding of crater tool wear mechanisms as it is brittle and prone to fracturing. TiC is accurately predicted at the interface (Figure 4.4f, Z3 and Z4) but is also shown to be present deep in the surface of the tool which is not observed experimentally. $M_{12}C$ is also present at the interface which can be seen in Figure 4.4f in Z5.

6.3.4 α+β titanium alloy: Ti-54M and WC-6%Co

Figures 6.5a to h show the individual elemental diffusion profiles for the Ti-54M and WC-6%Co diffusion couple. Figure 6.5i shows the DICTRA simulation plot of TiC and $M_{12}C$ formation at the theoretical diffusion couple interface.
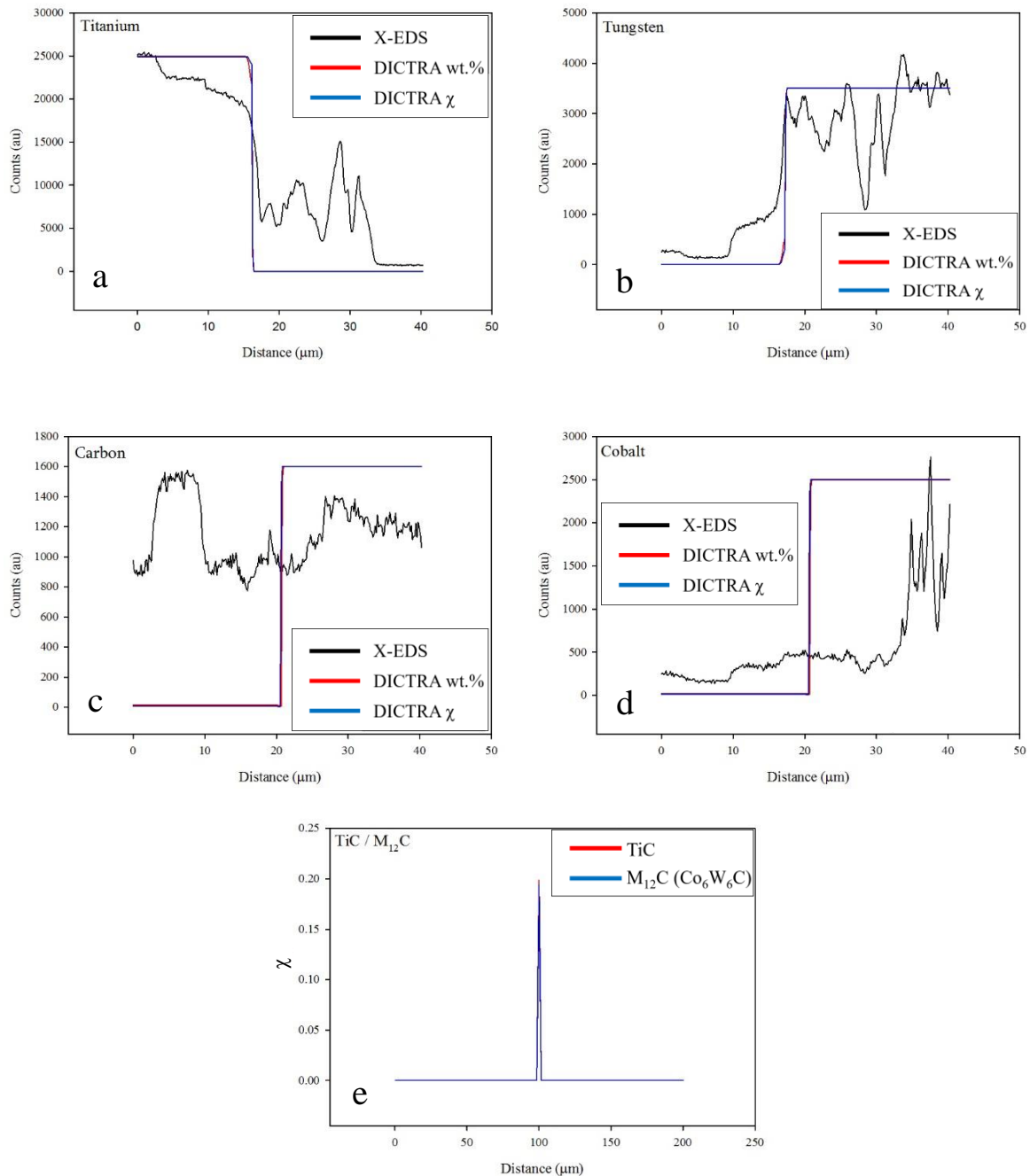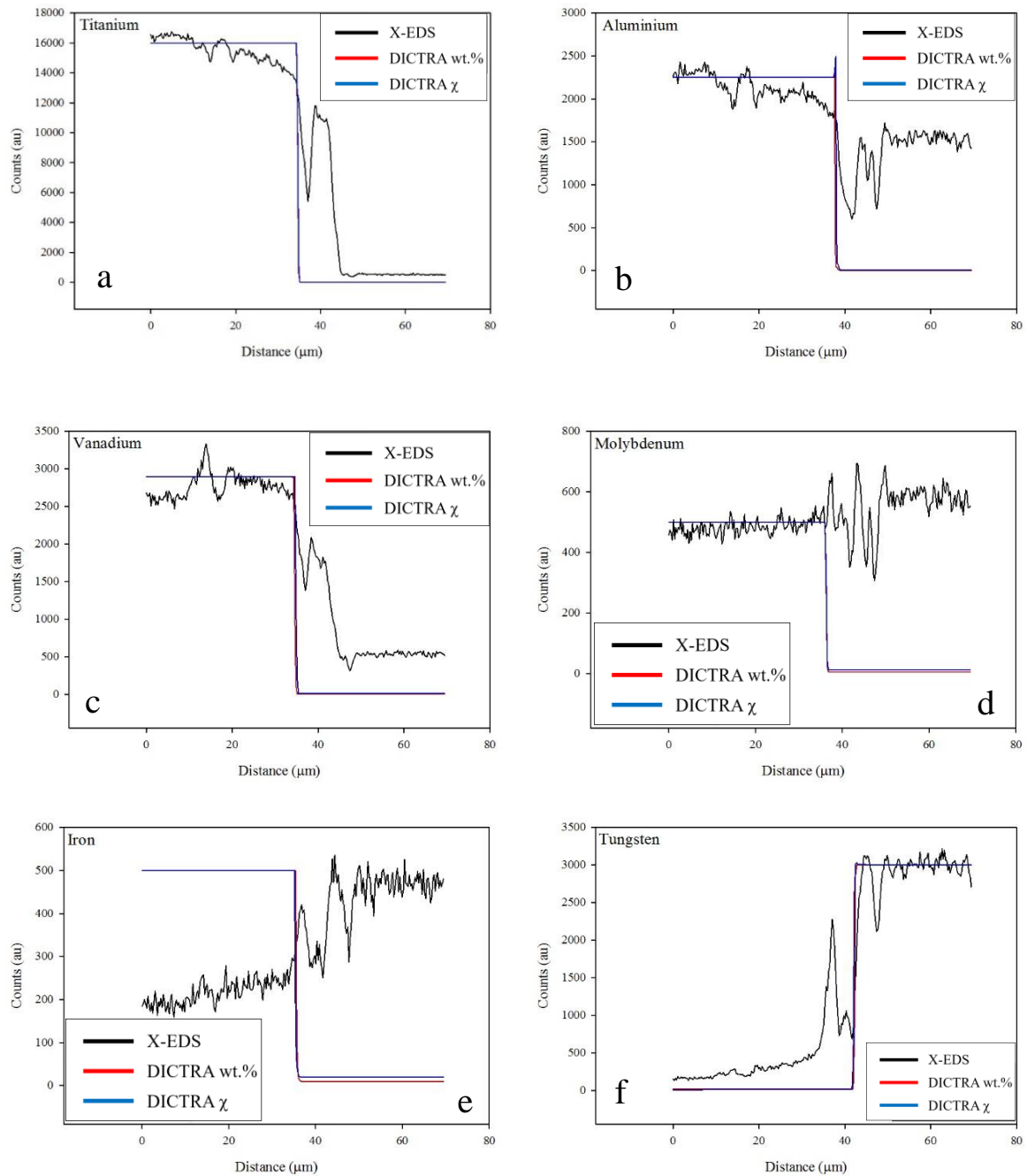

Figure 6.5. DICTRA plots and X-EDS data for the Ti-54M and WC-6%Co diffusion couple showing (a) titanium, (b) aluminium, (c) vanadium, (d) molybdenum, (e) iron and (f) tungsten.
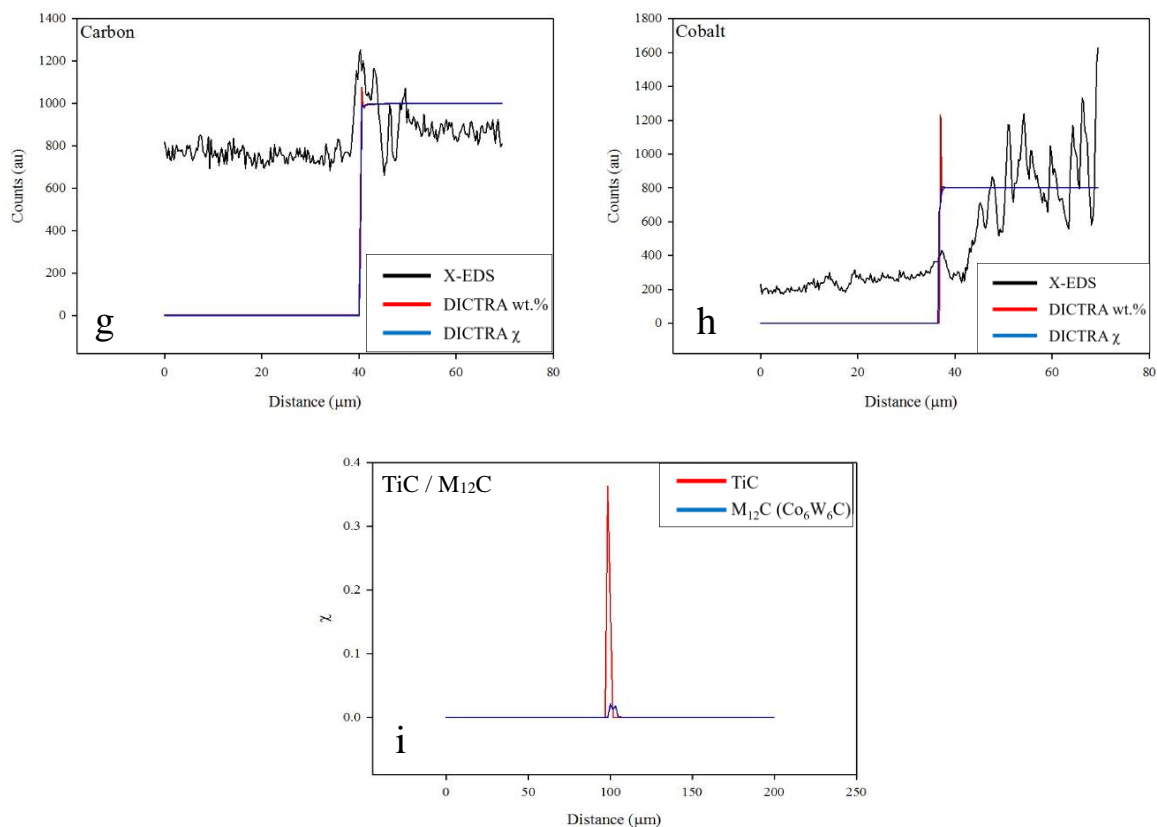
Figure 6.5. DICTRA plots and X-EDS data for the Ti-54M and WC-6%Co diffusion couple showing (g) carbon and (h) cobalt. DICTRA predictions of (i) TiC and $M_{12}C$.

The DICTRA plots for the primary workpiece elements of titanium, aluminium and vanadium (Figure 6.5a, b and c) only show fair agreement with the X-EDS data. DICTRA accurately predicts the position of the interface but only shows a slight diffusion profile for these elements into the tool. The DICTRA plots for the trace workpiece elements of molybdenum and iron (Figure 6.5d and e) show poor agreement with the X-EDS data. The X-EDS data actually shows higher quantities of molybdenum and iron in the tool. DICTRA does not predict molybdenum and iron to diffuse into the tool substrate.

The DICTRA profile for tungsten (Figure 6.5f) is similar to that of titanium. There is not much detail resolved save for the interface and a negligible amount of diffusion from the tool to the interface. For the DICTRA carbon profile (Figure 6.5g), there is a peak in wt.% at the interface (40 μm) but the carbon is not predicted to diffuse into the workpiece subsurface. Experimentally, the diffusion couples have shown TiC at the subsurface of the titanium alloy substrate. The DICTRA profiles for cobalt (Figure 6.5h) show a strong peak in wt.% at the interface which, as seen for Ti-64, corresponds to the $Ti_2Co+\beta$ phase observed in the diffusion couple experiment.

The DICTRA model is able to predict the presence of TiC and $M_{12}C$ at the interface of the Ti-54M and WC-6%Co diffusion couple (Figure 6.5i). The relative quantities of TiC and $M_{12}C$ is in strong agreement with what is observed experimentally in Z3, 4 and 5 in Figure 4.4h.

6.3.5 β rich, α+β titanium alloy: Ti-6246 and WC-6%Co

Figures 6.6a to h show the individual elemental diffusion profiles for the Ti-6246 and WC-6%Co diffusion couple. Figure 6.6i shows the DICTRA simulation plot of TiC and $M_{12}C$ formation at the theoretical diffusion couple interface.
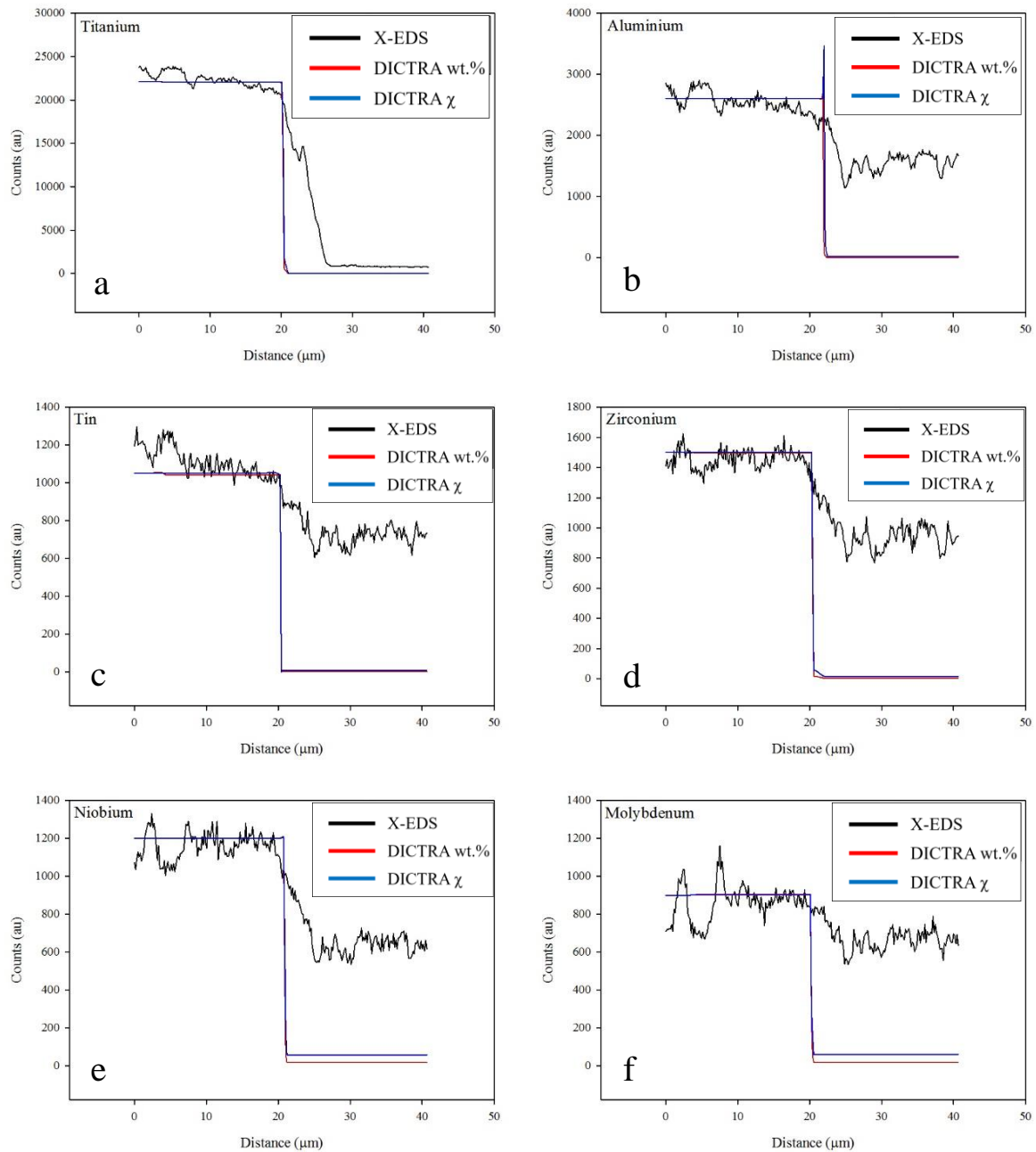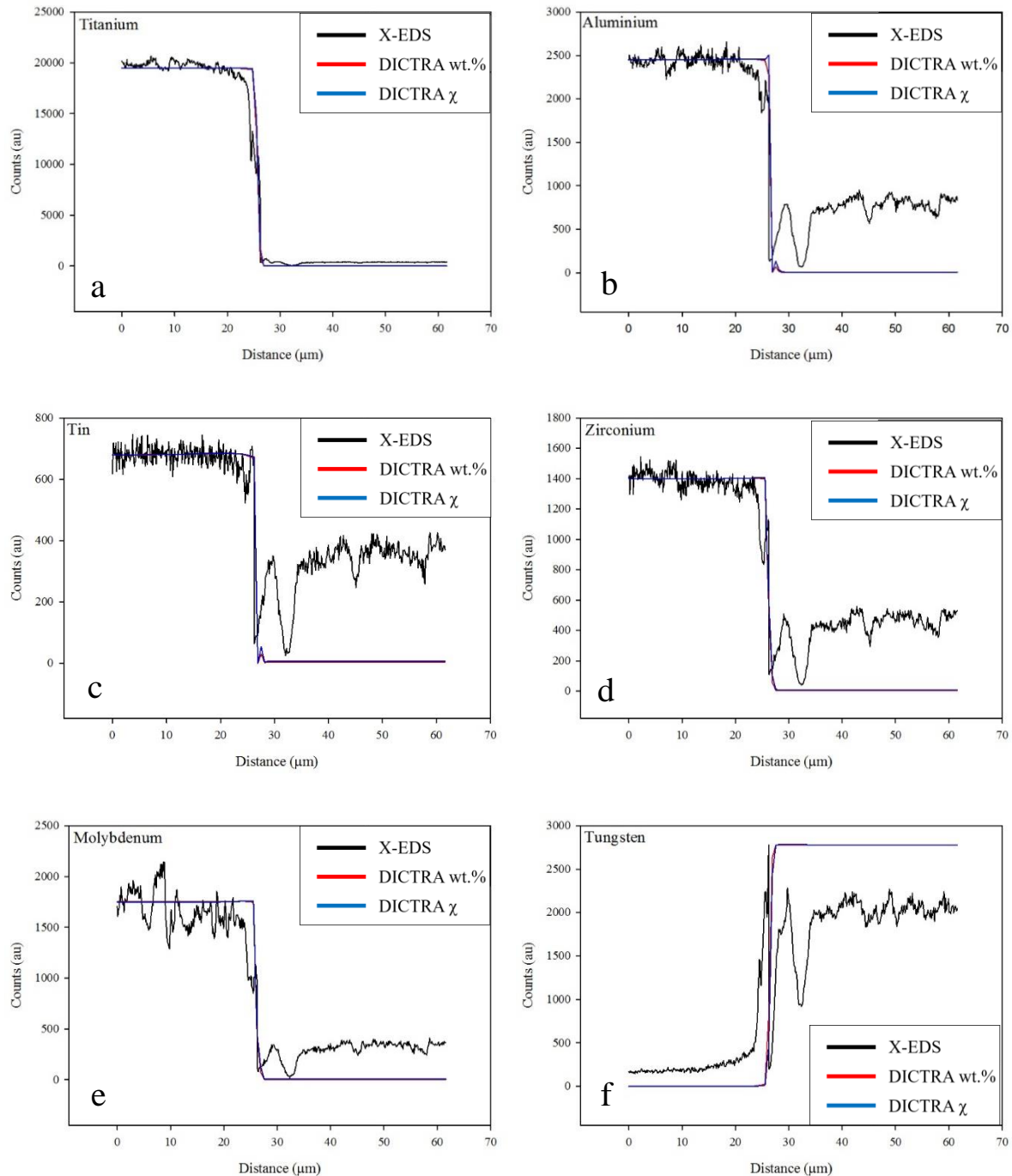

Figure 6.6. DICTRA plots and X-EDS data for the Ti-6246 and WC-6%Co diffusion couple showing (a) titanium, (b) aluminium, (c) tin, (d) zirconium, (e) molybdenum and (f) tungsten.
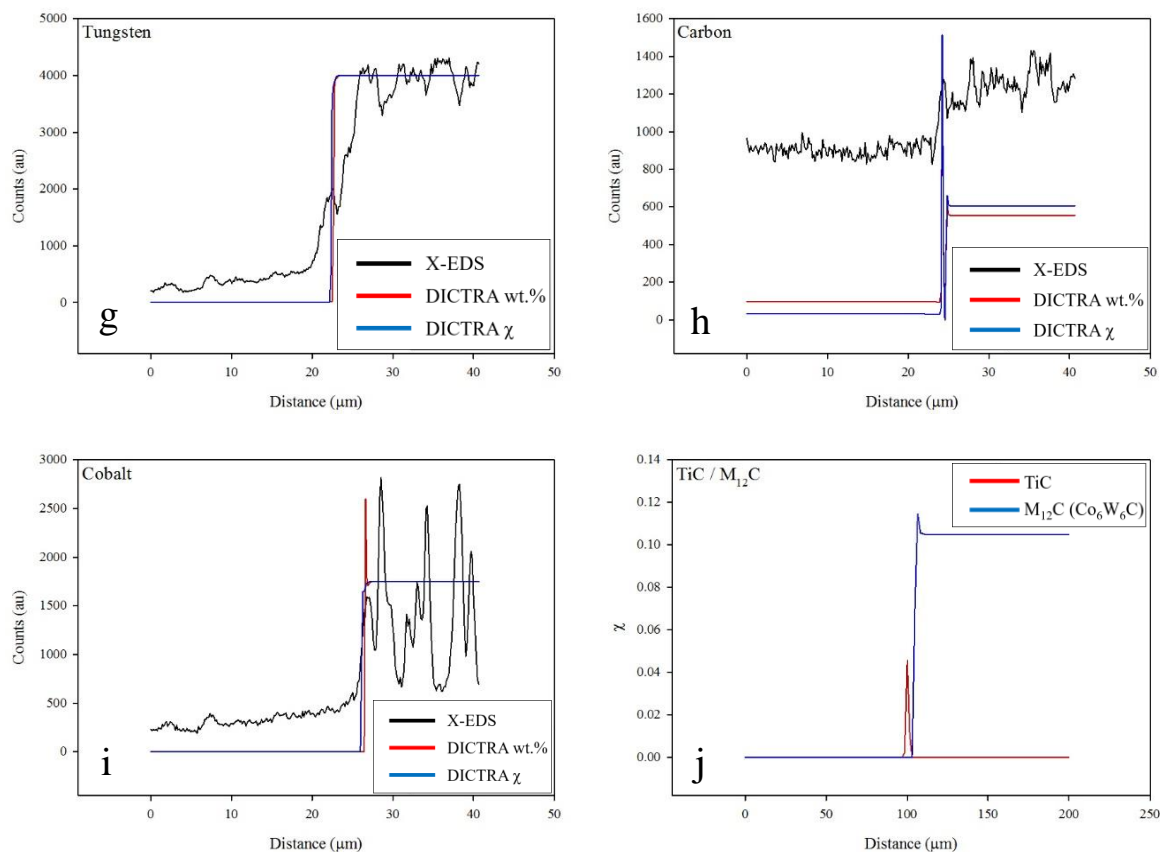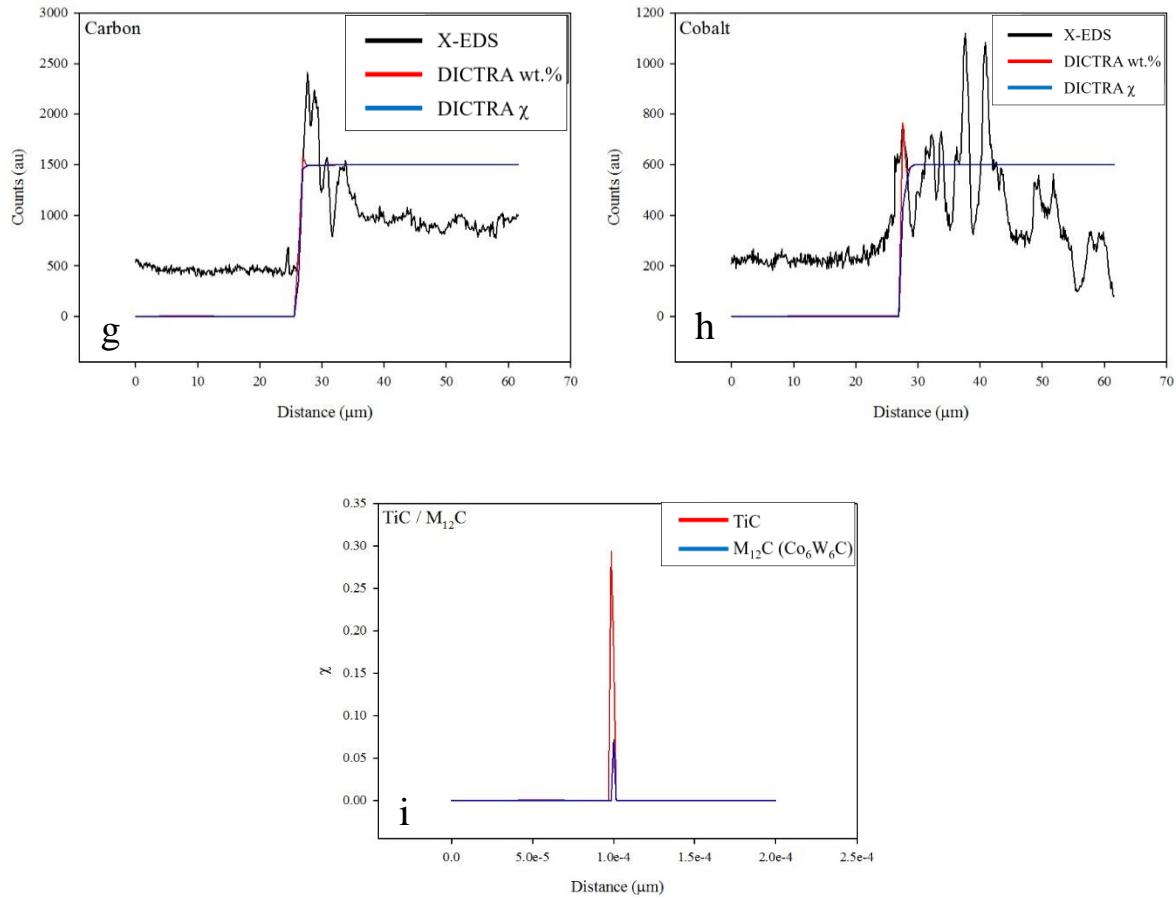
Figure 6.6. DICTRA plots and X-EDS data for the Ti-6246 and WC-6%Co diffusion couple showing (g) carbon and (h) cobalt. DICTRA predictions of (i) TiC and M_{12}C.

The DICTRA profile for titanium diffusion (Figure 6.6a) shows strong agreement with the experimental X-EDS data. Unlike the other titanium alloys, the Ti-6246 did not form a bond, yet the X-EDS does show some activity in terms of diffusion towards the surface of the tool and workpiece. For titanium, the gradient of titanium diffusion towards the surface in the DICTRA profile closely follows the X-EDS data. The DICTRA profile for aluminium diffusion (Figure 6.6b) also shows strong agreement with the X-EDS data. Small details such as the peak in aluminium at 28 μm are also predicted by DICTRA. The DICTRA profile for tin (Figure 6.6c) shows a similar profile to aluminium where the small peak in the X-EDS at 28 μm is accurately predicted by DICTRA. The DICTRA profile also closely follows the gradient of tin diffusion from the workpiece towards the interface observed in the X-EDS. The DICTRA plots for zirconium and molybdenum diffusion (Figure 6.6d and e) share a similar profile to each other. The peak in the X-EDS at 28 μm is predicted by DICTRA as both the mole fraction and wt.% increase. DICTRA and the X-EDS show that, despite the lack of bond in the diffusion couple experiment, the workpiece elements have still shown some diffusion towards the interface.

136

The DICTRA profiles for tungsten diffusion (Figure 6.6f) show strong agreement with the X-EDS data. In both the X-EDS and DICTRA, there is a deficit of tungsten before a strong peak at the surface of the tool which indicates diffusion of tungsten towards the interface. Similar trends are observed for carbon (Figure 6.6g) and cobalt diffusion (Figure 6.6h) whereby increased quantities of these elements are observed toward the interface. Strong agreement is found between the X-EDS data and the DICTRA simulations. Strengthening of the β phase was observed in the diffusion couple (Figure 4.4j, Z2) which corresponds to the diffusion of cobalt predicted by DICTRA. The diffusion couple also shows intermittent areas of bonded tool constituents to the titanium alloy where this strengthening of the β phase is observed (Figure 4.4j, Z3).

The DICTRA prediction for the formation of TiC and $M_{12}C$ at the interface of the diffusion couple between Ti-6246 and the WC-6%Co tool is shown in Figure 6.6i. A smaller quantity of TiC at the interface is predicted for Ti-6246 than Ti-54M which is also observed in the diffusion couple experiments (Chapter 4) and the machining trial study (Chapter 5). A small quantity of $M_{12}C$ is also predicted at the interface, but this was not observed experimentally. However, the Ti-6246 diffusion couple did show a small formation of M_6C at the subsurface of the tool (Figure 4.4j, Z4).

6.3.5 Metastable β titanium alloy: Ti-5553 and WC-6%Co

Figures 6.6a to i show the individual elemental diffusion profiles for the Ti-5553 and WC-6%Co diffusion couple. Figure 6.4j shows the DICTRA simulation plot of TiC and $M_{12}C$ formation at the theoretical diffusion couple interface.
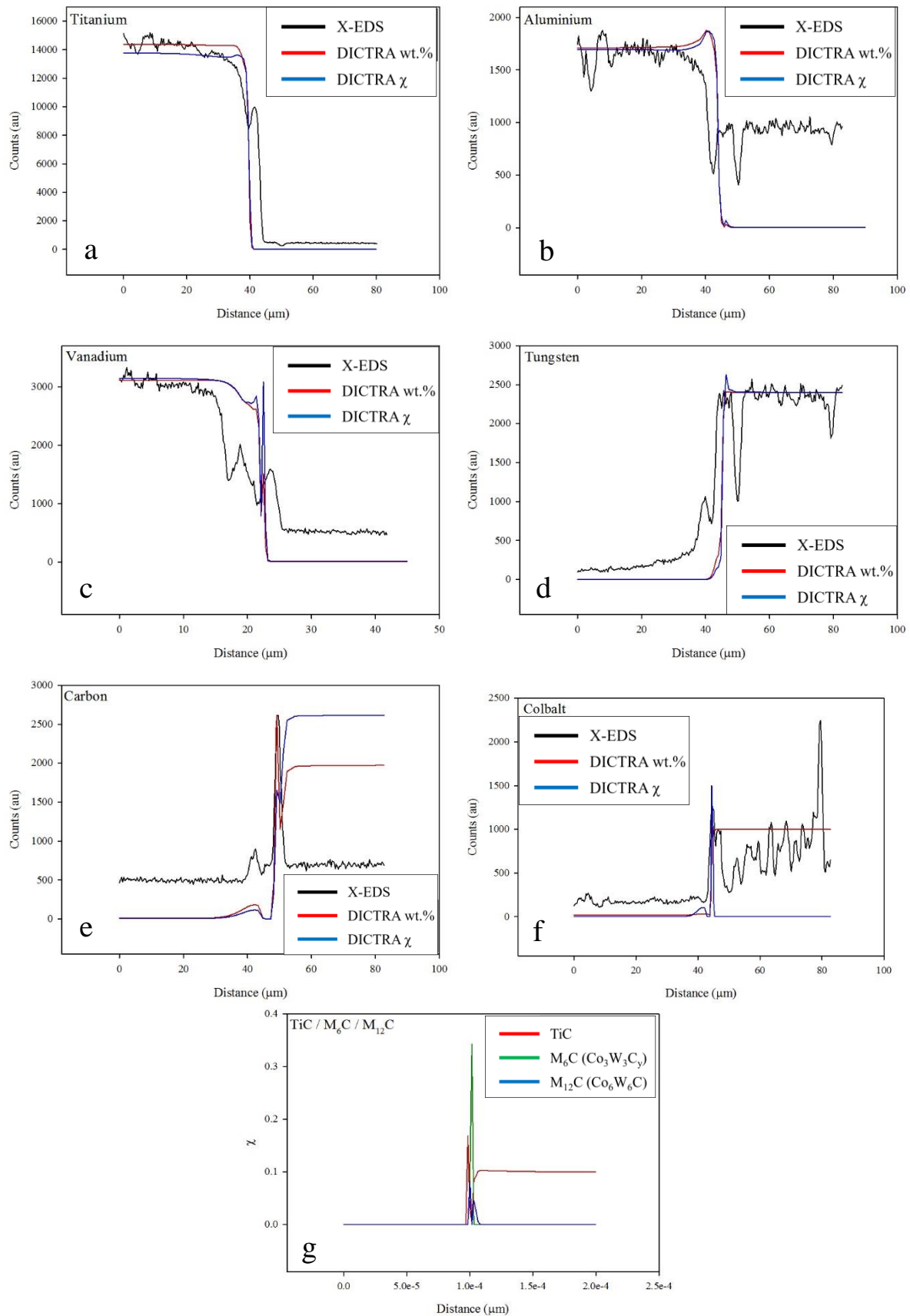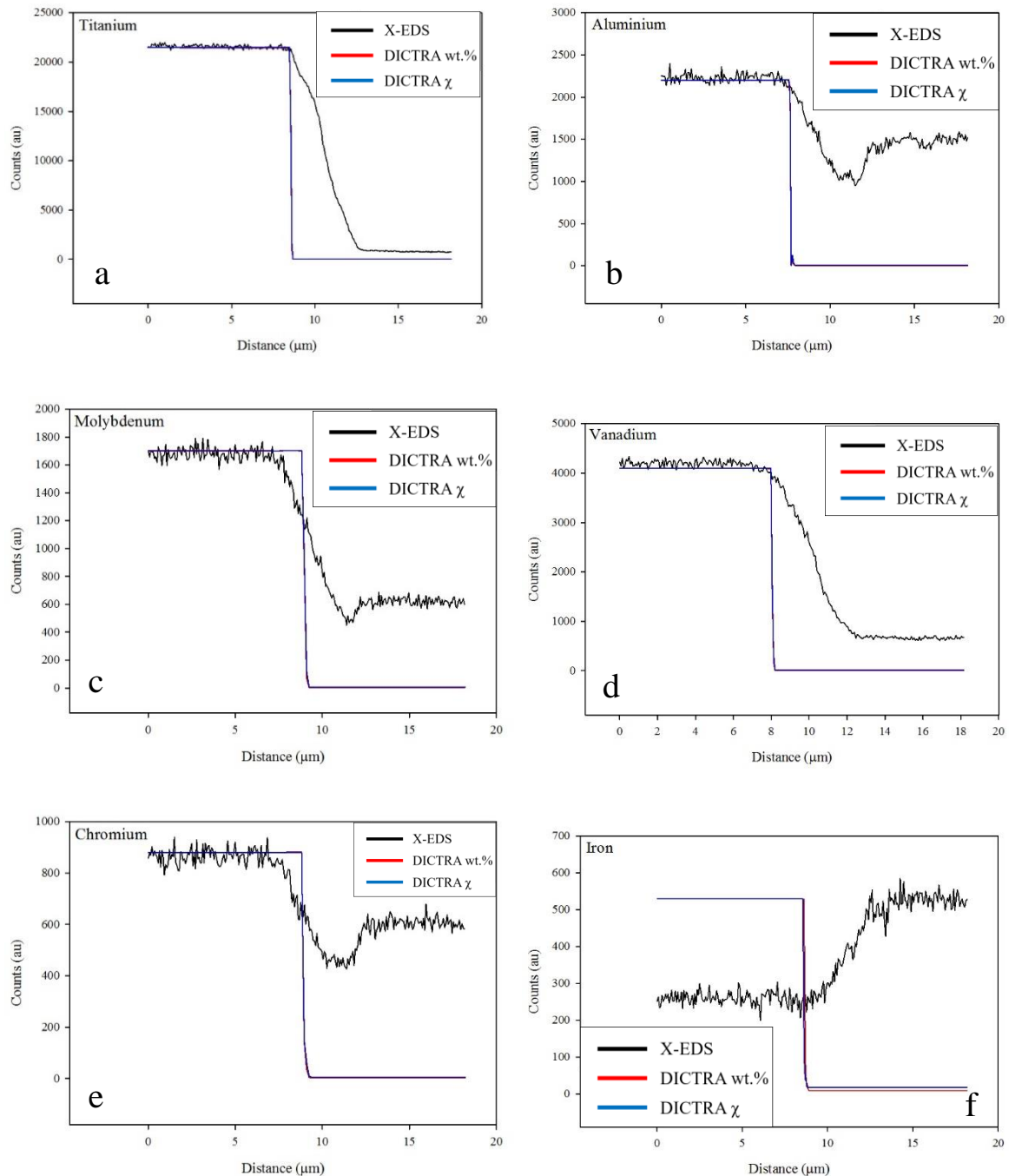

Figure 6.6. DICTRA plots and X-EDS data for the Ti-5553 and WC-6%Co diffusion couple showing (a) titanium, (b) aluminium, (c) molybdenum, (d) vanadium, (e) chromium, and (f) iron.
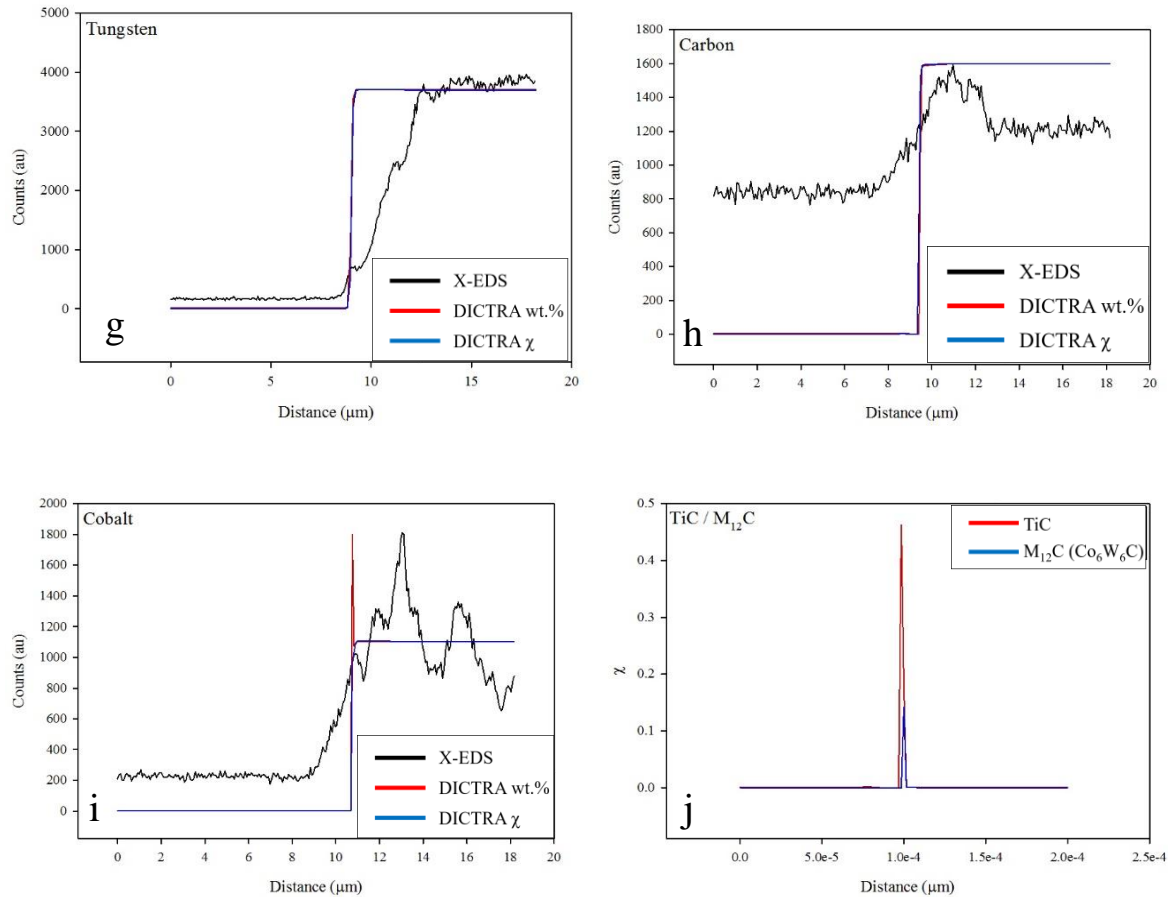
Figure 6.7. DICTRA plots and X-EDS data for the Ti-5553 and WC-6%Co diffusion couple showing (g) tungsten, (h) carbon and (i) cobalt. DICTRA predictions of (j) TiC and $M_{12}C$.

The DICTRA profiles for the diffusion of the workpiece elements: titanium (Figure 6.6a), aluminium (Figure 6.6b), molybdenum (Figure 6.6c), vanadium (Figure 6.6d) and chromium (Figure 6.6e) show some agreement with the X-EDS data. The X-EDS data shows profiles which represent a gradual diffusion of workpiece elements to the tool. The lack of clear, defined diffusion zones in the diffusion couple (Figure 4.4l) is represented by the lack of peaks in these elemental profiles. In the X-EDS data, there is a notable quantity of titanium at the interface which corresponds to the TiC observed experimentally. DICTRA only shows a negligible quantity of titanium at the interface. The DICTRA profile for iron diffusion (Figure 4.4f) is of poor agreement with the X-EDS data. Experimentally, a higher quantity of iron is found in the tool subsurface over the workpiece. DICTRA fails to replicate this pattern.

The DICTRA profiles for the tool elements of tungsten (Figure 6.6g) and carbon (Figure 6.6h) show weak agreement with the X-EDS data similarly to the workpiece elements. However, cobalt is predicted to diffuse from the tool towards the interface which is observed

experimentally. DICTRA represents this by a strong peak at ~10 µm (Figure 6.6i). DICTRA does not show a presence of carbon at the interface which is found in the diffusion couples as TiC.

The DICTRA profiles for the formation of TiC and $M_{12}C$ at the interface between Ti-5553 and the WC-6%Co tool is shown in Figure 6.6j. A quantity of TiC is predicted at the interface as is found in the diffusion couple (Figure 4.4f, Z2). Furthermore, the small quantity of $M_{12}C$ is predicted at the subsurface of the tool which is also observed in the diffusion couple (Figure 4.4f, Z3). DICTRA accurately predicts the location of these phases with respect to the tool and workpiece. However, the M_6C phase observed in the diffusion couple (Figure 4.4f, Z4) was not predicted by DICTRA.

6.4 Conclusions and chapter summary

An investigation was carried out in to creating a model to accurately simulate the diffusion couple experiments discussed in Chapter 4. Using the DICTRA module of Thermo-Calc, the model aimed to predict the diffusion of elements between the workpiece and tool. Furthermore, the model was used to predict the formation of reaction species at the diffusion interface as well as any phase changes.

Overall, the DICTRA model was able to give a good indication of elemental diffusion between the tool and workpiece, however, some simulations were more accurate than others in terms of resolution and information. The simulations for CP-Ti, Ti-54M and Ti-5553 correctly identified the interface region between the tool and workpiece, but only showed a negligible slope in elemental diffusion. They were generally quite weak at reproducing the experimental X-EDS data. Conversely, the simulations for Ti-834, Ti-64 and Ti-6246 followed the X-EDS data much more accurately. The simulation for Ti-64 was especially accurate in modelling the diffusion. Subtleties such as quantities of tungsten, carbon and cobalt present at the subsurface of the titanium alloy substrate were accurately modelled. In Ti-64, the workpiece elements of titanium, aluminium and vanadium also followed the profile of the X-EDS data carefully as they diffused towards the interface. The Ti-6246 model also predicted small quantities of tool constituents at the surface of the titanium alloy substrate which was observed experimentally (Figure 4.4j).

All simulations predicted the diffusion of cobalt from the tool towards the interface and titanium alloy substrate. This was also observed experimentally with the strengthening of the β phase observed in all VCR diffusion couples, identified experimentally as $Ti_2Co+\beta$ (Figures 4.4b, d, f, h, j and l). DICTRA predicted TiC and $M_{12}C$ phases to be present at the interface of all diffusion couples in varying quantities. Both phases were observed experimentally in the diffusion couples. All DICTRA simulations, with the exception of CP-Ti even predicted these phases to be present at the same locations as found in the diffusion couples i.e. TiC at the interface and towards the titanium alloy substrate, and $M_{12}C$ at the subsurface of the tool. It is important to recognise the limitations of DICTRA calculations though. For example, the quantities of TiC observed at the interface did not match those observed experimentally in the VW diffusion couples (Figures 4.4a, c, e, g, i and k). Furthermore, only the Ti-64 model was able to identify the M_6C phase observed experimentally. This is important to identifying tool wear as it is brittle and prone to fracture as observed in Chapter 4 (Figures 4.4d, f, h and l).

Without the guidance of the X-EDS data, some DICTRA elemental profiles such as those for CP-Ti are difficult to extract information from. Furthermore, DICTRA predicts the difference in TiC formation between Ti-54M and Ti-6246 to be only ~ 0.1 of a mole fraction which is quite far from what was observed in the machining trials of Chapter 5.

There are numerous reasons as to why these DICTRA simulations are not wholly accurate. Firstly, in the case of CP-Ti (§6.3.1) the diffusion between the titanium alloy and the WC-6%Co tool ceased completely after an initial precipitation of carbides at the interface after only 1 s. Secondly, in terms of heat treatment of the diffusion couples, these simulations did not replicate any kind of heating or cooling rate. They are at the target temperature from the first moment to the last. The tool and workpiece materials experience a steady heating rate of $16°C.min^{-1}$ in the diffusion couple experiments from room temperature right up to the target temperature of 1000°C. They also experience a cooling rate of approximately $1°C.min^{-1}$. This will have an effect on any phase changes and formation of any reaction species. Thirdly, both the thermodynamic and kinetic databases selected for these simulations were not titanium databases. As shown in Table 6.1, four of the six simulations used steel databases (for reasons discussed in §6.2). What is more, simulations for Ti-6246 and Ti-834 used the less accurate solid solutions thermodynamic database. Simulating elemental diffusion and reaction species formation between two different titanium alloys would allow the use of the thermodynamic and kinetic titanium databases and would perhaps yield more accurate representations of experimental observations. Lastly, DICTRA collects information on thermodynamic properties (Gibbs energy) and kinetic properties (mobility, diffusivity data) of a system from the literature (Figures 3.4 and 3.5). This may be the reason as to why the DICTRA simulations for Ti-64 are much more accurate than those of the other systems. There is much more knowledge and peer-reviewed experimental evidence on this alloy than any other titanium alloy. It is recognised that DICTRA is not a complete simulation tool as it can only handle simple geometries. These geometries are planar, cylindrical and spherical which importantly, can be reduced into one space variable. It is the multicomponent diffusion and thermodynamic data which DICTRA simulations are based upon. The accuracy of which rely on, not only the measured thermodynamic and kinetic data, but also on different assumptions e.g. choice of geometry [168]. During the diffusion couple experiments, one must be aware that there is a change in local surface geometry with time and temperature.

The DICTRA model used for this investigation could be improved in a number of ways. Firstly, by matching the length of heat treatment to that of the diffusion couples (2 h). Secondly, by incorporating a heating and cooling function to better represent the diffusion couples. Thirdly, by increasing the number of data points which DICTRA calculates. These extra points could be concentrated at the interface by using the double geometric grid (Figure 3.8). Of course all of these suggestions would lead to vastly increased computational times which may be unfeasible.

Table 6.2 summarises the degree of adherence between the DICTRA simulations and the reaction layers observed in the diffusion couples in Chapter 4. The table is qualitative as DICTRA cannot accurately calculate the 'thickness' of a reaction layer without using an unfeasible number of data points over a small geometric grid. This would result in simulation times lasting months when using a 4 GHz computational processor.

TABLE 6.2. SUMMARY TABLE OF EXPERIMENTAL REACTION LAYERS OBSERVED AND CORRESPONDING DEGREE OF ADHERENCE WITH DICTRA SIMULATIONS

| | Experimental Diffusion Couples | | | | | | DICTRA | | | | | | | | | | | |
| | Reaction species / phase formation layer thickness | | | | | | Reaction species / phase formation simulated? | | | | | | Agreement with experimental data? | | | | | |
Ti Alloy	TiC thickness (μm)	$Ti_2Co+\beta$ (μm)	TiC+WC +Co (μm)	TiC+WC +β(Ti,W) (μm)	$M_{12}C$ (μm)	M_6C (μm)	TiC conc. (χ)	$Ti_2Co+\beta$ (sim)	TiC+WC +Co (sim)	TiC+WC +β(Ti,W) (sim)	$M_{12}C$ (sim)	M_6C (sim)	TiC conc. (agr)	$Ti_2Co+\beta$ (agr)	TiC+WC +Co (agr)	TiC+WC +β(Ti,W) (agr)	$M_{12}C$ (agr)	M_6C (agr)
CP	28.7	10	12	12	2	6	✓	-	-	-	✓	-	-	-	-	-	-	-
834	8.6	12	3	3	1	5	✓	✓	✓	✓	✓	-	-	-	-	-	-	-
64	5.3	24	8	8	1	10	✓	✓	✓	✓	✓	✓	✓	✓	✓	✓	✓	✓
54M	4.2	18	4	6	1	7	✓	-	-	-	✓	-	-	-	-	-	✓	-
6246	trace	3	-	-	-	3	✓	✓	✓	✓	✓	-	-	✓	✓	✓	-	-
5553	trace	-	-	1	1	9	✓	✓	-	-	✓	-	-	✓	-	-	✓	-

Chapter 7 - Impact case study, conclusions and further work

7.1 Application of the tool-workpiece diffusion couple investigation on the machinability assessment of TIMETAL® 407 and TIMETAL® 575

It has been shown how the tool-workpiece diffusion couples in Chapter 4 can be used as a reliable, low-cost technique to replicate the diffusional tool wear mechanisms observed in titanium alloy machining (Chapter 5). The following case study applies some of the key findings that were made during the course of the EngD study by investigating the machinability of two new aerospace development alloys, TIMETAL® 407 (Ti-0.85Al-3.9V-0.25Si-0.25Fe, Ti-407) and TIMETAL® 575 (Ti-5.3Al-7.7V-0.25Fe-0.5Si-0.01C, Ti-575).

Ti-407 is an $\alpha+\beta$ titanium alloy developed by TIMET's Henderson Technical Laboratory in collaboration with TIMET UK. Importantly, it was developed as a direct replacement for the $\alpha+\beta$ alloys, Ti-64 and Ti-3Al-2.5V in airframe and jet engine components. It shows improved ductility allowing the alloy to exhibit increased machinability properties and low temperature forming capabilities. In terms of tool wear criteria, Ti-407 is expected to allow significantly faster machining than Ti-64 [136]. Ti-575, also developed by TIMET, is a high-strength $\alpha+\beta$ alloy with improved fatigue properties. It has been developed as a potential replacement for Ti-64 and Ti-6246 for applications in extreme environments such as gas turbine discs and blades [169, 170]. As of yet, there is no published literature on the machinability characteristics of Ti-575.

The VW diffusion couples in §4.3 revealed how the quantity of TiC formation at the tool-workpiece interface decreased as the β phase quantity of titanium alloys increased. Figure 7.1 shows a composite image of the VW diffusion couple interfaces for CP-Ti, Ti-834, Ti-64 and Ti-54M.
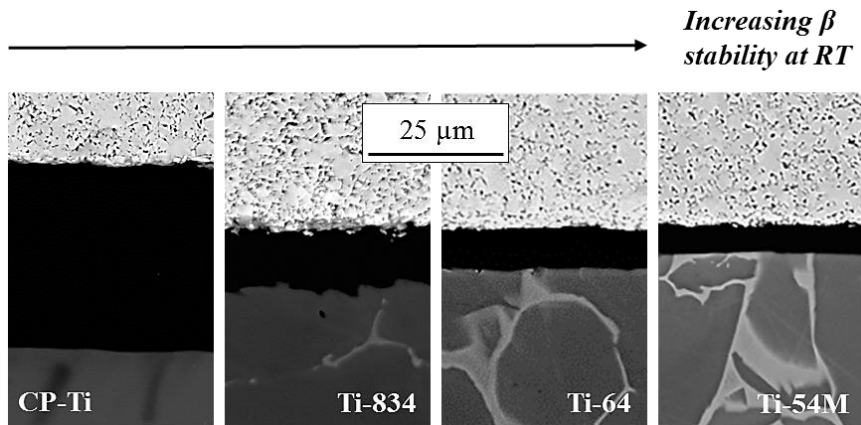
Figure 7.1. Backscattered electron micrographs of the TiC interface between the WC-6%Co tool insert and CP-Ti; Ti-834; Ti-64 and Ti-54M.

It was first highlighted in §1.1 that a shift from near α to α+β to metastable β alloys results in a decrease in machinability. This is due to increases in cutting forces and elevating interfacial temperatures resulting in excessive tool wear and poor surface integrity of the machined workpiece. This shift is also marked by an increase in molybdenum equivalent Mo_{eq} (see §4.3), a measure of the quantity of β stabilising elements in the alloy, given by Equation 7.1 [38].

$$Mo_{eq} = Mo + 0.2Ta + 0.28Nb + 0.4W + 0.67V + \\ 1.25Cr + 1.25Ni + 1.7Mn + 1.7Co + 2.5Fe \qquad \text{Equation 7.1}$$

The diffusion couple tests and turning study of alloys Ti-54M and Ti-6246 allows us to hypothesise that there is a relationship between an increase in Mo_{eq} with a corresponding decrease in TiC reaction layer thickness. This results in more severe tool crater wear during machining and the alloy can therefore be said to be 'less machinable' (see §2.5).

The hypothesis was strengthened further by exposing titanium-aluminium binary alloys to the same VW diffusion couple tests described in §4.2.1. Three binary alloys of Ti-2Al, Ti-4Al and Ti-6Al (supplied by TIMET UK) were selected for the study. The increasing aluminium content decreased the corresponding Mo_{eq} value to less than that of CP-Ti and allowed for the observation of TiC reaction layers in alloys with a higher α phase content.

Both the Ti-2Al and Ti-4Al binary alloys formed a bond with the tool, however Ti-6Al did not (*c.f.* Ti-6246). Figure 7.2 shows the same diffusion interfaces as seen in Figure 7.1 but with the addition of the titanium-aluminium binary alloy diffusion couples. Ti-6Al and Ti-6246 have been omitted from the figure as they were non-bonding.

Increasing α stability at RT ←————————————————→ *Increasing β stability at RT*

Ti-4Al Ti-2Al CP-Ti 25 µm Ti-834 Ti-64 Ti-54M
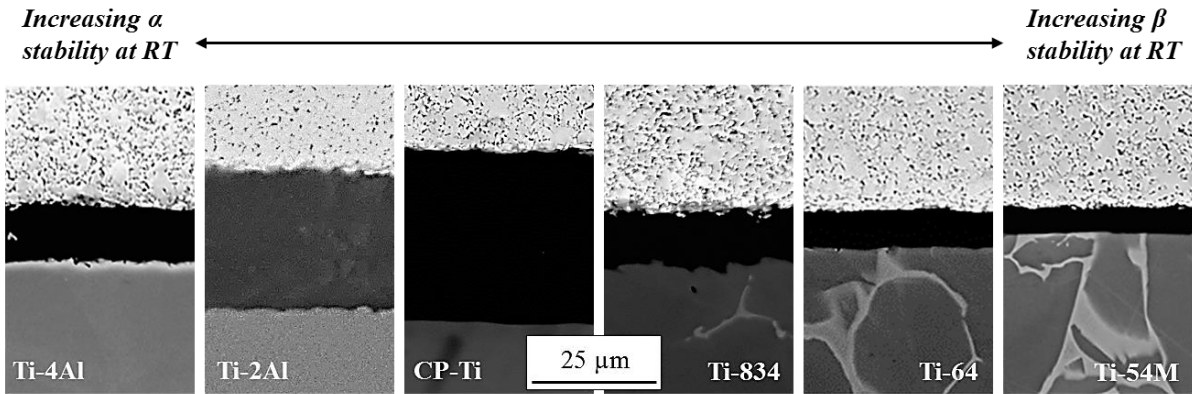
Figure 7.2. Backscattered electron micrographs of the reaction layer interface between the WC-6%Co tool insert and Ti-4Al; Ti-2Al; CP-Ti; Ti-834; Ti-64 and Ti-54M.

As the Mo_{eq} increases relative to CP-Ti, there is a marked decrease in the thickness of the TiC reaction layer. Furthermore, as the aluminium content of the alloy is increased, relative to CP-Ti, there is also a decrease in thickness of the TiC reaction layer. If the relationship between the Mo_{eq} value and the thickness of the TiC reaction layer is correct then Ti-407 (Mo_{eq} = 3.24) is predicted to have a TiC interface thickness between Ti-834 (Mo_{eq} = 0.63) and Ti-64 (Mo_{eq} = 3.68). Additionally, Ti-575 (Mo_{eq} = 5.78) is predicted to have a TiC thickness between that of Ti-54M (Mo_{eq} = 4.73) and Ti-6246 (Mo_{eq} = 6.38). Table 7.1 shows the nominal chemical compositions of the alloys used in Chapter 4 alongside Ti-407, Ti-575 and the titanium-aluminium binary alloys. They are listed with their respective Mo_{eq} values.

TABLE 7.1. NOMINAL CHEMICAL COMPOSITION OF THE TITANIUM ALLOYS USED IN THE DIFFUSION COUPLE STUDY ALONGSIDE THEIR RESPECTIVE MOLYBDENUM EQUIVALENT VALUES.

Alloy	Nominal elemental composition (wt.%)									Mo_{eq}
	Mo	V	Fe	Cr	Al	Sn	Zr	Si	C	
Ti-6Al	0	0	0.20	0	6.00	0	0	0	0.08	0.50
Ti-4Al	0	0	0.20	0	4.00	0	0	0	0.08	0.50
Ti-2Al	0	0	0.20	0	2.00	0	0	0	0.08	0.50
CP-Ti	0	0	0.30	0	0	0	0	0	0.08	0.75
Ti-834	0.50	0	0.05	0	5.8	4.00	3.50	0.35	0.06	0.63
Ti-407	0	3.90	0.25	0	0.85	0	0	0	0	3.24
Ti-64	0	4.00	0.40	0	6.00	0	0	0	0.08	3.68
Ti-54M	0.80	4.00	0.50	0	5.00	0	0	0	0	4.73
Ti-575	0	7.70	0.25	0	5.30	0	0	0.50	0.01	5.78
Ti-6246	6.00	0	0.15	0	6.00	2.00	4.00	0	0	6.38
Ti-5553	5.00	5.00	0.60	3.00	5.00	0	0	0	0	13.60

To examine the TiC reaction layer thickness between the WC-6%Co tool and titanium alloys Ti-407 and Ti-575, diffusion couple tests were conducted as described in §4.2.1. Figure 7.3 shows micrographs of the interface layer of the diffusion couples of Ti-407 and Ti-575.
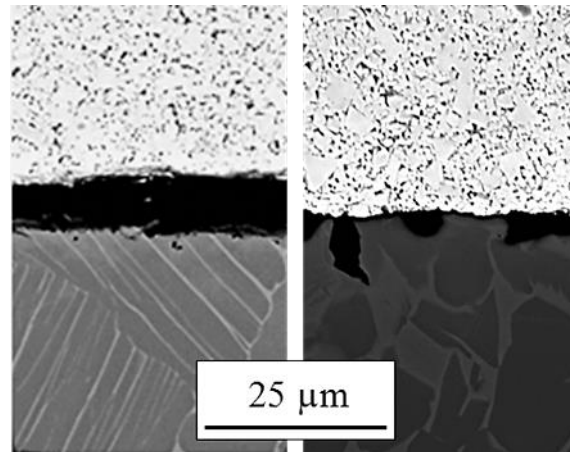
Figure 7.3. Backscattered electron micrographs of the reaction layer interface between the WC-6%Co tool insert and Ti-407 and Ti-575.

Ti-407 and Ti-575 show a TiC interface thickness of 6.3 and 2.1 μm respectively. Figure 7.4 plots the values of the interfacial TiC thickness layer for all 10 alloys tested.
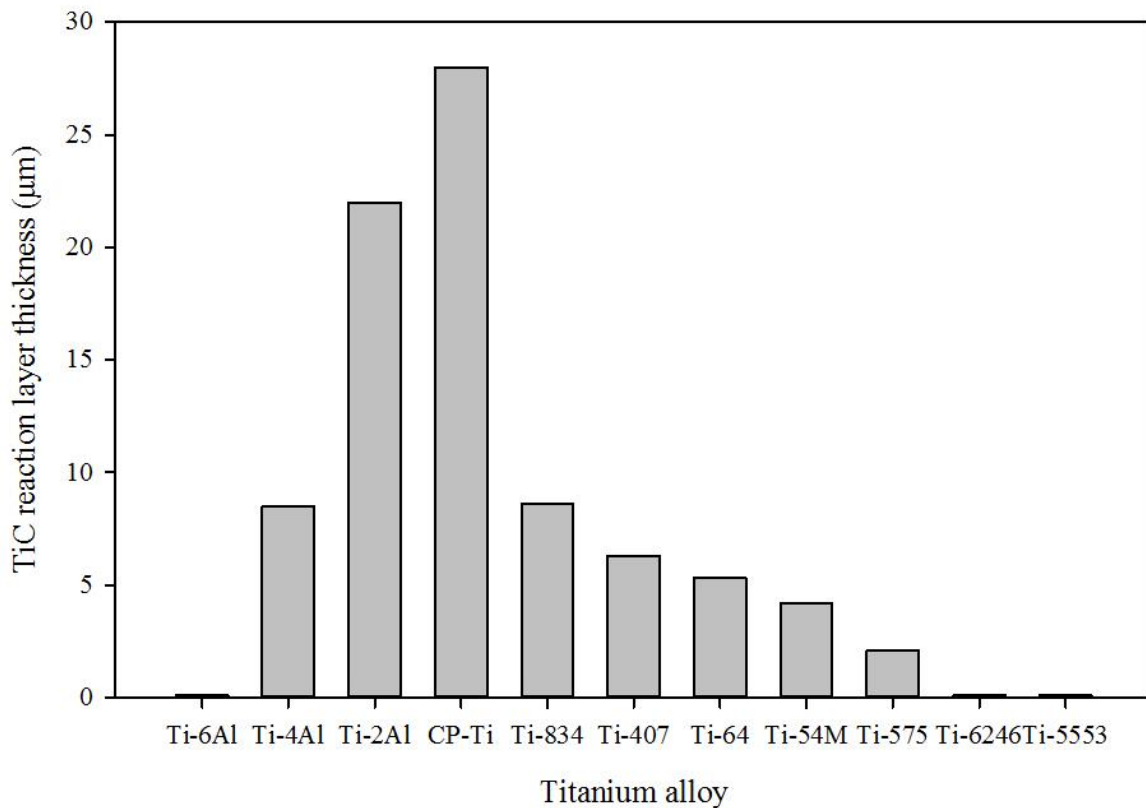
Figure 7.4. A plot of TiC reaction layer thickness for the diffusion couples of the WC-6%Co tool insert and Ti-6Al, Ti-4Al, Ti-2Al, CP-Ti, Ti-834, Ti-407, Ti-64, Ti-54M, Ti-6246 and Ti-5553.

148

Ti-407 and Ti-575 fit the hypothesis relating TiC formation to the Mo_{eq} value of the alloy. Ti-407 falls between Ti-834 and Ti-64; and Ti-575 falls between Ti-54M and Ti-6246. Figure 7.5 shows a composite image of the reaction layer interfaces for Ti-4Al, Ti-2Al, CP-Ti, Ti-834, Ti-407, Ti-64, Ti-54M and Ti-575.
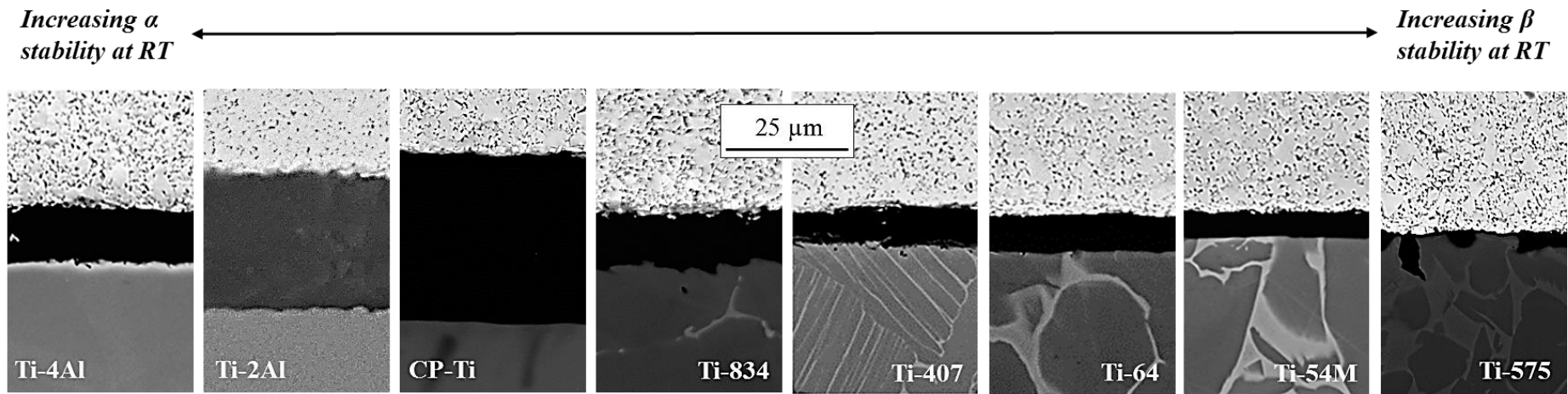
Figure 7.5. Backscattered electron micrographs of the reaction layer interface between the WC-6%Co tool insert and Ti-4Al; Ti-2Al; CP-Ti; Ti-834; Ti-407; Ti-64; Ti-54M and Ti-575.

Looking at Figure 7.5, a clear pattern emerges for TiC formation at the interface between the WC-6%Co tool insert and titanium alloy substrate. Starting with CP-Ti and moving right to Ti-834, Ti-407, Ti-64, Ti-54M and Ti-575 there is decrease in TiC reaction layer thickness. This corresponds to an increase in β phase quantity for the alloy, and also an increase in the alloy's molybdenum equivalent value. Increasing the β phase quantity and Mo_{eq} value further e.g. Ti-6246, results in a very small quantity of TiC being formed at the interface. The high molybdenum content of Ti-6246 causes the alloy to preserve a protective oxide layer, significantly reducing the TiC reaction layer growth rate. This contributed to the alloy not bonding with the tool insert during the diffusion couple investigation. Starting with CP-Ti and moving left through the binary alloys of Ti-2Al and Ti-4Al there is also a decrease in TiC reaction layer thickness. This corresponds with an increase in aluminium content and therefore α phase. Increasing the aluminium content and α phase quantity further, e.g. Ti-6Al, results in a very small quantity of TiC being formed at the interface. This resulted in Ti-6Al not bonding with the tool insert during the diffusion couple investigation.

Rosenberg [171] attempted to express the effect of α stabilising elements in multicomponent titanium alloys as an equivalent aluminium content (Al_{eq}, Equation 7.2).

$$Al_{eq} = Al + 0.17Zr + 0.33Sn + 0.4W + 10\,O \qquad\qquad \text{Equation 7.2}$$

The calculated Al_{eq} values for the alloys used in this investigation are listed in Table 7.2.

TABLE 7.2. NOMINAL CHEMICAL COMPOSITION OF THE TITANIUM ALLOYS USED IN THE DIFFUSION COUPLE STUDY ALONGSIDE THEIR RESPECTIVE ALUMINIUM EQUIVALENT VALUES.

Alloy	Nominal elemental composition (wt.%)										Al_{eq}
	Mo	V	Fe	Cr	Al	Sn	Zr	Si	C	O	
Ti-6Al	0	0	0.20	0	6.00	0	0	0	0.08	0.10	7.00
Ti-4Al	0	0	0.20	0	4.00	0	0	0	0.08	0.10	5.00
Ti-2Al	0	0	0.20	0	2.00	0	0	0	0.08	0.10	3.00
CP-Ti	0	0	0.30	0	0	0	0	0	0.08	0.25	2.50
Ti-834	0.50	0	0.05	0	5.80	4.00	3.50	0.35	0.06	0.15	9.22
Ti-407	0	3.90	0.25	0	0.85	0	0	0	0	0.15	2.35
Ti-64	0	4.00	0.40	0	6.00	0	0	0	0.08	0.20	8.00
Ti-54M	0.80	4.00	0.50	0	5.00	0	0	0	0	0.20	7.00
Ti-575	0	7.70	0.25	0	5.30	0	0	0.50	0.01	0.18	7.10
Ti-6246	6.00	0	0.15	0	6.00	2.00	4.00	0	0	0.15	8.84
Ti-5553	5.00	5.00	0.60	3.00	5.00	0	0	0	0	0.10	6.00

Looking to the left of CP-Ti in Figure 7.5, the behaviour observed for the Ti-Al binaries follows an Al_{eq} pattern similar to the Mo_{eq} pattern observed to the right of CP-Ti. As the Al_{eq} value increases, the quantity of interfacial TiC formation decreases. This is only true for the Ti-Al binary alloys however. Table 7.2 illustrates how the Al_{eq} values do not follow a specific pattern for the alloys listed after CP-Ti. The Al_{eq} values rise and fall from CP-Ti through Ti-5553.

Care must be taken when comparing the binary Ti-Al alloys (going left from CP-Ti, Figure 7.5) with the titanium alloys of increasing β phase content (going right from CP-Ti, Figure 7.5). The binary alloys offer a good insight into how the Al content affects the thickness of the TiC reaction layer in diffusion couple experiments. However, they behave differently to more complex titanium alloys e.g. Ti-834 because here, there are seven alloy additions and therefore more possible permutations and combinations of interactions between these elements. This makes it difficult to understand titanium alloying behaviour solely on the basis of binary Ti-X systems and values such as Mo_{eq} and Al_{eq}. For example, alloying elements such as Zr and Sn are generally considered as α stabilising elements. This arises from Zr having a chemical similarity to titanium and Sn can replace aluminium in the hexagonal Ti_3Al phase [38]. When tin is present together with aluminium, it behaves as an α stabiliser.

The VW diffusion couples seen in §4.3 produced a pattern whereby an increase in β phase quantity corresponded with a decrease in the TiC reaction layer thickness. This trend of TiC reaction layer thickness is illustrated via the bar chart in Figure 7.4 and has allowed for this case study where the TiC reaction layer thickness for untested titanium alloys has been predicted. This is important as it has been shown that TiC formation at the tool-workpiece interface is directly related to the rate of tool crater wear during machining (Figure 5.16). Therefore, it can be said that this novel low cost diffusion couple method allows for a rapid, simple and inexpensive way of assessing a titanium alloy's machinability (in terms of tool crater wear) early on in the alloy design and development process. The method can also be used to assess different tool-workpiece material combinations in terms of chemical affinity and its relation to tool crater wear during machining processes.

This investigation predicts that Ti-407 will exhibit greater machinability properties in terms of tool crater wear than Ti-64. More TiC is formed at the interface in the diffusion couples and it is therefore expected that more TiC is formed on the rake face of the tool insert during

machining. This results in longer tool life during machining processes (§5.4). Machinability V15 tests (speed of cutting tool worn out within 15 min) have been carried out on Ti-407 [136]. It was found that Ti-407 showed a machinability V15 turning factor of 153 m.min^{-1}. This was in fact double the tool life of the baseline Ti-64 test which exhibited a V15 turning factor of 72 m/min^{-1}. The impact of being able to predict machinability characteristics of titanium alloys early on in the design process is huge. To be able to have an understanding of how a material might behave during machining before actual machining trials take place has the potential to result in large cost savings. From calculations outlined in a TIMET sponsored PhD thesis [172], the approximate cost of a conventional machining trial equated to £21,600 considering typical market values for Ti-64. In comparison, the costings for the VW and VCR diffusion couple tests are presented in Table 7.3.

Table 7.3. APPROXIMATE COSTINGS OF THE VW AND VCR DIFFUSION COUPLE TESTS.

Equipment and materials	Approximate cost	
	VW method	VCR method
Tool insert	£2	£2
Titanium coupon	£40/kg = 32p	£40/kg = 32p
Vacuum furnace time	£30	£120
Total	£32.32	£122.32

The above costs pale in comparison with the expense of traditional machining trials. Incorporating such testing into the alloy design process could result in a better understanding of tool-workpiece material couplings for increased efficiency in titanium alloy machining.

7.2 Conclusions

Incorporating both chemistry and materials science disciplines, this work has investigated tool wear in titanium alloy machining via methods with an emphasis on low cost and simplicity. The following subsection outlines the key findings made during this EngD research project, the most fundamental of which was predicting tool crater wear via a novel low cost diffusion couple method.

The low cost diffusion couple method can provide a strong indication of the complex reaction mechanisms occurring at the tool-chip interface during high speed machining of titanium alloys. The novel approach has demonstrated that tool inserts used to machine the heavily stabilised β alloy Ti-6246 are more susceptible to crater wear than when machining Ti-54M due to the formation of a protective TiC coating at the interface of the Ti-54M. However, Ti-6246 is more resilient to subsurface damage than Ti-54M, even when the tool insert is damaged through crater wear. From a workpiece standpoint, such a testing regime will be incorporated into alloy design programmes to inform the industry about the "machinability" qualities at a much earlier stage before expensive machining trials. Such a method will also aid tool manufacturers to tailor tool carbide grades as well as new coatings to specific alloy chemistries. This combinatorial approach will increase the efficiency of titanium alloy machining and help meet the future aircraft build production targets.

The work first discussed the metallurgical background of titanium which included: applications; alloy classification; thermomechanical processing; diffusion; corrosion; and oxidation. What followed was a discussion of the mechanics of machining and the principles of tool wear. The use of modern tool materials in machining was considered in conjunction with the importance of alloy chemistry. Carefully examining the available literature, it soon became apparent that a large gap in knowledge was appearing with respect to tool wear and titanium alloy machining as researchers tended to focus on mechanical engineering aspects of machining over those of chemistry and materials science. The gap concerned the understanding of the effect of chemistry and microstructure condition on the mechanisms of subsurface damage and tool wear behaviour in titanium alloy machining. This is particularly apparent in that tool manufacturers offer the same tool irrespective of which alloy is to be machined. This is despite the fact that the literature has shown how phase morphology of

titanium alloys significantly affects their machinability. Consequently, this study has investigated tool wear via diffusion mechanisms in the machining of titanium alloys.

The first interesting result was that when subject to both the VW and VCR diffusion couple methods, the alloy Ti-6246 did not bond with the WC-6%Co tool. Those alloys which did bond with the tool saw notable amounts of TiC formation at the tool-workpiece interface. The high molybdenum content of Ti-6246 was found to significantly reduce the growth rates of TiC. This observation was supported by key literature outlining how molybdenum helps preserve a protective oxide layer (§4.3). The results of the OD turning trials of Ti-54M and Ti-6246 show strong agreement with the diffusion couple experiments. For Ti-54M where diffusion bonding is observed, a high quantity of TiC formation occurs on the rake face of the tool insert. For Ti-6246 where diffusion bonding did not occur, only a negligible amount of TiC is observed on the rake face of the tool insert. This corresponds to the more severe tool wear observed for machining Ti-6246 compared with Ti-54M. The agreement between the diffusion couple tests and turning trials put confidence in using the diffusion couple tests to predict the machinability of new aerospace development alloys. The $\alpha+\beta$ alloy Ti-407 was predicted to be more machinable than Ti-64. This was later confirmed by a 2016 paper [136]. Furthermore, Ti-575 was predicted to be more machinable than Ti-6246.

In addition to the molybdenum content of Ti-6246 preventing a diffusion bond being formed with the tool insert, a trend involving Mo_{eq} vales was observed. As the Mo_{eq} of the alloy increases, the quantity of interfacial TiC formation decreases. This trend was also echoed with the Ti-Al binaries. As the quantity of Al increased, the amount of TiC formation decreased.

In a continued drive towards low cost solutions for tool wear prediction, aspects of this work were also underpinned by thermodynamic modelling. The DICTRA module of Thermo-Calc software allowed for the creation of a model to simulate the diffusion couple tests including elemental diffusion, phase changes and interfacial reaction species formation. Modelling such complex systems is still in its infancy, but some success was achieved, particularly in matching the X-EDS profile for the Ti-64 system. DICTRA was able to predict the diffusion of cobalt from the tool towards the interface and titanium alloy substrate. This was also observed experimentally with the strengthening of the β phase observed in all VCR diffusion couples, identified experimentally as $Ti_2Co+\beta$. DICTRA also predicted TiC and $M_{12}C$ phases

to be present at the interface of all diffusion couples in varying quantities. Both phases were observed experimentally in the diffusion couples. All DICTRA simulations, with the exception of CP-Ti even predicted these phases to be present at the same locations as found in the diffusion couples i.e. TiC at the interface and towards the titanium alloy substrate, and $M_{12}C$ at the subsurface of the tool.

7.3 Further work

It is apparent from this investigation that more work needs to be done in order to optimise tool materials for the machining of specific titanium alloys. Low cost methods such as those outlined in this thesis offer a reliable alternative to costly machining trials. The following subsection outlines important areas of research that have been generated as topics of further work from the EngD programme.

- Currently no machinability data exists in the literature for Ti-575. Therefore, the author suggests that OD turning trials of this alloy are conducted in order to confirm the accuracy of the Ti-575 diffusion couple. This proposed investigation will require the same machining parameters to be followed as outlined in §5.2.2. The rake face of the tool should be analysed for TiC formation, as well as the machined chip and workpiece. Alicona scans of the rake face of the tool will indicate the extent to which the tool has worn via a diffusion crater wear mechanism.

- All titanium alloys throughout this study were supplied in the as forged condition. Therefore, the author recommends an investigation into the effect of the condition of the titanium alloy with regards to its machinability from a tool wear standpoint. Ti-64 for example, could be subject to diffusion couple tests in four different as-supplied conditions: mill annealed, STA, β annealed and as forged. Observations of the tool-workpiece diffusion couple interface can then be verified with OD turning trials.

- There is a general consensus in the literature [93, 113, 114, 116] that tool coatings generally do not benefit tool life or workpiece surface integrity in titanium alloy machining. However, some machinability improvements have been found [117, 118]. Thus, the author proposes an investigation into various coated tools on their susceptibility to tool crater wear during titanium alloy machining. This would be via the diffusion couple study and subsequent validation with OD turning trials as discussed in this thesis. The author recommends coatings such as TiAlN (recommended for heat resistant and super alloys [97]), TiSiCN (recent evidence of improved machinability for titanium alloys [173]) and TiN (recommended for hardened materials [97]) with Ti-64 as a starting point. Currently, DICTRA is unable to accurately predict diffusion systems involving tool coatings. The problem is to get reasonable diffusion coefficients for the coatings e.g. TiN. These have not yet been assessed. The TiN would normally correspond to the FCC#2 phase. The mobilities

that have been assessed for the FCC phase should only be used for reasonably low carbon/nitrogen contents i.e. not for nitrides and carbonitrides. However, one can enter one's own estimates of the mobilities in the TiN coating. This would be a very difficult simulation.

- In this work, the formation of $Ti_2Co+\beta$ was hypothesised to experience a rapidly accelerating diffusion rate acting as a driving force for further diffusion, phase changes, and reaction species formation. The formation of $Ti_2Co+\beta$ was found to be due to the diffusion of cobalt binder from the tool insert into the titanium alloy substrate. In order for a deeper understanding of this hypothesis, the author suggests a diffusion couple investigation involving binderless tungsten carbide i.e. WC without any cobalt content. This will allow for chemical analysis of the tool-workpiece interface which will offer an insight into how the WC behaves without the cobalt binder. It will perhaps change which phases are observed at the interface and subsurface of the titanium alloy substrate.

- Following the observation of TiC formation at the time and temperature in this work, the author recommends an investigation into the time and temperature dependence on the TiC reaction layer between titanium alloys and tungsten carbide tools. This would allow for the observation of critical times and temperatures for which enough TiC forms for a diffusion bond to be successful. The effect of alloying elements on the critical times and temperatures could also be studied.

- This work used Ti-Al binaries to demonstrate how an increase in aluminium content resulted in a decrease in TiC formation. The author recommends further study of different Ti-X binary alloy systems in order to analyse individual elemental effects. It has been previously discussed in this chapter that one must consider how Ti-X binary alloys will behave differently to more complex titanium alloys (see §7.1, p.152). Titanium alloy binary systems containing molybdenum and chromium would offer an interesting place to start due to the behaviour of Ti-6246 and Ti-5553 observed in this work. The author recommends binary alloys of Ti-5Mo, Ti-10Mo and Ti-15Mo; as well as Ti-5Cr, Ti-10Cr and Ti-15Cr.

- This work saw some interesting TEM observations of the crater worn rake face of the tool inserts (§5.3.1). The author suggests further high resolution electron microscopy into the interface of diffusion couple tests. Sample foil lift outs could be achieved in various diffusion zones outlined in §4.3. X-EDS could also be performed on such

samples allowing for accurate chemical analysis. Electron energy loss spectroscopy (EELS) could also be performed in tandem with high resolution TEM study of the crater region of the cutting tool. This would provide further evidence of diffusion of chemical species in the cutting tool.

- There have been recent developments into NbN coatings for titanium alloy machining such as SECO's MS2050 grade [174]. It is advertised as offering increased tool life and resistance to BUE formation which allows for higher cutting speeds. The author suggests using such tools in diffusion couples and subsequent machining trials for validation as outlined in this work.

- Since different titanium alloys would yield different cutting temperatures when machining, the author proposes a temperature study where different titanium alloys should be machined at a predetermined cutting speed. The temperatures recorded at the tool-chip interface should then be replicated in diffusion couple experiments and the subsequent reaction layers compared to the machining trials.

- It was mentioned that one of the problems with the DICTRA model in this work is that no heating or cooling function was implemented into the simulation (§6.4). This could potentially affect the accuracy of such thermodynamic predications. Further work needs to be done on improving the model presented here by allowing for a heating/cooling function. This should be possible using the homogenisation function however, difficulties will arise when two of the same phase are stable different temperatures. At low temperatures where diffusion is very slow, the composition of the equilibrium phases can be very different than at higher temperatures. For example, if there is a stable BCC phase at 1000°C, and a second stable BCC phase below 450°C (e.g. V-Cr phase), upon cooling, the first BCC phase will also change its composition and will continue to do so as the temperature falls even lower. The two BCC phases may give rise to numerical problems in the DICTA simulation, and also strange diffusivity values.

References

[1]   Roskill. "Titanium: Market Outlook to 2018." 2013. [Online]. Available: http://www.roskill.com/product/titanium-metal-market-outlook-2013. [Accessed: 21-Apr-2016].

[2]   Airbus. "Global Market Forecast 2015-2032." [Online]. Available: http://www.airbus.com/company/market/forecast. [Accessed: 21-Apr-2016].

[3]   Innovate UK. "High Value Manufacturing." 2014. Available: https://www.innovateuk.org/documents/1524978/2139688/High+Value+Manufacturing+Strategy+2012-15/9b7e55f0-ed9a-4efe-89e5-59d13b2e47f7. [Accessed: 21-Apr-2016].

[4]   F. H. Froes, Titanium - Physical Metallurgy, Processing and Applications. ASM International, 2015, p. 5.

[5]   M. Jackson and R. R. Boyer, "Titanium and its Alloys: Processing, Fabrication and Mechanical Properties, Encyclopedia of Aerospace Engineering," ed. Chichester: Wiley, 2010, pp. 2117-2132.

[6]   A. K. Nandy, M. C. Gowrishankar, and S. Paul, "Some studies on high-pressure cooling in turning of Ti-6Al-4V," Int. J. Mach. Tool. Manuf., vol. 49, no. 2, pp. 182-198, 2009.

[7]   C. J. Pretorius, S. L. Soo, D. K. Aspinwall, P. M. Harden, R. M'Saoubi, and A. L. Mantle, "Tool wear behaviour and workpiece surface integrity when turning Ti-6Al-2Sn-4Zr-6Mo with polycrystalline diamond tooling," in CIRP Annals-Manuf. Technol., vol. 64, no. 1, pp. 109-112, 2015.

[8]   C. R. Dandekar, Y. C. Shin, and J. Barnes, "Machinability improvement of titanium alloy (Ti-6Al-4V) via LAM and hybrid machining," Int. J. Mach. Tool. Manuf., vol. 50, no. 2, pp. 174-182, 2010.

[9]   M. Dhananchezian and M. P. Kumar, "Cryogenic turning of the Ti-6Al-4V alloy with modified cutting tool inserts," Cryogenics, vol. 51, no. 1, pp. 34-40, 2011.

[10]   G. Rotella, O. W. Dillon, Jr., D. Umbrello, L. Settineri, and I. S. Jawahir, "The effects of cooling conditions on surface integrity in machining of Ti6Al4V alloy," Int. J. Adv. Manuf. Technol., vol. 71, no. 1-4, pp. 47-55, 2014.

[11]   F. Nabhani, "Wear mechanisms of ultra-hard cutting tools materials," J. Mater. Process. Technol., vol. 115, no. 3, pp. 402-412, 2001.

[12]   K.-D. Bouzakis, N. Michailidis, G. Skordaris, E. Bouzakis, D. Biermann, and R. M'Saoubi, "Cutting with coated tools: Coating technologies, characterization methods and performance optimization," in CIRP Annals-Manuf. Technol., vol. 61, no. 2, pp. 703-723, 2012.

[13]   R. M'Saoubi, D. Axinte, S. L. Soo, C. Nobel, H. Attia, G. Kappmeyer, S. Engin and W. Sim., "High performance cutting of advanced aerospace alloys and composite materials," in CIRP Annals-Manuf. Technol., vol. 64, no. 2, pp. 557-580, 2015.

[14]   Kennametal Inc., "High-Temperature Alloy Turning Guide", Metal Working Solutions and Service Group, Latrobe, USA. A03-65DIST/16/H3. 2003.

[15]   C. H. C. Haron, A. Ginting, and H. Arshad, "Performance of alloyed uncoated and CVD-coated carbide tools in dry milling of titanium alloy Ti-6242S," J. Mater. Process. Technol., vol. 185, no. 1-3, pp. 77-82, 2007.

[16]   A. Ginting and M. Nouari, "Surface integrity of dry machined titanium alloys," Int. J. Mach. Tool. Manuf., vol. 49, no. 3-4, pp. 325-332, 2009.

[17]   J. Hou, W. Zhou, H. Duan, G. Yang, H. Xu, and N. Zhao, "Influence of cutting speed on cutting force, flank temperature, and tool wear in end milling of Ti-6Al-4V alloy," Int. J.Adv. Manuf. Technol., vol. 70, no. 9-12, pp. 1835-1845, 2014.

[18]   M. Mori, M. Fujishima, and O. Yohei, "5 axis mill turn and hybrid machining for advanced application," Fifth CIRP Conf. on High Performance Cutting, vol. 1, pp. 22-27, 2012.

[19]   J. Sheikh-Ahmad and J. A. Bailey, "Flow Instability in the Orthogonal Machining of CP Titanium," J. Manuf. Sci. Eng., vol. 119, pp. 307-313 1997.

[20]   P. Crawforth, B. Wynne, S. Turner, and M. Jackson, "Subsurface deformation during precision turning of a near-alpha titanium alloy," Scripta Mater., vol. 67, no. 10, 2012.

[21]   M. Armendia, P. Osborne, A. Garay, J. Belloso, S. Turner, and P. J. Arrazola, "Influence of Heat Treatment on the Machinability of Titanium Alloys," Mater. Manuf. Process., vol. 27, no. 4, pp. 457-461, 2012.

[22]   V. Wagner, M. Baili, and G. Dessein, "The relationship between the cutting speed, tool wear, and chip formation during Ti-5553 dry cutting," Int. J. Adv. Manuf. Technol., vol. 76, no. 5-8, pp. 893-912, 2015.

[23]   E. O. Ezugwu and Z. M. Wang, "Titanium alloys and their machinability - A review," J. Mater. Process. Tech., vol. 68, no. 3, pp. 262-274, 1997.

[24]   E. Trent and P. Wright, Metal Cutting, Butterworth–Heinemann, 2000.

[25]   B. M. Kramer and N. P. Suh, "Tool wear by solution - a quantitative understanding," J. Eng. Ind-T. ASME, vol. 102, no. 4, pp. 303-309, 1980.

[26]   P. D. Hartung and B. M. Kramer, "Tool wear in titanium machining," in CIRP Annals – Manuf. Technol., vol. 31, no. 1, pp. 75-80, 1982.

[27]   M. Wang and Y. Z. Zhang, "Diffusion wear in milling titanium-alloys," Mater. Sci. Technol., vol. 4, no. 6, pp. 548-553, 1988.

[28]   S. Joshi, P. Pawar, A. Tewari, and S. S. Joshi, "Tool wear mechanisms in machining of three titanium alloys with increasing beta-phase fraction," Proc. IMechE, Part B: J. Eng. Manuf. vol. 228, no. 9, pp. 1090-1103, 2014.

[29]   S. J. Sun, M. Brandt, and J. P. T. Mo, "Evolution of tool wear and its effect on cutting forces during dry machining of Ti-6Al-4V alloy," Proc. IMechE Part B: J. Eng. Manuf. vol. 228, no. 2, pp. 191-202, 2014.

[30]   J. Hua and R. Shivpuri, "A cobalt diffusion based model for predicting crater wear of carbide tools in machining titanium alloys," ASME J. Eng. Mater. Technol. vol. 127, no. 1, pp. 136-144, 2005.

[31]   N. Corduan, T. Himbart, G. Poulachon, M. Dessoly, M. Lambertin, J. Vigneau, B. Payoux, "Wear mechanismes of new tool materials for Ti-6Al-4V high performance machining," CIRP Annals – Manuf. Technol. vol. 52, no. 1, pp. 73-76, 2003.

[32]   D. G. Bhat, V. A. Bedekar, and S. A. Batzer, "A preliminary study of chemical solubility of ultra-hard ceramic AlMgB$_{14}$ in titanium: Reconciliation of model with experiment," Mach. Sci. Technol., vol. 8, no. 3, pp. 341-355, 2004.

[33]   D. Jianxin, L. Yousheng, and S. Wenlong, "Diffusion wear in dry cutting of Ti-6Al-4V with WC/Co carbide tools," Wear, vol. 265, pp. 1776-1783, 2008.

[34]   S. Zhang, J. F. Li, J. X. Deng, and Y. S. Li, "Investigation on diffusion wear during high-speed machining Ti-6Al-4V alloy with straight tungsten carbide tools," Int. J. Adv. Manuf. Technol., vol. 44, no. 1-2, pp. 17-25, 2009.

[35]   M. J. Donachie, Titanium: A Technical Guide, ASM International, 1998, p. 1.

[36]   R. R. Boyer, Thermec 2003, International Conference on Processing and Manufacturing of Advanced Materials, Trans Tech, Zurich, 2003.

[37]   R. R. Boyer, "Attributes, Characteristics, and Applications of Titanium and Its Alloys," Jom, vol. 62, no. 5, pp. 21-24, 2010.

[38]   G. Lütjering and J. Williams, Titanium, 2nd ed. Springer, 2007.

[39]   C. Leyens and M. Peters, Titanium and Titanium Alloys. Wiley-VCH, 2003, p. 532.

[40]   H. M. Flower, "Microstructural development in relation to hot working of titanium alloys," Mat. Sci. and Tech., vol. 6, pp. 1082-1093, 1990.

[41]   R. W. Schutz and D. E. Thomas, "Corrosion of titanium and titanium alloys," ASM Handbook, vol. 13, pp. 669-706, 1987.

[42]   K. Sakurai, Y. Itabashi, and A. Komatsu, "Titanium '80, Science and Technology," AIME, p. 299, 1980.

[43]   P. Crawforth, "Towards a Micromechanistic Understanding of Imparted Subsurface Deformation During Machining of Titanium Alloys," PhD, Department of Materials Science and Engineering, The University of Sheffield, 2014.

[44]   R. E. Goosey, "Development in Titanium Alloys for Aerospace," Met. Mater., vol. 5, no. 8, pp. 451-455, 1989.

[45]   R. R. Boyer, "Titanium and Its Alloys: Metallurgy, Heat Treatment and Alloy Characteristics, Encyclopedia of Aerospace Engineering," ed. Chichester: Wiley, 2010, pp. 2105-2115.

[46]   R. R. Boyer and R. D. Briggs, "The Use of beta Titanium Alloys in the Aerospace Industry," J. Mater. Eng. Perform., vol. 22, no. 10, pp. 2916-2920, 2013.

[47]   A. Carman, L. C. Zhang, O. M. Ivasishin, D. G. Savvakin, M. V. Matviychuk, and E. V. Pereloma, "Role of alloying elements in microstructure evolution and alloying elements behaviour during sintering of a near-beta titanium alloy," Mater. Sci. Eng. A, vol. 528, no. 3, pp. 1686-1693, 2011.

[48]   T. D. Massalski, H. Okamoto, P. R. Subramanian, and L. Kasprzak, Binary Alloys Phase Diagrams. ASM International, 1990, p. 1485.

[49]   G. Neumann and C. Tuijn, Self-diffusion and Impurity Elements Diffusion in Pure Metals: Handbook of Experimental Data. Pergamon Materials Series, Elsevier, 2009, pp. 151-161.

[50]   H. Nakajima, M. Koiwa, Y. Minonishi, and S. Ono, "Diffusion of cobalt in single-crystal alpha-titanium," Transactions of the Japan Institute of Metals, vol. 24, no. 10, pp. 655-660, 1983.

[51]   R. F. Peart and D. H. Tomlin, "Diffusion of solute elements in beta-titanium," Acta Metall., vol. 10, p. 123, 1962.

[52]   Y. Mishin and C. Herzig, "Diffusion in the Ti-Al system," Acta Mater., vol. 48, no. 3, pp. 589-623, 2000.

[53]   A. J. Mortlock and D. H. Tomlin, "The atomic diffusion of chromium in the titanium-chromium system," Philosophical Magazine, vol. 4, no. 41, pp. 628-643, 1959.

[54]   G. B. Gibbs, D. H. Tomlin, and D. Graham, "Diffusion in titanium and titanium-niobium alloys," Philosophical Magazine, vol. 8, no. 92, p. 1269, 1963.

[55]   A. M. Huntz and S. C. Tsai, "Diffusion in oxide scales - application to Cr_2O_3 scales," J. Mater. Sci. Lett., vol. 13, no. 11, pp. 821-825, 1994.

[56]   H. Nakajima, K. Ogasawara, S. Yamaguchi, and M. Koiwa, "Diffusion of chromium in alpha-titanium and its alloys," Mater. Trans. JIM, vol. 31, no. 4, pp. 249-254, 1990.

[57]   S. Y. Lee, Y. Iijima, and K. Hirano, "Diffusion of chromium and palladium in beta-titanium," Mater. Trans. JIM, vol. 32, no. 5, pp. 451-456, 1991.

[58]   R. E. Seebold, "Electron Probe Analysis of the Diffusion Systems Beta-Titanium-Vanadium, Beta-Titanium-Niobium and Chromium-Vanadium, Report," ed. Washington, USA: Naval Research Lab., 1964.

[59]   Z. Liu and G. Welsch, Metall. Trans., vol. A, no. 22A, pp. 946-947, 1991.

[60]   O. M. Ivasishin, D. Eylon, V. I. Bondarchuk, and D. G. Savvakin, "Diffusion during powder metallurgy synthesis of titanium alloys," Diffusion and Diffusional Phase Transformations in Alloys, vol. 277, pp. 177-185, 2008.

[61]   O. M. Ivasishin and D. G. Savvakin, "The Impact of Diffusion on Synthesis of High-Strength Titanium Alloys from Elemental Powder Blends," Cost-Affordable Titanium III, vol. 436, pp. 113-121, 2010.

[62]   R. W. Schutz, Metallurgy and Technology of Practical Titanium Alloys. Warrendale, USA: TMS, 1994.

[63]   J. C. Griess, "Crevice corrosion of titanium in aqueous salt solutions," Corrosion, vol. 24, no. 4, p. 96, 1968.

[64]   B. Vicentini, D. Sinigaglia, and G. Taccani, "Crevice corrosion of titanium - behavior of galvanic cell between shielded and unshielded titanium in sulfuric acid," Corros. Sci., vol. 15, no. 8, pp. 479-492, 1975.

[65]   L. A. Yao, F. X. Gan, Y. X. Zhao, C. L. Yao, and J. L. Bear, "Microelectrode monitoring the crevice corrosion of titanium," Corrosion, vol. 47, no. 6, pp. 420-423, 1991.

[66]   X. H. He, J. J. Noel, and D. W. Shoesmith, "Temperature dependence of crevice corrosion initiation on titanium grade-2," J. Electrochem. Soc., vol. 149, no. 9, pp. B440-B449, 2002.

[67]   R. W. Schutz, "2003 FN. Speller Award Lecture: Platinum group metal additions to titanium: A highly effective strategy for enhancing corrosion resistance," Corrosion, vol. 59, no. 12, pp. 1043-1057, 2003.

[68]   X. He, J. J. Noel, and D. W. Shoesmith, "Effects of iron content on microstructure and crevice corrosion of Grade-2 titanium," Corrosion, vol. 60, no. 4, pp. 378-386, 2004.

[69]   N. D. Tomashov, R. M. Altovsky, and G. P. Chernova, "Passivity and corrosion resistance of titanium and its alloys," J. Electrochem. Soc., vol. 108, no. 2, pp. 113-119, 1961.

[70]   N. D. Tomashov, G. P. Chernova, Y. S. Ruscol, and G. A. Ayuyan, "Passivation of alloys on titanium bases," Electrochim. Acta, vol. 19, no. 4, pp. 159-172, 1974.

[71]   R. S. Glass and Y. K. Hong, "Transpassive behavior of titanium-molybdenum alloys in H_2SO_4," Electrochim. Acta, vol. 29, no. 10, pp. 1465-1470, 1984.

[72]   Y. J. Kim and R. A. Oriani, "Electrochemical-behavior of Ti-30Mo in a gamma-radiolysis environment," Corrosion, vol. 43, no. 1, pp. 56-58, 1987.

[73]   D. G. Kolman and J. R. Scully, "Electrochemistry and passivity of a Ti-15Mo-3Nb-3Al beta-titanium alloy in ambient-temperature aqueous chloride solutions," J. Electrochem. Soc., vol. 140, no. 10, pp. 2771-2779, 1993.

[74]   S. Y. Yu, C. W. Brodrick, M. P. Ryan, and J. R. Scully, "Effects of Nb and Zr alloying additions on the activation behavior of Ti in hydrochloric acid," J. Electrochem. Soc., vol. 146, no. 12, pp. 4429-4438, 1999.

[75]   C. S. Brossia and G. A. Cragnolino, "Effects of environmental and metallurgical conditions on the passive and localized dissolution of Ti-0.15%Pd," Corrosion, vol. 57, no. 9, pp. 768-776, 2001.

[76]   T. Nishimura, "Effect of Molybdenum on the Crevice Corrosion for Titanium Alloys," presented at the Ti-2007 conference, Kyoto, Japan, 2007, p. 1237.

[77]   N. D. Tomashov, G. P. Chernova, G. S. Kalnina, P. B. Budberg and A. L. Gavze, Zashchita metallov., vol. 7, no. 387, 1971.

[78]   G. Lal, Introduction to machining science, 2009, p. 15.

[79]   Sandvik Coromant, Modern Metal Cutting: a Practical Handbook. 1996.

[80]   G. Dieter, Mechanical Metallurgy. McGraw-Hill Companies, 1986, p. 776.

[81]   H. Ernst and M. E. Merchant, Chip formation friction and finish. Cincinnati milling machine company, 1940, p.48.

[82]   M. E. Merchant, "Basic mechanics of the metal cutting process," J. Appl. Mech., pp. 168-175, 1944.

[83]   E. Merchant, "Mechanics of the metal cutting process 1. Orthogonal cutting and a type-2 chip," J. Appl. Phys., vol. 16, no. 5, pp. 267-275, 1945.

[84]   P. J. Arrazola, A. Garay, L. M. Iriarte, M. Armendia, S. Marya, and F. Le Maitre, "Machinability of titanium alloys (Ti6Al4V and Ti555.3)," J. Mater. Process. Technol., vol. 209, no. 5, pp. 2223-2230, 2009.

[85]   R. Komanduri and B. F. Vonturkovich, "New observations on the mechanism of chip formation when machining titanium-alloys," Wear, vol. 69, no. 2, pp. 179-188, 1981.

[86]   M. Cotterell and G. Byrne, "Characterisation of chip formation during orthogonal cutting of titanium alloys Ti-6Al-4V," in CIRP J. Manuf. Sci. Technol., vol. 1, pp. 81-85, 2008.

[87]   D. M. Turley, E. D. Doyle, and S. Ramalingam, "Calculation of shear strains in chip formation in titanium," Mater. Sci. Eng., vol. 55, no. 1, pp. 45-48, 1982.

[88]   N. He, T. C. Lee, W. S. Lau, and S. K. Chan, "Assessment of deformation of a shear localized chip in high speed machining," J. Mater. Process. Technol., vol. 129, no. 1-3, pp. 101-104, 2002.

[89]   D. Sagapuram, H. Yeung, Y. Gao, A. Mahato, R. M'Saoubi, W. D. Compton, K. P. Trumble and S. Chandrasekar, "On control of flow instabilities in cutting of metals," in CIRP Annals-Manuf. Technol., vol. 64, no. 1, pp. 49-52, 2015.

[90]   R. Komanduri and Z. B. Hou, "On thermoplastic shear instability in the machining of a titanium alloy (Ti-6Al-4V)," Metall. Mater. Trans. A, vol. 33, no. 9, pp. 2995-3010, 2002.

[91]   J. Barry and G. Byrne, "Study on acoustic emission in machining hardened steels Part 1: Acoustic emission during saw-tooth chip formation," Proc. Ins. Mech. Eng. B-J. Eng. Manuf., vol. 215, no. 11, pp. 1549-1559, 2001.

[92]   S. Sun, M. Brandt, and M. S. Dargusch, "Characteristics of cutting forces and chip formation in machining of titanium alloys," Int. J. Mach. Tool. Manuf., vol. 49, no. 7-8, pp. 561-568, 2009.

[93]   P. A. Dearnley and A. N. Grearson, "Evaluation of principal wear mechanisms of cemented carbides and ceramics used for machining titanium-alloy IMI 318," Mater. Sci. Technol., vol. 2, no. 1, pp. 47-58, 1986.

[94]   W. Konig, "Proc. 47th Meeting of AGARD Structural and Materials Panel, Florence, Sept. 1978," pp. 1-10.

[95]   M. Thomas, S. Turner, and M. Jackson, "Microstructural damage during high-speed milling of titanium alloys," Scripta Mater., vol. 62, pp. 250-253, 2010.

[96]   Sandvik Coromant, "Wear on cutting edges," [Online]. Available: http://www.sandvik.coromant.com/en-gb/knowledge/materials/cutting_tool_materials/wear_on_cutting_edges/pages/default.aspx. [Accessed 10-Mar-2016].

[97]   Sandvik Coromant, "Technical Guide," Sandviken, Sweden, 2010.

[98]   E. M. Trent, "I.S.I. Report No.94," pp. 11,77,179, 1967.

[99]   B. M. Kramer and P. D. Hartung, Cutting Tool Materials. Am. Soc. for Metals, 1981.

[100]   D. Thakur, B. Ramamoorthy, and L. Vijayaraghavan, "Effect of high speed cutting parameters on the surface characteristics of superalloy Inconel 718," Proc. World Congress Eng. vol. 3, 2010.

[101]   P. Albrecht, "New Developments in the Theory of the Metal-Cutting Process: Part I, The Ploughing Process in Metal Cutting," J. Eng. Ind., vol. 82, no. 4, p. 557, 1960.

[102]   B. M. Kramer and B. von Turkovic, "A Comprehensive Tool Wear Model," CIRP Ann. - Manuf. Technol., 1986, vol. 35, no. 1, pp. 67-70.

[103] N. Muthukrishnan and P. Davim, "Influence of Coolant in Machinability of Titanium Alloy (Ti-6Al-4V)," J. Surf. Eng. Mater. Adv. Technol., vol. 1, no. 1, pp. 9-14, 2011.

[104] K. Dass and S. R. Chauhan, "Machinability Study of Titanium (Grade 5) Alloy Using Design of Experiment Technique," Engineering, vol. 3, no. 6, pp. 609-621, 2011.

[105] J. Taylor, "The tool wear-time relationship in metal cutting," Int. J. Mach. Tool Des. Res., vol. 2, no. 2, pp. 119-152, 1962.

[106] S. I. Jaffery and P. T. Mativenga, "Assessment of the machinability of Ti-6Al-4V alloy using the wear map approach," Int. J. Adv. Manuf. Technol., vol. 40, no. 7-8, pp. 687-696, 2009.

[107] C. Y. H. Lim, S. C. Lim, and K. S. Lee, "Wear of TiC-coated carbide tools in dry turning," Wear, vol. 225, pp. 354-367, 1999.

[108] S. C. Lim, S. H. Lee, Y. B. Liu, and K. H. W. Seah, "Wear maps for uncoated high-speed steel cutting tools," Wear, vol. 170, no. 1, pp. 137-144, 1993.

[109] N. H. Rafai, M. A. Lajis, and N. A. J. Hosni, "Investigation of Tool Wear, Tool Life and Surface Roughness When Machining AISI 02 Hardened Steel Using PVD TiAlN Coated Carbide Tools," 4th Mech. Manuf. Eng., Pts 1 and 2, vol. 465-466, pp. 1098-1102, 2014.

[110] K. Aslantas, I. Ucun, and A. Cicek, "Tool life and wear mechanism of coated and uncoated Al_2O_3/TiCN mixed ceramic tools in turning hardened alloy steel," Wear, vol. 274, pp. 442-451, 2012.

[111] D. Kurniawan, N. M. Yusof, and S. Sharif, "Hard Machining of Stainless Steel Using Wiper Coated Carbide: Tool Life and Surface Integrity," Mater. Manuf. Process., vol. 25, no. 6, pp. 370-377, 2010.

[112] Y.-J. Lin, A. Agrawal, and Y. Fang, "Wear progressions and tool life enhancement with AlCrN coated inserts in high-speed dry and wet steel lathing," Wear, vol. 264, no. 3-4, pp. 226-234, 2008.

[113] S. Y. Hong, I. Markus, and W. Jeong, "New cooling approach and tool life improvement in cryogenic machining of titanium alloy Ti-6Al-4V," Int. J. Mach. Tool. Manu., vol. 41, no. 15, pp. 2245-2260, 2001.

[114] J. Vigneau and S. Derrien, "High Speed Milling of Difficult to Machine Alloys," presented at the First French and German Conference on High Speed Machining, Metz, 1997.

[115] L. N. Lopez de lacalle, J. Perez, J. I. Llorente, and J. A. Sanchez, "Advanced cutting conditions for the milling of aeronautical alloys," J. Mater. Process. Technol., vol. 100, no. 1-3, pp. 1-11, 2000.

[116] A. Jawaid, S. Sharif, and S. Koksal, "Evaluation of wear mechanisms of coated carbide tools when face milling titanium alloy," J. Mater. Process. Technol., vol. 99, no. 1-3, pp. 266-274, 2000.

[117] Z. M. Wang, E. O. Ezugwu, T. Soc, and E. Lubricat, "Performance of PVD-coated carbide tools when machining Ti-6Al-4V," Asme/Stle Tribology Conference, pp. 113-118, 1996.

[118] N. L. Cadena, R. Cue-Sampedro, H. R. Siller, A. M. Arizmendi-Morquecho, C. I. Rivera-Solorio, and S. Di-Nardo, "Study of PVD AlCrN Coating for Reducing Carbide Cutting Tool Deterioration in the Machining of Titanium Alloys," Materials, vol. 6, no. 6, pp. 2143-2154, 2013.

[119] S. H. I. Jaffery and P. T. Mativenga, "Wear mechanisms analysis for turning Ti-6Al-4V-towards the development of suitable tool coatings," Int. J. Adv. Manuf. Technol., vol. 58, no. 5-8, pp. 479-493, 2012.

[120] N. Narutaki, A. Murakoshi, S. Motonishi, and H. Takeyama, "Study of machining of titanium alloys," in CIRP Annals - Manuf. Technol., vol. 32, no. 1, pp. 65-69, 1983.

[121] P. A. Dearnley, M. Schellewald, and K. L. Dahm, "Characterisation and wear response of metal-boride coated WC-Co," Wear, vol. 259, pp. 861-869, 2005.

[122] R. Cherukuri and P. Molian, "Lathe turning of titanium using pulsed laser deposited, ultra-hard boride coatings of carbide inserts," Mach. Sci. Technol., vol. 7, no. 1, pp. 119-135, 2003.

[123] M. Fitzsimmons and V. K. Sarin, "Development of CVD WC-Co coatings," Surf. Coat. Technol., vol. 137, no. 2-3, pp. 158-163, 2001.

[124] E. O. Ezugwu, R. B. Da Silva, J. Bonney, and A. R. Machado, "Evaluation of the performance of CBN tools when turning Ti-6Al-4V alloy with high pressure coolant supplies," Int. J. Mach. Tool. Manuf., vol. 45, no. 9, pp. 1009-1014, 2005.

[125] E. O. Ezugwu, Z. M. Wang, and A. R. Machado, "Wear of coated carbide tools when machining nickel (Inconel 718) and titanium base (Ti-6A1-4V) alloys," Tribol. Trans., vol. 43, no. 2, pp. 263-268, 2000.

[126] H. A. Kishawy, C. E. Becze, and D. G. McIntosh, "Tool performance and attainable surface quality during the machining of aerospace alloys using self-propelled rotary tools," J. Mater. Process. Technol., vol. 152, no. 3, pp. 266-271, 2004.

[127] S. K. Bhaumik, C. Divakar, and A. K. Singh, "Machining Ti-6Al-4V alloy with a wBN-cBN composite tool," Mater. Des., vol. 16, no. 4, pp. 221-226, 1995.

[128] N. Khanna and K. S. Sangwan, "Machinability analysis of heat treated Ti64, Ti54M and Ti10.2.3 titanium alloys," Int. J. of Prec. Eng. Manuf., vol. 14, no. 5, pp. 719-724, 2013.

[129] S. Joshi, P. Pawar, A. Tewari, and S. S. Joshi, "Effect of beta phase fraction in titanium alloys on chip segmentation in their orthogonal machining," J. Man. Sci. Tech., vol. 7, pp. 191-201, 2014.

[130] A. Ugarte, R. M'Saoubi, A. Garay, and P. J. Arrazola, "Machining behaviour of Ti-6Al-4V and Ti-5553 alloys in interrupted cutting with PVD coated cemented carbide," Fifth CIRP Conf. High Performance Cutting, vol. 1, pp. 202-207, 2012.

[131] Y. Kosaka and S. P. Fox, "Influences of alloy chemistry and microstructure on the machinability of titanium alloys," Cost-Affordable Titanium: Symposium Dedicated to Professor Harvey Flower, pp. 169-176, 2004.

[132] M. Armendia, A. Garay, L. M. Iriarte, and P. J. Arrazola, "Comparison of the machinabilities of Ti6Al4V and TIMETAL 54M using uncoated WC-Co tools," J. Mater. Process. Technol., vol. 210, no. 2, pp. 197-203, 2010.

[133] E. A. Rahim, S. Sharif, Z. A. Ahmad, A. S. Mohruni, and I. A. Syed, "Machinability investigation when drilling titanium alloys," presented at the International Conference on Leading Edge Manufacturing in 21st Century, Nagoya, Japan, pp. 553-557, 2005.

[134] J. S. Hewitt, P. D. Davies, M. J. Thomas, P. Garratt, and M. R. Bache, "Titanium alloy developments for aeroengine fan systems," Mater. Sci. Technol., vol. 30, no. 15, pp. 1919-1924, 2014.

[135] M. Jackson, Ti-2015 World Titanium Report, [Online], Available: http://www.iom3.org/materials-world-magazine/news/2015/sep/03/ti2015-world-titanium-report. [Accessed 17-Mar-2016].

[136] S. James, Y. Kosaka, R. Thomas and P. Garratt, "Timetal 407: A titanium alloy to enable cost reduction," Proc. 13th World Conference on Titanium, San Diego, CA, USA, pp. 721-725, 2015.

[137] W. G. Moffatt, The Handbook of Binary Phase Diagrams. Schenectady, New York: The General Electric Company, 1981.

[138] E. Rudy, "Ternary Phase Equilibrium in Transition Metal-Boron-Carbon-Silicon Systems, Part V, Compendium of Phase Diagram Data," ed: Technical Report AFML-TR-65-2, 1969.

[139] M. Hansen, Constitution of the Binary Alloys. New York: McGraw-Hill, 1958.

[140] R. Elliott, Constitution of the Binary Alloys, First Supplement. New York: McGraw-Hill, 1965.

[141] N. Cook and P. Nayak, "The Thermal Mechanics of Tool Wear," J. Eng. Ind., vol. 88, no. 1, p. 93, 1966.

[142] B. Kramer, D. Viens, and S. Chin, "Theoretical consideration of rare earth metal compounds as tool materials for titanium machining," CIRP Annals, vol. 42, no. 1, pp. 111-114, 1993.

[143] M. Palcut, R. Knibbe, K. Wiik, and T. Grande, "Cation inter-diffusion between LaMnO$_3$ and LaCoO$_3$ materials," Solid State Ionics, vol. 202, no. 1, pp. 6-13, 2011.

[144] M. Palcut, "Determination of MN^{3+} DIffusion in LaMnO$_3$ based on solid state reaction method," Department of Materials Technology, Norwegian University of Science and Technology, 2003.

[145] Thermo-Calc Software, ver. 2015b, Available: http://www.thermocalc.com

[146] H. Larsson and L. Hoglund, "Multiphase diffusion simulations in 1D using the DICTRA homogenization model," Calphad, vol. 33, no. 3, pp. 495-501, 2009.

[147] H. Larsson, "A model for 1D multiphase moving phase boundary simulations under local equilibrium conditions," Calphad, vol. 47, pp. 1-8, 2014.

[148] O. Wiener, "Die Mittelwertsätze für Kraft, Polarisation und Energie," vol. 32, ed. Leipzig Abhandl. der math.-phys Klasse der K. Sächs. Gesellschaft der Wissenschaften, 1912.

[149] Z. Hashin and S. Shtrikman, "A variational approach to theory of effective magnetic permeability of multiphase materials," J. Appl. Phys., vol. 33, no. 10, p. 3125, 1962.

[150] A. Engstrom, L. Hoglund, and J. Agren, "Computer-simulation of diffusion in multiphase systems," Metall. Mater. Trans. A, vol. 25, no. 6, pp. 1127-1134, 1994.

[151] A. P. Markopoulos, Finite Element Method in Machining Processes. SpringerBriefs in Manufacturing and Surface Engineering, 2013.

[152] J. A. Bailey, "Friction in metal machining - mechanical aspects," Wear, vol. 31, pp. 243-275, 1975.

[153] A. Molinari and M. Nouari, "Modeling of tool wear by diffusion in metal cutting," Wear, vol. 252, no. 1-2, pp. 135-149, 2002.

[154] E. K. Molchanova, Phase diagrams of titanium alloys, Israel Program for Scientific Translations, Jerusalem, 1965, p. 90.

[155] R. G. Coltters, "Thermodynamics of binary metallic carbides: a review," Mater. Sci. Eng., vol. 76, pp. 1-50, 1985.

[156] A. S. Kurlov, Tungsten Carbides, Springer, Ekaterinburg, 2013, pp. 25-28.

[157] J. R. Davis, Alloying: understanding the basics. ASM International, Ohio, 2001.

[158] K. Fox, "Modelling of high temperature interfacial reactions in continuously reinforced Ti-SiC metal matrix composites," Journal de Physique IV Colloque, vol. 3, no. C7, pp. 1699-1704, 1993.

[159] A. Henjered, M. Hellsing, H. O. Andren, and H. Norden, "Quantitative microanalysis of carbide carbide interfaces in WC-Co-base cemented carbides," Mater. Sci. Technol., vol. 2, no. 8, pp. 847-855, 1986.

[160] G. Östberg, K. Buss, M. Christensen, S. Norgren, H. Andrén, D. Mari, G. Wahnström and I. Reineck, "Mechanisms of plastic deformation of WC-Co and Ti(C, N)-WC-Co," Int. J. Refract. Met. H., vol. 24, no. 1-2, pp. 135-144, 2006.

[161] G. Östberg and H. Andrén, "Microstructural changes during wear by plastic deformation of cemented carbide and cermet cutting inserts," Metall. Mater. Trans. A, vol. 37A, no. 5, pp. 1495-1506, 2006.

[162] M. Christensen and G. Wahnström, "Co-phase penetration of WC(1010)/WC(1010) grain boundaries from first principles," Phys. Rev. B, vol. 67, no. 11, 2003.

[163] Thermo-Calc Software, DICTRA module, ver. 2015b.

[164] Thermo-Calc Software, "TCFE8 Steels/Fe-alloys database ver. 8." [Online] Available: http://www.thermocalc.com/media/10864/dbd_tcfe8.pdf. [Accessed: 07-Jan-2016].

[165] Thermo-Calc Software, "MOBFE3 Steels/Fe-alloys mobility database ver. 3." [Online] Available: http://www.thermocalc.com/media/6014/dbd_mobfe3.pdf. [Accessed: 07-Jan-2016].

[166] Thermo-Calc Software, "SSOL4 SGTE Solutions database ver. 4." [Online] Info. ver. 6 available: http://www.thermocalc.com/media/11309/ssol6_extended_info.pdf. [Accessed 07-Jan-2016].

[167] Thermo-Calc Software, "MOB2 mobility database ver. 2." [Online] Available: http://www.thermocalc.com/media/6015/dbd_mob2_bh.pdf. [Accessed: 07-Jan-2016].

[168] A. Borgenstam, A. Engstrom, L. Hoglund, and J. Agren, "DICTRA, a tool for simulation of diffusional transformations in alloys," J. Phase Equilib., vol. 21, no. 3, pp. 269-280, 2000.

[169] M. Thomas, J. Hewitt, M. Bache, R. Thomas, P. Garratt, and Y. Kosaka, "TIMETAL 575: A novel high strength forgeable alpha/beta titanium alloy," Proc. 13th World Conference on Titanium, San Diego, CA, USA, 2016, pp. 1537-1541.

[170] D. Rugg, M. Dixon, and F. P. E. Dunne, "Effective structural unit size in titanium alloys," J. Strain Anal. Eng. Des., vol. 42, no. 4, pp. 269-279, 2007.

[171] H. W. Rosenberg, The Science, Technology and Application of Titanium. Oxford, UK: Pergamon Press, 1970.

[172] L. Marshall, "The influence of aluminium additions on titanium during machining through the application of a novel orthogonal cutting test method," PhD, The University of Sheffield, 2014.

[173]   Y.-j. Zheng, Y.-x. Leng, X. Xin, Z.-y. Xu, F.-q. Jiang, R. Wei and N, Huang, "Evaluation of mechanical properties of Ti(Cr)SiC(O)N coated cemented carbide tools," Vacuum, vol. 90, pp. 50-58, 2013.

[174]   Seco Tools, "MS2050 grade". [Online]. Available: http://www.secotools.com/ms2050. [Accessed: 12-Oct-2016].